Multi-Trace Element Distribution in Olivine from the Eastern Deeps Deposit, Voisey's Bay Intrusion, Labrador: Olivine Composition as a Record of Ore-forming Processes in Evolved Magma Systems

by

© Florian Bulle

A Dissertation submitted to the School of Graduate Studies

in partial fulfillment of the requirements for the degree of

Doctor of Philosophy

Department of Earth Sciences

Memorial University of Newfoundland

May 2014

St. John's, Newfoundland

ABSTRACT

The distribution of Ni-Mg-Fe in olivine is used extensively to characterize mafic intrusions, and, in combination with other geochemical tools, assess their Ni-Cu-Co sulfide mineralization potential. Despite the availability of sensitive analytical techniques (e.g., Secondary Ion Mass Spectrometry – SIMS) and the proven importance of olivine multi-trace element studies to igneous petrology, a more comprehensive geochemical approach of determining multiple trace elements in olivine has never been adopted for economic geology applications. For this dissertation I implemented a refined SIMS analytical protocol for the determination of multiple major-trace elements in olivine from the Eastern Deeps Intrusion (EDI), a part of the Voisey's Bay Intrusion (VBI), Labrador. The study demonstrated that systematic, lithology-dependent trace element variations in olivine, particularly in Ni, Co, Cr, Mn, and Zn, characterize critical ore-forming processes and indicate the proximity to zones of massive sulfide mineralization in the EDI.

SIMS is an analytical technique for the in-situ, micrometer-scale determination of elements in a solid sample with very low detection limits. Chapter 2 introduces the SIMS analytical parameters applied for the olivine analyses and further discusses the reference material development and the sequential empirical calibration.

The subsequent chapters detail the SIMS studies of olivine from the EDI and Pants Lake Intrusion (PLI). Chapter 3 demonstrates that lithostratigraphic variations in olivine Ni-Co contents (~80–2,500 ppm Ni; ~170–370 ppm Co) in the EDI indicate magmatic episodicity and multiple sulfide saturation events. The basal, incongruent olivine Mn-Zn enrichment (up to 12,000 ppm Mn; up to 680 ppm Zn) reflects country rock

ii

contamination followed by a diffusive trace element exchange with surrounding sulfide liquid. Chapter 4 discusses the application of the olivine trace chemistry as a lateral vector towards sulfide mineralization in the EDI, and as a fertility indicator for mafic intrusions on a regional scale (ex. PLI). Progressively increasing contents of Mn-Zn in olivine towards the inner basal margin of the EDI indicate spatial (vertical and lateral) proximity (~150m) to massive sulfides. A strong compositional bimodality (e.g., Ni-enriched and Ni-depleted) of olivine also increases the potential for inherent economic mineralization (ex. VBI). This study considerably improved our understanding of systematic compositional variations in olivine as a response to essential ore-forming processes in mineralized mafic magmatic systems.

ACKNOWLEDGEMENTS

appreciate especially Peter's knowledgeable and constructive feedback to parts of my Ph.D. thesis, concerning the geochemistry and petrology of the VBI.

I also acknowledge that Rod Smith permitted me to examine samples from his study of the Pants Lake Intrusion(s), which provided a crucial additional field test for our SIMS olivine method and important geochemical discrimination criteria for barren to sub-economic mafic intrusions.

The years I spend pursuing my Ph.D. research were made enjoyable in large parts due to the many friends and various Ultimate Frisbee Teams that became part of my life. I am especially grateful to "zee" other Germans (LMS, DH, PH, EK) who walked this sometimes rocky road with me, for so many educated, silly, and helpful discussions during our coffee breaks and the numerous exciting trips around the island.

Lastly I would like to thank my family for their unfaltering love and encouragement. For my parents and my brother who supported me in all my pursuits. And of course for my loving, encouraging, and patient partner Lina, whose moral support during the final stages of this thesis is so greatly appreciated.

It is at times difficult to put the magnitude of all the not-directly-university-related support in proper words, but to the best of my knowledge I would say, it kept me steady and afloat during the last five years and represented a safe and sound shoreline to turn to when needed. *Thank you*.

Florian Bulle

Memorial University

August 2013

TABLE OF CONTENTS

LIST OF TABLES

LIST OF FIGURES

CHAPTER 3

CHAPTER 4

CHAPTER 5

CO-AUTHORSHIP STATEMENT

The doctoral thesis and the research papers presented here (Chapter 2–4) have been prepared predominantly by the thesis author, with guidance from my supervisor Dr. Graham D. Layne. Some of the SIMS analyses presented in Chapter 3 were conducted by Glenn Piercey in 2011. The Voisey's Bay samples used in Chapter 4 were collected in summer 2011 by Jennifer Glasgow. The samples from the Pants Lake Intrusion presented in Chapter 4 were made from existing offcuts from the Smith (2006) study with permission from Rod Smith. Lina M. Stolze generously offered her assistance with some of the statistical analyses presented in Chapter 3 and Chapter 4. Beside these contributions, the design of the research proposal, the sample collection, preparation, and processing, the analytical work, the data collection, and interpretation, as well as the manuscript preparation was conducted exclusively by the thesis author.

CHAPTER 1 - Introduction

1.1. Aim and Content of the Study

1.1.1. General Background

Economic magmatic Ni-Cu-Co-(PGE) sulfide deposits are almost exclusively associated with mafic to ultramafic igneous rocks, and thus, their formation is generally an integral part of the petrogenesis of their host intrusive (e.g., Noril'sk, Bushveld, Duluth Complex, Jinchuan, Voisey's Bay) or extrusive rocks (e.g., Kambalda-type deposits) (e.g., Keays, 1995; Lesher et al., 2001; Arndt et al., 2005; Naldrett, 2010a, and references therein). However, the potential of economic Ni-Cu ore-formation hinges on some key requirements (Fig.1.1):

1) The presence of a "primitive" (high-Mg) and chalcophile element-rich mafic to ultramafic magma.

2) The mafic magma must attain sulfide saturation and subsequently segregate an immiscible sulfide liquid.

3) The sulfide melt must interact dynamically with a high volume of silicate magma (high silicate:sulfide ratio - R-factor; Campbell and Naldrett, 1979) that effectively upgrades the metal tenor of the sulfide liquid (e.g., Bremond d'Ars et al., 2001; Maier et al., 2001).

4) The enriched sulfide fraction must be concentrated in economic quantity (Fig.1.1; e.g., Naldrett, 1997; 1999; Arndt et al., 2005; Naldrett, 2010b).

There are of course several factors that individually constrain these requirements, especially during magma ascent, dynamic transport and emplacement. The necessity of the mafic magma to assimilate externally-derived sulfur to promote sulfide saturation (e.g., Keays and Lightfoot, 2010; Ripley and Li, 2013, and references therein) and a favorable regional tectonic setting are, for instance, both widely regarded as essential factors governing economic Ni-Cu sulfide mineralization (e.g., Naldrett, 1997; 1999; 2010b, and references therein). A "favorable" tectonic setting in this context must facilitate the transfer of sufficient quantities of mafic magma from the upper mantle into crustal levels (e.g., Keays, 1995; Naldrett, 1999; Lightfoot and Keays, 2005; Maier and Groves, 2011; Maier et al., 2012). Further, it also needs to stimulate the economic accumulation and concentration of sulfides in restricted morphological traps (Fig.1.1; e.g., Evans-Lamswood et al., 2000; Lightfoot et al., 2012, and references therein).

A wide range of lithogeochemical exploration methods are commonly applied to discern if some or even all of the above mentioned requirements are satisfied in a Ni-Cu exploration target. Methods include analyses of whole-rock compositions (e.g., Pd/Cu, Cu/Zr ratios, Mg#, incompatible elements), the determination of the mineral chemistry (e.g., Mg# and Ni content in olivine and orthopyroxene), and (bulk) stable isotope measurements (δ^{34}S or δ^{18}O). Reviews of some of the most commonly used techniques can be found in Naldrett (1997), Maier et al. (1998), Lesher et al. (2001) and Lamberg (2005). These mineral exploration techniques have been validated over the years through the description and delineation of existing ore deposits to formulate models that can be extrapolated to predict potential exploration targets.
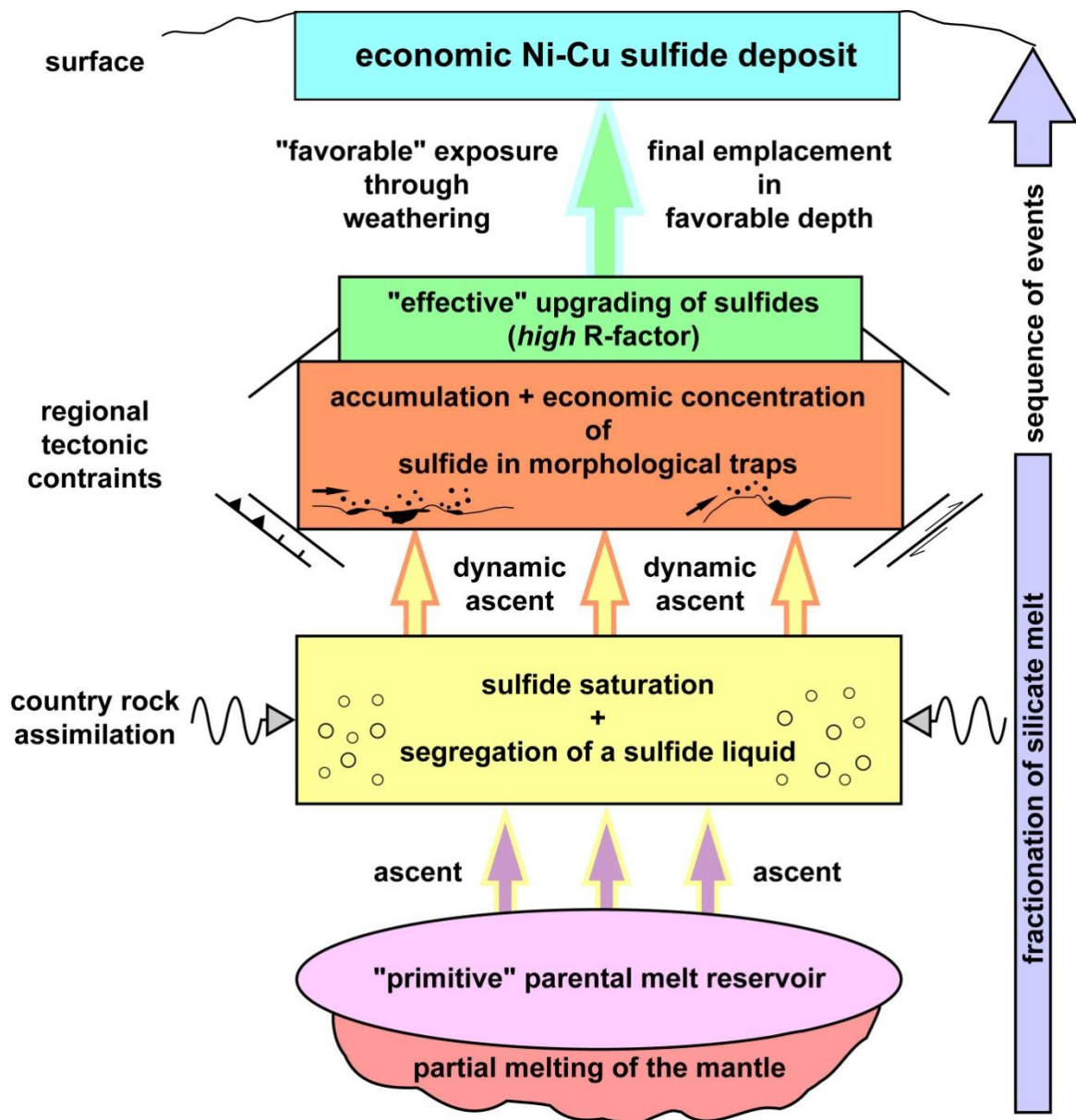
Fig. 1.1: Key stages and requirements in the formation of an economic Ni-Cu-Co magmatic sulfide deposit (after Naldrett, 2010 and references therein; Lightfoot et al., 2012).

In the case of some PGE and many Ni-Cu sulfide deposits, the olivine composition is used to infer the primitiveness of the parental melt (Mg# or forsterite content) and to determine the extent of sulfide segregation (Ni depletion) (e.g., Lightfoot et al., 1984; Chai and Naldrett, 1991; Li and Naldrett, 1999; Li et al., 2000; Li et al., 2002; Li et al., 2003a; Li et al., 2004; Ripley et al., 2007; Maier et al., 2010). Olivine is an early-crystallizing phase in host intrusions of most sulfide deposits, and its compositional variations thus reflect many early-magmatic conditions and processes (e.g., silicate melt composition and early differentiation, magma mixing, assimilation and fractional crystallization). Olivine-normative magmas have generally higher Ni contents and a higher liquidus temperature than more silicic melts, which means they can assimilate sulfide-bearing country rock more readily and thus have a higher potential to form economic Ni sulfide deposits (e.g., Naldrett, 1999). The geochemical importance of olivine as an indicator mineral is therefore undeniable. The use of olivine is further promoted because the basic compositional information (Mg, Fe, and Ni content) can be determined easily by Electron-Probe Micro Analysis (EPMA). However, to utilize the full potential of the olivine chemistry as a possible sulfide fertility indicator, which is applicable even in grass-roots Ni-exploration, the distribution of elements other than Mg, Fe, and Ni must be considered. For instance, the partitioning of several compatible and incompatible chalcophile (Co, Ni, Cu), lithophile (Ca, Sc, Ti, V, Sr, Y, Zr) and siderophile (Cr, Mn, Fe, Zn) elements might reflect several of the key factors in Ni-Cu sulfide ore-formation, instead of just sulfide segregation. This could in turn increase the geochemical resolution and consequently increase the chance of successful early-stage

Ni-target generation. The distribution of trace elements in general is much more sensitive to "economically-desired" petrological perturbations (Arndt et al., 2005) during normal petrogenesis of a mafic to ultramafic intrusion than are major element mineral and bulk-rock data.

1.1.2. Problem Statement

Olivine is ubiquitous in most mafic intrusions associated with magmatic Ni-Cu-Co-(PGE) sulfide deposits, and thus its chemical composition (namely MgO-FeO-NiO contents; see Sato, 1977; Hart and Davis, 1978) has been widely used in mineral exploration as a tracer for (concealed) sulfide segregation (e.g., Lightfoot et al., 1984; Maier et al., 1998 and references therein; Li and Naldrett, 1999). However, beyond this traditional application, the trace element distribution of olivine has never been investigated in a Ni-Cu ore-forming environment, nor as a complementary nor potentially more powerful geochemical (exploration) tool, even though many studies demonstrate the petrological importance of (systematic) variations in the olivine trace element composition (see also paragraph 1.3.).

A geochemical identification and discrimination between the key ore-forming processes based on the distribution of certain compatible and incompatible trace elements in olivine is thus an attempt to: 1) close this existing gap with a comprehensive database for the well-characterized Voisey's Bay Intrusion (VBI), Labrador; 2) demonstrate the geochemical advantages of olivine trace element data for characterizing ore-forming

environments (ex. VBI); and 3) to establish a readily applicable and feasible geochemical (exploration) method for evolved mafic magma systems, such as the VBI. The olivine trace element chemistry and the included petrogenetic information are the focal point of this thesis and was investigated for the economic Voisey's Bay Ni-Cu deposit in Labrador, Canada (Chapter 3 and 4) and the geologically similar, but barren to sub-economic Pants Lake deposit, Labrador (Chapter 4). Secondary Ion Mass Spectrometry (SIMS) is the analytical technique utilized in this study to measure trace elements in olivine at appropriate detection limits of less than 1 ppm.

1.1.3. Research Objectives

The primary scientific objective of this study is **to identify the key ore-forming processes active during the petrogenesis of the Eastern Deeps Intrusion (EDI) in the VBI and discriminate them as a function of their petrological significance based on variations in the trace element composition of olivine.** The applied methodological approach and the olivine trace element systematics should then translate into a practical and feasible geochemical exploration tool that provide additional vectors towards zones of sulfide mineralization at the VBI and elsewhere, and assists in first-order discrimination between barren and mineralized mafic intrusions.

The main objective is tripartite and encompasses, **analytical**, **geochemical**, and **exploration** benefits. In order of appearance these include specific scientific aims:

1) *analytical aspect* – the purpose is to establish a SIMS analytical approach that allows routine accurate and precise determination of the forsterite content and multiple trace elements in compositionally variable olivine (forsterite-fayalite) in **one** feasible analytical step;

2) *geochemical aspect* – the intent is to use the element distribution of Ca, Sc, Ti, V, Cr, Mn, Co, Ni, Cu, Zn, Sr, Y, Zr (or the most practical subset) as well as the forsterite content (Mg/Fe molar ratio) of olivine from primarily the Eastern Deeps segment of the VBI to identify the geochemical processes that are key to ore-formation (e.g., magma mixing, melt differentiation, contamination, sulfide saturation) and interpret systematic variations based on the evolved mafic character of the VBI, the silicate/sulfide melt interaction, and the dynamics of an economically mineralized magma conduit system;

3) *exploration aspect* – the previous aspects are eventually combined to establish a practicable (time- and cost-effective) trace element-in-olivine routine that expands the traditionally applied Mg-Fe-Ni olivine exploration approach and ultimately increases the geochemical sensitivity and applicability to better discriminate between barren and mineralized environments and potentially predict zones of massive sulfide concentrations in the VBI and fertility on a regional scale and elsewhere.

1.1.4. Potential Limitations

All of the specific objectives of this study contain potential limitations that might hamper their achievement.

1) *analytical* – the selected suite of analytes includes (trace) elements with highly variable chemical characteristics (e.g., charge/size ratio, compatibility etc.) and hence highly variable contents in olivine (≤ 0.1 ppm to ≥ 10.000 ppm). Although the SIMS instrumental approach was specifically designed to routinely analyze this suite of elements, individual atomic species are variably affected by energy filtering and consequently elemental sensitivities and detection limits might vary. This analytical compromise could then bias the quantification of some of the very low abundance elements (e.g., Sc, Cu, Zr);

2) *geochemical* – many olivine trace element studies show that individual partitioning behavior depends on melt composition, temperature, pressure, and oxygen fugacity. Therefore, the use of this extended suite of trace elements also complicates geochemical interpretation and petrological modeling of the data. The VBI constitutes a complex, open system, which experienced episodic magma mixing, country rock contamination, and possibly several sulfide saturation events. In this less-constrained system, the distribution behavior of many trace elements (e.g., V, Cr, Co, Mn, Zn) is still poorly understood. This might challenge the interpretation of the data and the use of (empirical) petrogenetic models that utilize partition coefficients, since those can vary extensively with the above mentioned parameters (e.g., Rollinson, 1993);

3) *exploration* – systematic trace element variations in different olivine populations from the VBI (barren and mineralized) may be ambiguous or completely absent and thus limit or even prevent the use of this approach as a geochemical (mineralogical indicator) exploration tool. Furthermore, olivine from the EDI is the main focus of this study and thus extrapolating the results to other geological environments (at the VBI or elsewhere) might be equivocal and not uniformly applicable until a versatile and robust regional olivine database is established.

1.2. Key Geological Features of the Voisey's Bay Ni-Cu-Co Sulfide Deposit

The Voisey's Bay intrusion (VBI; 1,332.7 ±1.0 Ma; Amelin et al., 1999) is an evolved mafic member of the Mesoproterozoic Nain Plutonic Suite (NPS). The NPS occupies a vast area in northern Labrador, and is composed of a suite of bimodal mafic (anorthositic, troctolitic, ferrodioritic) and felsic (monzonitic and granitic), mid- to upper-crustal igneous rocks emplaced between 1,350 and 1,290 Ma proximal to the Torngat orogen (Ryan, 2000; and references therein). This tectonic suture zone represents the Paleoproterozoic amalgamation of the mainly Proterozoic Churchill Province in the west and the mostly Archean Nain Province in the east (Ryan, 2000; and references therein). Proximal to this major tectonometamorphic zone, a so-far unique, major Ni-Cu-Co sulfide deposit is hosted by the olivine-gabbroic to troctolitic VBI (e.g., Lightfoot and

Naldrett, 1999; Evans-Lamswood et al., 2000; Lightfoot et al., 2012). After almost two decades of intense research and exploration activity, it is currently understood that:

1) the deposit is associated with several troctolitic to olivine-gabbroic bodies (subchambers), which are linked by a complex olivine-gabbro feeder system (magma conduits); and that

2) the presently identified bodies of major massive and disseminated sulfide mineralization occur either close to or within the feeder dike (Reid Brook, Discovery Hill, Mini-Ovoid and Ovoid), or at the entry line of the feeder system into an upper subchamber (Eastern Deeps) (e.g., Lightfoot and Naldrett, 1999; Li and Naldrett, 1999; Li et al., 2000; Evans-Lamswood et al., 2000; Lightfoot et al., 2012).

However, unlike other large Ni-Cu sulfide deposits (Noril'sk or Jinchuan), the VBI is an evolved mafic magma system where sulfide formation and ore localization is also genetically related to the flow dynamics and the (tectonically) confined geometry of the magma conduit(s) (e.g., Evans-Lamswood et al., 2000; Lightfoot et al., 2012). Several pulses of variable differentiated mafic magma are responsible for entraining, transporting and subsequently upgrading sulfides during the formation of the VBI, inasmuch as they precipitated and concentrated sulfides in physical traps or zones of reduced flow velocity, for example, in widened parts of the conduit or at the entry point into the Eastern Deeps Intrusion (EDI; Evans-Lamswood et al., 2000; Lightfoot et al., 2012).

The combination of several key magmatic ore-formation requirements (see above) makes the VBI, and especially the EDI, a prime target for a detailed study of olivine trace element geochemistry. The petrological information contained in olivine from different

stratigraphic intervals and lithologies might reflect several key stages (e.g., primitive melt, country rock contamination, sulfide saturation-segregation-transportation, and upgrading, as well as economic concentration) in the petrogenesis of the VBI and the associated magmatic Ni-Cu sulfide deposit (Chapter 3 and 4). The data can then be applied to further refine the geological model, yield a potential geochemical vector towards zones of massive sulfide accumulation, and might be extrapolated to predict mineralization in comparable mafic magmatic environments.

1.3. Olivine – Crystallography, Chemistry and Petrological Significance

Olivine is a major constituent in any ultramafic and many mafic igneous rocks (i.e., dunite, peridotite, basalt, gabbro) and the dominant mineral phase in the Earth's upper mantle. The olivine-group comprises orthosilicates with orthorhombic symmetry with the general formula M_2SiO_4 where M is a combination of Mg, Fe^{2+} and Ca, Mn (e.g., Putnis, 1992; Deer et al. 1997). The structure is composed of isolated $[SiO_4]$ tetrahedra (4-fold coordinated T-site) linked to two distinct 6-fold coordinated octahedral sites (M1 and M2) primarily containing the divalent cations Mg^{2+} and Fe^{2+} (Fig.1.2). These M lattice positions are slightly distorted and thus not perfectly symmetrical, with M1 being somewhat smaller and less distorted than M2 (Fig.1.2; Putnis, 1992; Deer et al., 1997). Therefore, the olivine structure is only approximately arranged in a hexagonally close-packed oxygen array where the M cations fill merely 1/2 of the potential octahedral sites and the Si cations 1/8 of the potential tetrahedral sites. The replacement of the smaller Mg

(0.72 Å) by the slightly larger Fe^{2+} (0.78 Å) cation in the forsterite-fayalite solid solution (Fo_{100}: Mg_2SiO_4 – Fa_{100}: Fe_2SiO_4) is reflected by a linear increase in unit cell parameters (Deer et al., 1997; Fig.1.2).

In general, compositions in the olivine group form extensive solid solutions, and primarily vary between forsteritic (senso lato in ultramafic to mafic igneous rocks) and fayalitic (s.l. in ferrogabbros to felsic igneous rocks) (Fig.1.3A). Rare Ca-bearing compositions can occur (monticellite: $CaMgSiO_4$ and kirschsteinite: $CaFeSiO_4$), whereas fayalite also displays a complete diadochy with the rare Mn-endmember tephroite (Mn_2SiO_4). However, virtually no solid solution exists between the Ca-bearing olivine and the ferromagnesian compositions (Fig.1.3A), since the cation size discrepancy between Ca (1.00 Å) and Fe-Mg, respectively, exceeds the strain tolerance of the olivine structure (e.g., Davidson and Mukhopadhyay, 1984). Although, the structural response to an increase in temperature is a significant increase in size of the M1 and M2 sites, which promotes the substitution of larger cations, for instance, Ca into the olivine structure (e.g., Hazen 1976, 1977; O'Reilly et al., 1997). An increase in pressure on the other hand, has the opposite effect on the olivine structure and is equivalent to a temperature decrease (e.g., Hazen 1976, 1977). In consequence, substitution of Fe-Mg ($\pm Si^{4+}$) by other cations is primarily controlled by the physical properties of the olivine crystal lattice and the ionic radii and valence states (Fig.1.3B) of partitioning cations (e.g., Beattie, 1994; Zanetti et al., 2004; Grant and Wood, 2010, and references therein). An increasing size/charge discrepancy then results in an increasing incompatibility, for instance, Ca^{2+} (1.00 Å; $D^{Ca}_{Ol/Sil}$ <<1) and Mn^{2+} (0.83 Å; $D^{Mn}_{Ol/Sil}$ ~1) (e.g., Beattie, 1994; Kohn and Schofield,

1994; Zanetti et al., 2004, and references therein). Therefore, concentrations of most altervalent (1+, 3+, 4+, 5+) cations are nearly always in trace concentration-range and thus very close to or below the detection limit for EPMA (e.g., Zanetti et al., 2004).

The $Mg_2SiO_4 - Fe_2SiO_4$ system is considered an almost "ideal" solid solution, and only the Fe/Mg ratio is controlling the relatively simple compositional range. However, the petrological importance of olivine stems primarily from the fact that it is the first phase to crystallize at low pressure on the liquidus of mantle-derived ultramafic to mafic magmas, and its composition thus reflects the composition of the mantle source region (e.g., Bowen and Schairer, 1935; Roeder and Emslie, 1970; Sato, 1977; Hart and Davis, 1978). After Bowen and Schairer (1935) experimentally defined the phase boundaries of the $FeO-MgO-SiO_2$ system (Fig.1.4), Roeder and Emslie (1970) experimentally developed and empirically calibrated the Fe-Mg exchange equilibrium (equilibrium constant K_d) between olivine and silicate liquid that now allows quantification of the temperature and the composition of a parental melt in equilibrium with crystallizing olivine. This is a key constraint in any model of (basaltic) magma petrogenesis (e.g., Pearce, 1978; Thomson and Maclennan, 2013, and references therein). This discovery has thus become a cornerstone in igneous petrology (Canil et al., 2001), even though its established Fe-Mg K_d value of 0.3 (±0.03; Roeder and Emslie, 1970) is now known to vary with changes in pressure, temperature, melt composition, melt polymerization and oxygen fugacity (e.g., Putirka, 2008; Thomson and Maclennan, 2013). However, because of its wide application in basalt petrogenesis and upper mantle evolution, the Fe-Mg exchange has been further implemented by numerous olivine-liquid trace element partitioning studies (e.g., Häkli

and Wright, 1967; Duke, 1976; Sato, 1977; Colson et al., 1988; Beattie et al., 1991; Snyder and Carmichael, 1992; Beattie, 1994; Gaetani and Grove, 1997; Taura et al., 1998; Zanetti et al., 2004; Bédard, 2005; Grant and Wood, 2010; DeHoog et al., 2010). These are either applied to refine the composition of the upper mantle source region (e.g., Sato, 1977; Hart and Davis, 1978; O'Reilly et al., 1997; Canil and Fedortchouk, 2001; DeHoog et al., 2010), to characterize the input of recycled crustal material into the mantle to decipher mantle heterogeneity (e.g., Sobolev et al., 2007; Herzberg et al., 2013), or to monitor thermobarometric constraints (e.g., Häkli and Wright, 1967; Köhler and Brey, 1990; Falloon et al., 2007; Putirka, 2008). Other applications however, focus on the petrogenesis of extraterrestrial bodies, such as the crustal evolution of the Moon and the fractionation of the lunar magma ocean (e.g., Papike et al., 2005; Shearer et al., 2006; Hagerty et al., 2006; Filiberto et al., 2009; Longhi et al., 2010), or study core formation and early differentiation events of the terrestrial planets by the partitioning of siderophile elements between olivine and silicate (or immiscible sulfide-metal) melt(s) (e.g., Gaetani and Grove, 1997; Holzheid et al., 1997; Holzheid and Grove, 2005).

The trace element partitioning between olivine and silicate melt is not only attributable to the composition (and other intensive parameters) of the parental melt, but is also very sensitive to sulfide saturation and the fractionation of a sulfide liquid (e.g., Clark and Naldrett, 1972; Hart and Davis, 1978; Rajamani and Naldrett, 1978; Fleet et al., 1981; Fleet and McRae, 1983; Li et al., 2003b). This process is critical during the formation of a Ni-Cu sulfide deposit and is reflected primarily in a Ni-depletion of olivine (e.g., Lightfoot et al., 1984; Li and Naldrett, 1999; Li et al., 2000).
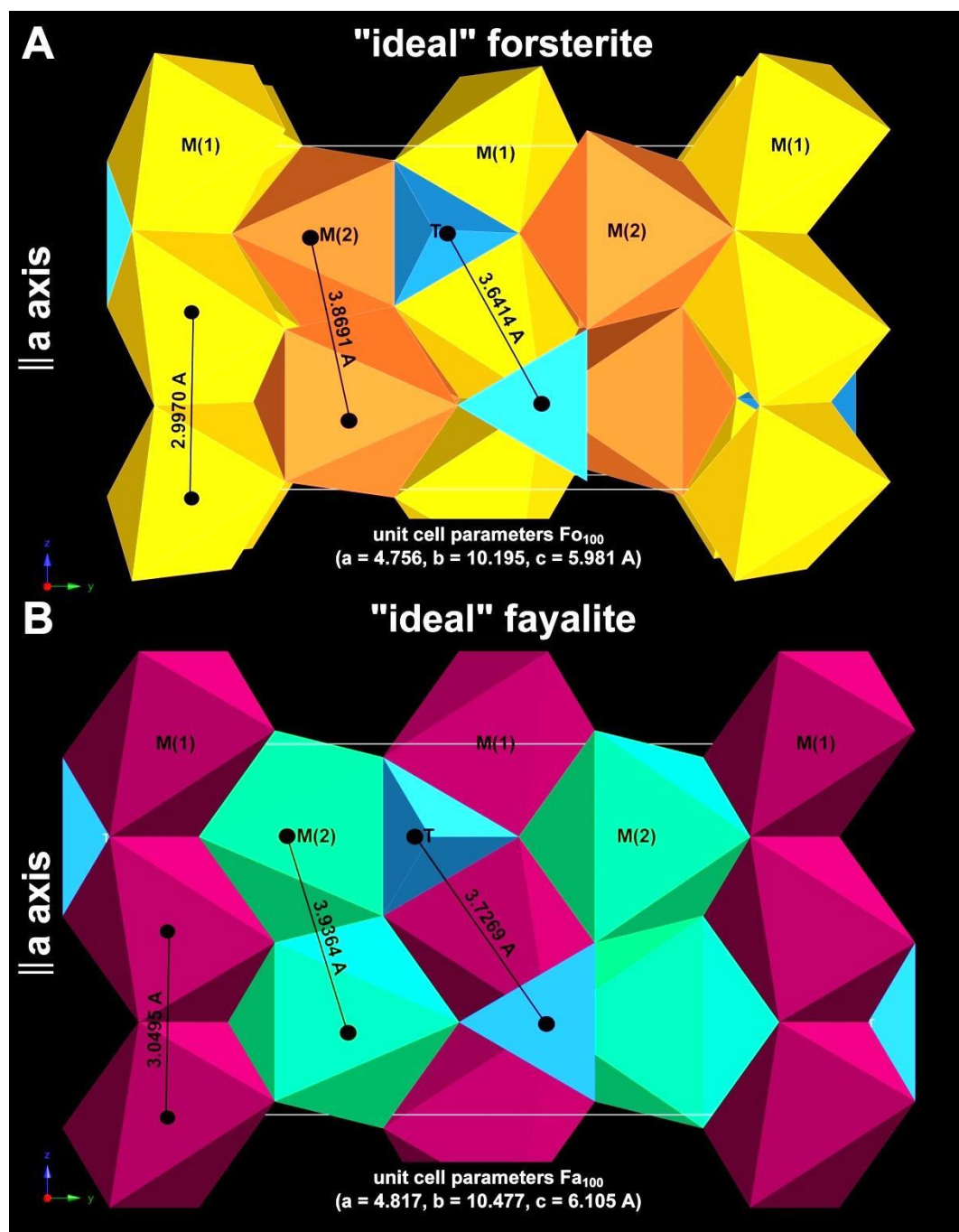
Fig. 1.2: "Ideal" forsterite-fayalite structure parallel to (100) plane. 4-fold coordinated tetrahedral sites are marked as T, and 6-fold coordinated octahedral sites as M(1) and M(2). Mg-Fe atoms are distributed almost randomly between both sites (ordering is temperature-dependent; Zanetti et al., 2004). Bond distances (in Å) are indicated by black lines, and increase from forsterite to fayalite. Images were generated using CrystalMaker®.

Although the olivine trace element chemistry and partitioning behavior is successfully applied in mantle-petrology and basalt petrogenesis, it has never been fully utilized in an economic geology framework, or as a geochemical exploration tool ("fertility indicator"). This might partly be because most trace element concentrations in olivine are extremely low (less than 10 ppm) and thus not detectable with EPMA, and barely quantifiable even with more sophisticated analytical instruments such as laser ablation-inductively coupled plasma-mass spectrometry (LA-ICP-MS) or SIMS.
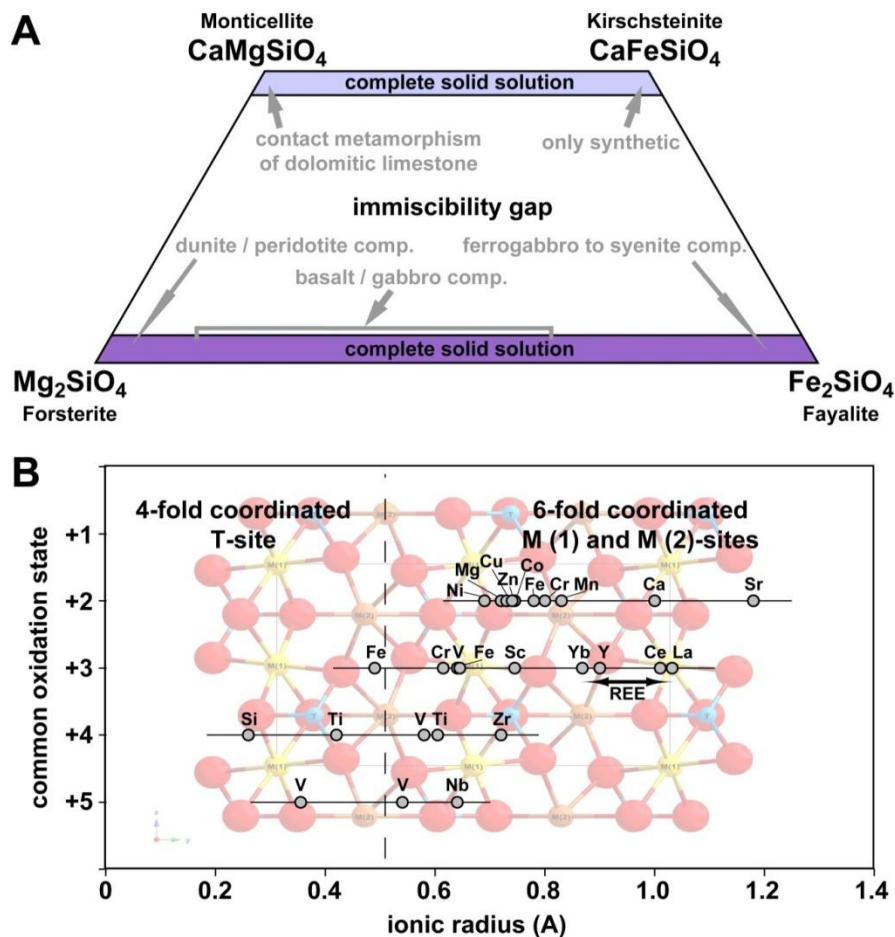
Fig. 1.3: A) Olivine quadrilateral (after Papike et al., 2005) and the most common solid solutions in their respective geological environment. B) Site preferences for common trace elements in the olivine structure as a function of ionic radius and valence state (and coordination numbers) (after DeHoog et al., 2010).
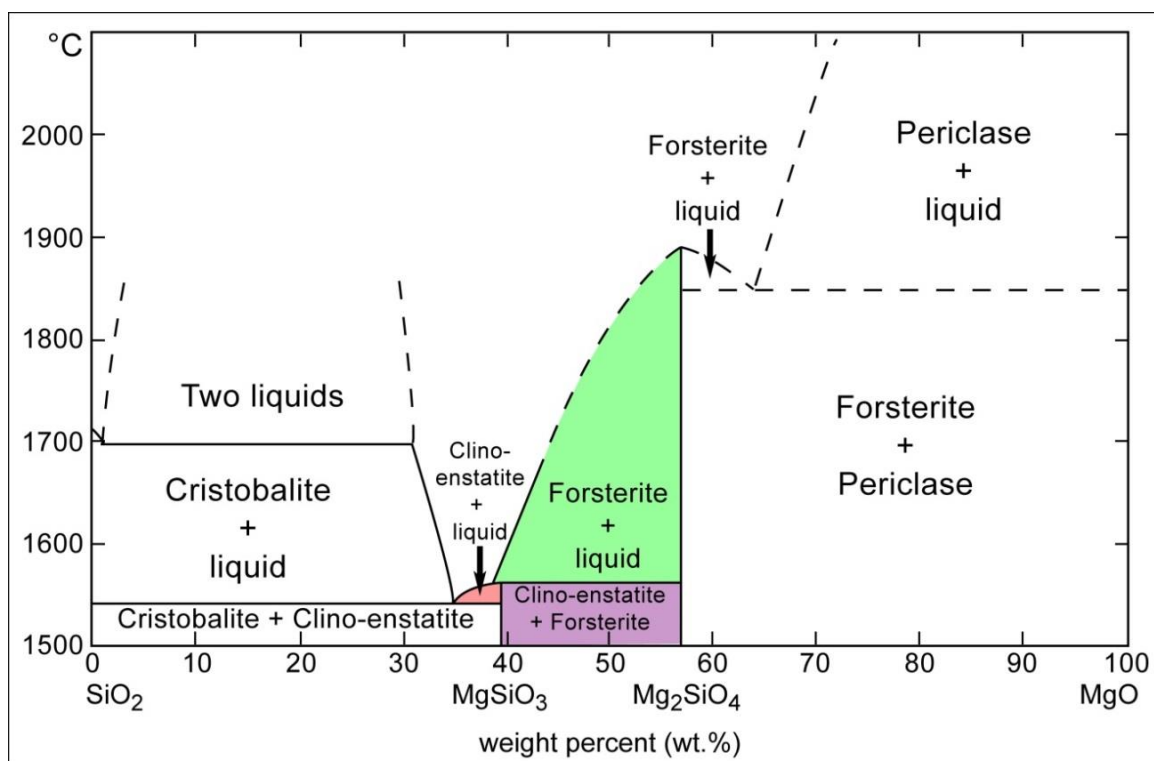
Fig. 1.4: Phase diagram of the MgO-SiO$_2$ system (after Bowen and Schairer, 1935). Given a SiO$_2$ melt content between circa 43 to 61 wt.%, olivine crystallizes (equilibrium crystallization) until around 1550°C, before it reacts with the liquid to form a MgSiO$_3$ pyroxene (e.g. clinoenstatite).

Although advances have been made in the use of SIMS in olivine analyses (e.g., Shimizu et al., 1978; Reed et al., 1979; Steele et al., 1981; Shimizu and Hart, 1982; Weinbruch et al., 1993; Taura et al., 1998; Ito et al., 1999; Ottolini et al., 2002; Lehmann, 2003; De Hoog et al., 2010), the application is still severely limited to Mg-rich compositions (as found in mantle xenoliths and ultramafic rocks), because analytical difficulties (namely isobaric interferences and matrix effects; Shimizu and Hart, 1982 and references therein) considerably bias the quantification of more fayalitic olivine. Fe-rich compositions (Fo$_{40}$ to Fo$_{75}$), however, are dominant in many economic Ni-Cu sulfide deposits associated with

more evolved mafic rocks (especially Voisey's Bay, Duluth Complex, etc.; e.g., Lightfoot and Naldrett, 1999; Ripley et al., 2007). Therefore, a specifically designed SIMS analytical approach that copes with these limitations was developed and successfully applied in this thesis and is described in detail in Chapter 2. It utilizes the major strengths of the SIMS, namely the high sensitivity and the high spatial resolution (e.g., Shimizu and Hart, 1982; Stern, 2009).

1.4. The Analytical Strengths of Secondary Ion Mass Spectrometry (SIMS)

In geological applications the SIMS technique is primarily used for trace element and (light) stable isotope analyses (e.g., Shimizu et al., 1978; Shimizu and Hart, 1982; Williams, 1985; Reed, 1989; Hinton, 1990; Stern, 2009, and references therein). For this thesis, the small geometry Cameca IMS 4f instrument (schematics in Fig.1.5) located at Memorial University's CREAIT MAF IIC facility in the *Bruneau Centre for Research and Innovation* was used for all presented olivine analyses. The analytical setup and instrument parameters are described in detail in Chapter 2. A brief description of the fundamental concepts of the SIMS technique is given here to supplement the information in Chapter 2.

The "modern" SIMS instrument design, such as the Cameca IMS 4f (now 7f), has been diversely applied in geochemistry and cosmochemistry since the initial development of the first commercial SIMS in the mid-1960's. The need to conduct mass spectrometry at a

very high spatial resolution (micrometer-scale), combined with a high sensitivity for a wide range of elements, was partly motivated by NASA's lunar program (Stern, 2009 and references therein). As a consequence of the inherently low analytical backgrounds of the SIMS technique, very low detection limits can be achieved. Since then, many studies have improved and advanced the field of SIMS analyses and detailed reviews of geological applications, basic concepts, and instrumental aspects were presented by Shimizu et al. (1978), Shimizu and Hart (1982), Williams (1985), Benninghoven et al. (1987), Reed (1989), Hinton (1990), and most recently by Stern (2009).

Briefly, the fundamental process in SIMS analyses is the bombardment of a solid (polycomponent) sample by an energetic primary ion beam (here O^- with 10 keV) that generates secondary ions through a "collision cascade" in the upper atomic layers of the target matrix. Particles that are subsequently ejected from the solid surface in a process known as "sputtering" (Fig.1.6) are mostly neutral. However, a small fraction of the released material (around 0.1 to 10%; e.g., Williams, 1985; Stern, 2009) is ionized, accelerated by a high secondary potential (here 4.5 keV) and then extracted towards the mass spectrometer. Electrostatic and magnetic analyzers subsequently separate the ions based on their mass/charge ratio (m/z), before they are finally counted in an ion detector (here electron-multiplier). In an interference- and fractionation-free environment, this measured ion fraction reflects the chemical composition of the (solid) sample and further quantification of the actual element content can then be achieved by correlating the measured unknown element ratio (here normalized on $^{30}Si^+$) with the same ratio in a reference material of known composition (e.g., Shimizu and Hart, 1982; Stern, 2009).

Relating these secondary ion intensities to the actual element abundances is a critical step in SIMS data reduction and requires the use of well-characterized reference materials of comparable composition to the unknown sample for empirical calibration of instrumental bias (e.g., Shimizu et al., 1978; Shimizu and Hart, 1982; Williams, 1985; Hinton, 1990; Stern, 2009, and references therein). The primary bias results from the sputtering process and the secondary ion specificity.
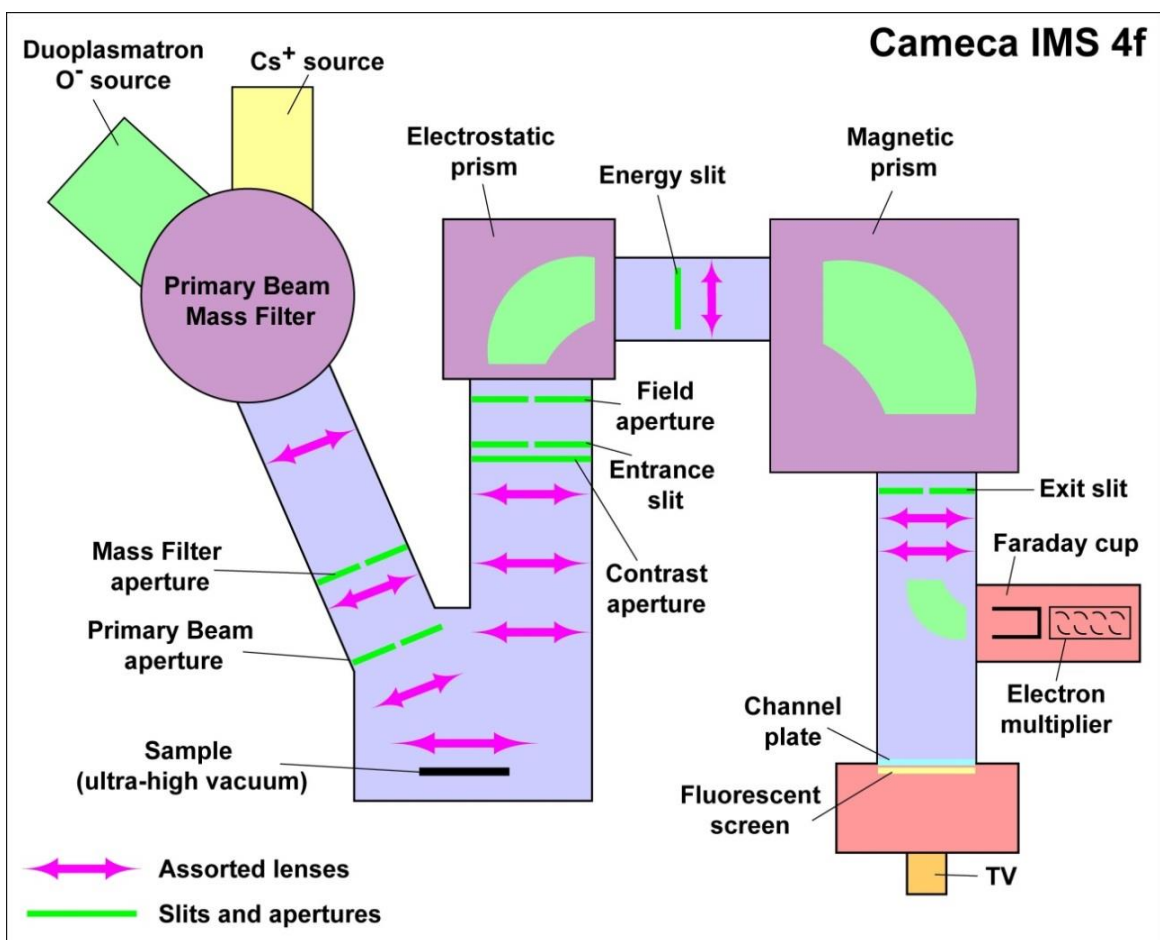
Fig. 1.5: Schematic illustration of the Cameca IMS 4f instrument. Key components are illustrated, as well as the approximate position of key lenses, slits and apertures.
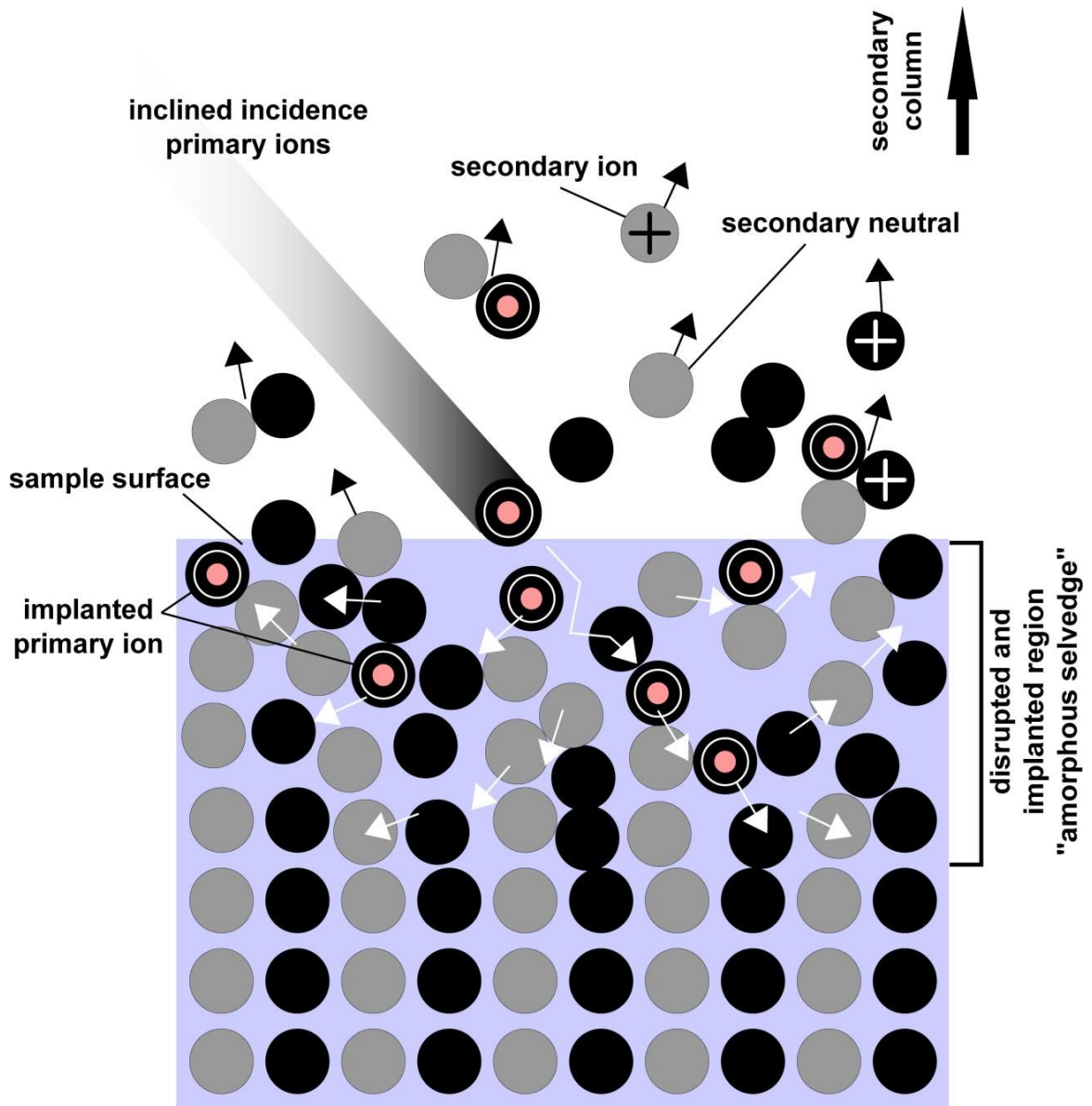
Fig. 1.6: Depiction of the sputtering process at the atomic scale. An inclined primary ion beam (O⁻ ions) penetrates the solid surface and produces a collision cascade in the upper atomic layers of the sample (knock-on effects indicated by white arrows). Sputtered material (neutral and charged atoms, molecules, dimers etc.) is ejected from the implanted and structurally damaged upper layers and subsequently extracted towards the secondary column (after Stern, 2009).

Since sputtered particles also include more complex molecular ion species (Fig.1.6; oxides, hydroxides, dimers, etc.) the resulting "isobaric interferences" on the desired monatomic ions can seriously influence the secondary ion mass spectra and hence the final quantification (e.g., Shimizu et al., 1978; Shimizu and Hart, 1982; Williams, 1985; Hinton, 1990; Stern, 2009). Two different techniques (or a combination of both) are most commonly applied to reduce or completely eliminate isobaric interferences:

1) *energy filtering*, which is applied in this study, exploits the fact that molecular ions (lower high-energy component) and monatomic ions (higher high-energy component) have distinctively different energy distributions, so that molecular ion species can be discriminated by accepting only the high-energy monatomic secondary ions (e.g., Shimizu et al., 1978; Reed, 1989),

2) *high mass resolution* (mass-to-base-width ratio or M/ΔM, commonly at 10% peak intensity; e.g., Shimizu et al., 1978; Shimizu and Hart, 1982; Stern, 2009) separates ion species based on incremental differences in their masses.

However, both methods work at the expense of the secondary ion intensity, because energy filtering reduces the secondary ion energy and high mass resolution drastically reduces ion transmission. The latter limitation was largely resolved by the introduction of large geometry sensitive high resolution ion microprobes, such as the SHRIMP (now SHRIMP II) and the Cameca IMS 1270 (now 1280), which revolutionized in-situ U–Pb geochronology of accessory minerals (Stern, 2009 and references therein). In spite of this, for the small geometry Cameca IMS 4f instrument, a combination of low mass resolution (mass resolving power; MRP of ~350) and element-dependent energy filtering (at –80 eV

and −105 eV) is capable of effectively eliminating most isobaric interferences on major and trace elements by measuring only ions with high kinetic energy (e.g., Shimizu et al., 1978). In cases where isobaric interferences are persistent, noticeably affected natural isotopes are, if possible, omitted in favor of unaffected ones (e.g., $^{60}Ni^+$ instead of $^{58}Ni^+$ ~ $^{58}Fe^+$).

In addition to isobaric interferences, another complexity has hampered quantitative SIMS trace element analyses − the so-called "matrix effect". Especially in a complex silicate matrix (e.g., olivine), the secondary ion yield of one element (e.g., Mg or Ni) can be enhanced as a function of the concentration of another element (here Fe in olivine). The secondary ion intensity therefore depends on the chemical composition of the sample (e.g., Shimizu and Hart, 1982 and references therein). In case of olivine, several SIMS studies (e.g., Shimizu et al., 1978; Reed et al., 1979; Steele et al., 1981; Weinbruch et al., 1993; Lehmann, 2003, and references therein), were unfortunately performed only on a limited range of olivine compositions (Fo_{90} to Fo_{75}), noted that the ionization of Mg and Ni is enhanced as a function of increasing Fe content. Even though no universal physico-chemical or crystallographic explanation is established to date for the interaction and (enhanced) ionization between the different components in olivine, SIMS analyses of a set of chemically well-characterized olivine reference materials covering the forsterite-fayalite solid solution should adequately describe and accommodate this matrix effect, and yield high-quality major and trace element data. However, virtually no SIMS data exist for many trace elements spanning the complete olivine solid solution, let alone accurately defined and accessible forsterite-fayalite reference materials, since the scope of

most petrological studies are on selected minor elements in high-Mg mantle olivine ($\sim$Fo$_{90}$). As a result, determination of accurate and precise major and trace element data in compositionally diverse olivine is a challenging task. As a prerequisite for addressing the questions raised in this thesis, it was necessary to develop a comprehensively applicable SIMS analytical protocol that fully characterizes and successfully copes with the matrix effect in high-Fe olivine (Chapter 2).

1.5. References

Amelin, Y., Li, C., Naldrett, A.J., 1999. Geochronology of the Voisey's Bay intrusion, Labrador, Canada, by precise U-Pb dating of coexisting baddeleyite, zircon, and apatite. Lithos 47, 33–52.

Arndt, N.T., Lesher, C.M., Czamanske, G.K., 2005. Mantle-derived magmas and magmatic Ni-Cu-(PGE) deposits. Economic Geology 100th Anniversary Volume, 5–23.

Beattie, P., 1994. Systematics and energetics of trace-element partitioning between olivine and silicate melts: Implications for the nature of mineral/melt partitioning. Chemical Geology 117, 57–71.

Beattie, P., Ford, C., Russell, D., 1991. Partition coefficients for olivine-melt and orthopyroxene-melt systems. Contributions to Mineralogy and Petrology 109, 212–224.

Bédard, J.H., 2005. Partitioning coefficients between olivine and silicate melts. Lithos 83, 394–419.

Benninghoven A., Rüdenauer F.G., Werner H.W., 1987. Secondary ion mass spectrometry: Basic concepts, instrumental aspects, application and trends. Wiley, New York, 1230 pp.

Bowen, N.L., Schairer, J.F., 1935. The system MgO-FeO-SiO$_2$. American Journal of Science 229, 151–217.

Bremond d'Ars, J., Arndt, N.T., Hallot, E., 2001. Analog experimental insights into the formation of magmatic sulfide deposits. Earth and Planetary Science Letters 186, 371–381.

Campbell, I.H., Naldrett, A.J., 1979. The influence of silicate:sulfide ratios on the geochemistry of magmatic sulfides. Economic Geology 74, 1503–1505.

Canil, D., Fedortchouk, Y., 2001. Olivine-liquid partitioning of vanadium and other trace elements, with application to modern and ancient picrites. The Canadian Mineralogist 39, 319–330.

Chai, G., Naldrett, A.J., 1992. The Jinchuan ultramafic intrusion: Cumulate of a high-Mg basaltic magma. Journal of Petrology 33, 277–303.

Clark, T., Naldrett, A.J., 1972. The distribution of Fe and Ni between synthetic olivine and sulfide at 900°C. Economic Geology 67, 939–952.

Colson, R.O., McKay, G.A., Taylor, L.A., 1988. Temperature and composition dependencies of trace element partitioning: Olivine/melt and low Ca pyroxene/melt. Geochimica et Cosmochimica Acta 52, 539–553.

Davidson, P.M., Mukhopadhyay, D.K., 1984. Ca–Fe–Mg olivine: phase relations and a solution model. Contributions to Mineralogy 86, 256–263.

Deer, W.A., Howie, R.A., Zussman, J., 1997. Rock forming minerals: Orthosilicates, 2ed. Geological Society of London. 932 pp.

De Hoog, J.C.M., Gall, L., Cornell, D.H., 2010. Trace-element geochemistry of mantle olivine and application to mantle petrogenesis and geothermobarometry. Chemical Geology 270, 196–215.

Duke, J.M., 1976. Distribution of the period four transition elements among olivine, calcic clinopyroxene and mafic silicate liquid; experimental results. Journal of Petrology 17(4): 499–521.

Evans-Lamswood, D.M., Butt, D.P., Jackson, R.S., Lee, D.V., Muggridge, M.G., Wheeler, R.I., Wilton, D.H.C., 2000. Physical controls associated with the distribution of sulfides in the Voisey's Bay Ni-Cu-Co deposit, Labrador. Economic Geology 95, 749–769.

Falloon, T.J., Danyushevsky, L.V., Ariskin, A., Green, D.H., Ford, C.E., 2007. The application of olivine geothermometry to infer crystallization temperatures of parental liquids: Implications for the temperature of MORB magmas. Chemical Geology 241, 207–233.

Filiberto, J., Jackson, C., Le, L., Treiman, A.H., 2009. Partitioning of Ni between olivine and an iron-rich basalt: Experiments, partition models, and planetary implications. American Mineralogist 94, 256–261.

Fleet, M.E., MacRae, N.D., Osborne M.D., 1981. The partition of Ni between olivine, magma and immiscible sulfide liquid. Chemical Geology 32, 119–127.

Fleet, M.E., MacRae, N.D., 1983. Partition of Ni between olivine and sulfide and its application to Ni-Cu sulfide deposits. Contribution to Mineralogy and Petrology 83, 75–83.

Gaetani, G.A., Grove, T.L., 1997. Partitioning of moderately siderophile elements among olivine, silicate melt, and sulfide melt: Constraints on core formation in the Earth and Mars. Geochimica et Cosmochimica Acta 61, 1829–1846.

Grant, K.J., Wood, B.J., 2010. Experimental study of the incorporation of Li, Sc, Al and other trace elements into olivine. Geochimica et Cosmochimica Acta 74, 2412–2428.

Hagerty, J.J., Shearer, C.K., Vaniman, D.T., Burger, P.V., 2006. Identifying the effects of petrologic processes in a closed basaltic system using trace-element concentrations in olivine and glasses: Implications for comparative planetology. American Mineralogist 91, 1499–1508.

Häkli, T., Wright, T.L., 1967. The fractionation of nickel between olivine and augite as a geothermometer. Geochimica et Cosmochimica Acta 31, 877–884.

Hart, S.R., Davis, K.E., 1978. Nickel partitioning between olivine and silicate melt. Earth and Planetary Science Letters 40, 203–290.

Hazen, R.M., 1976. Effects of temperature and pressure on the crystal structure of forsterite. American Mineralogist 61, 1280–1293.

Hazen, R.M., 1977. Effects of temperature and pressure on the crystal structure of ferromagnesian olivine. American Mineralogist 62, 286–295.

Herzberg, C., Asimow, P.D., Ionov, D.A., Vidito, C., Jackson, M.G., Geist, D., 2013. Nickel and helium evidence for melt above the core–mantle boundary. Nature 493, 393–398.

Hinton, R.W., 1990. Ion microprobe trace-element analysis of silicates: Measurement of multi-element glass. Chemical Geology 83, 11–25.

Holzheid, A., Palme, H., Chakraborty, S., 1997. The activities of NiO, CoO and FeO in silicate melts. Chemical Geology 139, 21–38.

Holzheid, A., Grove, T.L., 2005. The effect of metal composition on Fe–Ni partition behavior between olivine and FeNi-metal, FeNi-carbide, FeNi-sulfide at elevated pressure. Chemical Geology 221, 207–224.

Ito, M., Yurimoto, H., Morioka, M., Nagasawa, H., 1999. Co^{2+} and Ni^{2+} diffusion in olivine determined by secondary ion mass spectrometry. Physics and Chemistry of Minerals 26, 425–431.

Keays, R.R., 1995. The role of komatiitic and picritic magmatism and S-saturation in the formation of ore deposits. Lithos 34, 1–18.

Keays, R.R., Lightfoot, P.C., 2010. Crustal sulfur is required to form magmatic Ni–Cu sulfide deposits: evidence from chalcophile element signatures of Siberian and Deccan Trap basalts. Mineralium Deposita 45, 241–257.

Köhler, T.P., Brey, G.P., 1990. Calcium exchange between olivine and clinopyroxene calibrated as a geothermobarometer for natural peridotites from 2 to 60 kb with applications. Geochimica et Cosmochimica Acta 54, 2375–2388.

Lamberg, P., 2005. From genetic concepts to practice: lithogeochemical identification of Ni-Cu mineralized intrusions and localization of the ore. Geological Survey of Finland Bulletin 402, pp. 264.

Lehmann, H., 2003. Investigation of the matrix effect of Mg, Si, Ca, Sc, Fe, Y, La and Lu in pyroxene composition synthetic silicate glasses by ion microprobe. Geostandards Newsletter 27, 99–117.

Lesher, C.M., Burnham, O.M., Keays, R.R., Barnes, S.J., Hulbert, L., 2001. Trace-element geochemistry and petrogenesis of barren and ore-associated komatiites. The Canadian Mineralogist 39, 673–696.

Li, C., Lightfoot, P.C., Amelin, Y., Naldrett, A.J., 2000. Contrasting petrological and geochemical relationships in the Voisey's Bay and Mushuau intrusions, Labrador, Canada: implications for ore genesis. Economic Geology 95, 771–799.

Li, C., Naldrett, A.J., 1999. Geology and petrology of the Voisey's Bay intrusion: Reaction of olivine with sulphide and silicate liquids. Lithos 47, 1–31.

Li, C., Ripley, E.M., Maier, W.D., Gromwe, T.E.S., 2002. Olivine and sulfur isotope compositions of the Uitkomst Ni–Cu sulfide ore-bearing complex, South Africa: evidence for sulfur contamination and multiple magma emplacements. Chemical Geology 188, 149–159.

Li, C., Ripley, E.M., Naldrett, A.J., 2003a. Compositional variations of olivine and sulfur iIsotopes in the Noril'sk and Talnakh intrusions, Siberia: Implications for ore-forming processes in dynamic magma conduits. Economic Geology 98, 69–86.

Li, C., Ripley, E.M., Mathez, E.A., 2003b. The effect of S on the partitioning of Ni between olivine and silicate melt in MORB. Chemical Geology 201, 295–306.

Li, C., Xu, Z., de Waal, S.A., Ripley, E.M., Maier, W.D., 2004. Compositional variations of olivine from the Jinchuan Ni–Cu sulfide deposit, western China: Implications for ore genesis. Mineralium Deposita 39, 159–172.

Lightfoot, P.C., Keays, R.R., 2005. Siderophile and chalcophile metal variations in flood basalts from the Siberian Trap, Noril'sk region: Implications for the origin of the Ni-Cu-PGE sulfide ores. Economic Geology 100, 439–462.

Lightfoot, P.C., Keays, R.R., Evans-Lamswood, D.M., Wheeler, R., 2012. S saturation history of Nain Plutonic Suite mafic intrusions: Origin of the Voisey's Bay Ni–Cu–Co sulfide deposit, Labrador, Canada. Mineralium Deposita 47, 23–50.

Lightfoot, P.C., Naldrett, A.J., 1999. Geological and geochemical relationships in the Voisey's Bay intrusion, Nain Plutonic Suite, Labrador, Canada. *In* Dynamic processes in magmatic ore deposits and their application in mineral exploration (Keays, R.R., Lesher, C.M., Lightfoot, P.C., Farrow, C.E.G., eds.). Geological Association of Canada Short Course Notes 13, 1–30.

Lightfoot, P.C., Naldrett, A.J., Hawkesworth, C.J., 1984. The geology and geochemistry of the Waterfall Gorge section of the Insizwa complex with particular reference to the origin of the nickel sulfide deposits. Economic Geology 79, 1857–1879.

Longhi, J., Durand, S.R., Walker, D., 2010. The pattern of Ni and Co abundance in lunar olivine. Geochimica et Cosmochimica Acta 74, 784–798.

Maier, W.D., Barnes, S.J., Groves, D.I., 2012. The Bushveld complex, South Africa: formation of platinum– palladium, chrome- and vanadium-rich layers via hydrodynamic sorting of a mobilized cumulate slurry in a large, relatively slowly cooling, subsiding magma chamber. Mineralium Deposita DOI 10.1007/s00126-012-0436-1.

Maier, W.D., Barnes, S.J., Sarkar, A., Ripley, E., Li, C., Livesey, T., 2010. The Kabanga Ni sulfide deposit, Tanzania: I. Geology, petrography, silicate rock geochemistry, and sulfur and oxygen isotopes. Mineralium Deposita 45, 419–441.

Maier, W.D., Barnes, S.J., de Waal, S.A., 1998. Exploration for magmatic Ni–Cu–PGE sulphide deposits: a review of recent advances in the use of geochemical tools, and their application to some South African ores. South African Journal of Geology 101, 237–253.

Maier, W.D., Groves, D.I., 2011. Temporal and spatial controls on the formation of magmatic PGE and Ni–Cu deposits. Mineralium Deposita 46, 841–857.

Maier, W.D., Li, C., de Waal, S.A., 2001. Why are there no major Ni-Cu sulphide deposits in large layered mafic-ultramafic intrusions? The Canadian Mineralogist 39, 547–556.

Naldrett, A.J., 1997. Key factors in the genesis of Noril'sk, Sudbury, Jinchuan, Voisey's Bay and other world-class Ni-Cu-PGE deposits: Implications for exploration. Australian Journal of Earth Sciences 44, 283–315.

Naldrett, A.J., 1999. World-class Ni-Cu-PGE deposits: key factors in their genesis. Mineralium Deposita 34, 227–240.

Naldrett, A.J., 2010a. Secular variation of magmatic sulfide deposits and their source magmas. Economic Geology 105, 669–688.

Naldrett, A.J., 2010b. From the mantle to the bank: the life of a Ni-Cu-(PGE) sulfide deposit. South African Journal of Geology 113, 1–32.

O'Reilly, S., Chen, D., Griffin, W.L., Ryan, C.G., 1997. Minor elements in olivine from spinel lherzolite xenoliths: implications for thermobarometry. Mineralogical Magazine 61, 257–269.

Ottolini, L., 2002. Accurate SIMS analysis of Ca in olivine based on high-energy doubly charged secondary ions. Journal of Analytical and Atomic Spectrometry 17, 280–283.

Papike, J.J., Karner, J.M., Shearer, C.K., 2005. Comparative planetary mineralogy: Valence state partitioning of Cr, Fe, Ti, and V among crystallographic sites in olivine, pyroxene, and spinel from planetary basalts. American Mineralogist 90, 277–290.

Pearce, T.H., 1978. Olivine fractionation equations for basaltic and ultrabasic liquids. Nature 276, 771–774.

Putirka, K.D., 2008. Thermometers and barometers for volcanic systems. *In* Minerals, inclusions and volcanic processes (Putirka, K.D., Tepley, F.J., III eds.). Mineralogical Society of America and Geochemical Society, Reviews in Mineralogy and Geochemistry 69, 61–120.

Putnis, A., 1992. Introduction to mineral sciences. Cambridge University Press, Cambridge, 457 pp.

Rajamani, V., Naldrett, A.J., 1978. Partitioning of Fe, Co, Ni, and Cu between sulfide liquid and basaltic melts and the composition of Ni-Cu sulfide deposits. Economic Geology 73, 82–93.

Reed, S.J.B., 1989. Ion microprobe analysis – a review of geological applications. Mineralogical Magazine 53, 3–24.

Reed, S.J.B., Scott, E.R.D., Long, J.V.P., 1979. Ion microprobe analysis of olivine in pallasite meteorites for nickel. Earth and Planetary Science Letters 43, 5–12.

Ripley, E.M., Li, C., 2013. Sulfide saturation in mafic magmas: Is external sulfur required for magmatic Ni-Cu-(PGE) ore genesis? Economic Geology 108, 45–58.

Ripley, E.M., Taib, N.I., Li, C., Moore, C.H., 2007. Chemical and mineralogical heterogeneity in the basal zone of the Partridge River intrusion: implications for the origin of Cu–Ni sulfide mineralization in the Duluth complex, midcontinent rift system. Contributions to Mineralogy and Petrology 154, 35–54.

Rollinson, H.R., 1993. Using geochemical data: Evaluation, presentation, interpretation. Longman, UK. 352 pp.

Roeder, P.L., Emslie, R.F., 1970. Olivine-liquid equilibrium. Contributions to Mineralogy and Petrology 29, 275–289.

Ryan, B., 2000. The Nain-Churchill boundary and the Nain Plutonic Suite: A regional perspective on the geologic setting of the Voisey's Bay Ni-Cu-Co deposit. Economic Geology 95, 703–724.

Sato, H., 1977. Nickel content of basaltic magmas: identification of primary magmas and a measure of the degree of olivine fractionation. Lithos 10, 113–120.

Shearer, C.K., McKay, G., Papike, J.J., Karner, J.M., 2006. Valence state partitioning of vanadium between olivine-liquid: Estimates of the oxygen fugacity of Y980459 and application to other olivine-phyric martian basalts. American Mineralogist 91, 1657–1663.

Shimizu, N., Hart, S.R., 1982. Application of the ion microprobe to geochemistry and cosmochemistry. Annual Reviews of Earth and Planetary Sciences 10, 483–526.

Shimizu, N., Semet, M.P., Allègre, C.J., 1978. Geochemical applications of quantitative ion-microprobe analysis. Geochimica et Cosmochimica Acta 42, 1321–1334.

Snyder, D.A., Carmichael, S.E., 1992. Olivine-liquid equilibria and the chemical activities of FeO, NiO, Fe_2O_3, and MgO in natural basic melts. Geochimica et Cosmochimica Acta 56, 303–318.

Sobolev, A.V., Hofmann, A.W. et al., 2007. The amount of recycled crust in sources of mantle-derived melts. Science 316, 412–417.

Steele, I.M., Hervig, R.L., Hutcheon, I.D., Smith, J.V., 1981. Ion microprobe techniques and analyses of olivine and low-Ca pyroxene. American Mineralogist 66, 526–546.

Stern, R.A., 2009. An introduction to secondary ion mass spectrometry (SIMS) in geology. *In* Secondary ion mass spectrometry in the earth sciences: Gleaning the big picture from a small spot (Fayek, M., ed.). Mineralogical Association of Canada Short Course Series 41, 1–18.

Taura, H, Yurimoto, H., Kurita, K., Sueno, S., 1998. Pressure dependence on partition coefficients for trace elements between olivine and the coexisting melts. Physics and Chemistry of Minerals 25, 469–484.

Thomson, A., Maclennan, J., 2013. The distribution of olivine compositions in Icelandic basalts and picrites. Journal of Petrology 54, 745–768.

Weinbruch, S., Specht, S., Palme, H., 1993. Determination of Fe, Mn, Ni and Sc in olivine by secondary ion mass spectrometry. European Journal of Mineralogy 5, 37–41.

Williams, P., 1985. Secondary ion mass spectrometry. Annual Reviews of Material Sciences 15, 517–548.

Zanetti, A., Tiepolo, M., Oberti, R., Vannucci, R., 2004. Trace-element partitioning in olivine: Modeling of a complete data set from a synthetic hydrous basanite melt. Lithos 75, 39–54.

CHAPTER 2 - Secondary Ion Mass Spectrometry for the Quantification of Multiple Trace Elements in Forsterite-Fayalite

Florian Bulle[1*], Graham D. Layne[1]

[1]Department of Earth Sciences, Memorial University of Newfoundland, St. John's, Canada NL A1B 3X5

*Corresponding author. Fax +1-709 737 2589; Email: fbulle@mun.ca

Abstract

Trace element analysis of olivine by Secondary Ion Mass Spectrometry (SIMS) may be strongly biased by major element matrix effects as composition varies between the forsterite and fayalite end-members, especially for the elements Mn, Co, Ni, Cu and Zn. This necessitates a more detailed procedure of multi-reference material calibration and sequential data reduction to provide accurate quantitative trace element analysis.

In this study, seven compositionally divergent olivine (Fo_{100} to $Fo_{0.5}$) were assessed as potential reference materials to enable an empirical calibration approach that would allow routine integral determination of forsterite (Fo) content along with a suite of 13 trace elements (Ca, Sc, Ti, V, Cr, Mn, Co, Ni, Cu, Zn, Sr, Y, Zr). In the first step of data reduction, the forsterite (Fo) content of an unknown sample is extracted from a calibration of $R^{25}Mg^+/(R^{25}Mg^+ + R^{57}Fe^+)$ (where $R^M X^+$ is the intensity ratio of an analyte ion to $^{30}Si^+$, as measured by SIMS), against accepted values for Fo for the seven reference materials, as originally determined by Electron Probe Microanalysis (EPMA), using a non-linear regression of the form $y = (a + x)/(b + cx)$. The resulting calibrations show an excellent correlation ($R^2=0.999$) and allow the simultaneous determination of the Fo content and the concentrations of MgO, FeO and SiO_2 along with the trace elements listed above. Subsequently, traditional working lines ($R^M X^+$ versus accepted values for atomic weight ratio) and element-specific relative sensitivity factor (RSF) working curves (RSF versus Fo) were produced for all 13 trace elements. Analyte peaks were selected to effectively eliminate isobaric interferences using an energy filtering approach. Based on observed elemental sensitivities (relative secondary ion signal intensities), two major groupings

were established: Group I elements ($^{40}Ca^{++}$, $^{51}V^+$, $^{52}Cr^+$, $^{55}Mn^+$, $^{59}Co^+$, $^{60}Ni^+$, $^{63}Cu^+$, $^{66}Zn^+$) generally yield relatively high secondary ion (SI) intensities from natural olivine and exhibit good precisions and homogeneities and, consequently, very good working line correlations. Group II elements ($^{45}Sc^{++}$, $^{47}Ti^+$, $^{88}Sr^+$, $^{89}Y^+$, $^{90}Zr^+$) have low SI signals in the natural olivine studied and quantification was based on conventional working lines derived from one natural olivine reference material (usually San Carlos olivine) combined with NIST 610 and 612 glass reference materials.

Even though traditional working lines for many of the elements studied display near linear relationships, plots of RSF values versus Fo content revealed significant variations with olivine composition. This effect was particularly pronounced for Mn, Co, Ni, and Zn. RSF-based working lines for those elements yield polynomial regressions with good correlations ($R^2 \geq 0.986$). However, when the major element content is included explicitly in the regression calculation, strong linear correlations ($R^2 \geq 0.983$) appear between RSF and expressions of the form ($aSiO_2 + bMgO + cFeO$). Thus, for elements with significant matrix effects related to Fo content, considering all three major elemental components in olivine improves the total co-variation compared to utilizing only the Fo content (MgO-FeO); this consequently enables an equally precise quantification of the trace elements over the complete range of olivine compositions.

Comparison of SIMS vs. EPMA was performed using highly homogeneous mantle olivine (Fo$_{90}$) from a garnet-peridotite (Western Gneiss Region, Norway) and more compositionally variable olivine (Fo$_{74-89}$) from a volcanic ash deposit (2010 Eyjafjallajökull eruption, Iceland). SIMS determinations of Fo, Ni and Mn compared

accurately with those by EPMA – with SIMS providing a substantially improved precision for Mn and Ni, particularly for concentrations below 200 ppm, and a detection limit of ≤1 ppm for Ni. A specific goal of this technique development was to ensure that SIMS analyses do not produce artifact trends when the data are interpreted using standard plots of trace element composition against Fo.

The capability of SIMS for precise quantification of Fo, Ni, and an extended set of trace elements is particularly valuable in studies where olivine Fo compositions vary over a large range. For example, those pertaining to melt evolution in magmatic Ni-Cu-Co deposits.

2.1. Introduction

Olivine $(Mg,Fe)_2[SiO_4]$ is one of the most abundant minerals on Earth, as well as the dominant phase in the upper mantle. The understanding of its geochemical behavior is vital in deciphering the complexity of mantle and basalt petrogenesis (e.g., Roeder and Emslie, 1970; Sato, 1977; Frey et al., 1978; Zanetti et al., 2004; Bédard, 2005; Sobolev et al., 2007; De Hoog et al., 2010; Thompson and Maclennan, 2013) and as a petrogenetic tracer of a variety of ore-forming processes, especially during the formation of Ni-Cu-Co sulfide deposits (e.g., Li and Naldrett, 1999; Li et al., 2000, 2003; Maier et al., 2010). Although the fundamental mineralogy and the major phase transitions in the FeO-MgO-SiO$_2$ system were thoroughly documented during the mid-20th century (e.g., Bowen and Schairer, 1935; Roeder and Emslie, 1970), the detailed study of multi-trace element distribution and partitioning behavior in olivine has only more recently emerged (e.g., Colson et al., 1988; Beattie et al., 1991; Snyder and Carmichael, 1992; Beattie, 1994; Gaetani and Grove, 1997; Taura et al., 1998; Ito et al., 1999; Zanetti et al., 2004; Lee et al., 2007; Grant and Wood, 2010; De Hoog et al., 2010). This is in part due to continuing advances in microanalytical techniques, such as Secondary Ion Mass Spectrometry (SIMS), which routinely allows in-situ detection and quantification of trace elements in solid materials with ppb sensitivity and high spatial resolution (e.g., Shimizu et al., 1978; Reed et al., 1979; Steele et al., 1981; Shimizu and Hart, 1982b; Yurimoto et al., 1989; Hinton, 1990; Jones and Layne, 1997; Shimizu, 2000; Hervig et al., 2006; Stern, 2009). In contrast to Electron Probe Microanalysis (EPMA), which only enables detection of

major elements and limited minor elements (Ca, Ni, Mn) in olivine, SIMS can provide the capability to analyze a combination of major and trace elements in one analytical step.

Due to its importance as a proxy for petrological processes in the upper mantle, many SIMS studies have exclusively focused on olivine in the restricted compositional range of Fo_{89} to Fo_{94} (e.g., Sato, 1977; Kurosawa et al., 1992; Weinbruch et al., 1993; Taura et al., 1998; Ito et al., 1999; De Hoog et al., 2010). A small number of studies have presented limited trace element data for more fayalitic olivine ($<Fo_{70}$) (e.g., Reed et al., 1979; Steele et al., 1981; Weinbruch et al., 1993). Despite their common occurrence in many mafic and Fe-rich felsic rocks and their importance to ore-forming processes (e.g., Li and Naldrett, 1999; Li et al., 2000), less effort has been invested in characterizing appropriate olivine reference materials for less forsteritic compositions, and developing a SIMS procedure for systems with wide variation in olivine Fo content. Unlike many rock-forming silicate minerals, for instance pyroxene (e.g., Shimizu et al., 1978; Shimizu and Hart, 1982b; Jones and Layne, 1997), the quantification of SIMS analyses of trace elements in olivine is complicated by substantial matrix effects (Shimizu et al., 1978; Reed et al., 1979; Steele et al., 1981; Shimizu and Hart, 1982b, Weinbruch et al., 1993; Lehmann, 2003), as secondary ion yields for several important elements vary considerably with major chemical composition of the olivine – an effect that has further hampered the development of validated reference data for less forsteritic olivine. These effects also have the potential to induce false trends in trace element versus major element (or Fo) plots for olivine if not properly calibrated and corrected. Our study presents an improved analytical approach for quantifying both Fo content and an extended suite of 13

trace elements simultaneously in compositionally variable olivine, using SIMS microanalysis.

2.2. Experimental Procedure

2.2.1. Reference Material (RM) Characterization

The quality of SIMS trace element analyses, especially of notoriously trace element-poor minerals like olivine, depends intimately on the selection and characterization of suitable reference materials (RM). SIMS studies have shown that olivine analyses, specifically, are highly influenced and often biased by matrix effects ("*chemical fractionation of a secondary ion (SI) population relative to the (solid) sample*"; Shimizu, 2000) (Shimizu et al., 1978; Reed et al., 1979; Steele et al., 1981; Shimizu and Hart 1982b). In the case of olivine, SI yields of Mg, Fe and Ni especially have been previously documented as prone to, and strongly impacted by, matrix effects (Shimizu et al., 1978; Reed et al., 1979; Steele et al., 1981; Shimizu and Hart, 1982b; Weinbruch et al., 1993; Lehmann, 2003 and references therein). Therefore, well-characterized RM with matrix compositions spanning those of the unknowns are essential in determining accurate element concentrations (Weinbruch et al., 1993; Stern, 2009). However, many SIMS studies focusing on trace element distribution in olivine only use basaltic glass or the NIST 600-series glasses (e.g., Pearce et al., 1997) along with only one natural olivine RM (mantle olivine, usually from San Carlos, Arizona) for empirical calibration (e.g., Kurosawa et al., 1992; Taura et al., 1998; Bell et al., 2009; De Hoog et al., 2010). While this is a reasonable approach for the

study of trace elements in exclusively high-Mg olivine, it is not adequate for a more extensive range of lower-Mg/higher-Fe olivine, where this strategy could potentially produce artifact trends in trace element versus Fo correlations. Despite the analytical and empirical uncertainties that are known to complicate olivine SIMS measurements, no attempt has been made so far to overcome them with a set of well-characterized olivine RM that cover the complete Mg-Fe compositional range.

To establish serviceable SIMS olivine RM, we used compositionally homogeneous olivine ranging between $Fo_{100.0}$ and $Fo_{0.5}$. Some are well-characterized olivine mantle xenolith occurrences (San Carlos and Kilbourne Hole; Weinbruch et al., 1993; Taura et al., 1998; Bell et al., 2009; De Hoog et al., 2010; Grant and Wood, 2010). Others (see Table 2.1) were thoroughly tested and characterized during this study, for the purpose of serving as potential RM for less forsteritic olivine.

Characterization of 7 olivine RM (Table 2.1) was carried out using three independent analytical techniques: EPMA was used to determine the major element content and to verify major element homogeneity at a micrometer scale for all selected olivine RM. A suite of 13 minor and trace elements was then analyzed with solution ICP-MS and ICP-OES techniques (Table 2.1) on replicate small samples. SIMS microanalyses were then performed in several sessions, between July 2009 and March 2011.

Table 2.1: Chemical composition of potential olivine reference materials

Sample Code	Ol-1 (EPMA)	*Ol-1*	Ol-2	*Ol-2*	Ol-3	*Ol-3*	Ol-4	*Ol-4*	Ol-5	*Ol-5*	Ol-6	*Ol-6*	Ol-7	*Ol-7*	
Location	SanCarlos		RedSea		Kilbourne H		Tanzanion		Fo55		Tasisuak L.		Lyon Mtn.		Fayalite
(n=)	20[x]	*1σ*[y]	20	*1σ*	30	*1σ*	20	*1σ*	40	*1σ*	32	*1σ*	3	*1σ*	ideal
wt.%															
MgO	48.34	0.31	49.47	0.14	49.23	0.54	56.66	0.13	24.71	0.20	2.42	0.09	0.20	0.01	
SiO2	40.48	0.12	40.61	0.12	40.49	0.20	42.44	0.10	35.45	0.23	30.36	0.24	29.23	0.17	29.49
CaO	0.08	0.01	0.07	0.01	0.07	0.02	bdl		0.09	0.17	0.05	0.02	0.05	0.01	
Cr2O3	0.02	0.01	0.02	0.01	0.02	0.01	0.01	0.01	0.01	0.01	0.01	0.01	0.01	0.01	
TiO2	0.01	0.01	bdl		bdl		bdl		bdl				0.02		
MnO	0.15	0.01	0.13	0.01	0.14	0.01	bdl		0.53	0.02	1.04	0.05	2.04	0.03	
FeO	10.77	0.06	9.29	0.06	9.67	0.65	0.01	0.01	39.77	0.22	67.59	0.25	68.35	0.65	70.51
NiO	0.37	0.02	0.38	0.03	0.37	0.02	0.01	0.01	0.11	0.02					
Total	99.19	0.55	99.98	0.38	99.98	1.45	99.13	0.25	100.42	0.86	101.47	0.67	99.91	0.88	100.00
ppm															
Mg	291555	1864	298351	858	296878	3258	341719	784	149045	1177	14595	550	1227	79	
Si	189229	540	189837	553	189256	922	198384	467	165721	1078	141915	1114	136635	1049	137848
Ca	580	82	492	50	475	128	25	40	624	1230	369	158	353	62	
Cr	148	74	128	71	109	91	45	41	37	47	53	86	61	67	
Ti	42	72	29	51	24	51	16	35	17	29			135		
Mn	1195	106	1039	108	1055	110	22	41	4094	130	8054	397	15833	169	
Fe	83737	476	72204	456	75181	5014	48	64	309113	1713	525384	1975	531287	3892	548081
Ni	2927	167	2987	203	2943	173	53	69	892	175					
# of ions[1]															
Mg^{2+}	1.772	0.011	1.807	0.005	1.801	0.020	1.995	0.005	1.037	0.008	0.118	0.004	0.010	0.001	
Ca^{2+}	0.002	0.000	0.002	0.000	0.002	0.001			0.003	0.005	0.002	0.001	0.002	0.000	
Cr^{2+}															
Mn^{2+}	0.003	0.000	0.003	0.000	0.003	0.000			0.013	0.000	0.029	0.001	0.059	0.001	
Fe^{2+}	0.223	0.001	0.190	0.001	0.199	0.013			0.939	0.005	1.856	0.007	1.942	0.018	2.000
Ni^{2+}	0.007	0.000	0.007	0.001	0.007	0.000			0.003	0.001					
[Y]^6	2.007	0.014	2.009	0.008	2.012	0.034	1.995	0.005	1.993	0.020	2.005	0.014	2.012	0.020	2.000
Si^{4+}	0.996	0.003	0.995	0.003	0.994	0.005	1.002	0.002	1.003	0.007	0.997	0.008	0.993	0.006	1.000
Ti^{4+}													0.001	0.000	
Fo %	**88.9**	*0.1*	**90.5**	*0.1*	**90.1**	*0.7*	**100.0**	*0.0*	**52.5**	*0.2*	**6.00**	*0.22*	**0.53**	*0.04*	**0.0**
Fo #	**0.89**	*0.00*	**0.90**	*0.00*	**0.90**	*0.01*	**1.00**	*0.00*	**0.52**	*0.00*	**0.06**	*0.00*	**0.01**	*0.00*	**0.00**

[x]: no. of analyses
[y]: standard deviation of n analyses (1s)
[1]: on the basis of 4 oxygens

ICP-MS (ppm)	Ol-1	*1σ*	Ol-2	*1σ*	Ol-3	*1σ*	Ol-4	*1σ*	Ol-5	*1σ*	Ol-6	*1σ*	error (RSD %)[+]
Al	205	11	175	9.0	16424	846	96.3	5.0	566	29	4681	241	5.15
Ca	2571	175	1951	132	6129	416	627	43	1769	120	3340	227	6.79
Ti	39.1	13	46.9	16	45.5	15	4.25	1.4	185	62	292	98	33.6
V	4.30	0.374	8.27	0.719	6.58	0.572	394	34	12.9	1.1	3.85	0.334	8.69
Cr	160	11	135	9.5	102	7.2	3.85	0.271	66.2	4.7	4.34	0.305	7.03
Mn	876	26	1002	30	1097	33	7.85	0.234	3929	117	8725	260	2.98
Co	134	4.4	137	4.5	138	4.5	2793	92	321	11	21.5	0.707	3.29
Ni	2890	31	2930	31	2931	31	7.60	0.081	906	9.6	5.90	0.063	1.06
Cu	4.20	2.0	4.73	2.2	2.10	1.0	3.02	1.4	106	50	4.32	2.0	47.1
Zn	64.1	3.1	51.0	2.5	49.9	2.4	5.03	0.244	221	11	2632	128	4.85
Li	1.40	0.09	1.45	0.097	2.23	0.150	17.0	1.1	9.76	0.7	25.7	1.7	6.72
Sr	0.440	0.058	0.438	0.057	1.20	0.157	0.350	0.046	1.13	0.148	0.220	0.029	13.1
Y	0.031	0.003	0.064	0.006	0.129	0.013	1.62	0.158	0.567	0.055	42.6	4.2	9.75
Zr	0.752	0.134	0.784	0.140	1.40	0.249	1.99	0.355	9.37	1.7	3.23	0.577	17.8
Nb	< 0.027		0.038	0.008	0.115	0.023	0.093	0.019	0.904	0.184	0.875	0.178	20.4
Ce	0.047	0.011	0.121	0.027	0.127	0.029	0.079	0.018	0.394	0.089	19.7	4.4	22.6
Yb	< 0.013		< 0.012		< 0.046		6.76	1.2	0.237	0.041	10.0	1.7	17.1

solution ICP-MS data; < below detection limit (bdl); 1σ relative error calculated based on duplicate analyses

ICP-OES (ppm)	Ol-1	*1σ*	Ol-2	*1σ*	Ol-3	*1σ*	Ol-4	*1σ*	Ol-5	*1σ*	Ol-6	*1σ*	error (RSD %)[+]
Ca	633	3.8	480	2.9	22882	137	21.7	0.130	1312	7.9	3822	23	0.6
Ti	< 105		156	65	548	230	< 136		154	64	101	42	42.0
V	12.7	2.8	13.7	3.0	73.5	16	618	136	29.2	6.4	12.8	2.8	22.0
Cr	216	1.3	181	1.1	1721	10	6.59	0.040	48.5	0.291	1.24	0.007	0.6
Mn	865	1.7	999	2.0	1148	2.3	7.08	0.014	3601	7.2	6960	14	0.2
Co	138	0.276	142	0.283	118	0.237	3123	6.2	343	0.686	< 19.2		0.2
Ni	3248	3.2	3314	3.3	2561	2.6	9.49	0.009	948	0.948	< 263		0.1
Cu	16.5	2.6	16.3	2.6	19.2	3.1	12.6	2.0	351	56	11.3	1.8	16.0
Zn	61.7	0.617	59.0	0.590	51.2	0.512	< 3.68		242	2.4	2522	25	1.0
Pb	65.4	1.3	73.7	1.5	81.9	1.6	< 3.73		275	5.5	471	9.4	2.0
Zr	10.2	0.203	11.0	0.221	12.9	0.257	11.7	0.234	20.5	0.411	28.4	0.567	2.0

solution ICP-OES data; < bdl; 1σ relative error calculated based on duplicate analyses

2.2.1.1. Potential RM Identified in this Study

After characterization by EPMA, ICP-MS, ICP-OES (Table 2.1) and SIMS, the 7 tested olivine RM (6 natural and 1 synthetic) were found sufficiently homogeneous for use in this study:

Ol-1: Fo_{89}, San Carlos, Arizona, USA (e.g., De Hoog et al., 2010; Spandler and O'Neill, 2010).

Ol-2: Fo_{90}, Zabargad Island, Red Sea, Egypt (see Brooker et al., 2004).

Ol-3: Fo_{90}, Kilbourne Hole, New Mexico, USA (e.g., Lee et al., 2007; Grant and Wood, 2010).

Ol-4: Fo_{100} (Synthetic), Co doped, (Tanzanion™).

Ol-5: Fo_{52}, Gabbro, location unknown, Mineral collection of Memorial University.

Ol-6: Fo_6, Nain Plutonic Suite (Tasisuak Lake), Labrador, Canada (courtesy of B. Ryan, GSNL).

Ol-7: $Fo_{0.5}$, Lyon Mountain Granite, New York, USA (courtesy of P. Valley, USGS).

2.2.2. Electron Probe Microanalysis (EPMA)

Major and minor elements (SiO_2, TiO_2, Cr_2O_3, FeO_T, MnO, MgO, CaO, NiO) for all RM were measured in two different sessions with a JEOL JXA 8900 Superprobe at the Department of Mineralogy at the University of Münster, Germany. The instrument was operated with an accelerating voltage of 15 kV, a beam current of 15 nA using wavelength-dispersive (WD) spectrometry. The samples were handpicked single-crystals

embedded in epoxy resin. The mounts were polished to a standard petrographic finish and then cleaned and carbon coated. Measurements of 20 to 40 spots were conducted along the longitudinal and lateral axes of individual olivine grains in order to determine their homogeneity. Typical detection limits (ppm) were as follows: MgO, 145; SiO_2, 185; CaO, 194; Cr_2O_3, 240; MnO, 245; FeO, 271; NiO, 236. Concentrations were calculated using the ZAF correction method. Data are given in Table 2.1.

For the purpose of inter-technique comparison, quantitative analyses of additional "unknown" olivine test samples were obtained with a CAMECA SX100 Electron Probe Micro Analyzer at the Department of Geosciences at the University of Oslo, Norway. Measurements included MgO, SiO_2, Cr_2O_3, MnO, FeO, and NiO. Typical detection limits for Cr, Mn and Ni were 400–650 ppm. The analytical setup and standardization is described in Plümper et al. (2012). Data are given in Table 2.5.

2.2.3. Solution ICP-MS and ICP-OES

Trace elements were also measured with routine ICP-MS and ICP-OES solution techniques. Between 0.4 g and 1.0 g of 6 different olivine crystals (Ol-1 to Ol-6) were handpicked and checked for inclusions and other impurities under a reflected-light microscope. Ol-7 was only measured with EPMA due to small grain sizes and local intergrowth with other mineral phases. Material from Ol-5 and Ol-6 was harvested through surface drilling with a NewWave Research MicroMill sampling system to ensure highest possible purity. Subsequently, samples were acid digested in HF-HNO_3 and diluted in an aqueous solution to appropriate elemental concentrations before they were

measured with standard ICP-MS (Jenner et al., 1990) and ICP-OES (Navarro et al., 2002) methods, provided at the Department of Earth Sciences and the CREAIT MAF-IIC microanalysis facility at Memorial University of Newfoundland. Data are given in Table 2.1.

2.2.4. Secondary Ion Mass Spectrometry (SIMS)

After characterization of the potential olivine RM, major and trace element analyses were performed by SIMS using a CAMECA IMS 4f instrument with improved primary lensing and detection systems (Memorial University MAF-IIC microanalysis facility). The grain mounts used for EPMA characterization were re-polished, cleaned and sputter coated with a 30–50 nm layer of gold to minimize charging of the sample during analysis. A primary beam of O^- ions, accelerated through a nominal potential of 10 kV and providing a current of 15–25 nA, was electrostatically focused into a 30 to 40 μm diameter spot on the sample. A combination of the 150 μm image field setting of the Transfer Lens optics and a physical Field Aperture (FA) of 750 μm limited the effective Field of View of the sample to a 68 μm diameter. A 250 μm Contrast Aperture (CA) was used, with the Entrance Slit narrowed to impinge on the CA image slightly, increasing the effective mass resolving power (MRP) (M/ΔM) to >350.

Each analysis comprised at least 10 cycles of counting on peaks that included $^{40}Ca^{++}$, $^{45}Sc^{++}$, $^{25}Mg^+$, $^{30}Si^+$, $^{47}Ti^+$ ($^{48}Ti^+$, $^{49}Ti^+$), $^{51}V^+$, $^{52}Cr^+$ ($^{53}Cr^+$), $^{55}Mn^+$, $^{57}Fe^+$ ($^{54}Fe^+$), $^{59}Co^+$, $^{60}Ni^+$ ($^{61}Ni^+$, $^{62}Ni^+$), $^{63}Cu^+$ ($^{65}Cu^+$), $^{66}Zn^+$, $^{88}Sr^+$, $^{89}Y^+$, $^{90}Zr^+$ ($^{92}Zr^+$) plus counting on a background position (usually 19.67 Da) to monitor detection noise. Very low abundance

elements were measured for at least 6–10 s per cycle, whereas major elements (and background) and first row transition metals were measured for 2 and 6 s per cycle, respectively. Total acquisition time for each trial spot was thus 16–20 minutes, not including a pre-sputtering period of 2 minutes with a slightly rastered beam to eliminate surface contamination. Each individual cycle was monitored to detect any obvious inhomogeneities resulting from the primary beam sputtering micro-inclusions with advancing depth in the sample; such outlier cycles were rejected during initial reduction of the data.

Secondary ions (SI) were energy filtered (Shimizu et al., 1978; Ottolini et al., 1993, 2000; Hervig et al., 2006) by applying a voltage offset to the nominal +4500 V sample accelerating voltage: −105 V for elements with atomic mass ≤66 Da (i.e., ^{66}Zn) and −80 V for elements with atomic mass >66 Da. This was combined with an energy window of ±60 eV to suppress isobaric interferences, and potentially reduce (Fe-dependent) matrix effects (Lehmann, 2003), by preferentially selecting higher-energy SI. Energy filtering is at times unable to effectively eliminate (major) molecular ion interferences, depending on the concentrations of certain contributing major or minor elements relative to those of the trace elements of interest. Hervig et al (2006), for example, noted several potential interferences relevant to this study, in particular, ^{48}Ti$^+$ by ^{48}Ca$^+$, (^{24}Mg$_2$$^+$), ^{56}Fe$^+$ by ^{28}Si$_2$$^+$, ^{51}V$^+$ by ^{25}Mg^{26}Mg$^+$, ^{52}Cr$^+$ by ^{26}Mg$_2$$^+$, ^{60}Ni$^+$ by ^{30}Si$_2$$^+$ and ^{90}Zr$^+$ by ^{58}Ni^{16}O$_2$$^+$. The transition metal isotopes in the mass range of 55 Da (Mn) to 66 Da (Zn) are especially susceptible to persistent molecular interferences from olivine major element species (Mg-Si-Fe; Table 2.2). Therefore, a major initial part of this study comprised an assessment of

important isobaric interferences that might affect accurate determinations of the elements studied.

Table 2.2: Potential isobaric interferences on SIMS analytical peaks

isotope	potential interferences	assumed significant interferences	isotope pair used	H / L* accpt ratio	H / L^x SIMS ratio	relative^y Δ H / L (%)
$^{40}Ca^{++}$	none	none				
$^{45}Sc^{++}$	none	none				
$^{25}Mg^+$	none	none				
$^{30}Si^+$	none	none				
$^{47}Ti^+$	$^{29}Si^{18}O^+$, $^{23}Na^{24}Mg^+$	none				
$^{48}Ti^+$	$^{48}Ca^+$, $^{24}Mg_2^+$	$^{24}Mg_2^+$				
$^{49}Ti^+$	$^{24}Mg_2H^+$, $^{24}Mg^{25}Mg^+$	$^{24}Mg_2H^+$, $^{24}Mg^{25}Mg^+$	49 / 47	0.7272	0.7824	7.1
$^{51}V^+$	$^{25}Mg^{26}Mg^+$	$^{25}Mg^{26}Mg^+$				
$^{52}Cr^+$	$^{26}Mg_2^+$, $^{24}Mg^{28}Si^+$	$^{26}Mg_2^+$, $^{24}Mg^{28}Si^+$				
$^{53}Cr^+$	$^{26}Mg_2H^+$, $^{25}Mg^{28}Si^+$, $^{24}Mg^{29}Si^+$	$^{26}Mg_2H^+$, $^{25}Mg^{28}Si^+$, $^{24}Mg^{29}Si^+$	53 / 52	0.1134	0.1477	23.2
$^{55}Mn^+$	$^{26}Mg^{29}Si^+$, $^{25}Mg^{30}Si^+$	$^{26}Mg^{29}Si^+$, $^{25}Mg^{30}Si^+$				
$^{54}Fe^+$	$^{27}Al_2^+$, $^{24}Mg^{30}Si^+$	none				
$^{57}Fe^+$	$^{56}FeH^+$, $^{25}Mg^{16}O_2^+$, $^{28}Si^{29}Si^+$	$^{56}FeH^+$	57 / 54	0.3625	0.3915	7.4
$^{59}Co^+$	$^{27}Al^{16}O_2^+$, $^{43}Ca^{16}O^+$, $^{29}Si^{30}Si^+$	$^{29}Si^{30}Si^+$				
$^{60}Ni^+$	$^{30}Si_2^+$, $^{44}Ca^{16}O^+$, $^{28}Si^{16}O_2^+$	none				
$^{62}Ni^+$	$^{46}Ca^{16}O^+$, $^{26}Mg^{18}O_2^+$, $^{30}Si^{16}O_2^+$	none	62 / 60	0.1386	0.1365	-1.5
$^{63}Cu^+$	$^{47}Ti^{16}O^+$, $^{62}NiH^+$	none				
$^{65}Cu^+$	$^{49}Ti^{16}O^+$, $^{24}Mg^{25}Mg^{16}O^+$	$^{24}Mg^{25}Mg^{16}O^+$	65 / 63	0.4457	0.4822	7.6
$^{66}Zn^+$	$^{50}Ti^{16}O^+$, $^{50}Cr^{16}O^+$	none				
$^{88}Sr^+$	$^{56}Fe^{16}O_2^+$	none				
$^{89}Y^+$	$^{57}Fe^{16}O_2^+$	none				
$^{90}Zr^+$	$^{58}Ni^{16}O_2^+$, $^{45}Sc_2^+$	none				
$^{92}Zr^+$	$^{46}Ca_2^+$, $^{60}Ni^{16}O_2^+$, $^{46}Ti_2^+$, $^{56}Fe^{18}O_2^+$	$^{56}Fe^{18}O_2^+$	92 / 90	0.3330	0.4228	21.2

*: accepted Heavy / Light isotope ratio (natural abundance)

^x: mean SIMS Heavy / Light isotope ratio

^y: relative deviation (%) of SIMS H / L ratio from accepted H / L ratio

preferred analyte for polyisotopic elements are italiced and boldface; tested in Fig. 2.1 and 2.2

Secondary ions were counted with an ETP 133H electron multiplier operated in pulse-counting mode with an overall counting system dead time of ~12 ns. Maximum count rates on Mg, Fe and Si were maintained at $<10^6$ counts per second (cps). The background

signal ("dark noise") of the electron multiplier was typically lower than 1 count per minute. Calculated optimum detection limits were assessed following the procedure of Jones and Layne (1997). In our case, a synthetic background signal of 1 count per minute, plus two times the estimated standard deviation (2σ; essentially ±1 count per minute), was used to calculate detection limits for 10 cycles of analysis. Typical detection limits (interference-free environment) calculated based on analyses of San Carlos olivine ranged from less than 5 ppb for V, Cr, Mn, Cu, Sr, Y, Zr to 10–40 ppb for Ca, Ti, Co, and Ni to circa 90 ppb for Sc and Zn (Table 2.3).

2.3. Detailed Analytical Considerations

The two major factors affecting the accuracy of elemental determinations by SIMS are; 1) isobaric interferences, mainly due to polyatomic ion species (dimers, oxides, hydrides etc.), which can significantly influence the apparent SI signals of the monatomic ion species generally selected as analytes (e.g., Shimizu et al., 1978; Shimizu and Hart, 1982b, Hinton, 1990; Shimizu, 2000; Hervig et al. 2006), and 2) major element matrix effects on SI yields. Both factors were recognized early in the study of polycomponent silicate materials with SIMS (*cf.* Shimizu et al., 1978; Reed et al., 1979; Steele et al., 1981; Shimizu and Hart, 1982b; Weinbruch et al., 1993; Lehmann, 2003). In the case of olivine there are significant, sometimes non-linear, matrix effects (category 2, above) on several trace elements – including Cr, Co, Mn, and Zn – which have never been fully investigated for the natural solid solution range of this mineral.

Table 2.3: Average SI raw counts normalized to $^{30}Si^+$ for measured trace elements in olivine RM and NIST glasses for analytical sessions in 2011

Sample Code	Ol-1		Ol-2	Ol-3	Ol-4	Ol-5	Ol-6	Ol-7	NBS 612	NBS 610	Typical detection limits
	SanCarlos		RedSea	Kilbourne H	Tanzanion	Fo55	Tasisuak L.	Lyon Mtn.	NIST glass	NIST glass	based on Ol-1 $^{30}Si^+$ c/s
$(M^+ / ^{30}Si^+)$	(x 10^{-4})	RSF_{M+}*	(x 10^{-4})	(x 10^{-4})	(x 10^{-4})	(x 10^{-4})	(x 10^{-4})	(x 10^{-4})	(x 10^{-4})	(x 10^{-4})	(ppb)
$^{40}Ca^{++}$	70.3	0.00051	60.7	34.5	1.18	164.3	510.0	136.7	5190	5534	36
$1\sigma^x$	3.20		2.54	2.18	0.352	32.9	19.5	29.2	58.2	72.7	
$^{45}Sc^{++}$	0.092	0.00016	0.162		0.283	0.579	10.5		0.904	11.1	83
1σ	0.065		0.495		1.34	0.262	1.25		0.052	0.319	
$^{25}Mg^+$	102322	0.00142	99202	101226	110304	88841	9868	817.7	14.3	110.5	11
1σ	3474		3679	2654	3251	4469	322.1	3.15	0.488	2.39	
$^{47}Ti^+$	4.89	0.00050	3.15	2.04	0.274	9.90	7.92	6.10	3.37	40.6	27
1σ	0.699		0.901	0.460	0.236	6.60	1.73	0.466	0.149	1.34	
$^{51}V^+$	10.1	0.00937	9.33	3.14	486.3	5.86	0.103	0.044	32.8	362.2	3
1σ	1.52		0.927	0.636	21.8	3.52	0.019	0.012	1.25	18.74	
$^{52}Cr^+$	238.6	0.00673	236.8	156.7	128.4	108.4	11.6	1.25	18.5	230.9	2
1σ	16.0		16.9	25.5	28.0	8.01	0.657	0.487	1.03	7.47	
$^{55}Mn^+$	835.8	0.00286	711.8	746.6	5.46	5956	15252	29856	20.0	233.1	4
1σ	19.4		34.6	71.8	1.20	601.6	946.0	709.5	0.603	4.33	
$^{57}Fe^+$	1155	0.00006	929.8	937.4	7.77	12327	22280	20384	10.7	15.6	209
1σ	189		134.9	158.2	1.88	3743	3680	747	0.39	0.70	
$^{59}Co^+$	70.5	0.00211	64.1	48.01	973.3	383.0	54.1	14.07	6.82	86.9	8
1σ	1.68		2.11	3.90	35.3	24.4	1.21	2.35	0.593	1.98	
$^{60}Ni^+$	182.1	0.00025	180.2	182.7	2.86	154.3	1.13	2.30	6.52	21.6	37
1σ	4.79		2.05	4.63	2.96	8.35	0.047	2.79	0.232	0.566	
$^{63}Cu^+$	3.00	0.00293	4.19	0.481	1.43	8.05	6.35		4.94	23.7	5
1σ	0.693		0.805	0.127	1.56	4.10	0.717		0.318	0.661	
$^{66}Zn^+$	2.77	0.00018	1.68	1.52	0.263	19.3	295.0		0.41	3.39	91
1σ	0.189		0.113	0.193	0.100	1.01	3.92		0.139	0.236	
$^{88}Sr^+$	0.641	0.00583	0.666	0.651	0.220	0.655	0.275		79.1	560.6	2
1σ	0.217		0.157	0.072	0.074	0.198	0.056		2.40	19.6	
$^{89}Y^+$	0.110	0.01418	0.157	0.104	2.76	0.417	31.8		52.7	662.8	1
1σ	0.056		0.044	0.052	0.200	0.160	20.5		1.72	24.4	
$^{90}Zr^+$	0.096	0.00026	0.149	0.126	0.113	0.241	0.524		21.1	258.1	4
1σ	0.027		0.077	0.106	0.090	0.125	0.283		0.656	7.74	

x: standard deviation of the mean of multiple analyses in 2010-2011 (see Fig. 2.4, 2.5, and 2.7 for no. of individual analyses per session)

*: element-specific relative sensitivity factor RSF = $((IM^+ / I^{30}Si^+)_{SIMS-RM}$ x SiO_2 (wt.%)) / M $(ppm)_{ACCPT-RM}$; see text for discussion

2.3.1. Isobaric Interferences and Analyte Peak Selection

Energy filtering, originally described by Shimizu et al. (1978) as "a method for suppressing intensities of interfering molecular ion species relative to single-atom ions based on the kinetic energy distribution of secondary ions" can effectively remove most of the isobaric interferences for the elements of interest in this study, without reducing SI signals below an acceptable level of precision.

We evaluated multiple mass peaks of certain polyisotopic elements to assess the impact of potential isobaric interferences (Table 2.2) and to make the best possible selection of analyte mass. These were Ti (^{47}Ti vs. ^{48}Ti and ^{49}Ti), Cr (^{52}Cr vs. ^{53}Cr), Fe (^{54}Fe vs. ^{57}Fe), Ni (^{60}Ni vs. ^{61}Ni and ^{62}Ni), Cu (^{63}Cu vs. ^{65}Cu), Zr (^{90}Zr vs. ^{91}Zr, ^{92}Zr, ^{94}Zr, ^{96}Zr). Figures 2.1 and 2.2 illustrate that some of these peaks in selected RM olivine are strongly biased by interferences: especially, ^{49}Ti$^+$ (Fig. 2.1A), ^{92}Zr$^+$ (Fig. 2.2B). Others show less pronounced effects (^{53}Cr$^+$, ^{65}Cu$^+$; Fig.2.1B and 2.2A) or are not perceptibly influenced relative to the accepted natural isotope ratio and the normal magnitude of mass dependent fractionation predicted from previous studies such as Shimizu and Hart (1982a) (^{54}Fe$^+$, ^{57}Fe$^+$, ^{60}Ni$^+$, ^{62}Ni$^+$; Fig.2.1C–D).

All effectively non-interfered isotopes however, should also have linear regressions with intercepts (within the SIMS analytical error, 2SE) at the point of origin on isotope ratio diagrams (Fig.2.1 and 2.2). Additionally, the SIMS SI ratio of two selected isotopes should match their natural isotope ratio (accepted ratio), accounting for some degree of preferential detection of the lighter isotope due to instrumental fractionation (not isobaric interferences) (Slodzian et al., 1980; Shimizu and Hart, 1982a, b), as is the case for ^{62}Ni/^{60}Ni (Fig.2.1D). According to Shimizu and Hart (1982a), this mass-dependent light/heavy (L/H) isotope fractionation is in the range of +1.5 (Cr) to +3.7 (Si) % per Da in pure metals and might be less in silicate minerals like olivine. An important conclusion of the Shimizu and Hart (1982a) study was that virtually all elements analysed by SIMS using O$^-$ sputtering and positive secondary ion analytes show a preferential detection of *light* over *heavy* isotopes.

SIMS trial sessions in 2010 and 2011 implied that several of the tested isotope pairs are indeed affected by potential molecular ion interferences. Plots of one isotope against another of the same element (Fig.2.1 and 2.2) are used to demonstrate the difference (%) from the accepted isotope ratios due to potential isobaric interferences in olivine.
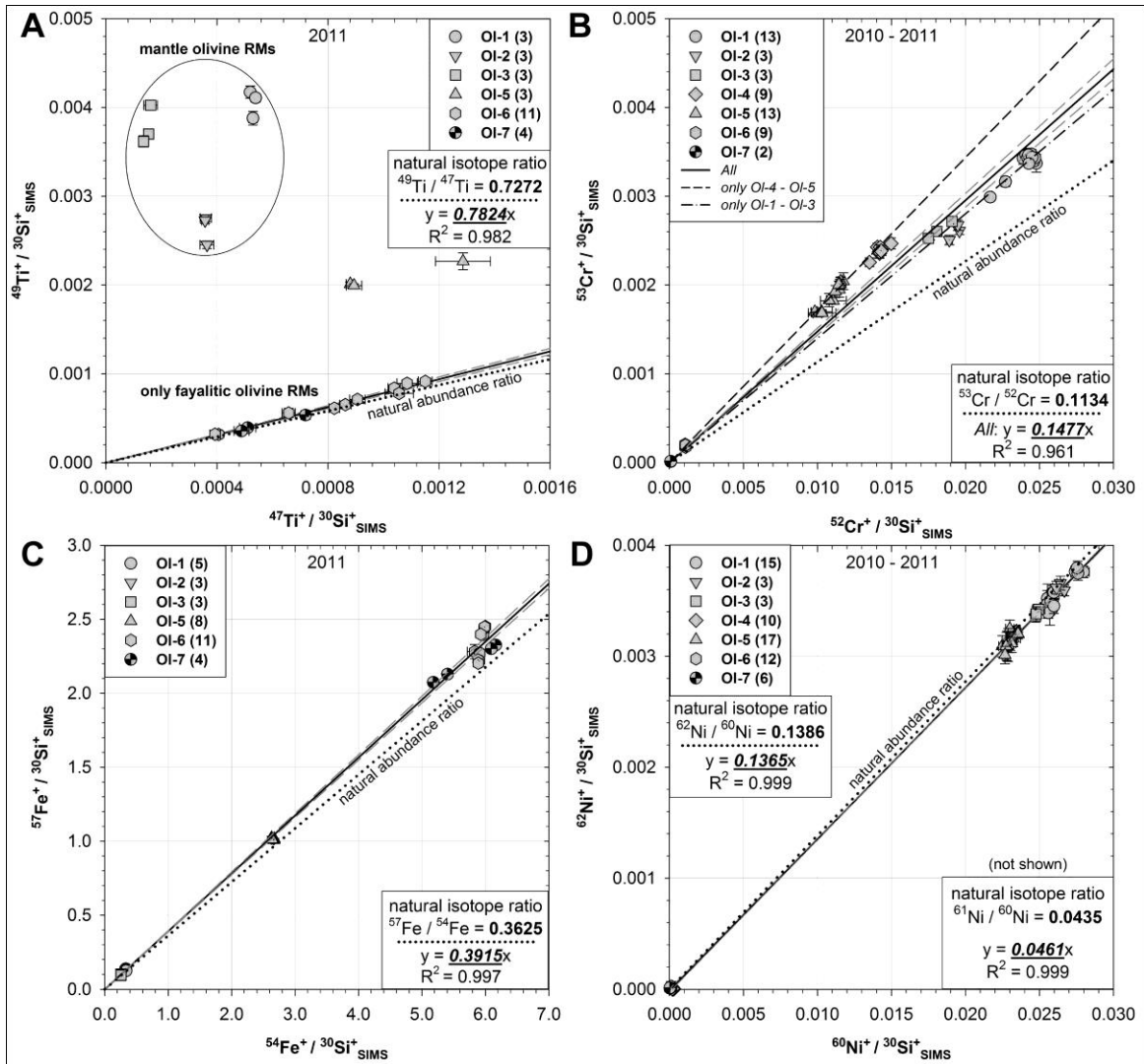
Fig. 2.1: Three-isotope plots for determination of potential mass interferences. Symbols on diagrams denote individual measurements with analytical error (2 times standard error – 2 SE). A) $^{49}Ti^+$ versus $^{47}Ti^+$, B) $^{53}Cr^+$ versus $^{52}Cr^+$, C) $^{57}Fe^+$ versus $^{54}Fe^+$, D) $^{62}Ni^+$ versus $^{60}Ni^+$. Dark grey dashed lines indicate 95% confidence interval.
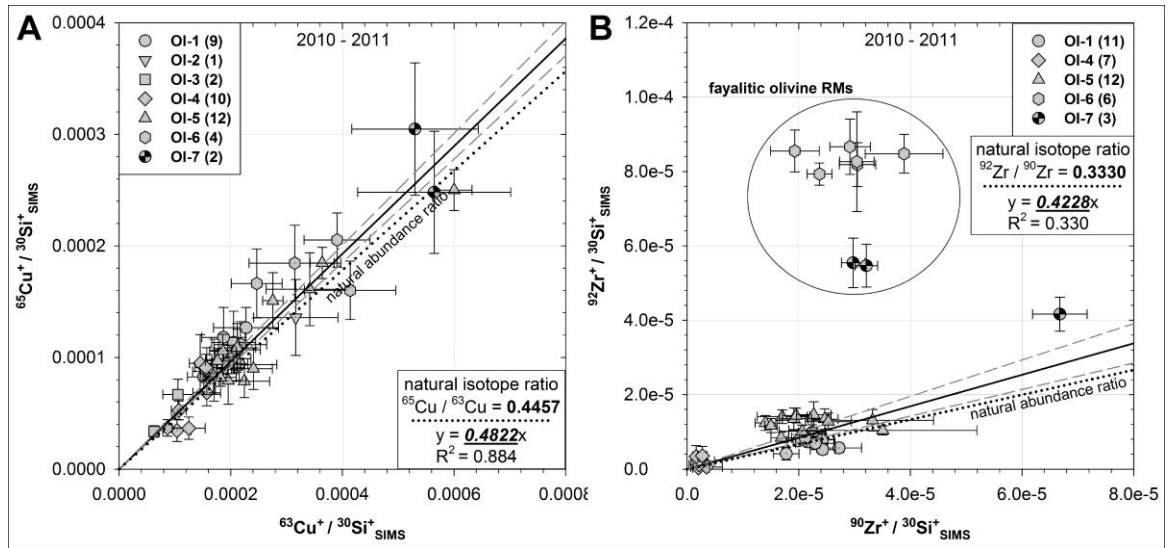
Fig. 2.2: Three-isotope plots for determination of potential mass interferences. Symbols on diagrams denote individual measurements with analytical error (2 times standard error – 2 SE). A) $^{65}Cu^+$ versus $^{63}Cu^+$, B) $^{92}Zr^+$ versus $^{90}Zr^+$. Dark grey dashed lines indicate 95% confidence interval.

2.3.1.1. Observed Isobaric Interferences

For Ti, SI yields for isotopes 48 (not shown) and 49 (Fig.2.1A) are obviously stronlgy biased to higher $^{49}Ti^+$ in the Mg-rich (mantle olivine) RM (Ol-1 to Ol-3), whereas the extremely fayalitic olivine (Ol-6 and Ol-7) yield $^{49}Ti/^{47}Ti$ ratios reasonably close to the value expected from natural abundances – although the 7% deviation (Table 2.2) of the SIMS 49/47 ratio from the accepted ratio implies that the *heavy* isotope ($^{49}Ti^+$) is preferentially detected. This effect seems to correlate with the Mg content of olivine and becomes progressively less pronounced from forsteritic (Ol-1 to Ol-3), through intermediate (Ol-5), to fayalitic (Ol-6 and Ol-7), compositions. Therefore, a strong molecular interference from a persistent Mg-species ($^{24}Mg^{25}Mg^+$, $^{24}Mg_2H^+$ etc.; Table 2.2) on $^{49}Ti^+$ is most likely responsible. Similar species are expected to interfere with $^{48}Ti^+$. As a consequence, $^{47}Ti^+$ is the preferred analyte peak for Ti, as there are no simple Mg-based isobaric interference possible at this mass.

The empirical fit for the tested Cr isotopes, 52 and 53 (Fig.2.1B), suggests an isobaric signal contribution to $^{53}Cr^+$, most pronounced in Ol-4 and Ol-5 (measured 53/52 ratio of 0.1693 versus natural 53/52 ratio of 0.1134). Using the slope of the regression line incorporating all olivine RM, the relative deviation is circa 23% (Table 2.2), implying preferential detection of the *heavy* isotope, most likely through interference from persistent Mg- (i.e. $^{26}MgH^+$) and MgSi-species (i.e. $^{24}Mg^{29}Si^+$ or $^{25}Mg^{28}Si^+$) (Table 2.2).

Possible interferences on Fe analyte masses were examined for $^{54}Fe^+$ and $^{57}Fe^+$. The linear regression (Fig.2.1C) implied a minimum deviation of the SIMS 57/54 ratio from the accepted ratio of circa 7% (Table 2.2). The *heavy* isotope thus appears slightly enriched,

which is probably a result of minor signal contributions from $^{25}Mg^{16}O_2{}^+$, $^{28}Si_2H^+$, and $^{56}FeH^+$ (Table 2.2). However, the contributions from these isobaric interferences are at a level that produces no discernible error in the determination of Fo content using the $^{57}Fe^+$ analyte.

Nickel has been documented as prone to substantial matrix effects in olivine (*cf.* Shimizu et al., 1978; Reed et al., 1979; Steele et al., 1981; Shimizu and Hart, 1982b; Weinbruch et al., 1993) but was first tested for isobaric interferences by using analyte masses $^{60}Ni^+$, $^{61}Ni^+$, and $^{62}Ni^+$. The relative deviation of the SIMS $^{62}Ni/^{60}Ni$ ratio from the accepted ratio is −1.5% (Fig.2.1D; Table 2.2). This demonstrates the normally expected enhanced production of the *light* isotope relative to the *heavy* isotope, implying an essentially interference-free signal from both masses (e.g., Shimizu and Hart, 1982a). $^{60}Ni^+$ was selected as the preferred analyte mass based on its higher isotopic abundance, and, quantification of the $^{60}Ni^+$-based analyses return excellent correlation with EPMA results (see Section 4.3.).

Determinations of $^{63}Cu^+$ and $^{65}Cu^+$ yield a good linear regression, with a $^{65}Cu/^{63}Cu$ ratio close to the natural abundance ratio (Fig.2.2A). The overall SIMS 65/63 deviation is circa 8% (Table 2.2), which implies a minor isobaric signal contribution to $^{65}Cu^+$. This is likely from $^{64}ZnH^+$, since Zn is uniformly more abundant than Cu in the olivine studied here (Table 2.1). At higher masses (≥60 Da) hydride interferences are also more difficult to remove by energy filtering than monoxide or dimer species (Shimizu and Hart, 1982b). Consequently, $^{63}Cu^+$ was selected as the preferred analyte mass.

The $^{92}Zr^+$ signal is excursively affected at the Fe-rich extreme of the olivine solid solution (Fig.2.2B). In the most fayalitic olivine (Ol-6 to Ol-7), the $^{92}Zr^+$ signal appears significantly enhanced by $^{56}Fe^{18}O_2^+$ and $^{46}Ti_2^+$ signal contribution. The SIMS 92/90 deviation based only on data from Ol-1 to Ol-5 is 21% (Table 2.2), which still suggests a significant isobaric interference on $^{92}Zr^+$. However, the 92/90 ratios determined in high-Mg mantle olivine (e.g., Ol-1) evidence no signal contributions from possible Ni species isobars, such as the possible $^{58}Ni^{16}O_2^+$ interference (Hervig et al., 2006), despite a Ni abundance of ~3000 ppm (and a Ni/Zr ratio of >300:1). Observations from additional test runs in 2011 with all five Zr isotopes confirmed empirically that no isobaric interference due to a Ni species is detectable in the olivine studied herein. Consequently, $^{90}Zr^+$ was selected as the preferred analyte mass based on its higher isotopic abundance.

In summary, based on the analytical and empirical assessments mentioned above, the following analytical peaks are preferred: $^{47}Ti^+$, $^{52}Cr^+$, $^{57}Fe^+$, $^{60}Ni^+$, $^{63}Cu^+$, and $^{90}Zr^+$. $^{40}Ca^{++}$ was selected as the analyte peak for Ca – to avoid the overwhelming interference by $^{24}MgO^+$ on $^{40}Ca^+$, and similar effects on the other singly charged Ca isotope species.

2.3.2. Matrix Effects

Shimizu et al. (1978), Steele et al. (1981) and Shimizu and Hart (1982b) recognized that the secondary ion (SI) yield of Mg^+ in olivine is strongly enhanced as a function of Fe content. However, some minor elements are also similarly affected, and Reed et al. (1979) and Steele et al. (1981) observed that SI yields of Ni are also a strong function of the Fe content. Recently, Weinbruch et al. (1993) reiterated this observation, but only for

olivine within a limited compositional range (0–17 wt.% FeO; Fo_{100}-Fo_{80}). They concluded that compositional matrix effects could be neglected for analyses of Fe and Mn, but that Ni was very sensitive (along with Sc) – with variations of the RSF_{Ni} of about 60% over their limited range of reported FeO contents. In this study, we report an increase of the RSF_{Ni} of ~139% from Ol-1 (10.71 wt.% FeO) to Ol-5 (39.66 wt.% FeO) (see Section 4; Fig.2.5B). In order to calibrate for these significant effects, a wide range of olivine composition RM is essential.

Most of the elements studied show reasonably linear correlations on traditional working line plots (e.g., Ca, V and Cr in Figs.2.4A–C, respectively) – implying that their SI yields are substantially independent of major element matrix effects. However, several elements show significant degrees of curvature on plots of Relative Sensitivity Factor (RSF) against Fo content – i.e., Mn, Co, Ni, Cu and Zn in Figures 2.4 and 2.5 – implying a substantial matrix effect on SI yield. Notably, Ca was also documented as sensitive to matrix effects by Shimizu et al. (1978), Ottolini (2002) and Lehmann (2003), but our use of $^{40}Ca^{++}$ (avoiding potential variable interference from $^{24}Mg^{16}O^{+}$) may have mitigated this effect. The variations in the elemental RSF values are an additional demonstration of the significant amplitude of the matrix effect over a range of olivine compositions (Mg-Fe-Si). Multivariate regression (Fig.2.6) revealed good linear correlations (e.g., R^2=0.983 for $^{60}Ni^{+}$; Fig.2.6D) between the elemental RSF and the major components of olivine, SiO_2, MgO and FeO. Thus calibration with suitable RM can compensate for the matrix effect and enable a precise quantification of the element concentrations. This departure from the "conventional" calibration working line approach (e.g., as used for plagioclase,

garnet, clinopyroxene and silicate glass analyses by SIMS; Shimizu et al., 1978; Yurimoto et al., 1989; Jones and Layne, 1997; Shimizu, 2000; Lehmann, 2003) has previously been investigated in a preliminary fashion for some major and trace elements (Mg, Fe, Ni, Sc) in olivine, but not yet for the extended suite of trace elements analyzed in this study. Nonetheless, for comprehensive and accurate SIMS olivine study, the knowledge of the interaction of SI yields of "matrix-sensitive" trace elements with varying olivine composition is imperative. The introduction of a set of new olivine RM has thus the potential to expand the field of olivine trace element geochemistry with SIMS and make it robust for compositionally diverse suites of olivine.

2.4. Results and Discussion

SIMS olivine RM measurements were made in multiple extended sessions from 2009 to 2011. During the sessions in 2009, we analyzed a total of 82 spots on 5 different olivine RM (Ol-1 to Ol-5). In 2010 we measured a total of 157 spots on 7 different olivine RM (Ol-1 to Ol-7) and in 2011 a total of 135 spots on 5 different olivine RM (Ol-1, Ol-2, Ol-4 to Ol-6). The last set is considered the most appropriate olivine RM subset.

2.4.1. Calculation of the Forsterite Content

Following the empirical approach outlined in the Appendix (Chapter 6.1.), we produced a working line for extracting the Fo content of individual olivine and, by corollary calculation, the concentrations of the major elements Mg, Fe and Si.

The results for the Fo calibration procedure are depicted in Figure 2.3A and in Table 2.4. The averages of multiple (8 to 109) spot analyses of olivine analyzed throughout 2009 to 2011 are plotted in Fig.2.3A, demonstrating excellent long term stability of the secondary ion ratio determinations. The relative external precision is generally better than $\pm1\%$ (1σ), with the exception of Ol-5 ($\pm2.5\%$ 1σ), Ol-6 ($\pm9.7\%$ 1σ) and Ol-7 ($\pm6.3\%$ 1σ). The low SI signal deviation over a period of circa 28 months confirms the long-term instrumental stability of the MAF-IIC Cameca IMS 4f and demonstrates the small magnitude of instrumental drift affect on the measurements, as well as the generally adequate homogeneity of the RM (especially when averages of multiple spot measurements are used for calibration curves). The data displayed in Fig.2.3A illustrate a smooth trend with a pronounced inflection in the interval of circa $Fo_{20–50}$, anchored and described by the Ol-5 and Ol-6 samples. Average R_{Fo} ratios (where R_{Fo} is defined as $I^{25}Mg^+/I^{30}Si^+)/(I^{25}Mg^+/I^{30}Si^+ + I^{57}Fe^+/I^{30}Si^+)$ for Ol-5 and Ol-6 were 0.880 (±0.022 1σ) and 0.310 (±0.030 1σ), respectively. Inhomogeneities in either MgO or FeO contents can be ruled out as a source of the higher long-term error, since the EPMA results show little relative variation in major element content. Therefore, the slightly more elevated standard deviation of the fayalitic olivine is likely a reflection of the variable contribution of the SIMS matrix effect during sessions several years apart, since both olivine have high FeO contents, 39.66 wt.% in Ol-5 and 67.59 wt.% in Ol-6, which would account for a higher bias through variable matrix effect (Shimizu et al., 1978; Shimizu and Hart, 1982b; Lehmann 2003). This effect would, therefore, be reduced by using specific calibration sets for individual analytical sessions.

Considering the trend of our curve, and published data (e.g., Shimizu et al., 1978; Reed et al., 1979; Steele et al., 1981; Weinbruch et al., 1993), the matrix effect seems to be less pronounced for compositions ranging from Fo_{82-100} or Fo_{0-10}. For both intervals the impact of the FeO content on the MgO content and vice versa, and thus the potentially enhanced production and ionization of either SI species, is only minor, which limits the degree of bias. In accordance with our data, Shimizu et al. (1978), on the basis of results from a limited range of olivine compositions ($Fo_{\geq 80}$), predicted the highest influence at compositions between Fo_{34-80}, obviously the range where FeO and MgO concentrations are most equitable, which would result in a maximum impact of the matrix effect.

The empirical relationship between R_{Fo} and Fo (EPMA)$_{ACCPT}$ is best characterized by a non-linear regression, using a fourth order rational equation with 3 parameters. Fitting the following regression (Eq. 1) to our data in Fig 2.3A achieves an $R^2=0.999$ with the equation:

(Eq. 1) $\qquad\qquad x = (0.0003 - R_{Fo} \times 0.1391) / (R_{Fo} \times 0.8601 - 1)$

where x represents the Fo (EPMA) value and R_{Fo} equals $(I^{25}Mg^+/I^{30}Si^+)/(I^{25}Mg^+/I^{30}Si^+ + I^{57}Fe^+/I^{30}Si^+)$. The coefficients a, b and c can easily be calculated with scientific data analysis and graphing software (e.g., SigmaPlot$^®$). Once established, the Fo working curve can be applied to accurately determine the Fo content of olivine of diverse compositions from a variety of origins and host rocks (see Appendix 6.1.).

Considering the high reproducibility (external precision) of the results, even over a period of almost 28 months (relative spread around the average R_{Fo} values recovered of between 0.002% (Ol-3, 1σ) and 9.7% (Ol-6, 1σ), mean standard deviation (2σ) for measured $^{25}Mg^+/^{30}Si^+$ of better than 1.5% and $^{57}Fe^+/^{30}Si^+$ of better than 4.4% – resulting in an analytical uncertainty for R_{Fo} of ~1% 2σ; 2011 session), this technique is equivalently accurate for major element determination of olivine to EPMA – with the added benefit that Fo is determined simultaneously, and in exactly the same analytical volume, as the trace element analyses. For example, for the Fe-rich Ol-6 the relative analytical error (2σ) for the Fo content was ~5.3% with EPMA and ~2.9% with SIMS, diminishing to <0.1% for the Mg-rich Ol-1 to Ol-3.

Minor and trace element concentrations are generally less than 1 wt.% in natural olivine (Deer et al., 1997). Consequently, they will fall close to stoichiometrically determined curves between the ideal Fo-Fa endmembers – allowing straightforward calculation of the contents of MgO, FeO and SiO_2 using the Fo content determined by SIMS. This procedure is portrayed graphically by plotting the wt.% of the major elements (Mg-Fe-Si) versus the Fo contents (accepted values as determined by EPMA) of the reference olivine selected for this study (Fig.2.3B). The computed Fo value of an unknown olivine can then be inserted to solve the individual equations for the major element concentrations in stoichiometrically pure olivine (see Appendix 6.1.).
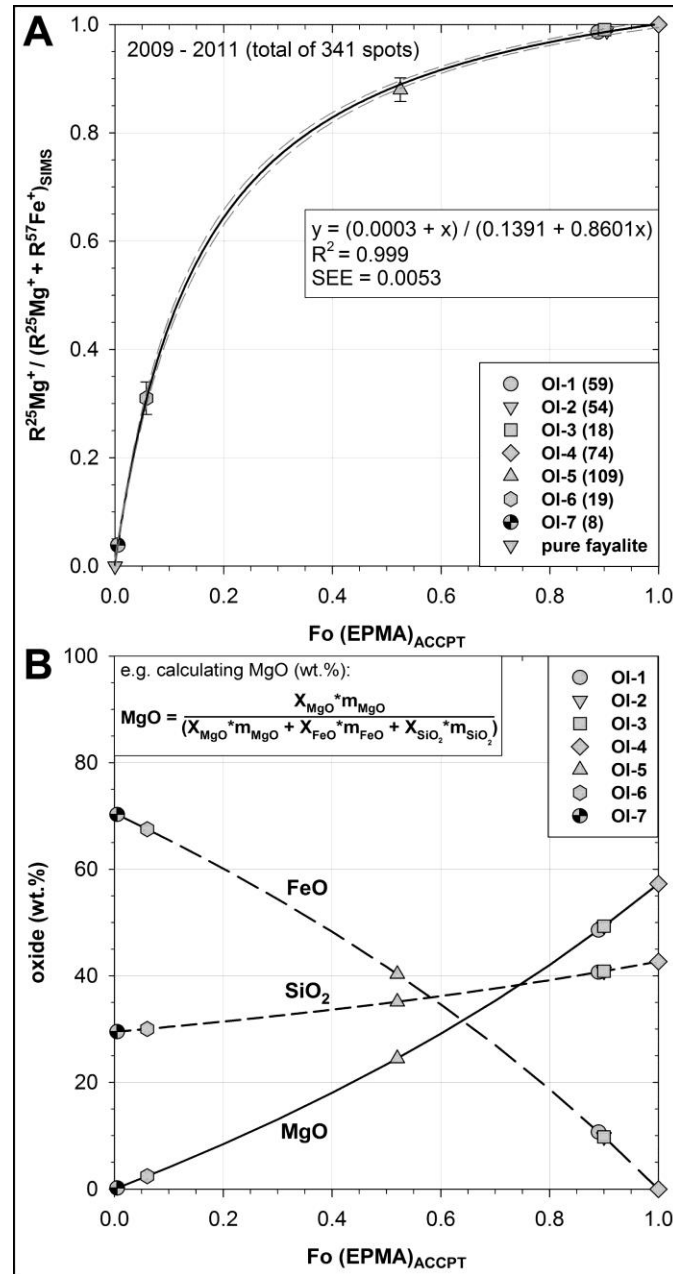
Fig. 2.3: A) Average raw R_{Fo} determined by SIMS against the average accepted Fo (EPMA) values (Table 2.4). This relationship (Step 1) allows the calculation of the unbiased Fo content of any olivine. The number in brackets behind sample identification refers to the sum of measured spots on each sample over a 28 month period. The error bars are the standard deviation of the average (1σ). Dark grey dashed line is the 95% confidence interval. SEE denotes standard error of the estimate. B) Weight concentration of major elements in (perfectly stoichiometric) olivine (MgO, FeO, SiO_2) versus Fo content determined with EPMA (Appendix 6.1.).

Table 2.4: Average forsterite content of reference olivine determined with EPMA and SIMS

RM's	Fo (EPMA)	SD (1 σ)	1 σ (%)	nˣ	R_Fo (SIMS)ᵞ	SD (1 σ)	1 σ (%)	nᶻ	Fo (SIMS)[1]	SD (1 σ)
Ol-1	0.888	0.001	0.06	15	0.986	0.005	0.52	59	0.901	0.005
Ol-2	0.905	0.001	0.05	20	0.988	0.003	0.28	54	0.914	0.003
Ol-3	0.901	0.007	0.78	30	0.991	0.002	0.17	18	0.930	0.002
Ol-4	1.000	0.000	0.01	20	1.000	0.000	0.00	74	0.992	0.000
Ol-5	0.525	0.002	0.42	38	0.880	0.022	2.49	109	0.502	0.012
Ol-6	0.057	0.002	3.60	31	0.310	0.030	9.72	19	0.058	0.006
Ol-7	0.005	0.000	0.00	3	0.039	0.002	6.31	8	0.005	0.000
fayalite	0.000				0.000				0.000	

ˣ: no. of EPMA analyses from multiple sessions in 2009

ᵞ: calculated based on relationship $R^{25}Mg^+ / (R^{25}Mg^+ + R^{57}Fe^+)$; see text for discussion

ᶻ: no. of SIMS analyses from multiple sessions between 2009 - 2011

[1]: forsterite content calculated with empirical relationship from Fig.2.3

In summary, a straightforward calibration of SIMS olivine analyses with suitable RM, allows a reasonably precise determination of the Fo content (generally ±1.5% 2σ; see Appendix 6.2.) and thus the major element concentrations of an unknown olivine, plus a suite of geochemical versatile trace elements in just one analytical step.

2.4.2. Quantification of Minor and Trace Elements

Based on the analytical trials of the 2009 to 2011 SIMS sessions, our suite of trace elements can be usefully subdivided into two groups: Group I comprises isotopes with an atomic mass $\leq^{66}Zn$ where analysis is generally (with the possible exception of ^{63}Cu) straightforward and highly precise, in large part due to the relatively high abundances of these elements in natural olivine. Group II is composed of isotopes with an atomic mass $>^{66}Zn$ but $\leq^{90}Zr$, which have very low abundances in natural olivine (ppm to sub-ppm), increasing the difficulty of precise analyses. This subdivision is therefore strictly based on

analytical strategy and performance (abundance and SI yield) and does not reflect any intrinsic geochemical (melt composition, pressure – temperature or oxygen fugacity dependence, partition coefficients etc.) or mineralogical (i.e., incompatibility, oxidation state, ionic radius, electronegativity, site preference) affinities of these element Groups. A detailed discussion of trace element partitioning behavior in olivine is beyond the scope of this paper and the interested reader is referred to recent publications of Taura et al. (1998), Zanetti et al. (2004), Bédard (2005), De Hoog et al. (2010), and Grant and Wood (2010).

2.4.2.1. Group I Elements (^{40}Ca, ^{51}V, ^{52}Cr, ^{55}Mn, ^{59}Co, ^{60}Ni, ^{63}Cu, ^{66}Zn)

This group largely comprises elements that occur in olivine in concentrations that yield SI intensities that allow reasonably precise analysis. Further, the specific analyte peaks selected in this study are not prone to significant isobaric interferences when adequate energy filtering is applied.

An exception within this group is copper (^{63}Cu), which has a very low natural abundance in olivine and also a relatively high first ionization energy (therefore relatively low secondary ion yield; see also Hervig et al., 2006), and thus cannot be determined with very high confidence. This is consequent to the poor counting precision of the low SI intensities, combined with high analytical uncertainties in the accepted concentrations measured by the solution ICP-MS and ICP-OES techniques.

Working lines produced with the conventional calibration curve method (Appendix 6.1.3. – Step 3) (e.g., Shimizu et al., 1978; Shimizu, 2000) for the Group I elements Ca, V and

Cr (Fig.2.4A–C) reveal strong linear relationships, with R^2 of 0.987 for ^{52}Cr, 0.997 for ^{40}Ca, and 0.999 for ^{51}V. RSF-based working lines are plotted against Fo content (see Appendix 6.1.3. – Step 4A) for the remaining elements, analysed as ^{55}Mn$^+$, ^{59}Co$^+$, ^{60}Ni$^+$, ^{63}Cu$^+$ and ^{66}Zn$^+$, in Figures 2.4D and 2.5A–D. These plots display curved trends and are best described by (polynomial) regressions – which all yield R^2 >0.99.

Representative plots of RSF values alternately expressed as a function of MgO-FeO-SiO$_2$ (see Appendix 6.1.3. – Step 4B) are depicted in Figure 2.6. The detailed use of these plots in the SIMS calibration procedure, as well as the characteristics and behavior of each element (ionic radii, most common oxidation state, first ionization energy (IE; eV)) are discussed below, with reference to Figures 2.4–2.6.

^{40}Ca (1.00 Å, 2+, IE 6.1132): Ca concentrations range from 21.8 ppm (Ol-4) to 3,822 ppm (Ol-6) and generally increase with decreasing Fo content in the olivine studied. Normalized SI ratios plotted against atomic (weight) ratios describe a near linear regression (R^2=0.997; Fig.2.4A), and RSF values are virtually identical for all RM over the measured Fo range (Fo$_{6–100}$). Therefore, the Fo-Fa matrix effect seems insignificant and quantification can be based on conventional working lines (Fig.2.4A).

^{51}V (0.64 Å, 3+, IE 6.7462): V concentrations are generally low, between 3.9 ppm (Ol-6) and 12.9 ppm (Ol-5); Ol-4 is an exception with 395 ppm. The conventional working line plotted against atomic (weight) ratios based on accepted concentrations from ICP-MS analyses yields a linear regression with a R^2=0.999 (Fig.2.4B). Despite this excellent correlation the "accepted" V concentrations for most of the lower-V olivine RM cause them to plot to the right of the regression line (Fig.2.4B, detail – grey symbols). This

implies that the ICP-MS results are biased towards higher V concentrations in these latter samples, which is the result of contamination through micro-inclusions of ilmenite or chrome diopside (SEM results). On the other hand, if the NIST 612/610 glasses are used independently to calibrate the V content of the RM olivine as measured by SIMS, accepted V concentrations appear more accurate and collinear (Fig.2.4B, detail − black symbols). For example, the accepted value of Ol-6 decreases from 3.8 ppm to 0.05 ppm, and an improved correlation with SI intensities is achieved for all the low V olivine (Ol-1 to Ol-6, except Ol-4; Fig.2.4B). Even though this back-calculation relies on the assumption of matrix equivalence between olivine and NIST 612/610, the slopes of the two respective working lines are within 11% relative error, and the V SI intensities reveal the apparent inclusion effect on "accepted" V concentrations from solution methods.

^{52}Cr (0.62 Å, 3+, IE 6.7665): Cr contents range from 4.3 ppm (Ol-6) to 142 ppm (Ol-1) and show a generally positive correlation with Fo content in the olivine samples studied. The conventional working line demonstrates a strong linear correlation, with R^2=0.987 (Fig.2.4C). Even though the element-specific RSF for Cr seems to be largely independent of the Fo content, a significant improvement in linear correlation is gained when plotted against a multivariate function of MgO-FeO-SiO$_2$ (R^2=0.999; Fig.2.6A). Following Step 4B (Appendix 6.1.3.), the more sophisticated RSF-based calculation can therefore be used to slightly improve the accuracy of the final quantification.

^{55}Mn (0.83 Å, 2+, IE 7.4340): Mn concentrations are routinely very high (up to 15,833 ppm in Ol-7) and commonly demonstrate a strong negative correlation with Fo content. RSFs show a strong dependence on the Fo content, and the RSF versus Fo content trend

is distinctly curved (R^2=0.999; Fig.2.4D), indicating a significant matrix effect bias. Quantification is most accurate when an RSF-based working line is utilized, either fitted against the Fo content or multivariate function of MgO-FeO-SiO_2. The correlation with MgO-FeO-SiO_2 produces a good linear regression (R^2=0.991; Fig.2.6B) but calculated Mn concentrations are almost identical using either RSF-based working line approach.

^{59}Co (0.65 Å, 2+, IE 7.8810): Co contents range from 21.5 ppm (Ol-6) to 3,123 ppm (Ol-4; Co-doped synthetic forsterite). A negative correlation with Fo content is visible from Fo_{90} (136.7 ppm) to Fo_{52} (321.2 ppm), whereas Fo_6 (Ol-6) is strongly depleted in Co. The element-specific RSF-based working lines display a near linear correlation with both the Fo content (Fig.2.5A; R^2=0.998) and when plotted against a multivariate function of MgO-FeO-SiO_2 (Fig.2.6C; R^2=0.988). However, calculation of the element concentration with Step 4A (Fig.2.5A) yields more accurate results, especially for high Co olivine, where quantification with Step 4B (Appendix 6.1.3.) (Fig.2.6C) displays an overestimation of circa 40% due to the statistical leverage of the Tanzanion standard (high MgO-SiO_2).

^{60}Ni (0.69 Å, 2+, IE 7.6398): Ni concentrations range from 6 ppm (Ol-6) to 2,931 ppm (Ol-3) and have a pronounced positive correlation with Fo content in the olivine studied. The RSF-based working line versus Fo content is strongly curved (Fig.2.5B; R^2=0.998), indicating a distinct matrix effect influence. In accordance with literature data (Reed et al., 1979; Steele et al., 1981; Shimizu and Hart, 1982b; Weinbruch et al., 1993) the bias is insignificant for Fo compositions from Fo_{95-85}, but is potentially severe in olivine with Fo_{80} and lower. When plotted against a multivariate function of MgO-FeO-SiO_2, a good

linear regression is obtained (Fig.2.6D; R^2=0.983). Both Step 4A and Step 4B approaches allow an accurate matrix effect-corrected quantification with similar results.

^{63}Cu (0.73 Å, 2+, or 0.77 Å, 1+, IE 7.7264): Cu contents are, with one exception (Ol-5, 105 ppm), very low (<5 ppm) and the "accepted" values from ICP-MS and ICP-OES techniques already have a high uncertainty – likely exacerbated by the presence of Cu-sulfide micro-inclusions. SI yields vary in precision and reproducibility during and between analytical sessions and thus display poor correlation with atomic (weight) ratios. RSF-based working lines (Fig.2.5C and Fig.2.6E) based on averaged data produce strong correlations (R^2≥0.992) between element-specific RSF and Fo content or major element concentrations. However, both approaches hinge primarily on the accepted Cu concentration in Ol-5, which is likely overestimated by solution-based techniques (note the varying Cu results of ICP-MS and ICP-OES techniques; Table 2.1). Therefore, Cu concentrations are more adequately quantified in the RM by simply utilizing a conventional NIST glass-based working line (Appendix 6.1.2. – Step 3). An improved certainty in accepted Cu contents for the RM would be highly desirable, since these values control the empirical calculation and therefore the accuracy of the final quantification, if a matrix effect-influence is to be considered – as indicated in this study (Fig.2.5C).

^{66}Zn (0.74 Å, 2+, IE 9.3942): Zn concentrations range from circa 5 ppm (Ol-4) to 2,631 ppm (Ol-6) and display a marked negative correlation with Fo content in the olivine studied. RSF-based working lines describe a curved trend with varying Fo content (Fig.2.5D; R^2=0.986), whereas the RSF expressed as a multivariate function of MgO-

FeO-SiO$_2$ produces a strong linear correlation (R^2=0.990; Fig.2.6F). As for Mn, quantification with either approach (Appendix 6.1.3. – Step 4A or 4B) yields almost identical results.
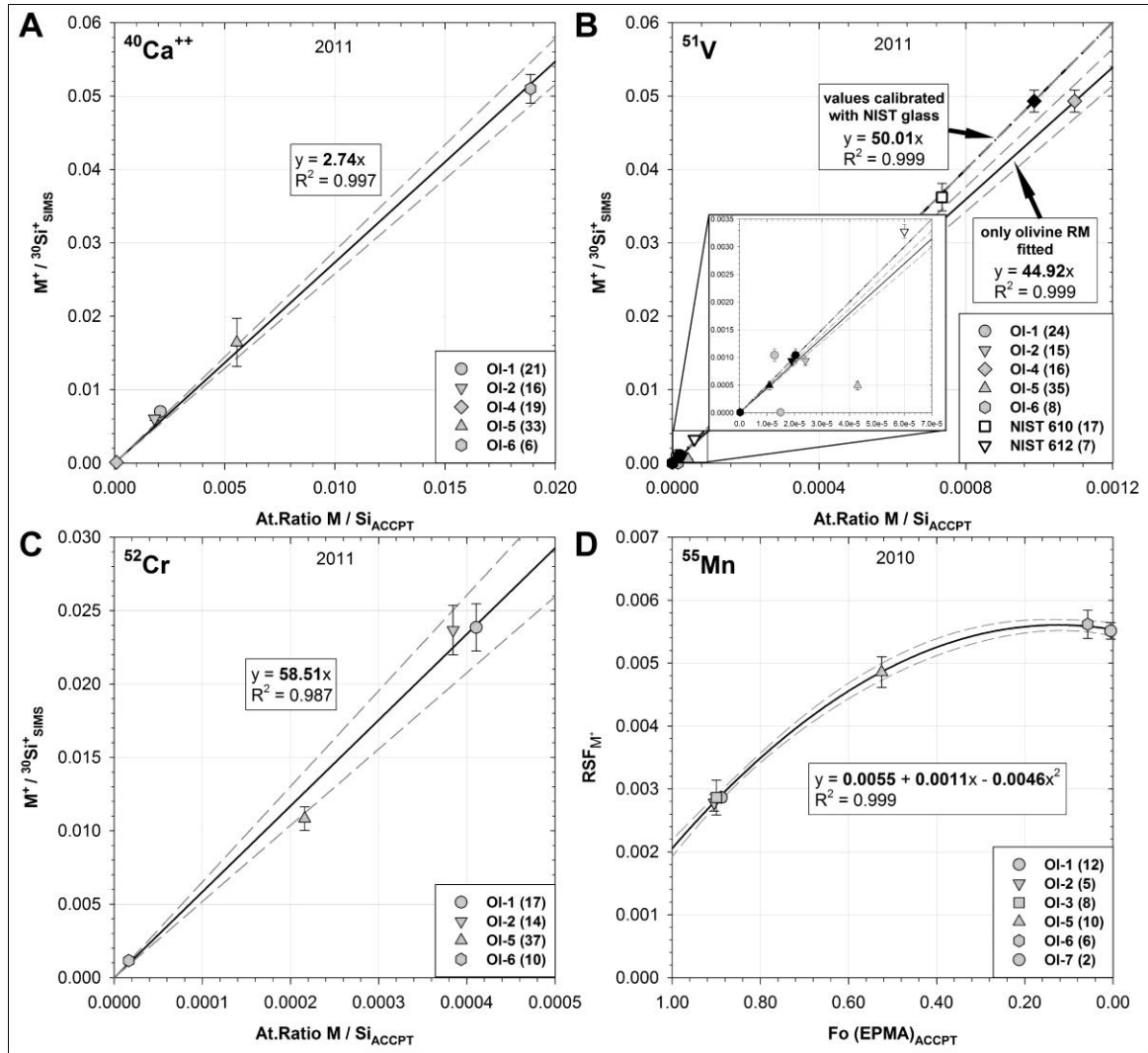
Fig. 2.4: Working lines for Group I elements (^{40}Ca, ^{51}V, ^{52}Cr, ^{55}Mn). A) to C) are conventional working lines of SI ratios fitted against atomic weight ratios, whereas D) is an element-specific RSF-based working line fitted against the accepted Fo content. The number in brackets behind sample identification refers to the sum of measured spots on each sample. The error bars are the standard deviation of the average (1σ). Figures 2.4A to C resemble Appendix 6.1. – Step 3, and Figure 2.4D resembles Appendix 6.1. – Step 4A in our empirical approach. Dark grey dashed lines indicate 95% confidence interval.
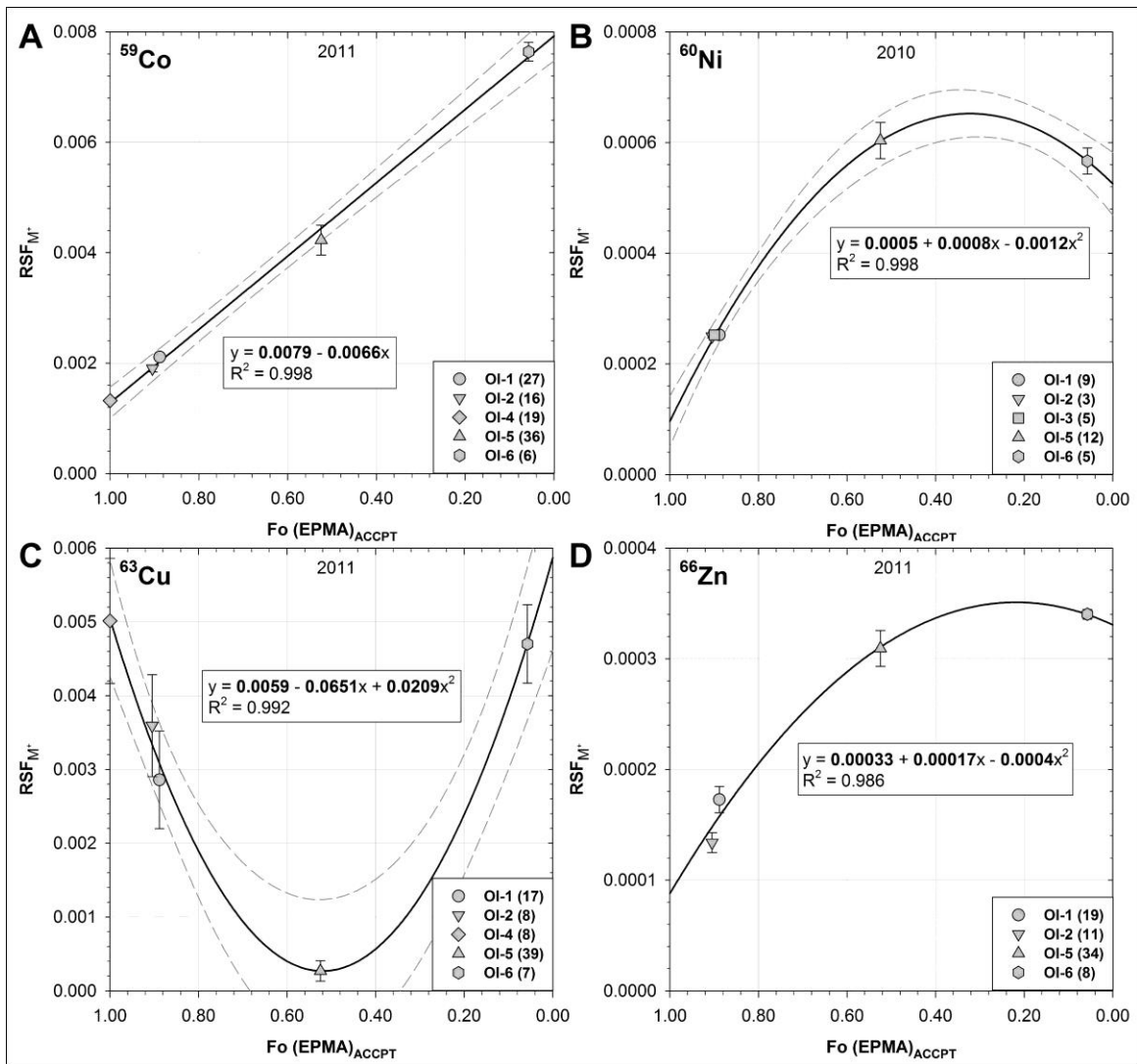
Fig. 2.5: Working lines for Group I elements (^{59}Co, ^{60}Ni, ^{63}Cu, ^{66}Zn). A) to D) are element-specific RSF-based working lines fitted against the accepted Fo content. The number in brackets behind sample identification refers to the sum of measured spots on each sample. The error bars are the standard deviation of the average (1σ). Figures 2.5A to D resemble Appendix 6.1. − Step 4A in our empirical approach. Dark grey dashed lines indicate 95% confidence interval.

The elements Mn, Co, Ni and Zn are geochemically similar to Mg^{2+} and Fe^{2+}, with comparable ionic radii (Mg^{2+}: 0.66 Å, Fe^{2+}: 0.74 Å) and identical oxidation states. Co and Ni are very compatible in Fo-rich olivine (e.g., Bédard, 2005; De Hoog et al., 2010), whereas Mn and Zn more readily substitute into Fa-rich olivine (Kohn and Schofield, 1994). Therefore, all four of these divalent elements can be relatively abundant in the olivine structure in place of Mg^{2+} and Fe^{2+}, preferentially occupying one of the two 6-fold coordinated octahedral lattice spaces (M1 and M2) (Ericsson and Filippidis, 1986; Ito et al., 1999 and references therein). However, the variable morphologies of the RSF-based curves (Fig.2.4 and 2.5) suggest that these elements are affected somewhat differently during sputtering. In particular, Mn, Ni and Zn share similar convex curve morphology, whereas Co displays a more nearly linear slope, and the Cu curve is strongly concave.

The geochemical resemblance of Co and Ni to Mg, and Mn and Zn to Fe suggests that structural/crystallographic parameters exert some control over the amplitude of the matrix effect, particularly when bivalent substitution mechanisms are responsible and the ionic radius of the incorporated elements is the main influence on unit cell parameters. If during SIMS ion bombardment of olivine surface layer(s), positive ion emission is in fact a result of bond-breaking caused by collision cascades and hence the so-called sputtering process (Slodzian et al., 1980), the greater secondary ion yield of, for instance, Mg (Ni, Mn, Zn etc.; Lehmann, 2003) with increasing Fe content, must be directly related to an enhanced ionization and emission of the affected atoms. In the forsterite-fayalite solid solution, the replacement of Mg^{2+} by the larger radius Fe^{2+} in the olivine structure weakens the cation-oxygen bonds and thus likely the physico-mechanical resistance to the

kinetic energy transfer of the sputtering process. This might in turn cause the elevated emission of ionized bivalent transition metals that occupy either of the two 6-fold coordinated lattice spaces with increasing amounts of Fe^{2+} in the olivine crystal structure. All these bivalent transition elements display a significant matrix effect in olivine, which militates against the use of the simple conventional SIMS working lines commonly used for trace element quantification.

Monovalent, trivalent, tetravalent and pentavalent cations (Sc, Ti, V, Cr, Cu, Y, Zr) on the other hand, beside their commonly much lower abundance in olivine, are much less affected by the matrix effect. They also require more complex substitution mechanisms in the olivine structure (discussed by Taura et al., 1998; Zanetti et al., 2004; De Hoog et al., 2010; Grant and Wood, 2010), including a coupled replacement in the 4-fold coordinated tetrahedral site commonly occupied by Si^{4+}. This may cause defect sites and vacancies in the olivine crystal lattice that subsequently alter its physical properties, which in turn might make these elements and the neighboring lattice space less likely to be influenced by the previously mentioned enhanced ionization effects. Even though a systematic link between the ionization behavior and cation ordering in the olivine structure cannot be explicitly established here, further research might unravel the underlying causality between the enhanced ionization of specific cations and their geochemical attributes and crystallographic preferences in olivine.
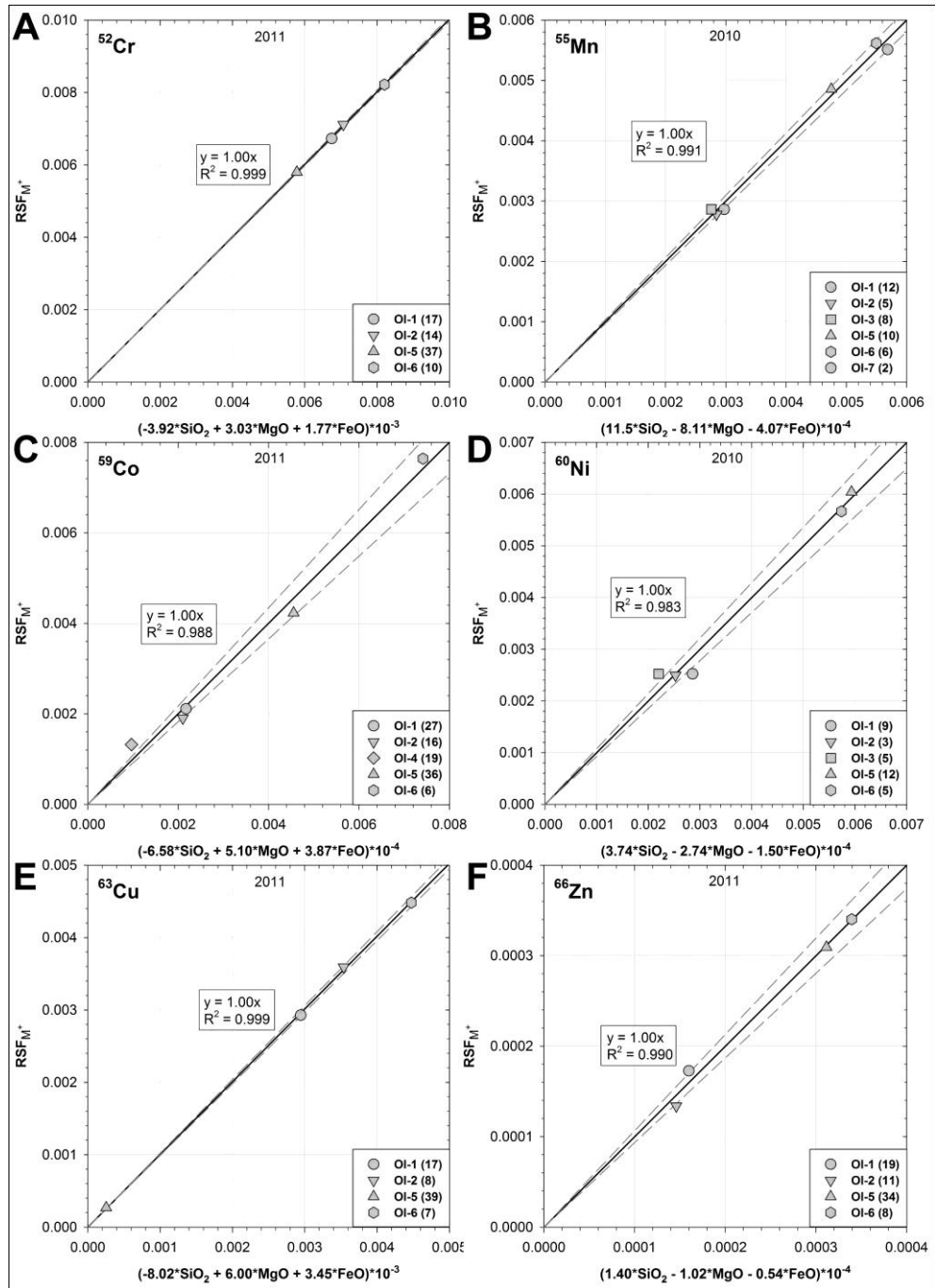
Fig. 2.6: Working lines for Group I elements (^{52}Cr, ^{55}Mn, ^{59}Co, ^{60}Ni, ^{63}Cu, ^{66}Zn) influenced by matrix effects. Element-specific RSF are fitted as a function of the three major element components in olivine in the form of (aSiO$_2$ + bMgO + cFeO) in a full model multiple regression. The number in brackets behind sample identification refers to the sum of measured spots on each sample. This Figure resembles Step 4B in our empirical approach (Appendix 6.1.).

2.4.2.2. Group II Elements (^{45}*Sc,* ^{47}*Ti,* ^{88}*Sr,* ^{89}*Y,* ^{90}*Zr)*

This group of elements has a considerably lower abundance in olivine than those in Group I. Element contents are generally less than 0.1 to 1 ppm, with some exceptions (Ol-4, synthetic Fo) and Ol-6 (metasomatic/hydrothermal fayalitic olivine) – and this significantly increases the difficulty of precise quantification. The process is further complicated by commonly strongly variable accepted element abundances from ICP-MS and ICP-OES measurements, likely caused by the inevitable contamination through micro-inclusions – which have very high leverage on the bulk concentration of these elements. Consequently, average SI ratios per session show a much higher relative variability with values between circa 10% (1σ) for ^{88}Sr in Ol-3 to 60% (1σ) for ^{90}Zr in Ol-5. Analyses are occasionally plagued by very poor analytical precision (high σ uncertainties reflecting Poisson counting statistics) and are thus only reportable as semi-quantitative in certain samples. To counter the above mentioned difficulties, final quantification of Group II elements was solely based on conventional working lines (e.g., Jones and Layne, 1997) while utilizing one olivine RM (usually Ol-1) in tandem with the NIST glasses 612 and 610 (Fig.2.7). This approach proves more acceptable, since Group II elements appear mostly independent from the Fo content and are thus probably far less biased by matrix effects. Each individual element in Group II is briefly discussed below, with reference to Figure 2.7.

^{45}Sc (0.75 Å, 3+, IE 6.5615): Sc was not determined by ICP-MS and ICP-OES techniques, and conventional working lines were produced with Ol-1 (literature data of

circa 2.4 ppm Sc from De Hoog et al., 2010) and NIST 612/610 glasses (Fig.2.7A; R^2=0.997). Analytical precision is high for fayalitic olivine (better than ±16% 2σ) and relatively poor for forsteritic olivine (circa ±90% 2σ). However, back-calculation of the Sc concentration of Ol-1 using this calibration yields comparable results (circa 2.3 ppm) within the error to the range of San Carlos olivine (2.4 to 3.0 ppm with SIMS) reported by De Hoog et al. (2010). Scandium therefore appears reasonably quantifiable with our analytical setup and a conventional working line approach.

^{47}Ti (0.61 Å, 4+, IE 6.8281): Ti contents vary from 4.3 ppm (Ol-4) to 292 ppm (Ol-6). Concentrations are highest in the low-forsterite olivine. Considerable uncertainties in the accepted concentrations (ppm) as determined by EPMA, ICP-MS and ICP-OES techniques, adversely affect the precision of the Ti working line, and thus the absolute accuracy of the calculated concentrations would benefit from better characterization of the accepted Ti concentrations in the olivine RM. However, using a conventional working line based on Ol-1 and NIST 612/610 (Fig.2.7B) yields a near perfect linear correlation (R^2=0.996) and allows reasonable determination of the Ti content in olivine.

^{88}Sr (1.18 Å, 2+, IE 5.6949): Sr abundances vary from 0.22 ppm (Ol-6) to 1.1 ppm (Ol-5) in the RM studied. On the basis of the conventional working lines, we tried to differentiate between biased and unbiased accepted concentrations of Sr, and concluded that those for samples Ol-1, Ol-4 and Ol-5 appeared most accurate and suitable. However, due to the high uncertainty of the accepted values from solution ICP-MS, probably due to contamination by micro-impurities (melt/fluid/mineral inclusions), analytical results were quantified based on a conventional working line with NIST 612/610 (Fig.2.7C;

R^2=0.995). Individual SIMS analyses of Ol-1, Ol-4, and Ol-5 have variable internal precisions with an average uncertainty of 40% (2σ) after rejection of outliers.

^{89}Y (0.9 Å, 3+, IE 6.2171): Y concentrations ranged from 0.03 ppm (Ol-1) to 42.6 ppm (Ol-6). The Fo_{90} samples (Ol-1 and Ol-2) have very low concentrations and higher analytical uncertainties (Ol-1 ~60% 2σ) than the more fayalitic samples (Ol-5 ~33% 2σ and Ol-6 ~37% 2σ). The synthetic Ol-4 (Fo_{100}) has the lowest analytical uncertainty (~16% 2σ). The Y concentrations in Ol-5 and Ol-6 seem to be artifacts of microinclusions. As a result, a conventional working line with Ol-1 and NIST 612/610 was used for quantification. The regression exhibits a linear correlation (Fig.2.7D) with an R^2=0.995. A recalculation of the Y concentration of Ol-1 and Ol-2 based in the NIST glass working line adjusted the "accepted" values from 0.25 to 0.05 ppm in Ol-1 and from 0.06 to 0.07 ppm in Ol-2.

^{90}Zr (0.72 Å, 4+, IE 6.6339): Zr varies from circa 0.8 ppm (Ol-1) to 9.4 ppm (Ol-5). Some analytical challenges for Zr have been discussed above, but the observed scatter in working lines probably stems from biases in the accepted Zr concentrations from solution ICP-MS data, rather than isobaric interferences during SIMS (see Section 2.3). As noted by Garrido et al. (2000), incompatible trace elements like REE, Zr, Nb, Ta and Sr in olivine, especially from mantle xenoliths (samples Ol-1 to Ol-3), are most likely concentrated in melt/fluid or mineral inclusions. Solution ICP-MS analysis is thus more prone to contamination than in-situ techniques and probably determines higher concentrations of those elements than actually present within the olivine. Consequently, a NIST 612/610-based conventional working line was utilized for quantification, which

yielded a strong linear correlation (R^2=0.997). This working line implies that the "accepted" Zr content of Ol-1 (San Carlos olivine) is also too high, and the SIMS recalculated concentration (versus NIST 612/610) is 0.24 ppm, compared to the 0.75 ppm from ICP-MS analysis.

In summary, the very low concentration of most trace elements in Group II makes them analytically more challenging, and often susceptible to lower internal precision. Despite those complications, Sc, Ti, Sr, Y, and Zr can be quantified in a useful manner. Secondary ion intensities demonstrate no perceptible dependency on the Fo content. We feel that this is strong proof (though not absolute) that matrix effects seem to be relatively insignificant, allowing the simple application of NIST glass-based conventional working lines.
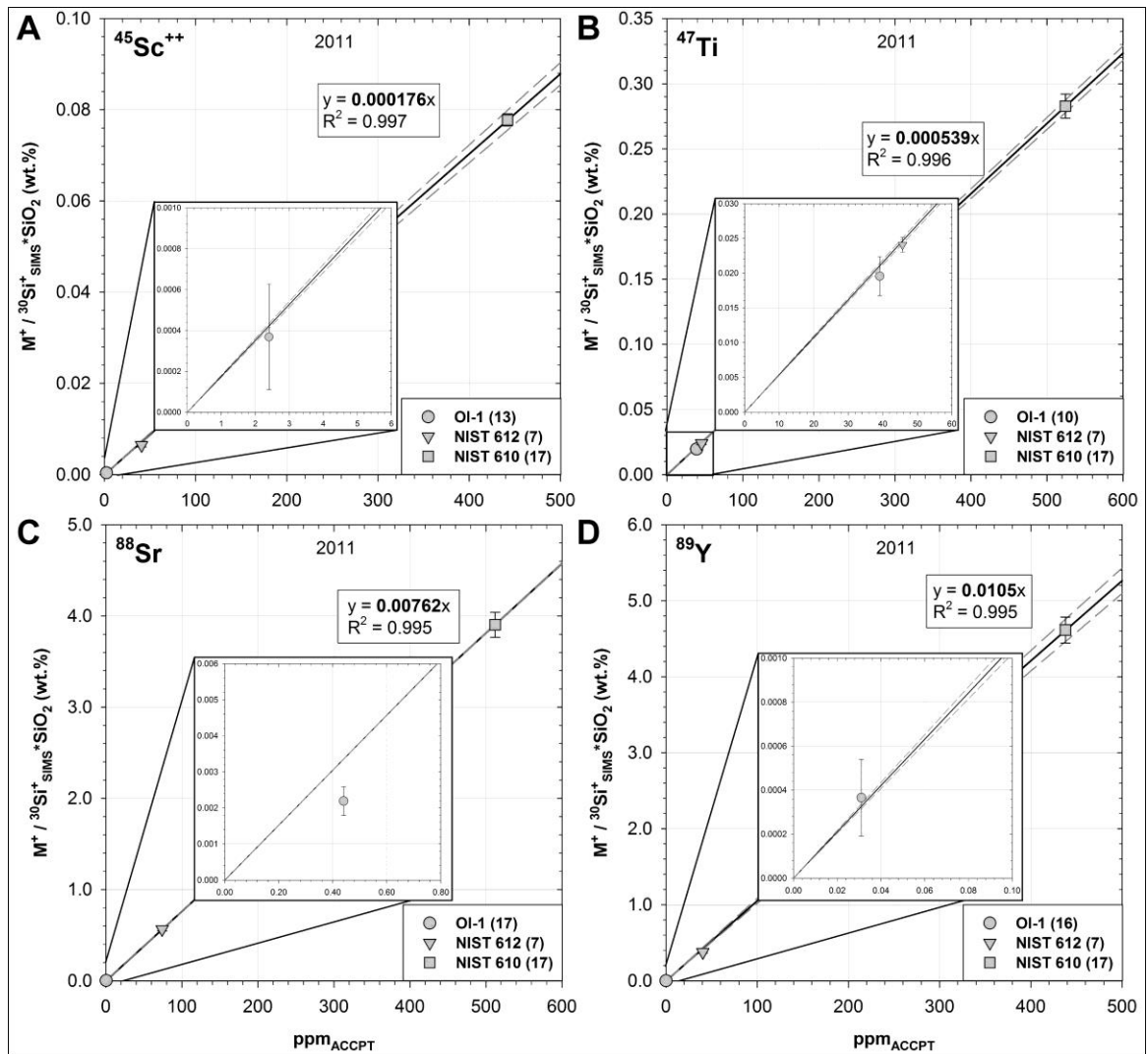
Fig. 2.7: Working lines for Group II elements ([45]Sc, [47]Ti, [88]Sr, [89]Y). All elements were quantified exclusively applying conventional working lines (e.g., Jones and Layne, 1997), utilizing one olivine RM (usually Ol-1) and the NIST glasses 612 and 610. Inset is a zoom-in of the point of origin with the position of Ol-1 relative to the regression line. The number in brackets behind sample identification refers to the sum of measured spots on each sample. The error bars are the standard deviation of the average (1σ). This Figure resembles a slightly adjusted Step 3 in our empirical approach (Appendix 6.1.). Dark grey dashed lines indicate 95% confidence interval.

2.4.3. SIMS and EPMA Inter-Technique Comparison

In order to test our SIMS analytical approach, two unknown olivine samples (WGR and ICE) were selected for comparative analyses. WGR is a garnet-peridotite from the Western Gneiss Region, Norway (e.g., Van Roermund, 2009; Brueckner et al., 2010) and ICE is from a volcanic ash deposit from the 2010 Eyjafjallajökull eruption, Iceland (e.g., Gislason et al., 2010). Multiple olivine from each sample were measured with both EPMA and SIMS for the purpose of a direct comparison of the major element (MgO, FeO, SiO_2) and minor element (Mn, Ni) concentrations determined with these different techniques.

WGR olivine are on average fairly homogeneous at Fo90 ±0.1 (1σ EPMA; ±0.6 1σ SIMS) and with average Ni and Mn concentrations of circa 3,400 ppm and 750 ppm, respectively (Fig.2.8 and Table 2.5). Both techniques yield very similar results for major and trace element contents in WGR olivine (Fig.2.8) with an excellent linear correlation (Fig.2.8A and B). Minimum and maximum values for Mn and Ni (Table 2.5) from the analyzed olivine population also correspond very well (i.e., Ni (EPMA) 2,964 ppm – 3,826 ppm versus Ni (SIMS) 3,042 ppm – 3,718 ppm). The forsterite values determined with SIMS, however, have a slightly higher uncertainty (~1.5% 2σ per spot) than analyzed with EPMA (~0.5% 2σ per spot). This results from the empirical calibration (Fo calculation; Fig.2.3A) and the intrinsically higher uncertainty of this calculation step compared to the more direct quantification with EPMA. The error of the empirical SIMS calibration is thus characterized by the standard error of the estimate at the 95% (~2σ)

confidence interval. The component of analytical uncertainty (2σ) for (SIMS) determination of R_{Fo} (WGR) is an insignificant contribution to this error (0.02%).

ICE olivine on the other hand displayed substantial variation in Fo values between grains, from 73–88 (SIMS), and 74–87 (EPMA), with an average of 80 for both techniques. Individual grains are mostly unzoned in major elements, whereas intra-grain Mn and Ni concentrations can vary considerably (up to ±800 ppm). A direct comparison between individual spots from EPMA and SIMS is difficult since the sampled olivine population was analyzed independently. However, excellent linear correlations between (average) major element and (average) Mn and Ni concentrations determined with EPMA and SIMS from the sampled olivine population exist (Fig.2.8A and B and Table 2.5) and further emphasize the general compositional diversity of the ICE olivine resolved by both techniques. Average Mn and Ni values are similar (e.g., Ni (EPMA) 1,699 ppm versus Ni (SIMS) 1,802 ppm), and minimum and maximum values correlate extremely well (e.g., Mn (EPMA) 1,163 ppm – 2,794 ppm versus Mn (SIMS) 1,158 ppm – 2,974 ppm). Data from both EPMA and SIMS demonstrate a strong negative correlation between Fo and Mn content and a strong positive correlation between the Fo and Ni concentration (Fig.2.8C and D).

In summary, the proposed SIMS analytical and empirical approach using compositionally diverse olivine as test samples yields similar results to EPMA for major elements and for the reasonably abundant minor elements detectable by EPMA in these samples (Mn, Ni). This confirms that the matrix effects and isobaric interferences that may influence SIMS analyses of more fayalitic olivine can be controlled, and that the desired performance

advantages of the SIMS (high sensitivity, high accuracy and extended suite of trace elements) can be readily utilized for these determinations, while maintaining accuracy relative to EPMA.

Table 2.5: Comparative EPMA and SIMS results for unknown olivine

Sample Code	WGR Ol*	WGR Ol	WGR Ol	WGR Ol	ICE Ol	ICE Ol	ICE Ol	ICE Ol
Method	EPMA	EPMA	SIMS	SIMS	EPMA	EPMA	SIMS	SIMS
(n=)	50[x]	1 σ[y]	24	1 σ	44	1 σ	32	1 σ
wt.%								
MgO	49.36	0.23	49.28	0.46	42.02	2.54	42.83	3.17
SiO2	39.96	0.36	40.86	0.11	38.47	0.65	39.27	0.73
CaO	0.01	0.01	0.01	0.00	0.25	0.03	0.46	0.12
Cr2O3	0.01	0.01	0.01	0.00	0.03	0.03	0.02	0.01
MnO	0.10	0.02	0.10	0.01	0.26	0.06	0.28	0.07
FeO	9.89	0.13	9.87	0.57	18.65	3.25	18.35	3.91
NiO	0.43	0.02	0.43	0.02	0.22	0.11	0.23	0.09
Total	99.76	0.78	100.55	1.16	99.89	6.68	101.43	8.10
ppm								
Mg	297686	1383	297208	2773	253450	15341	258308	19141
Si	186794	1679	190996	496	179817	3028	183540	3423
Ca	85	87	39	9	1795	214	3294	838
Cr	60	65	61	8	177	205	165	70
Mn	745	131	777	64	1980	433	2162	512
min.	467		689		1163		1158	
max.	996		871		2794		2971	
Fe	76882	978	76720	4398	144968	25297	142636	30362
Ni	3418	174	3405	166	1699	826	1802	699
min.	2964		3042		665		925	
max.	3826		3718		3587		3130	
# of ions[1]								
Mg^{2+}	1.814	0.008	1.793	0.017	1.607	0.097	1.610	0.119
Ca^{2+}					0.007	0.001	0.012	0.003
Cr^{2+}					0.001	0.001		
Mn^{2+}	0.002	0.000	0.002	0.000	0.006	0.001	0.006	0.002
Fe^{2+}	0.204	0.003	0.201	0.012	0.400	0.070	0.387	0.082
Ni^{2+}	0.009	0.000	0.008	0.000	0.005	0.003	0.005	0.002
$[Y]^6$	2.029		2.004		2.026		2.020	
Si^{4+}	0.985	0.009	0.997	0.003	0.987	0.017	0.990	0.018
Fo %	89.9	0.1	89.9	0.6	80.1	0.4	80.4	0.5
Fo #	0.899	0.001	0.899	0.006	0.801	0.037	0.804	0.045
	*: analytical data (averages)							
	[x]: no. of analyses							
	[y]: standard deviation of mean (n analyses)							
	[1]: on the basis of 4 oxygens							
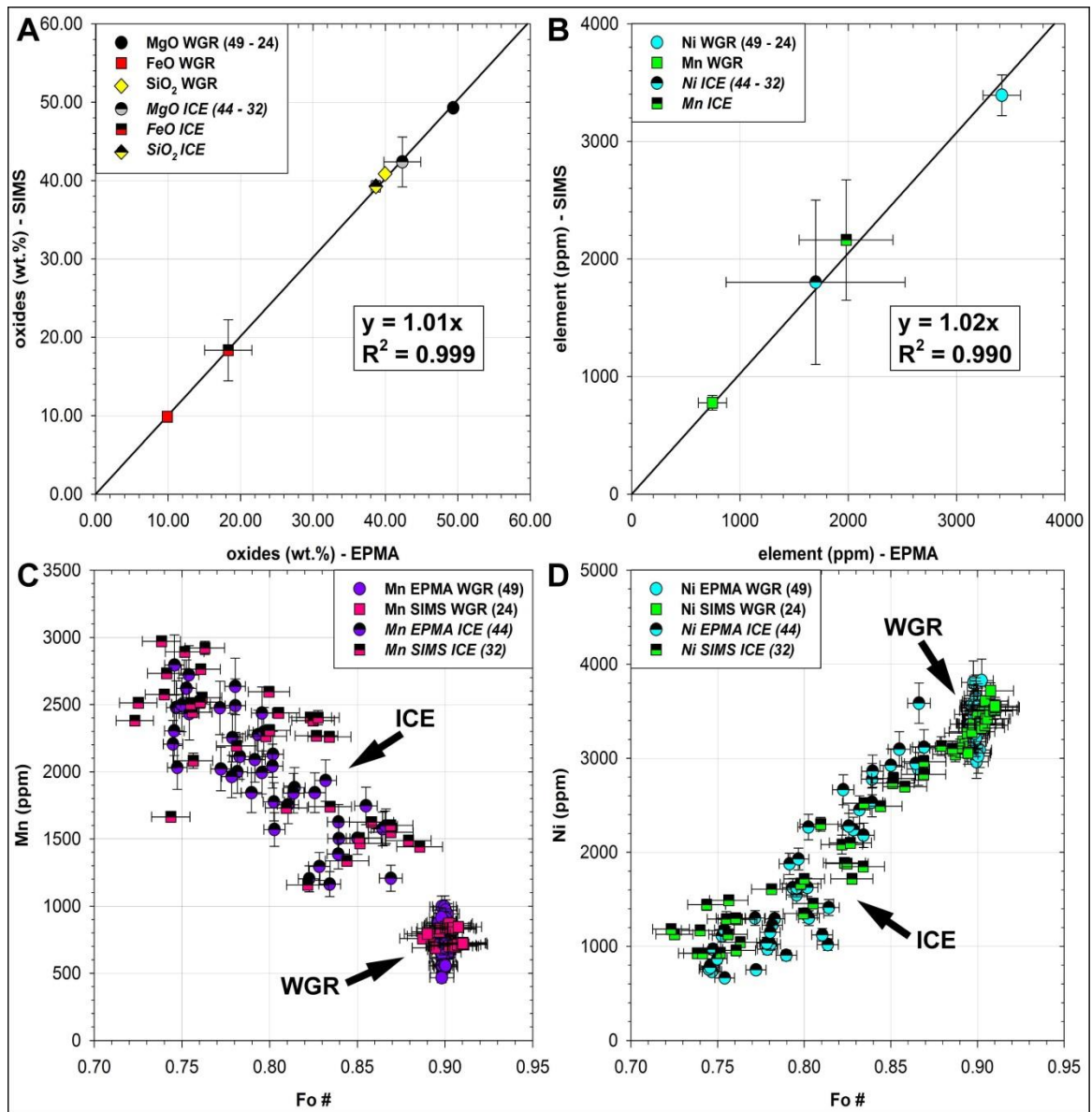
Fig. 2.8: Results of trial runs of unknown olivine samples. WGR denotes olivine from the Western Gneiss Region, Norway, whereas ICE symbolizes olivine from a volcanic ash deposit, Iceland. A direct comparison between EPMA (x-axis) and SIMS (y-axis) results for (average) major element contents (wt.% ±1σ) is depicted in A), whereas (average) minor element concentrations (ppm ±1σ; Mn and Ni) are displayed in B). The number in brackets behind sample identification reflects the sum of measured spots on each olivine population with the first value for EPMA and the second for SIMS analyses. Minor element concentrations (Mn and Ni) versus Fo content from EPMA and SIMS measurements are plotted in C) and D), with error bars denoting 2σ uncertainty.

2.5. Summary and Conclusions

1. Seven compositionally variable olivine were tested as potential SIMS RM. For the quantification of unknown olivine a subset of four RM, two primitive mantle olivine (Ol-1 and Ol-2), one intermediate olivine (Ol-5) and one fayalitic olivine (Ol-6), proved most accurate and yielded similar results for major (MgO, FeO, SiO_2) and trace element (Mn, Ni) concentrations in two unknown olivine populations to electron-probe microanalyses (EPMA).

2. Despite the documented matrix effect for Mg and Fe in olivine, it is possible to determine the forsterite content (and therefore the weight concentrations of MgO, FeO and SiO_2) of any olivine by SIMS using the above discussed empirical approach combined with an adequately diverse set of olivine RM.

3. Over the compositional range of potential RM examined in this study, Ol-5 (Fo_{52}) experienced the highest matrix effect bias. For olivine around this composition, MgO and FeO (wt.%) contents are similar in magnitude. This might lead to an amplification of the matrix effect, since an increasing Fe content is causing an enhanced emission of selected elements (Mg, Mn, Co, Ni, Zn). For quantification of major and trace elements in olivine of these intermediate compositions, matrix effects are therefore an important consideration. However, accurate quantification of the affected elements is achieved with the appropriate selection of well-characterized olivine RM, bracketing the composition of the sample olivine.

4. The impact of the matrix effect on trace element determinations varies significantly by element and seems to be highest for transition metals with geochemical similarities to Mg^{2+} and Fe^{2+} (ionic radii, valence state, site preference etc.) and concentrations over 50 ppm (Cr, Mn, Co, Ni, Cu, Zn), which mainly occupy the 6-fold coordinated lattice spaces. However, Ca, which can potentially comprise a major constituent in olivine ($CaMgSiO_4$ – Monticellite and $CaFeSiO_4$ – Kirschsteinite) seems largely unaffected by matrix effects in our study when determined using the $^{40}Ca^{++}$ analyte mass. This observation is in marked contrast to results from Ottolini et al. (2002) for olivine, Shimizu et al. (1978) for Ca-rich pyroxenes, or Lehmann (2003) for silicate glasses using the $^{40}Ca^{+}$ analyte mass.

5. The analytical and empirical calibration approach presented here further supports the effectiveness of quantitative SIMS in trace element analyses of compositionally diverse olivine and further extends its geochemical application to simultaneous Fo determination (typically ~1.5% 2σ) and high precision (typically ~5% 2σ) analyses of minor element concentrations of (Ca, V, Cr, Mn, Co, Ni, Zn). Trace elements such as (Sc, Ti, Cu, Sr, Y and Zr) may also be usefully quantified (typically 20–60% 2σ). A subset of these trace elements can be chosen based on the scientific/geochemical objective (mantle petrology or ore deposit characterization etc.) and optimally utilized, so this procedure enables the in-situ analysis of major and trace elements in olivine in a single small diameter spot.

2.6. References

Beattie, P., 1994. Systematics and energetics of trace-element partitioning between olivine and silicate melts: Implications for the nature of mineral/melt partitioning. Chemical Geology 117, 57–71.

Beattie, P., Ford, C., Russell, D., 1991. Partition coefficients for olivine-melt and orthopyroxene-melt systems. Contributions to Mineralogy and Petrology 109, 212–224.

Bédard, J.H., 2005. Partitioning coefficients between olivine and silicate melts. Lithos 83, 394–419.

Bell, D.R., Hervig, R.L., Buseck, P.R., Aulbach, S., 2009. Lithium isotope analysis of olivine by SIMS: Calibration of a matrix effect and application to magmatic phenocrysts. Chemical Geology 258, 5–16.

Bowen, N.L., Schairer, J.F., 1935. The system $MgO-FeO-SiO_2$. American Journal of Science 229, 151–217.

Brooker, R.A., James, R.H., Blundy, J.D., 2004. Trace elements and Li isotope systematics in Zabargad peridotites: Evidence of ancient subduction processes in the Red Sea mantle. Chemical Geology 212, 179–204.

Brueckner, H.K., Carswell, D.A., Griffin, W.L., Medaris Jr, L.G., Van Roermund, H.L.M., Cuthbert, S.J., 2010. The mantle and crustal evolution of two garnet peridotite suites from the Western Gneiss Region, Norwegian Caledonides: An isotopic investigation. Lithos 117, 1–19.

Colson, R.O., McKay, G.A., Taylor, L.A., 1988. Temperature and composition dependencies of trace element partitioning: Olivine/melt and low-Ca pyroxene/melt. Geochimica et Cosmochimica Acta 52, 539–553.

De Hoog, J.C.M., Gall, L., Cornell, D.H., 2010. Trace-element geochemistry of mantle olivine and application to mantle petrogenesis and geothermobarometry. Chemical Geology 270, 196–215.

Deer, W.A., Howie, R.A., Zussman, J., 1997. Rock forming minerals: Orthosilicates, 2ed. Geological Society of London. 932 pp.

Ericsson, T., Filippidis, A., 1986. Cation ordering in the limited solid solution Fe_2SiO_4-Zn_2SiO_4. American Mineralogist 71, 1502–1509.

Frey, F.A., Green, D.H., Roy, S.D., 1978. Integrated models of basalt petrogenesis: A study of quartz tholeiites to olivine melilitites from South Eastern Australia utilizing geochemical and experimental petrological data. Journal of Petrology 19, 463–513.

Gaetani, G.A., Grove, T.L., 1997. Partitioning of moderately siderophile elements among olivine, silicate melt, and sulfide melt: Constraints on core formation in the Earth and Mars. Geochimica et Cosmochimica Acta 61, 1829–1846.

Garrido, C.J., Bodinier, J.-L., Alard, O., 2000. Incompatible trace element partitioning and residence in anhydrous spinel peridotites and websterites from the Ronda orogenic peridotite. Earth and Planetary Science Letters 181, 341–358.

Gislason, S.R., Hassenkam, T., Nedel, S., Bovet, N., Eiriksdottir, E.S., Alfredsson, H.A., Hem, C.P., Balogh, Z.I., Dideriksen, K., Oskarsson, N., Sigfusson, B., Larsen, G., Stipp, S.L.S., 2010. Characterization of Eyjafjallajökull volcanic ash particles and a

protocol for rapid risk assessment. Proceedings of the National Academy of Sciences of the United States of America 108, 7307–7312.

Godon, A., Webster, J.D., Layne, G.D., Pineau, F., 2004. Secondary ion mass spectrometry for the determination of $\delta^{37}Cl$ Part II. Intercalibration of SIMS and IRMS for aluminosilicate glasses. Chemical Geology 207, 291–303.

Grant, K.J., Wood, B.J., 2010. Experimental study of incorporation of Li, Sc, Al and other trace elements into olivine. Geochimica et Cosmochimica Acta 74, 2412–2428.

Hervig, R.L., Mazdab, F.K., Williams, P., Guan, Y., Huss, G.R., Leshin, L.A., 2006. Useful ion yields for Cameca IMS 3f and 6f SIMS: Limits on quantitative analysis. Chemical Geology 227, 83–99.

Hinton, R.W., 1990. Ion microprobe trace-element analysis of silicates: Measurement of multi-element glass. Chemical Geology 83, 11–25.

Ito, M., Yurimoto, H., Morioka, M., Nagasawa, H., 1999. Co^{2+} and Ni^{2+} diffusion in olivine determined by secondary ion mass spectrometry. Physics and Chemistry of Minerals 26, 425–431.

Jenner G.A., Longerich H.P., Jackson S.E., Fryer B.J., 1990. ICP-MS – a powerful tool for high precision trace element analysis in Earth sciences: Evidence from analysis of selected U.S.G.S. reference samples. Chemical Geology 83, 133–148.

Jones, R.H., Layne, G.D., 1997. Minor and trace element partitioning between pyroxene and melt in rapidly cooled chondrules. American Mineralogist 82, 534–545.

Kurosawa, M., Yurimoto, H., Sueno, S., 1992. Quantitative analysis of H, Ca and Ni in olivine by secondary ion mass spectrometry. Annual report of the Institute of Geoscience, the University of Tsukuba 18, 83–88.

Lee, C.T.A., Harbert, A., Leeman, W.P., 2007. Extension of lattice strain theory to mineral/mineral rare-earth element partitioning: An approach for assessing disequilibrium and developing internally consistent partition coefficients between olivine, orthopyroxene, clinopyroxene and basaltic melt. Geochimica et Cosmochimica Acta 71, 481–496.

Li, C., Lightfoot, P.C., Amelin, Y., Naldrett, A.J., 2000. Contrasting petrological and geochemical relationships in the Voisey's Bay and Mushuau intrusions, Labrador, Canada: Implications for ore genesis. Economic Geology 95, 771–799.

Li, C., Naldrett, A.J., 1999. Geology and petrology of the Voisey's Bay intrusion: Reaction of olivine with sulphide and silicate liquids. Lithos 47, 1–31.

Li, C., Ripley, E.M., Naldrett, A.J., 2003. Compositional variations of olivine and sulfur isotopes in the Noril'sk and Talnakh intrusions, Siberia: Implications for ore-forming processes in dynamic magma conduits. Economic Geology 98, 69–86.

Navarro, M.S., Ulbrich, H.H.G.J., Andrade, S., Janasi, V.A., 2002. Adaptation of ICP–OES routine determination techniques for the analysis of rare earth elements by chromatographic separation in geologic materials: tests with reference materials and granitic rocks. Journal of Alloys and Compounds 344, 40–45.

Ottolini, L., 2002. Accurate SIMS analysis of Ca in olivine based on high-energy doubly charged secondary ions. Journal of Analytical and Atomic Spectrometry 17, 280–283.

Ottolini, L., Bottazzi, P., Vannucci, R., 1993. Quantification of lithium, beryllium, and boron in silicates by secondary ion mass spectrometry using conventional energy filtering. Analytical Chemistry 65, 1960–1968.

Ottolini, L., Oberti, R., 2000. Accurate quantification of H, Li, Be, B, F, Ba, REE, Y, Th, and U in complex matrixes: A combined approach based on SIMS and single-crystal structure refinement. Analytical Chemistry 72, 3731–3738.

Pearce, N.J.G., Perkins, W.T., Westgate, J.A., Gorton, M.P., Jackson, S.E., Neal, C.R., Chenery, S.P., 1997. A compilation of new and published major and trace element data for NIST SRM 610 and NIST SRM 612 glass reference materials. Geostandards Newsletter 21, 115–144.

Plümper, O., Piazolo, S., Austrheim, H., 2012. Olivine pseudomorphs after serpentinized orthopyroxene record transient oceanic lithospheric mantle dehydration (Leka Ophiolite complex, Norway). Journal of Petrology 53, 1943–1968.

Reed, S.J.B., Scott, E.R.D., Long, J.V.P., 1979. Ion microprobe analysis of olivine in pallasite meteorites for nickel. Earth and Planetary Science Letters 43, 5–12.

Roeder, P.L., Emslie, R.F., 1970. Olivine-liquid equilibrium. Contributions to Mineralogy and Petrology 29, 275–289.

Van Roermund, H., 2009. Mantle-wedge garnet peridotites from the northernmost ultra-high pressure domain of the Western Gneiss Region, SW Norway. European Journal of Mineralogy 21, 1085–1096.

Sato, H., 1977. Nickel content of basaltic magmas: identification of primary magmas and a measure of the degree of olivine fractionation. Lithos 10, 113–120.

Shimizu, N., 2000. Principles of SIMS and modern ion microprobes. In: Gill, R. (Ed.), Modern analytical geochemistry - An introduction to quantitative chemical analysis techniques for earth, environmental and material scienitists. Longman, pp. 235–242.

Shimizu, N., Hart, S.R., 1982a. Isotope fractionation in secondary ion mass spectrometry. Journal of Applied Physics 53, 1303–1311.

Shimizu, N., Hart, S.R., 1982b. Application of the ion microprobe to geochemistry and cosmochemistry. Annual Reviews of Earth and Planetary Sciences 10, 483–526.

Shimizu, N., Semet, M.P., Allègre, C.J., 1978. Geochemical applications of quantitative ion-microprobe analysis. Geochimica et Cosmochimica Acta 42, 1321–1334.

Slodzian, G., 2004. Challenges in localized high precision isotope analysis by SIMS. Applied Surface Science 231–232, 3–12.

Slodzian, G., Lorin, J., Havette, A., 1980. Isotopic effect on the ionization probabilities in secondary ion emission. Journal de Physique – Lettres 23, 555–558.

Snyder, D.A., Carmichael, S.E., 1992. Olivine-liquid equilibria and the chemical activities of FeO, NiO, Fe_2O_3, and MgO in natural basic melts. Geochimica et Cosmochimica Acta 56, 303–318.

Sobolev, A.V., Hofmann, A.W. et al., 2007. The amount of recycled crust in sources of mantle-derived melts. Science 316, 412–417.

Steele, I.M., Hervig, R.L., Hutcheon, I.D., Smith, J.V., 1981. Ion microprobe techniques and analyses of olivine and low-Ca pyroxene. American Mineralogist 66, 526–546.

Stern, R.A., 2009. An introduction to secondary ion mass spectrometry (SIMS) in geology. *In* Secondary ion mass spectrometry in the earth sciences: Gleaning the big

picture from a small spot (Fayek, M., ed.). Mineralogical Association of Canada Short Course Series 41, 1–18.

Taura, H, Yurimoto, H., Kurita, K., Sueno, S., 1998. Pressure dependence on partition coefficients for trace elements between olivine and the coexisting melts. Physics and Chemistry of Minerals 25, 469–484.

Thomson, A., Maclennan, J., 2013. The distribution of olivine compositions in Icelandic basalts and picrites. Journal of Petrology 54, 745–768.

Weinbruch, S., Specht, S., Palme, H., 1993. Determination of Fe, Mn, Ni and Sc in olivine by secondary ion mass spectrometry. European Journal of Mineralogy 5, 37–41.

Yurimoto, H., Yamashita, A., Nishida, N., Sueno, S., 1989. Quantitative SIMS analysis of GSJ rock reference samples. Geochemical Journal 23, 215–236.

Zanetti, A., Tiepolo, M., Oberti, R., Vannucci, R., 2004. Trace-element partitioning in olivine: Modeling of a complete data set from a synthetic hydrous basanite melt. Lithos 75, 39–54.

CHAPTER 3 - Trace Element Variations in Olivine from the Eastern Deeps Intrusion at Voisey's Bay, Labrador, as a Monitor of Assimilation and Sulfide Saturation Processes

Florian Bulle[1*], Graham D. Layne[1]

[1]Department of Earth Sciences, Memorial University, St. John's, Canada NL A1B 3X5

*Corresponding author. Fax +1-709 737 2589; Email: fbulle@mun.ca

Abstract

Ni-Cu-Co sulfide mineralization in the Mesoproterozoic Voisey's Bay Intrusion is spatially and genetically associated with magmatic breccia zones within an extensive dike system and, in particular, with the entry point of this system into a larger intrusion (Eastern Deeps Intrusion; EDI). The massive sulfide- and breccia-bearing inner basal margin of the EDI is enveloped by weakly mineralized variable-textured troctolite (VTT) that progressively decreases in sulfide content, contains fewer gneissic fragments and eventually grades into a largely sulfide-barren, homogeneous plagioclase and olivine (meso)cumulate, termed normal troctolite (NT), towards the top of the intrusion. Olivine from the NT, VTT, the basal breccia sequence (BBS), and the uppermost olivine gabbro (OG) lithology in the EDI, were analyzed with Secondary Ion Mass Spectrometry (SIMS). We present multi-trace element data (including V, Cr, Mn, Co, Ni, Zn, Sr, and Y) that show informative geochemical variability in olivine from the EDI. In particular, the homogeneous NT comprises some stratigraphic sections containing primitive, Ni-rich olivine (Fo79, ~2,600 ppm Ni), as well as sections containing differentiated and strongly Ni-depleted olivine (Fo66, ~78 ppm Ni). These narrow, irregular intervals in the upper part of the NT sequence are bracketed by NT horizons containing olivine of relatively uniform composition (~Fo77, ~1,600 ppm Ni). Olivine from the VTT shows a broad trend with depth; in the upper part of the VTT unit, close to the contact with the NT, olivine is relatively primitive (~Fo80, ~1,800 ppm Ni, ~3,000 ppm Mn, ~280 ppm Zn), whereas the lower, weakly mineralized and contaminated part of the unit comprises clearly more differentiated olivine (~Fo70, ~1,300 ppm Ni, ~4,100 ppm Mn, ~400 ppm

Zn). The increase in Fe-Mn-Zn with depth is continuous within the VTT and culminates in olivine from the massive sulfide-bearing BBS, which exhibits distinctively high Mn-Zn contents (e.g., mean Mn 10,150 ppm ±1,100 1σ; mean Zn 620 ppm ±41 1σ) relative to their forsterite contents (e.g., mean Fo62 ±2 1σ). BBS olivine have an average Ni concentration of ~820 ppm, but olivine grains that are enclosed by sulfide display homogeneous forsterite contents (~Fo62) with pronounced intra-grain trace element zonation (Mn>Ni>Co>Zn).

Four petrological processes important to ore formation are recorded by the compositional diversity of EDI olivine. The heterogeneous Ni-Co-Fo contents of olivine in the EDI (Co/Ni ratios in OG: 0.18–1.1; NT: 0.07–0.26; VTT: 0.11–0.29; BBS: 0.20–0.34) are due to variable modification of original compositions by reequilibration with trapped silicate and sulfide liquids. The abrupt changes of Fe and Ni contents and some trace elements (in particular Co, Sr, Y) in olivine from the barren upper NT indicate that olivine crystallized from separate pulses of magma with variable degrees of differentiation (Mg-Ni-rich versus Mg-Ni-depleted). The severe Ni depletion of one NT silicate melt batch (~10 ppm Ni vs. 290 ppm Ni for average NT magma) is likely a result of sulfide saturation and segregation, either in a deeper staging chamber, or in the conduit, prior or contemporary to olivine precipitation and emplacement. This Ni-rich sulfide fraction might be preserved as the high Ni tenor disseminated sulfides observed in the VTT. The gradational increase of Fe-Mn-Zn in olivine from the weakly mineralized and contaminated lower part of the VTT downward into the massive sulfide-bearing and strongly contaminated BBS is consistent with olivine fractionation from an increasingly country rock-contaminated,

sulfide-saturated, Fe-Mn-Zn-rich silicate magma. BBS olivine crystallized prior to or contemporaneously with the segregation of an immiscible sulfide liquid. Diffusion profiles (Mn-Ni) indicate a relatively short immersion time ($\ll$1,000 years) of BBS olivine grains in sulfide liquid, which resulted in the partial retention of Ni in the olivine. Olivine in the vicinity of massive sulfides in the EDI (VTT-BBS) have distinct trace element signatures (V-Cr-Mn-Co-Ni-Zn) compared to olivine from the barren NT and OG. A multiple regression analysis using these data yields a factor that describes the relative vertical proximity to massive sulfides in the EDI. In conjunction with the stratigraphic context of the host lithology, this information could potentially be used as a vector towards massive sulfide mineralization in the EDI and support Ni-exploration in other olivine-bearing mafic intrusions.

3.1. Introduction

Within the Ni-Cu-Co sulfide ore-bearing Voisey's Bay Intrusion (VBI) of northern Labrador, Canada, the outcropping Eastern Deeps Intrusion (EDI) contains a significant portion of the associated economic sulfide mineralization (e.g., Evans-Lamswood et al., 2000; Lightfoot et al., 2012; Fig.3.1). The EDI consists of olivine gabbro, barren and weakly disseminate sulfide mineralized troctolite, and a basal, country rock contaminated, massive sulfide-bearing breccia sequence, which forms the economic core of the deposit (e.g., Lightfoot and Naldrett, 1999). The two styles of mineralization (disseminated versus massive) have distinct differences in metal tenor (Ni-Cu); disseminated sulfides in the weakly mineralized variable-textured troctolite (VTT) have high Ni tenors ($[Ni]_{100}$=4−8%), and massive sulfides associated with the breccia sequence (BBS) at the base of the EDI have lower Ni tenors ($[Ni]_{100}$=3.5−4%) (Lightfoot et al., 2012). The disparate metal tenors are consistent with R-factor (silicate:sulfide melt ratio; Campbell and Naldrett, 1979) variations and the equilibration of sulfide with olivine-normative melts (Lightfoot et al., 2012). The distribution of Mg-Fe-Ni in olivine from EDI lithologies records important information about the magma source, fractional crystallization processes, and equilibration with trapped silicate and immiscible sulfide liquids (e.g., Li and Naldrett, 1999; Li et al., 2000, 2007; Venables, 2003).

Tracing sulfide segregation in mafic magmatic systems is the key application of olivine Mg-Fe-Ni analysis and can support Ni-exploration decisions (e.g., Fleet and McRae, 1983; Lightfoot et al., 1984; Tyson and Chang, 1984; Barnes and Naldrett, 1985; Chalokwu and Grant, 1987; Maier et al., 1998; Li et al., 2003a; Maier et al., 2010).

Previously published olivine composition data from the VBI reveal minor stratigraphic variations in Mg/Fe across the barren and mineralized EDI lithologies, whereas the Ni concentration of olivine appears mostly erratic. The decrease (up to 20 mol.%) in olivine forsterite (Fo) content with depth in the EDI is independent from olivine Ni concentrations, which also vary largely independently of Fo content, host lithology, depth, and style of associated mineralization – from ~260 ppm (olivine gabbro – OG, ~Fo73) to 2,200 ppm (barren normal troctolite – NT, ~Fo79). Li and Naldrett (1999) related the Ni diversity to interaction with segregated sulfides and reequilibration between olivine and surrounding sulfide liquid. Based on their olivine data, the authors concluded that the EDI troctolites (NT-VTT) are related through fractional crystallization and that the NT-VTT magma entrained existing sulfides and upgraded them in metal content. Venables (2003) on the other hand proposed that NT-VTT olivine were actually enriched in Ni by equilibration with a Ni-rich sulfide liquid and thus cannot be the metal source for the EDI sulfide-ore deposit. However, since EDI olivine from the barren NT, weakly mineralized VTT, and contaminated, massive sulfide-bearing BBS have overlapping Ni-Fo contents (Li and Naldrett, 1999; Li et al., 2000; Venables, 2003), the genetic relationship between NT-VTT olivine and immiscible sulfide liquid(s), and between the composition of BBS olivine and massive sulfide mineralization is uncertain.

In this study we use Secondary Ion Mass Spectrometry (SIMS) multi-trace element (Ca, Sc, Ti, V, Cr, Mn, Co, Ni, Cu, Zn, Sr, Y, and Zr) microanalysis of olivine to show that a systematic stratigraphic and genetic relationship exists between the olivine trace element composition and:

(1) The magmatic episodicity (and consequent variation in R-factor), particularly of the host troctolites (NT, VTT);

(2) The influence of country rock contamination on the origin of sulfide saturation in the mineralized VTT and BBS;

(3) The different styles of sulfide mineralization in the EDI (VTT – higher Ni tenor, disseminated, versus BBS – lower Ni tenor, massive; Li et al., 2000; Evans-Lamswood et al., 2000; Lightfoot et al., 2012).

The chemical diversity (Ni, Co, Cr, Mn, and Zn) of olivine in barren troctolite versus mineralized troctolite/basal breccia is further used to establish potentially systematic olivine trace element variations as geochemical vector towards zones with economic sulfide mineralization in the EDI.
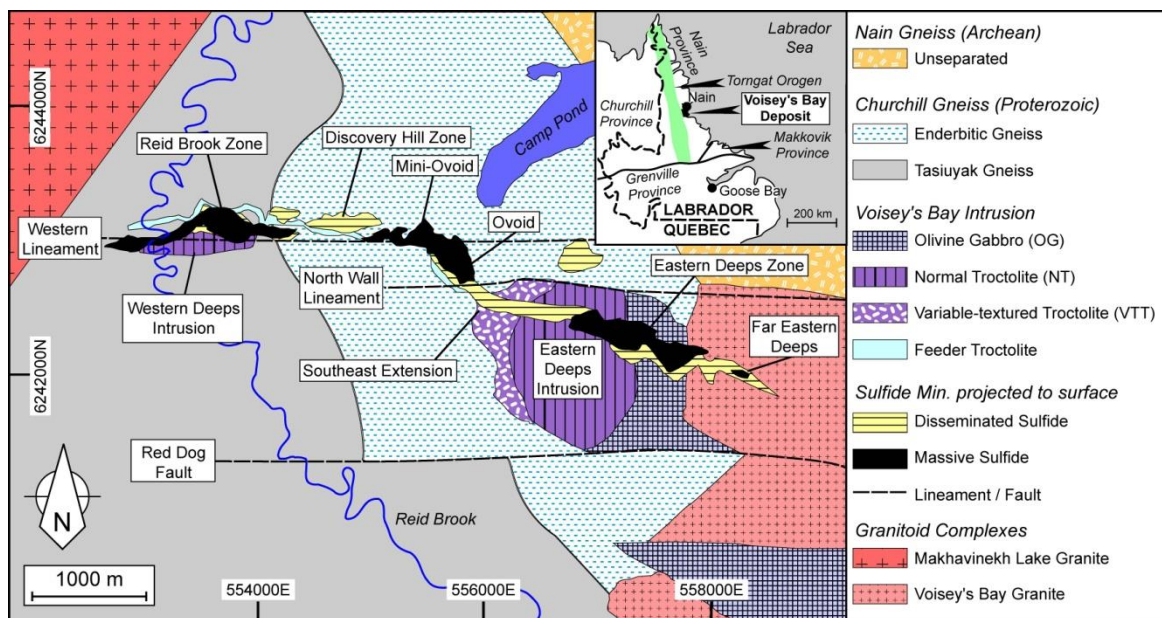
Fig. 3.1: Simplified geological map of the VBI with the olivine gabbroic to troctolitic rocks and major sulfide mineralization projected to the surface (after Evans-Lamswood et al., 2000). The inset shows the position of the VBI in the regional tectonic framework of coastal Labrador (after Li and Naldrett, 1999).

3.2. Geology and Mineralogy of the Voisey's Bay Intrusion

3.2.1. Geological Background

The olivine gabbroic to troctolitic rocks of the VBI (Fig.3.1) are part of the Nain Plutonic Suite (NPS). The NPS is a Mesoproterozoic anorthosite-mangerite-charnockite-granite (AMCG) suite, covering almost 20,000 km^2 of northern Labrador, Canada (Emslie et al., 1994; Ryan, 2000; and references therein). Numerous NPS intrusions – including anorthosite, troctolite, ferrodiorite and granitoid – punctured the Paleoproterozoic Nain-Churchill continental suture zone ("Torngat orogen") between circa 1,350 and 1,290 Ma, as a result of limited intracontinental rifting along this major terrane junction (e.g., Emslie et al., 1994; Ryan, 2000). West of this tectonic boundary, the Paleoproterozoic Torngat orogen, part of the Churchill Province, comprises interbanded garnet-sillimanite paragneisses, which are locally sulfide- and graphite-bearing and collectively known as "*Tasiuyak gneiss*", as well as minor massive to lineated enderbitic orthogneisses ("metaplutonic rocks"; Rawlings-Hinchey et al., 2003). To the east, the Archean Nain Province consists of interbanded quartzo-feldspathic and amphibolitic orthogneiss with retrogressed granulite- and amphibolite-facies mineral assemblages (e.g., Li and Naldrett, 1999; Ryan, 2000). U-Pb geochronology of baddeleyite and zircon implies an emplacement age of 1,332.7 ±1.0 Ma for most components of the VBI (Amelin et al., 1999) – making it the oldest known troctolitic member of the NPS.

The VBI comprises a group of olivine gabbroic to troctolitic chambers linked by an olivine gabbro dike (Fig.3.1); collectively these rocks host the economic Voisey's Bay

Ni-Cu-Co sulfide deposit. The VBI is subdivided into five major components (Fig.3.1), (1) a buried Lower Chamber (*Western Deeps* or *Reid Brook Intrusion*) in the west, comprising a thick sequence of plagioclase-rich troctolite (leucotroctolite – LUT) and olivine gabbro (OG), (2) a partially exposed Upper Chamber (*Eastern Deeps Intrusion* – EDI; detailed in Fig.3.2) in the east, containing a variable-textured troctolite (VTT) overlain by a homogeneous normal troctolite (NT) that is, in turn, overlain by an olivine gabbro (OG). The chambers of (1) and (2) are inferred to be connected by partially brecciated, semi-massive to massive sulfide-bearing gabbroic feeder sheet(s) of approximately 1km vertical extent, which are exposed at surface at the (3) *Discovery Hill Zone*, (4) the *Mini-Ovoid*, and (5) the *Ovoid* deposit. The Ovoid deposit is a bowl-shaped structure consisting of up to 110m of massive sulfide (currently mined in an open-pit operation) (e.g., Lightfoot and Naldrett, 1999; Li and Naldrett, 1999; Huminicki et al., 2011; Lightfoot et al., 2012).

Although the Western Deeps Intrusion (WDI) was emplaced mainly in the sulfide-bearing Tasiuyak paragneiss, the EDI primarily intruded the enderbitic orthogneiss and, to some extent, the Nain orthogneiss (e.g., Lightfoot and Naldrett, 1999). Zones of significant sulfide mineralization, with systematic variations in metal tenor (Ni-Cu), are spatially and genetically associated with magmatic breccia and country rock contaminated lithologies; specifically, the feeder breccia (FB) at the top of the Reid Brook Zone (base of the feeder dike), as well as the basal breccia sequences (BBS) which appear both in the feeder sheet (e.g., within the Ovoid deposit), and within the EDI, proximal to the entry point of the

feeder dike (e.g., Lightfoot and Naldrett, 1999; Li and Naldrett, 1999; Evans-Lamswood et al., 2000; Lightfoot et al., 2012).

3.2.2. Previous Studies

Published olivine compositional data indicates that there is a link between Fo content and stratigraphic position within the intrusion (Li and Naldrett, 1999; Li et al., 2000; Venables, 2003). The published data show a decrease in average forsterite content of olivine from NT (Fo73–77) and VTT (Fo69–75) through BBS (Fo66–72) – although a high intra-sample heterogeneity is observed in olivine from the VTT (Fo61–85) (Venables, 2003). In detail, the Ni concentrations appear decoupled from the Fo content and stratigraphic position in the EDI, and display no coherent trend within either the troctolite units or the BBS (Li and Naldrett, 1999; Li et al., 2000; Venables, 2003). One excursive horizon of Ni-rich olivine appears in the NT sequence in the EDI (VB266, ~109m, ~2,216 ppm Ni; Venables, 2003), whereas olivine with very low Ni concentrations (VB266, ~55 ppm Ni; Venables, 2003) occurs sporadically in the VTT and BBS. These very low contents are apparently outliers, since they seem to reflect individual spots on single olivine grains rather than multiple grains in a single sample (Venables, 2003). The majority of the VBI olivine grains analyzed to date by EPMA have Ni concentrations between 900 and 1,700 ppm (Li and Naldrett, 1999; Li et al., 2000; Venables, 2003). The lowest reported, analytically robust Ni contents are ~159 ppm and occur in olivine from the feeder OG unit within the conduit (as sampled by DDH VB315),

whereas the lowest values in the EDI are also found in OG (VB231; up to 262 ppm Ni) (Li and Naldrett, 1999; Li et al., 2000).

Even though the published Ni contents for VBI olivine demonstrate a strong heterogeneity, and almost no systematic relationship with the Fo content or stratigraphic position, the overall ranges in Ni concentrations presented by Li and Naldrett (1999), Li et al. (2000) and Venables (2003) overlap, except for the most extreme values from Venables (2003). These authors report somewhat different ranges in Fo content from several DDH (i.a., VB166, VB189, VB194, VB201, VB231) within the VBI. Li and Naldrett (1999) and Li et al. (2000) report the lowest average Fo values for VBI olivine (i.e., NT, Fo56–72; VTT, Fo54–72; BBS, Fo53–64) with ultramafic fragment (UMF) samples containing olivine with a maximum of Fo81 (overall range of Fo70–81). The Fo values from one DDH (VB266) in the EDI reported by Venables (2003) are on average much higher (see above). Given the compositional disparity and the limited set of elements in the published olivine data, it was not possible to correlate variations in the olivine chemistry to the different zones of sulfide mineralization (VTT and BBS) in the EDI.

3.2.3. Sampling and Analytical Methods

3.2.3.1. Sampling Approach

The stratigraphy of the EDI comprises the most complete succession of olivine gabbroic to troctolitic units in the entire VBI (Evans-Lamswood et al., 2000). The majority of our

samples were derived from diamond-drill holes (DDH) transecting the EDI (Fig.3.2). Samples were collected from 5 DDH (VB-98-451, VB-96-266, VB-00-544, VB-00-548, VB-01-552; in the following abbreviated) transecting the EDI from NW to SE roughly following the entry line of the feeder dike at the steep to sub-vertical north wall (Fig.3.2). These were supplemented by samples from VB-98-449, which sampled the top of the Reid Brook Zone (WDI). Between 4 (VB548) and 53 (VB266) representative samples of less than 0.5m long half core were acquired from top to base of each hole. All sampled DDH from EDI intersected the troctolitic units (NT and VTT) and the weakly mineralized (lower part of VTT) to heavily mineralized (BBS) basal portion of the intrusion, proximal to the entry point of the feeder dike (Fig.3.2). OG was intersected sporadically in the EDI (VB544 and VB552) and at the top of the Reid Brook Chamber (VB449). The core selected for analysis is the basis for a chemostratigraphy of the EDI directly above the economic mineralization and extends NW, approximately halfway towards the Ovoid deposit. Samples for olivine analysis were systematically chosen to cover a vertically continuous transect from the barren NT downhole to the mineralized BBS, with an average vertical resolution of one sample per 25m (VB266). This strategy was designed to allow a comparison between olivine from barren troctolite (NT), zones with high tenor disseminated sulfide (VTT) and zones with low tenor massive sulfide (BBS) − with the potential to reveal compositional trends associated with the timing and location of sulfide saturation and segregation. Further, VB266 has been intensively studied previously (Li and Naldrett, 1999; Li et al., 2000; Venables, 2003; Lightfoot et al., 2012; see above) and whole-rock geochemical characterization and EPMA olivine data were thus readily

available for comparison. Consequently, VB266 had the highest sample density in our study and provides an anchor point in the approximate center of the EDI.
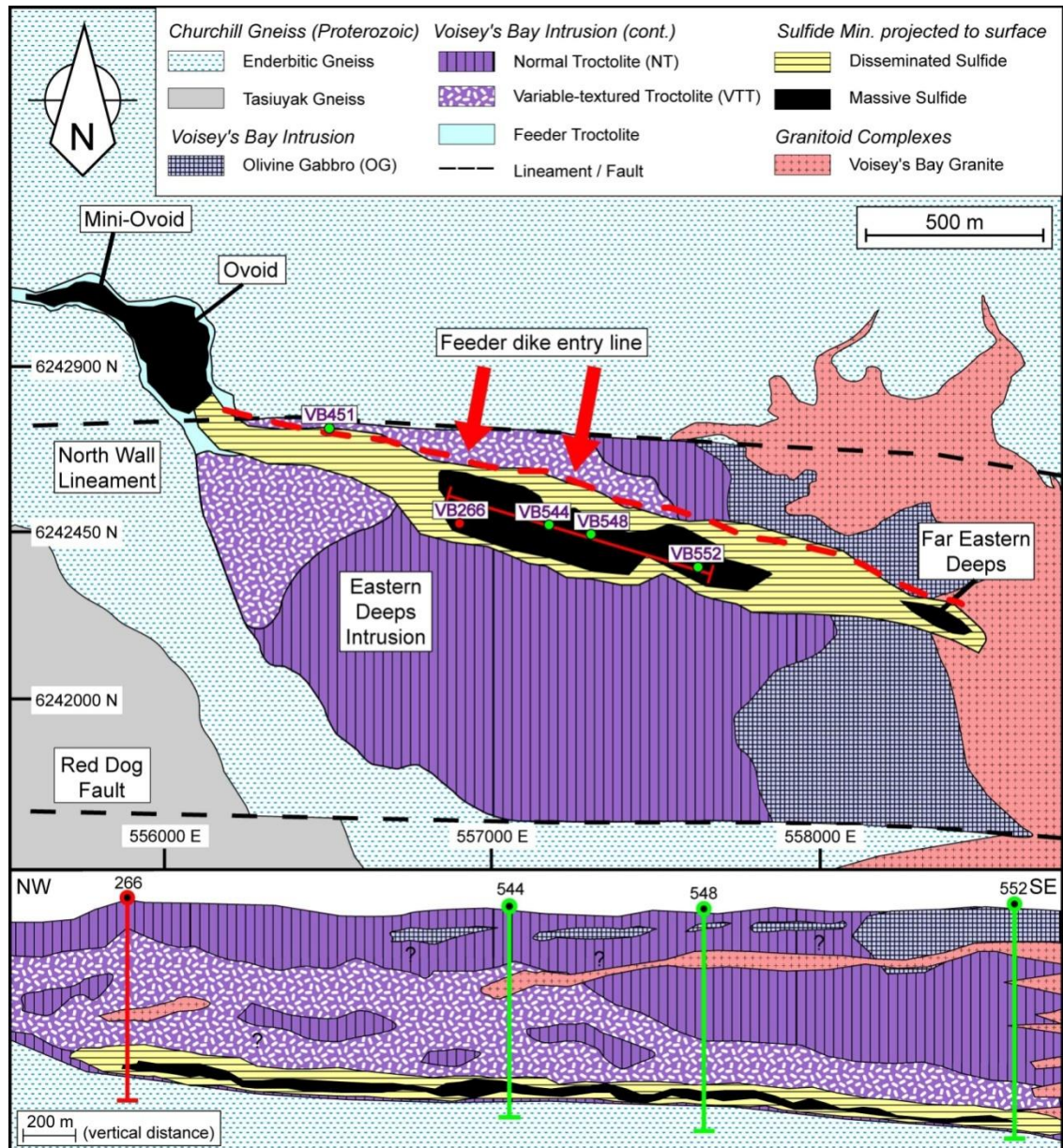
Fig. 3.2: Detailed geological map of the EDI in the eastern part of the VBI with sulfide mineralization projected to the surface (after Lightfoot et al., 2012). The positions of sampled DDH are marked with circles and their specific identification number. The cross-section (vertical exaggeration) shown is inferred based on the individual DDH log files (Vale, unpublished data) and assumes a contiguous longitudinal section through DDH VB266, VB544, VB548, and VB552.

3.2.3.2. Secondary Ion Mass Spectrometry (SIMS)

Major and trace element analyses were performed with a Cameca IMS 4f instrument at the Memorial University MAF-IIC microanalysis facility. Target areas from rectangular polished thin-sections were cut into 1" discs, then cleaned and coated with a $\leq 0.05 \mu m$ thick layer of gold to minimize charge build-up on the sample surface during analysis. A primary beam of O^- ions, accelerated through a nominal potential of 4.5 kV with a beam current of circa 20 nA, was focused to a 25 to $40 \mu m$ spot on the sample. Between 5 and 25 spot analyses were made in each sample, involving several discrete olivine grains. Each analysis comprised 10 cycles of peak counting on $^{40}Ca^{++}$, $^{45}Sc^{++}$, $^{25}Mg^+$, $^{30}Si^+$, $^{47}Ti^+$, $^{51}V^+$, $^{52}Cr^+$, $^{55}Mn^+$, $^{57}Fe^+$, $^{59}Co^+$, $^{60}Ni^+$, $^{63}Cu^+$, $^{66}Zn^+$, $^{88}Sr^+$, $^{89}Y^+$, $^{90}Zr^+$ plus counting on a background position to monitor detection noise. The measured count rates were normalized to the count rate of $^{30}Si^+$. Secondary ions were energy filtered (*cf.* Shimizu et al., 1978; Ottolini et al., 1993; Hervig et al., 2006) to effectively eliminate isobaric interferences (and reduce matrix effects) by preferentially selecting high-energy ions. Detection limits were estimated following the procedure of Jones and Layne (1997). Typical detection limits for an interference-free measurement, calculated based on the results for San Carlos olivine reference material, were; less than 5 ppb for V, Cr, Mn, Cu, Sr, Y, Zr; 10–40 ppb for Ca, Ti, Co, and Ni; ~90 ppb for Sc and Zn.

The relative analytical error (2σ) was estimated for each analytical spot using the internal precision (standard deviation of the mean) of each 10-cycle analysis. Typical precisions were ~3% for Mg, Mn and Fe; ~7.5% for Cr, Co, Ni, and Zn; ~30% for Ca, Ti and V; and ~45% for Sc, Cu, Sr, Y and Zr. The analysis of Sc, Cu, Sr, Y and Zr was partly hampered

by relatively high analytical errors due to very low (near detection limit) concentrations in the samples measured, and results for these elements were thus treated as semi-quantitative. The complete analytical approach, and the reference materials used, is described in detail in Chapter 2.

3.2.4. Petrography of the Eastern Deeps Intrusion

Detailed geological and mineralogical descriptions of the VBI host rocks, and their structural context, are presented by Lightfoot and Naldrett (1999), Li and Naldrett (1999), Evans-Lamswood et al. (2000), Lightfoot et al. (2012) and references therein. Consequently, we concentrate here on describing olivine from the four major lithologies of the EDI (from base to top: BBS, VTT, NT, OG), and review below their key petrographic characteristics and mineralogical associations in the context of each host lithology (photomicrographs of all measured samples are also in Appendix 6.6.).

3.2.4.1. Basal Breccia Sequence (BBS)

The BBS (in VB451, VB266, VB552) is a discontinuous basal sequence in the EDI, from 1m to 5m thick, that is associated with intervals of economic massive sulfide mineralization (Fig.3.1 and 3.2). The unit is highly contaminated – with up to 25 vol.% of cm-sized paragneiss fragments that commonly show syn-magmatic flattening, partial digestion and re-crystallization (see Lightfoot and Naldrett, 1999; Li and Naldrett, 1999; Li et al., 2000; Lightfoot et al., 2012). The sulfide content can be as high as 45 vol.%, and

it occurs either in massive stringers or occasionally as leopard-textured troctolite (LTT). Troctolitic and ultramafic inclusions (or ultramafic fragments – UMF) essentially strongly serpentinized melatroctolite and wehrlite fragments are also incorporated. The BBS comprises approximately 30–45 vol.% plagioclase, 5–15 vol.% orthopyroxene (±augite), 5–10 vol.% olivine. Biotite, greenish-brown hornblende and sulfides occur as interstitial phases (10–50 vol.%). Olivine is mostly fine- to medium-grained, irregular poikilitic or sub- to euhedral, and mildly to moderately altered (Fig.3.3F–H). Locally, plagioclase chadacrysts (less than 0.3mm; Fig.3.3F) are included in olivine. Individual olivine grains are commonly embayed, with signs of corrosion and resorption (Fig.3.3G), or completely included in sulfides and thus preserve a euhedral shape (Fig.3.3H). These latter olivine grains have a pronounced chemical zonation (Fig.3.4), which is not detectable with the petrographic microscope. Also, the euhedral olivine grains are usually separated from the surrounding sulfides by a thin selvage of biotite, ±greenish-brown hornblende (and, rarely, augite ±orthopyroxene), or a combination of all three of these silicate phases – a consistent textural feature that was observed in every major unit in the EDI. Locally, olivine grains are entirely serpentinized with rims of biotite, ±greenish-brown hornblende, ±Fe-Ti oxides.

3.2.4.2. Variable-textured Troctolite (VTT)

The VTT (in VB451, VB266, VB544, VB552) is a country rock-contaminated meso- to orthocumulate that can contain appreciable amounts of interstitial sulfides (up to 15 vol.%), and up to 15 vol.% partially digested and re-crystallized paragneiss inclusions

close to the footwall contact with the BBS. The cumulus phases are plagioclase (50–55 vol.%) and olivine (25–30 vol.%), with augite (±orthopyroxene), biotite and greenish-brown hornblende as major interstitial phases (10–20 vol.%). Grain sizes range from fine- to coarse-grained with local pegmatitic intervals. The degree of alteration is moderate to high, and includes sericitization of plagioclase, serpentinization of olivine and uralitization of augite (±orthopyroxene). Olivine and pyroxene grains are commonly completely replaced by mixtures of serpentine-group minerals, biotite, greenish-brown hornblende and Fe-Ti oxides. In general, olivine is fine- to medium-grained, equant to round where enclosed by plagioclase oikocrysts, and elsewhere subhedral to partially irregular poikilitic, locally enclosing small plagioclase laths (Fig.3.3D–E). Rare olivine grains have epitactic overgrowths of augite (±orthopyroxene) and exhibit signs of resorption and re-crystallization (Fig.3.3E). The VTT displays the widest range of olivine textures of all studied units in the EDI.

3.2.4.3. Normal Troctolite (NT)

This unit forms the upper troctolite in DDH (VB266, VB544, VB548, VB552), and crops out along the central part of the exposed EDI (Fig.3.2). It is essentially a homogeneous, weakly layered, dark-grey, medium-grained troctolite that is, based on the modal percentage of cumulus plagioclase (55–65 vol.%) and cumulus olivine (25–35 vol.%), the most primitive laterally and vertically correlatable unit in the intrusion. Olivine is typically medium-grained, with a range of crystal habits from equant and prismatic (sub- to euhedral) to partially poikilitic, enclosing plagioclase chadacrysts (Fig.3.3A–B). In

general, grains are fresh to moderately serpentinized, display kelyphitic-zones (Fig.3.3A; an intergrowth of brown hornblende and pyroxene lying between olivine and anorthite), or epitactic overgrowths of orthopyroxene (or augite), brown hornblende and biotite. The latter occur dominantly as selvages on olivine grains that are in contact with Fe-Ti oxides or sulfides (Fig.3.3B). These textures indicate that olivine formed prior to or at the same time as plagioclase, but always earlier than the other mineral phases.

3.2.4.4. Olivine Gabbro (OG)

The OG is the uppermost unit of the EDI and is exposed on surface at the eastern margin of the intrusion, and was intersected by VB544 and VB552 (Fig.3.2). This coarse to pegmatitic olivine-plagioclase cumulate has 60–70 vol.% plagioclase and 10–25 vol.% olivine. Interstitial augite (up to 15 vol.%) is present as coarse-grained oikocrysts enclosing olivine and plagioclase grains. Ilmenite (±titanomagnetite) occurs interstitially as cm-sized laths and elongate crystals in higher abundance than in other units (less than 8 vol.%). Olivine occurs as fine- to coarse-grained, equant, rarely irregular, but mostly prismatic (subhedral) crystals that are moderately to strongly serpentinized, and locally completely replaced by mixtures of serpentine-group minerals, ±biotite, ±brown-green hornblende, ±Fe-Ti oxides. Although some grains display minor epitactic overgrowths of orthopyroxene or augite (Fig.3.3C), this feature is less common in the OG than in the VTT and NT.
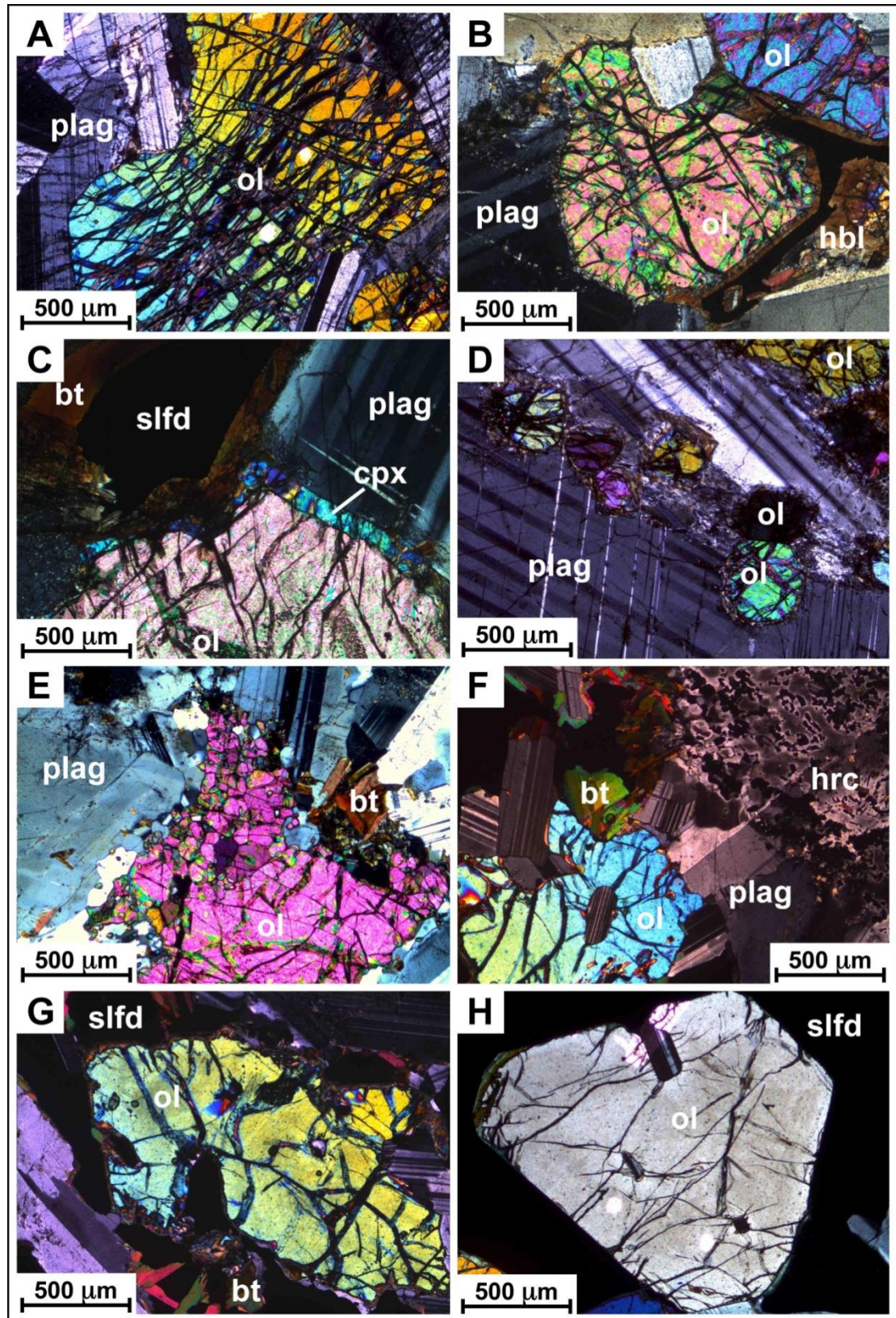
Fig. 3.3 (previous page): Photomicrographs of olivine grains that are texturally characteristic of the individual lithologies in the EDI. Cross-polarized light. A)–B) olivine in NT, C) in OG, D)–E) in VTT, F)–G) in BBS. Key for minerals: ol = olivine, plag = plagioclase, bt = biotite, hbl = hornblende, cxp = clinopyroxene, slfd = sulfide, hrc = hercynite.
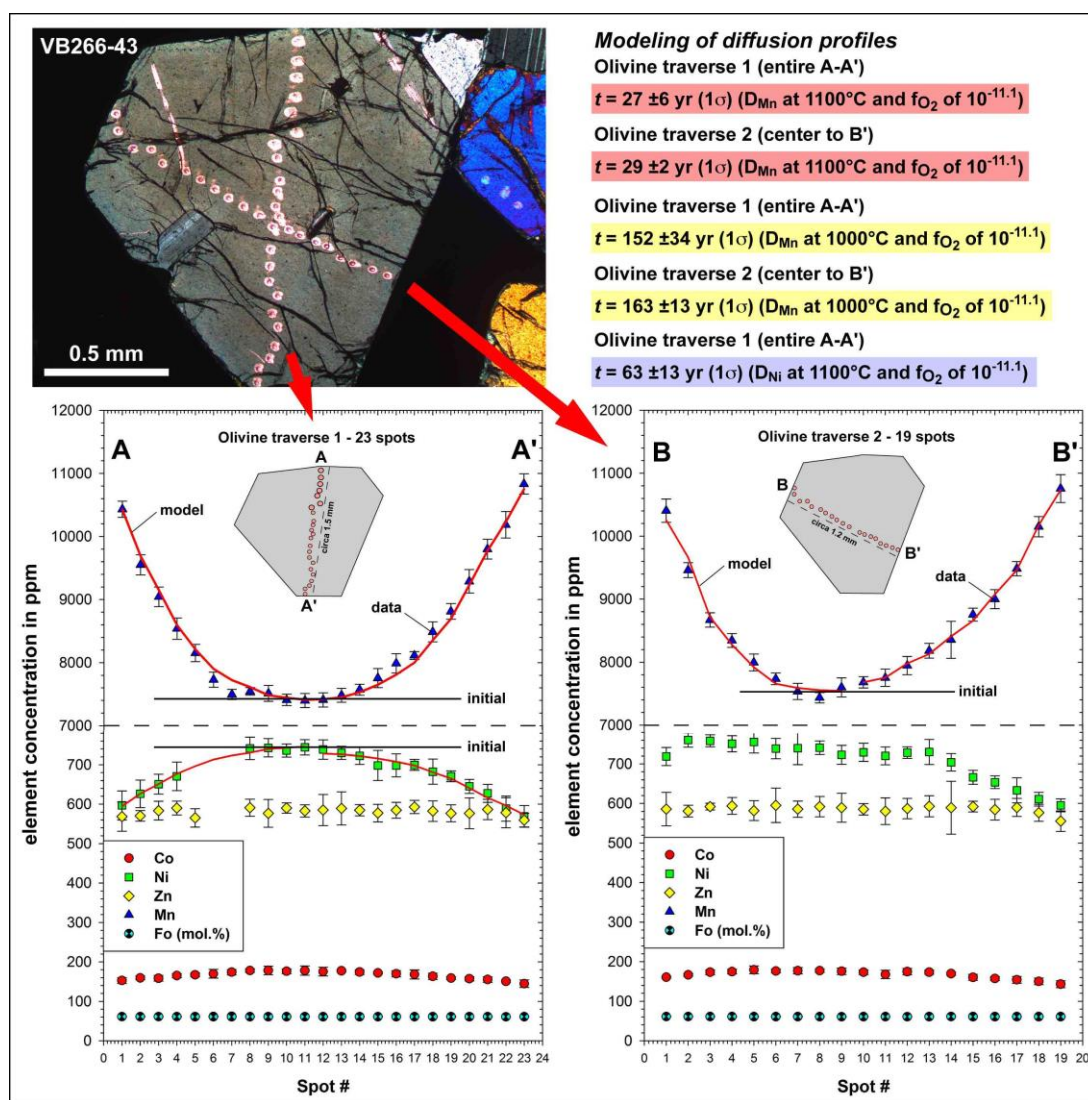
Fig. 3.4: Zonation in an olivine grain enclosed by sulfide minerals (VB266-43, BBS). Vertical profile (consisting of 23 analyses) is shown in A), and the horizontal profile (consisting of 19 analyses) in B) for the element concentrations of Ni, Co, Mn, Zn, and the Fo content. Results for the diffusion profile modeling are calculated with diffusion coefficients (D_{Ni} and D_{Mn}) for 1,100°C and 1,000°C from Petry et al. (2004). The calculation is presented and discussed in detail in Appendix 6.3.

Table 3.1: SIMS analytical data for olivine (averages) from the VBI

Sample	Rock type	depth	RVP[a]	RVP calc[b]	n	forsterite	1σ[3]	MgO	FeO	Ca	1σ	Sc	1σ	Ti	1σ	V	1σ	Cr	1σ	Mn	1σ	Co	1σ	Ni	1σ	Cu	1σ	Zn	1σ	Sr	1σ	Y	1σ	Zr	1σ
VB552-1	OG	4	0.00	0.31	7	72.8	0.6	37.04	24.15	677	108	6.84	1.23	75.1	5.2	3.70	0.38	67.9	2.7	4047	33	275	7	375	10	9.9	7.8	352	7.9	0.154	0.021	0.231	0.070	0.270	0.152
VB552-3	OG	77	0.08	0.43	14	72.7	1.3	36.98	24.29	558	112	6.09	1.69	42.3	19.3	1.58	0.29	53.7	2.7	3800	71	215	5	441	15	6.4	2.3	332	7.0	0.290	0.126	0.087	0.016	0.509	0.172
VB449-3	OG	474	N.M.	N.M.	6	67.0	1.1	33.37	28.80	492	85	8.98	1.69	34.4	4.4	2.47	0.05	77.8	6.4	3741	64	193	33	178	26	30.9	12.3	362	10.5	0.313	0.098	0.663	0.357	0.166	0.008
VB449-4.1	OG	513	N.M.	N.M.	9	69.1	0.7	34.71	27.14	496	116	7.11	0.72	40.9	11.1	1.93	0.55	52.3	2.0	4213	40	188	5	337	15	67.0	11.7	472	9.1	0.329	0.118	0.133	0.020	0.299	0.084
VB449-4.2	OG	513	N.M.	N.M.	6	71.8	1.0	36.41	25.00	370	42	N.M.	N.M.	23.4	11.5	1.15	0.22	56.2	3.8	3764	45	212	10	479	11	N.M.	N.M.	N.M.	N.M.	N.M.	N.M.	N.M.	N.M.	N.M.	N.M.
VB449-5	OG	611	N.M.	N.M.	12	64.9	1.2	32.07	30.41	500	79	7.91	2.82	27.1	9.9	1.76	0.27	61.0	3.5	4229	112	217	9	278	11	61.9	20.7	365	7.8	0.203	0.067	0.610	0.157	0.666	0.032
VB544-11.2	OG	375	0.54	0.46	10	69.4	1.4	34.83	26.96	264	110	2.04	0.70	46.2	17.7	2.52	0.15	78.7	4.2	2836	103	257	21	1252	91	N.M.	N.M.	225	16.5	1.169	1.650	0.085	0.056	0.999	0.947
VB544-12.1	OG	389	0.56	0.68	12	59.3	1.1	28.57	34.71	565	103	6.04	1.33	32.4	7.5	2.18	0.16	57.7	3.2	3994	37	189	5	1028	37	3.7	1.6	371	7.4	0.625	0.131	0.319	0.126	0.370	0.053
VB544-12.2	OG	390	0.56	0.66	18	59.9	0.7	28.90	34.30	708	89	3.66	0.88	41.0	6.7	1.95	0.21	62.3	3.4	4008	37	190	3	985	41	4.9	0.6	383	3.5	0.863	0.176	0.230	0.110	0.379	0.067
VB544-13.1	OG	404	0.58	0.59	9	61.5	1.1	29.87	33.09	442	84	2.37	0.49	21.5	4.7	1.87	0.15	66.9	1.2	3826	35	190	4	529	7	N.M.	N.M.	329	5.3	0.446	0.064	0.088	0.025	0.352	0.048
ED-NT	NT	0	0.00	0.19	28	77.9	1.2	40.69	19.77	449	103	4.05	1.24	304	122	6.07	1.32	85.1	7.9	2545	90	246	16	1247	54	43.6	25.6	236	14.0	1.009	0.541	0.140	0.070	1.133	0.656
VB266-1	NT	38	0.06	0.26	15	79.9	0.4	42.17	18.02	106	28	N.M.	N.M.	53.5	31.5	3.88	1.22	81.0	4.1	2599	53	305	8	1618	52	5.5	1.5	247	14.5	0.152	0.045	0.033	0.013	N.M.	N.M.
VB266-21	NT	47	0.07	0.27	15	79.2	0.7	41.70	18.59	159	15	N.M.	N.M.	46.5	30.6	3.50	0.38	79.6	3.0	2793	31	287	7	1428	31	5.3	1.6	264	12.4	0.375	0.048	0.047	0.018	0.332	0.173
VB266-23	NT	78	0.11	0.23	15	77.1	1.4	40.31	20.29	390	108	N.M.	N.M.	N.M.	N.M.	5.15	0.75	89.2	3.7	2624	83	263	13	1382	71	55.6	15.6	251	8.2	0.782	0.145	0.085	0.017	0.599	0.542
VB266-24.2	NT	101	0.15	0.30	4	80.0	0.3	42.00	18.19	327	33	2.09	1.40	43.7	8.3	3.62	0.30	82.0	5.0	2864	28	239	4	1525	17	10.5	3.2	292	1.2	0.333	0.041	0.047	0.015	0.175	0.035
VB266-24.1	NT	101	0.15	0.25	11	81.8	0.2	43.08	16.74	307	58	2.60	1.01	42.4	23.7	4.21	0.35	90.6	1.3	2562	27	240	4	1620	27	4.7	1.6	246	6.0	0.338	0.030	0.042	0.010	0.377	0.431
VB266-26	NT	106	0.15	0.29	39	79.5	0.9	41.67	18.53	406	135	2.79	0.95	76.2	60.5	3.75	0.68	86.9	11.1	2596	120	249	27	1541	74	25.6	26.7	241	22.3	0.672	0.298	0.070	0.069	0.398	0.334
VB266-27A	NT	108	0.16	0.45	31	76.8	0.9	39.33	21.44	348	56	4.29	1.05	224	170	4.68	1.13	87.5	7.8	2796	88	204	18	2451	117	22.5	14.0	284	31.0	0.506	0.283	0.131	0.063	0.442	0.282
VB266-27B	NT	108	0.16	0.31	12	79.0	0.6	41.21	19.06	391	44	4.61	1.77	130	100	4.86	0.56	83.4	2.3	2772	88	242	5	1884	34	3.8	1.0	271	7.0	0.414	0.028	0.151	0.054	0.821	0.664
VB266-3.1	NT	108	0.16	0.46	8	78.8	0.3	41.12	19.27	413	52	3.53	0.71	91.8	31.1	4.08	0.36	79.8	3.3	3011	27	193	15	2489	142	25.5	3.4	311	24.2	0.520	0.032	0.093	0.020	0.439	0.373
VB266-3.2	NT	108	0.16	0.41	6	79.4	0.4	41.69	18.57	392	55	3.04	0.95	69.3	13.5	3.94	0.52	79.6	3.2	2972	32	202	7	2200	138	30.3	9.3	309	9.3	0.471	0.083	0.089	0.024	0.340	0.202
VB552-5	NT	225	0.23	0.26	10	79.4	0.6	41.60	18.69	420	81	N.M.	N.M.	37.0	10.5	3.78	0.37	79.8	3.3	2994	32	236	4	1000	19	19.6	6.4	236	8.2	0.236	0.050	0.070	0.016	0.266	0.154
VB544-1	NT	11	0.02	0.42	11	79.8	0.7	41.79	18.35	136	37	1.01	1.00	13.0	3.4	2.74	0.74	74.3	19.3	2183	105	231	7	1976	42	4.7	2.5	97	15.3	0.581	0.234	0.029	0.020	0.159	0.099
VB544-2	NT	18	0.03	0.43	8	71.8	0.7	36.37	24.98	314	58	2.52	1.12	41.3	7.6	2.22	0.28	61.0	6.7	3090	47	275	4	1214	27	36.3	13.3	323	10.2	0.463	0.306	0.077	0.013	0.283	0.142
VB544-4.2	NT	36	0.05	0.42	12	73.1	1.1	37.20	23.95	274	67	2.50	1.13	31.7	1.8	2.36	0.31	59.9	1.9	3023	98	282	34	1355	85	8.7	1.2	321	11.3	0.320	0.053	0.056	0.014	0.216	0.070
VB544-5A	NT	67	0.10	0.38	11	65.6	1.6	32.43	29.93	447	50	2.78	0.51	57.1	15.5	2.82	0.44	71.6	5.4	2739	80	173	9	77.6	2	5.4	2.0	262	27.5	0.760	0.249	0.194	0.037	0.492	0.190
VB544-8.2	NT	247	0.35	0.35	10	75.1	0.8	38.54	22.28	189	39	1.62	0.60	32.7	6.7	2.40	0.18	63.3	5.1	2827	36	329	19	1299	56	28.9	8.4	290	7.1	0.316	0.073	0.034	0.011	0.242	0.049
VB544-9	NT	349	0.50	0.34	5	75.1	0.3	38.56	22.34	322	41	1.55	0.60	66.6	33.6	3.03	0.28	84.6	1.5	2710	36	243	2	1253	33	3.9	1.2	265	15.1	0.993	0.149	0.058	0.012	0.405	0.094
VB548-1	NT	27	0.03	0.45	10	72.4	0.9	36.74	24.52	606	109	6.86	1.52	26.2	9.8	2.51	0.18	100	1.7	4028	38	295	7	1344	21	48.2	13.8	429	9.5	0.330	0.053	0.364	0.128	0.264	0.049
VB548-2	NT	33	0.04	0.43	10	71.2	1.1	36.08	25.48	622	61	5.84	1.03	84.2	41.7	3.01	0.41	67.6	3.8	3250	57	238	6	1301	39	85.5	12.6	366	13.1	0.410	0.144	0.423	0.198	0.388	0.465
VB548-9.1	NT	567	0.73	0.48	6	70.5	0.4	35.65	26.01	170	41	3.43	0.51	113	16.4	3.05	0.13	70.0	3.6	2686	28	296	3	2113	23	30.8	4.6	328	3.9	0.625	0.230	0.060	0.025	0.310	0.070
VB548-10	NT	568	0.73	0.44	12	73.5	0.8	37.49	23.59	212	55	3.57	0.66	42.4	6.7	2.26	0.21	65.1	3.5	3265	58	366	34	1834	66	6.7	1.5	336	14.0	0.396	0.064	0.144	0.087	0.214	0.046
VB266-29	VTT	146	0.21	0.20	13	80.0	0.7	42.00	18.19	313	65	2.83	0.89	47.6	16.5	3.85	0.42	87.3	10.6	2910	54	253	9	926	35	11.0	4.6	282	35.5	0.279	0.081	0.083	0.050	0.205	0.047
VB266-31.1	VTT	217	0.32	0.20	6	80.4	0.2	42.26	17.88	360	57	N.M.	N.M.	77.4	66.8	4.62	0.42	102	4.3	3059	22	270	24	1135	22	3.8	1.2	240	6.6	0.201	0.020	0.059	0.015	0.311	0.230
VB266-33	VTT	262	0.38	0.30	6	80.6	0.2	42.39	17.72	386	66	N.M.	N.M.	62.2	43.0	4.23	0.33	93.0	6.1	3071	30	246	26	1619	127	3.8	1.1	250	27.4	0.308	0.036	0.113	0.105	0.394	0.183
VB266-34A	VTT	274	0.40	0.27	20	76.2	0.9	39.68	21.06	275	42	N.M.	N.M.	N.M.	N.M.	3.68	1.12	82.3	6.6	3035	66	281	6	990	28	47.7	12.6	267	9.0	1.083	0.264	0.184	0.071	0.791	0.464
VB266-6.2	VTT	290	0.42	0.30	4	80.3	0.3	42.24	17.91	314	34	N.M.	N.M.	16.5	2.0	3.97	0.38	100	1.7	2865	55	274	9	1799	58	3.7	0.6	226	16.1	0.270	0.028	N.M.	N.M.	0.131	0.011
VB266-7	VTT	357	0.52	0.32	11	77.5	1.8	40.57	19.96	196	27	N.M.	N.M.	N.M.	N.M.	4.51	0.86	91.4	5.1	2660	124	239	23	1708	169	99.5	17.1	227	13.9	0.702	0.151	0.113	0.025	1.918	0.868
VB266-8	VTT	385	0.56	0.38	14	75.2	0.9	39.02	21.88	259	36	N.M.	N.M.	N.M.	N.M.	5.01	1.14	83.8	2.2	2987	79	206	15	1813	151	43.4	12.2	267	34.8	1.220	0.379	0.173	0.055	0.906	0.573
VB266-37	VTT	402	0.59	0.27	6	80.9	0.5	42.63	17.44	242	60	N.M.	N.M.	76.0	57.1	4.62	0.35	101	4.8	2878	49	281	13	1853	59	3.9	2.6	250	22.9	0.323	0.080	N.M.	N.M.	0.270	0.130
VB266-39	VTT	453	0.66	0.39	14	74.3	0.7	38.42	22.61	196	30	N.M.	N.M.	N.M.	N.M.	3.57	0.55	79.0	2.9	3043	55	273	10	1654	63	111.8	28.0	280	5.5	1.238	0.215	0.075	0.023	1.443	0.663
VB266-10.3	VTT	501	0.73	0.30	6	77.6	0.5	40.39	20.18	529	80	N.M.	N.M.	44.4	24.0	4.22	0.50	93.0	6.5	3333	29	265	3	1344	11	31.5	6.0	287	14.2	0.302	0.029	0.271	0.113	0.216	0.063
VB552-6.2	VTT	587	0.61	N.M.	11	77.9	0.6	40.47	20.00	448	127	N.M.	N.M.	58.7	51.2	5.26	2.25	101	12.9	2947	90	240	12	1279	44	N.M.	N.M.	N.M.	N.M.	N.M.	N.M.	N.M.	N.M.	N.M.	N.M.
VB552-11.1	VTT	763	0.80	0.50	19	69.8	0.7	35.14	26.59	432	90	4.03	0.93	44.1	6.3	3.03	0.23	70.0	2.7	3558	65	203	18	1436	80	5.4	0.7	390	26.6	0.550	0.122	0.186	0.083	0.238	0.032
VB552-11.2	VTT	763	0.80	0.49	15	70.0	0.8	35.50	26.11	482	123	4.65	0.97	38.2	4.7	2.81	0.19	70.2	3.2	3449	31	248	7	1562	36	8.3	1.4	382	6.1	0.500	0.083	0.316	0.157	0.255	0.023
VB552-13.1	VTT	792	0.83	0.59	22	67.3	1.9	33.50	28.60	417	136	5.30	1.33	49.9	10.1	2.66	0.58	62.1	3.3	3924	83	223	30	1582	205	11.0	9.1	398	28.5	0.536	0.255	0.141	0.108	0.261	0.083

[a]: relative vertical proximity factor = sample depth / (depth of first massive sulfide occurence x relative sulfide content; e.g., RVP VB266-43 = 651 / (652.3 x 0.95)

[b]: relative vertical proximity factor calculated based on results from multiple regression of V-Cr-Mn-Fe-Co-Ni-Zn and RVP with olivine data from VB266, VB544, and VB552 (see Appendix 6.4.)

[3]: reported 1σ error is standard deviation of *n* analyses on individual sample ("inter-sample variability") - for average analytical error see Analytical Method section; (*N.M.*) - not measured

Table 3.1 (cont): SIMS analytical data for olivine (averages) from the VBI

Sample	Rock type	depth	RVP[a]	RVP calc[b]	n	forsterite	1σ³	MgO	FeO	Ca	1σ	Sc	1σ	Ti	1σ	V	1σ	Cr	1σ	Mn	1σ	Co	1σ	Ni	1σ	Cu	1σ	Zn	1σ	Sr	1σ	Y	1σ	Zr	1σ
VB451-1	VTT	12	0.01	0.35	23	75.0	2.2	38.55	22.38	474	104	4.99	1.15	201	118	4.41	0.63	74.9	11.4	3211	141	211	13	1310	64	5.0	1.2	322	15.8	0.342	0.081	0.170	0.088	1.486	1.019
VB451-3.1	VTT	25	0.01	0.44	6	68.8	1.3	34.46	27.40	717	91	3.27	0.98	83.8	59.0	3.79	0.90	69.3	1.9	3824	97	228	3	1030	15	6.9	1.9	401	9.2	0.369	0.038	0.139	0.044	0.505	0.208
VB451-3.2	VTT	25	0.01	0.42	11	72.3	1.4	36.68	24.65	526	54	2.85	0.89	43.2	22.9	2.85	0.42	70.1	3.9	3533	139	234	8	1081	43	5.5	0.9	352	23.4	0.308	0.024	0.072	0.013	0.236	0.062
VB451-4	VTT	171	0.09	0.42	10	73.2	3.0	37.34	23.84	316	101	4.29	0.96	42.0	15.3	3.68	0.96	75.0	5.9	3075	216	221	5	1617	78	4.1	0.7	330	47.5	0.414	0.045	0.067	0.014	0.346	0.248
VB544-10	VTT	355	0.51	0.34	15	77.8	0.3	40.38	20.09	309	44	3.52	0.61	45.2	12.0	4.04	0.90	91.5	6.0	2479	23	203	21	1675	120	7.1	0.9	214	23.7	0.540	0.091	0.091	0.014	0.573	0.291
VB544-15	VTT	557	0.80	0.27	11	79.5	0.7	41.48	18.63	289	68	4.96	1.24	189	155	4.59	1.77	73.2	7.3	2642	28	296	5	1791	62	58.2	17.6	277	6.6	0.358	0.046	0.185	0.078	1.419	1.189
VB544-17	VTT	622	0.89	0.59	6	62.3	0.7	30.39	32.41	385	51	1.03	0.61	33.0	6.9	1.73	0.64	49.3	4.7	3472	119	255	18	1083	117	18.7	5.2	371	17.8	0.935	1.055	0.036	0.008	0.356	0.083
VB544-18.1	VTT	663	0.95	0.57	10	64.8	0.6	31.90	30.58	555	82	3.70	1.25	253	227	2.74	0.58	69.2	2.5	4077	56	231	4	1198	24	7.0	2.3	392	4.7	0.671	0.072	0.108	0.022	0.647	0.334
VB544-18.2	VTT	663	0.95	0.52	13	65.9	0.5	32.60	29.71	349	90	2.73	0.54	91.0	109	2.20	0.26	70.8	1.5	3484	21	239	8	1097	68	20.7	3.8	355	10.2	0.593	0.075	0.085	0.030	0.519	0.155
VB552-20	LTT	900	0.94	0.72	7	68.4	0.6	34.30	27.69	276	89	N.M.	N.M.	46.6	8.1	2.65	0.26	67.6	3.8	6970	484	206	28	772	86	26.9	8.8	401	45.1	0.299	0.095	0.333	0.104	0.276	0.051
VB266-12	BBS	609	0.89	0.51	15	63.8	1.5	31.70	30.91	198	26	N.M.	N.M.	210	122	4.51	2.17	70.6	6.5	4600	105	244	8	1091	43	5.6	1.3	457	23.0	0.371	0.038	0.091	0.025	0.227	0.145
VB266-43	BBS	651	0.95	0.93	37	62.1	1.2	30.62	32.20	292	83	7.61	3.32	273	135	4.60	1.96	50.7	12.6	9928	1249	182	26	755	79	21.6	12.9	583	38.0	0.580	0.273	0.141	0.073	0.683	0.383
VB266-44	BBS	651	0.95	1.00	22	61.5	1.8	30.43	32.45	247	64	3.20	0.92	202	113	2.67	1.13	57.0	4.6	10148	1116	202	19	811	71	13.9	8.4	618	41.2	0.527	0.123	0.047	0.010	0.550	0.296
VB552-21.1	BBS	902	0.94	0.81	11	67.5	1.3	33.72	28.41	231	73	N.M.	N.M.	46.5	6.0	2.22	0.33	67.1	9.3	7700	569	196	28	726	91	44.2	13.7	408	38.0	0.378	0.238	0.279	0.132	0.559	0.490
VB451-7	BBS	292	0.16	0.53	11	65.1	0.8	32.09	30.34	516	88	3.31	0.84	40.2	9.1	2.47	0.63	61.6	1.8	4138	84	248	3	796	48	5.0	1.1	396	8.1	0.346	0.049	0.128	0.064	0.225	0.035
VB552-15B	UMF	836	0.87	0.43	28	72.7	2.5	37.00	24.29	290	109	9.51	3.66	63.4	42.7	4.10	1.28	74.0	8.0	3523	267	237	27	1268	94	11.7	6.2	240	45.3	0.329	0.056	0.261	0.185	0.207	0.062
Parameters for AFC modeling (compositions of model liquids)[1]																																			
basaltic liquid[X]								8.0	10					160		140		1600		60		290						140							
model gneiss[Y]								4.3	10.8					108		80		20000		30		50						250							
Partition coefficients (D_{min/melt}) for basaltic melt[2]																																			
olivine								5.2	1.6					0.03		0.80		1.3-1.6		3.5		9.0						1.5-2.2							
plagioclase								0.04	0.10					0.20		0.02		0.04		0.10		0.06						0							
clinopyroxene								2.5	0.65					6		34		1.2		1.3		2.1						0							
sulfide									9					0.60		0.90		0.30		61		200						1							
Fe-Ti oxide[Z]									1.3					60		15		1.9		2.2		3.8						0							

[a]: relative vertical proximity factor = sample depth / (depth of first massive sulfide occurrence x relative sulfide content; e.g., RVP VB266-43 = 651 / (652.3 x0.95)

[b]: relative vertical proximity factor calculated based on results from multiple regression of V-Cr-Mn-Fe-Co-Ni-Zn and RVP with olivine data from VB266, VB544, and VB552 (see Appendix 6.4.)

[1]: Rayleigh fractionation melt calculation: $C_L / C_O = F^{(D-1)}$ (Rollinson, 1993; Li et al., 2007); AFC modeling was performed using the equation $C_L / C_O = f + r / (r-1+D) \times C_A / C_O(1-f')$ from DePaolo (1981)

[X]: basaltic liquid composition inferred after Condie (1993) Proterozoic basalts

[Y]: model gneiss composition - Mn based on Mn-rich enderbitic/Nain orthogneiss (Vale, unpublished data); Zn based on Tasiuyak paragneiss (Vale, unpublished data)

[2]: mineral D values are from Bougault and Hekinian (1974); Paster et al., (1974); Duke (1976); Maclean and Shimazaki (1976); Rajmani and Naldrett (1978); Pederson (1979);
Kloeck and Palme (1988); Beattie (1994); Ewart and Griffin (1994); Kohn and Schofield (1994); Gaetani and Grove (1997); Jones and Layne (1997); Bindemann et al., (1998);
Li et al., (2003b); Klemme et al., (2006)

[Z]: the major Fe-Ti oxide phase is ilmenite (titanomagnetite), however variable amounts of magnetite occur. Where D values for ilmenite were unavailable, D values for magnetite were utilized instead

[3]: reported 1σ error is standard deviation of *n* analyses on individual sample ("inter-sample variability") - for average analytical error see Analytical Method section; (*N.M.*) - not measured

3.3. Results

3.3.1. Olivine Compositional Variations

We performed multiple spot analyses, mostly core-rim transects, on several olivine grains in each sample. Individual olivine grains in the EDI are not significantly zoned in major elements (see also Li and Naldrett, 1999; Li et al., 2000; Venables, 2003), although the inter-grain variability in a given sample appears to increase with increasing Fe content (e.g., Fo82 ±0.22 1σ versus Fo62 ±1.8 1σ). Intra-grain trace element zonation appears to be significant only for olivine from the VTT and BBS that is in direct contact with sulfide mineral phases. Partially enclosed olivine exhibits outer rim enrichments, primarily in Mn (±Zn) and, to a lesser extent, depletions in Ni and Co. When in contact with wetting sulfides, olivine from the VTT displays rims slightly depleted in Ni and Co. In particular, olivine rims in immediate contact with sulfide have up to 500 ppm Ni and 55 ppm Co less than rims of the same grain not in contact with sulfide (e.g., VB552-13.1). Major element concentrations, and Mn-Zn contents, are not perceptibly zoned in these VTT samples. In BBS sample VB266-44 (651m) an olivine grain distal to sulfides (but in contact with plagioclase) has 7,900 ±53 ppm (2σ) Mn, 622 ±13 ppm (2σ) Zn, 850 ±30 ppm (2σ) Ni, and 230 ±5 ppm (2σ) Co, whereas an olivine grain in direct contact with sulfides has Mn and Zn concentrations of 10,600 ±50 ppm (2σ) and 684 ±25 ppm (2σ), respectively, and around 50 ppm less Ni and Co. An olivine grain completely enclosed in sulfide minerals in VB266-43 (651m, Fig.3.3H) was further examined with line detailed orthogonal transects (Fig.3.4). The nearly symmetrical trace element profiles for Mn, Ni, and Co

demonstrate clear core-rim zonation in the magnitudes of Mn>Ni>Co, whereas Zn and the Fo content remain homogeneous. The concentration of Mn increases from core to rim (plus ~3,400 ppm Mn, factor of 1.4), whereas Ni and Co decrease (minus ~175 ppm, factor of 0.8, minus ~35 ppm, factor of 0.8) respectively (Fig.3.4).

In the absence of wetting sulfide, the intra-sample variability is similar to the average SIMS analytical uncertainty (e.g., sample VB552-1, n=7, Ni content is 375 ±10 ppm 1σ, with an average analytical spot precision of ±9 ppm 1σ). Intra-crystal compositional variations are thus only important for BBS olivine, and to a minor extent VTT olivine in contact with sulfides, and are reflected by higher absolute 1σ deviations in olivine populations (e.g., VB266-43, n=37, 9,928 ±1,249 ppm 1σ Mn; Table 3.1). Consequently, in Table 3.1 and Figures 3.5–3.11, average concentrations for multiple grains within individual samples are always denoted with the ±1σ intra-sample variability (standard deviation of n spot analyses), whereas individual spot analyses are denoted with their internal precision as ±2σ.

3.3.2. Chemostratigraphic Variations of Olivine

Figures 3.5 and 3.6 illustrate the olivine trace element stratigraphy for two selected DDH from the EDI (VB266 and VB544; see Fig.3.2 for DDH locations). Depicted is the Fo content (mol.%) and the abundances of Ni, Co, Cr, Mn, and Zn (ppm), as they vary with depth. The Fo content exhibits a basal decrease; most pronounced in VB266, with an average of Fo79 ±1 1σ in NT olivine, Fo78 ±2 1σ in VTT olivine, and then Fo62 ±1 1σ

in olivine from the BBS (Fig.3.5A). Non-monotonic variations in Fo number occur commonly in the individual DDH sections, as seen by excursions within the NT and VTT intervals (VB266; Fig.3.5A) – which are prominent in the downhole profiles, especially in VB544 (Fig.3.6A). These always coincide with excursions in other trace elements. In particular, samples with more primitive (higher) Fo contents (VB266: 108m, 290m, 400m; VB544: 11m, 355m, 557m) correlate well with higher Ni, Co and Cr contents, whereas more evolved olivine (lower Fo contents) have higher Mn and Zn concentrations (VB266: 600m, 650m; VB544: 400m, 620m, 660m). Although Co shows a broadly similar trend to Ni (and Cr), with a decrease towards the base of VB266 (Fig.3.5B–C) in the BBS sequence (less prominent in VB544; Fig.3.6B–C), Co-Ni abundances in olivine of several NT-VTT horizons (e.g., VB266: 108m, 146m, 274m; VB544: 11m, 355m) are negatively correlated. The basal decrease in Fo, Ni, Co, and Cr is more pronounced in olivine from VB266 (Fig.3.5A–D) than from VB544 (Fig.3.6 A–D). In contrast, Mn and Zn concentrations increase with greater depth – starting in the lower part of the VTT and continuing into the BBS – as displayed in VB266 (Fig.3.5E–F) and VB552 (not shown; Table 3.1), and to a lesser extent in VB544 (Fig.3.6 E–F).
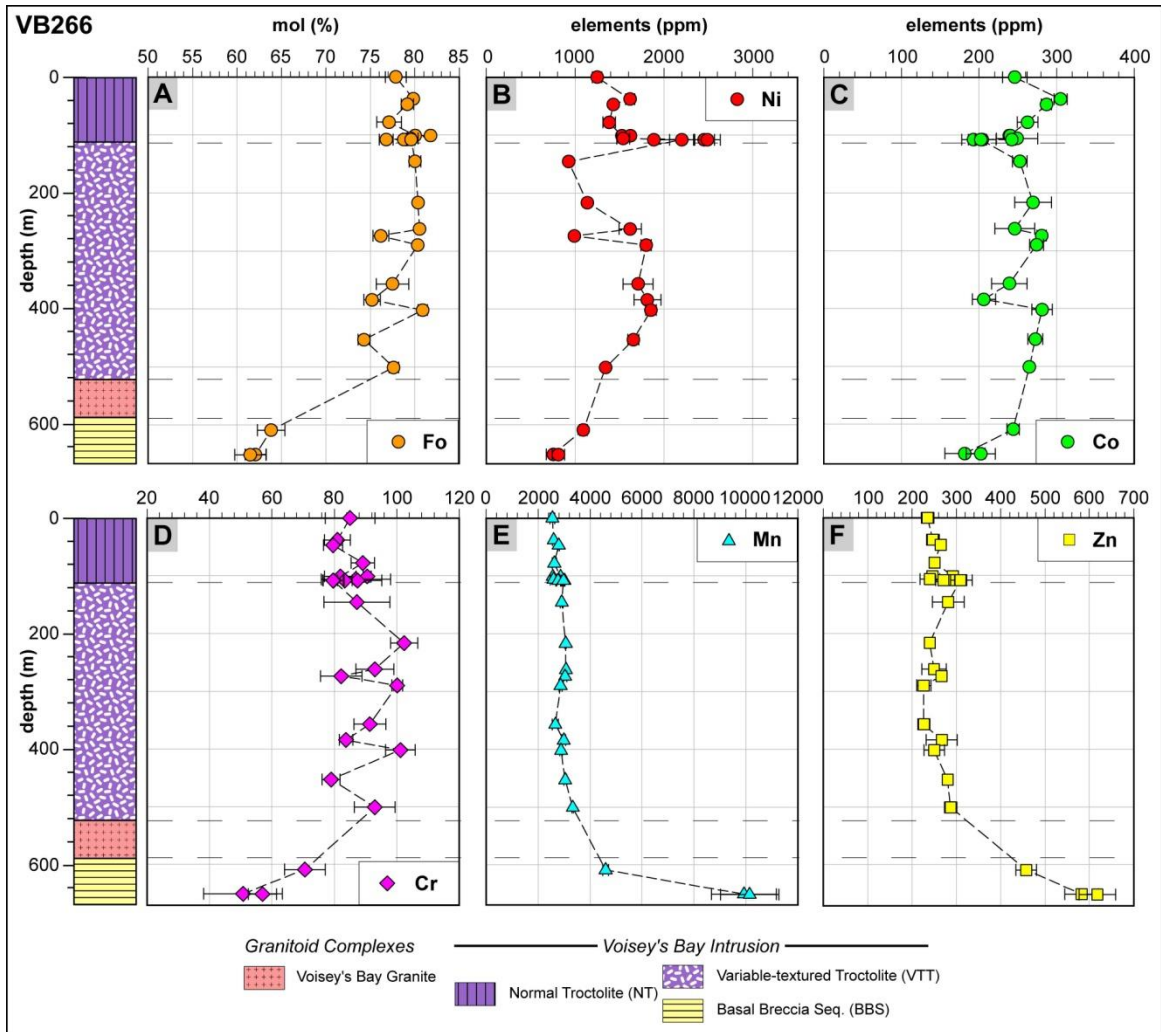
Fig. 3.5: Chemostratigraphy for olivine from DDH VB266 from zero meters to end of hole. A) shows the Fo content in mol (%). B) to F) show trace element concentrations in ppm.
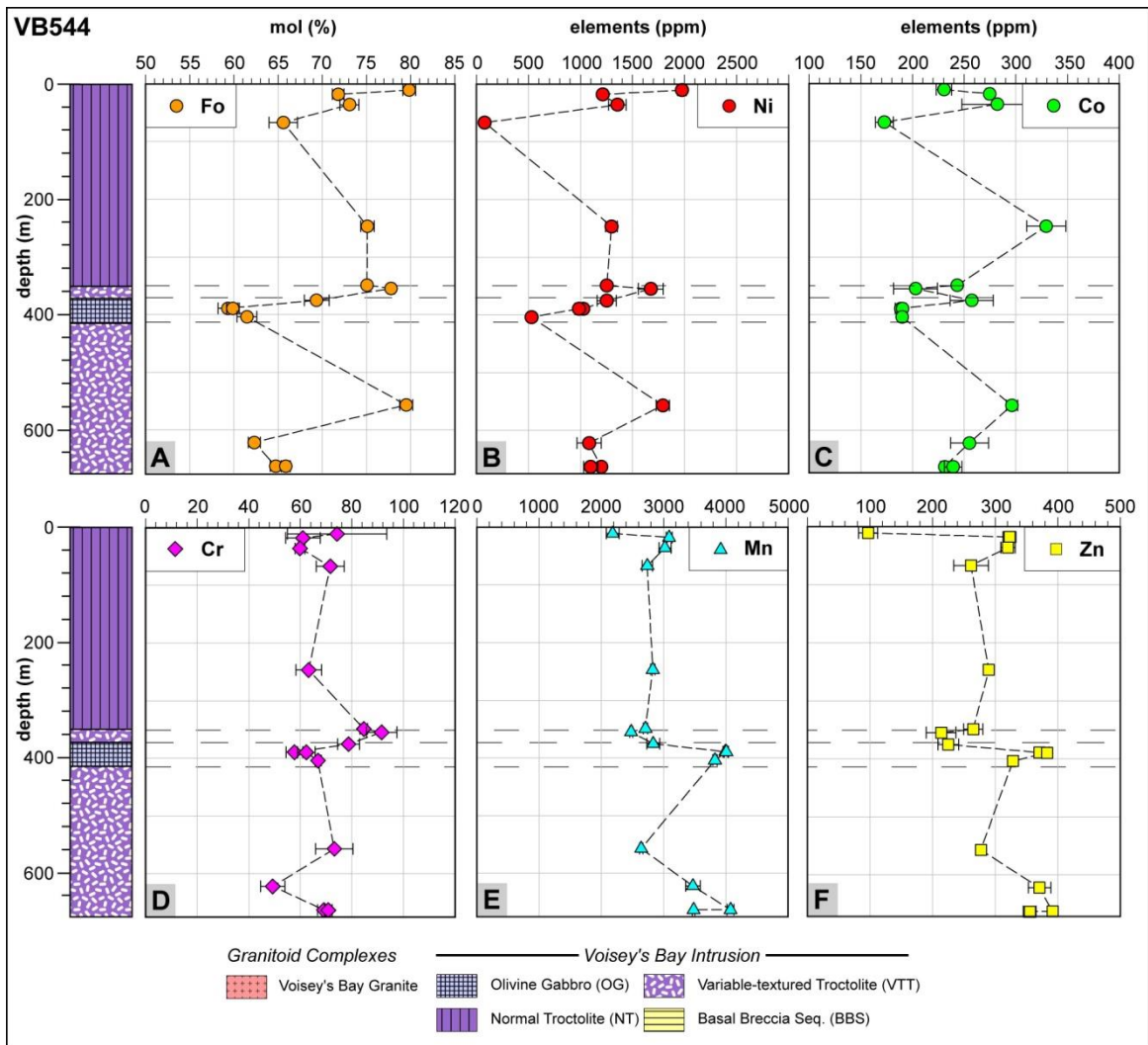
Fig. 3.6: Chemostratigraphy for olivine from DDH VB544 from zero meters to end of hole. A) shows the Fo content in mol (%). B) to F) show trace element concentrations in ppm.

3.3.3. Lithological Variations of Olivine

3.3.3.1. Olivine from the BBS

The BBS contains the most Fe-rich olivine, with a mean Fo number of only 64 ±2 (1σ; n=96) (Fig.3.7A). Ni values are low compared to the troctolitic units and range from 726 to 1,091 ppm (Fig.3.7B). The average Co/Ni ratio of BBS olivine is 0.25 ±0.03 (1σ; n=96), which reflects their Ni and Co deficiency relative to the troctolitic units (Fig.3.7B–C). In accord with this observation, the BBS olivine also has the lowest average Cr content of all EDI olivine (58 ±11 ppm 1σ n=96; Fig.3.7D). The most distinctive geochemical features, however, are the elevated Mn (≤12,250 ±277 ppm 2σ) and Zn (≤684 ±25 ppm 2σ) concentrations, which are up to 6x higher in Mn, and 3x higher in Zn, than the average values in olivine from the NT, VTT or OG (Fig.3.7E–F). These high values occur in chemically zoned olivine grains (Fig.3.4), which also explain the high Mn-Zn variability (Fig.3.7E–F) of BBS olivine compared to NT, VTT, and OG.

As mentioned above, some ultramafic fragments (UMF) are incorporated in the BBS. A serpentinized melatroctolite fragment (VB552-15B, 836m; Fig3.8D) contains fine-grained, fairly evolved and unzoned olivine with an average Fo content of ~73, and mean Ni and Co concentrations of ~1,300 ppm Ni and ~240 ppm Co, respectively (Fig.3.7A–C). The average Mn (~3,500 ppm) and Zn (~240 ppm) contents overlap with values from NT-VTT olivine (Fig.3.7E–F).

3.3.3.2. Olivine from the VTT

The VTT contains olivine with a wide range of compositions, from fairly primitive (Fo81; ~1,900 ppm Ni) to more evolved (Fo62; ~1,083 ppm Ni) (Fig.3.7A–B). The bulk of the VTT olivine has Fo74 ±5 (1σ; n=272), ~1,400 ppm Ni, ~240 ppm Co, and is relatively rich in Cr (78 ppm ±13 1σ) compared to either BBS or OG (Fig.3.7A–D). The Ni and Co concentrations in VTT olivine are variable (Fig.3.7B–C), with an average Co/Ni ratio of 0.18 ±0.05 (1σ; n=272). The Mn and Zn contents partly overlap with those of NT olivine (Fig.3.7E–F), but both elements are enriched approaching the contact with the BBS (e.g., VB552-13.1, 792m; ~3,900ppm Mn; ~400 ppm Zn; also Fig.3.5E–F). Thus, the increase from lower to higher Mn and Zn contents depicted in Figures 3.5E–F and 3.6E–F implies an almost continuous gradual progression from barren troctolite units in the hanging wall (NT, and top of VTT) towards the mineralized basal margin of the EDI (base of VTT into BBS; Fig.3.5–6).

3.3.3.3. Olivine from the NT

The olivine from the NT sequence have the most primitive composition (Fig.3.7A) and display a mean forsterite content of Fo77 ±4 (1σ; n=289), with maximum and minimum values of Fo82 (VB266-24.1) and Fo66 (VB544-5A), respectively. The major element range in NT olivine is accompanied by diverse Ni contents (Fig.3.7B) – with the highest values (~2,600 ppm; VB266-3.1 and -27; Table 3.1) approaching the primitive mantle olivine field in Ni versus Fo space (Fig.3.10A) and a minimum of ~80 ppm in the lowest

Fo sample (VB544-5A). In particular, petrographic observations demonstrate that olivine of the Ni-rich (Fig.3.8A) and Ni-poor (Fig.3.8B) type, although broadly similar in texture and sulfide content (~3 vol.%), is not compositionally identical. Epitactic overgrowth of orthopyroxene (±augite) on mostly medium-grained olivine is more abundant in the Ni-poor sample, which also has a slightly higher content of intercumulus phases (biotite, amphibole). Based simply on petrographic observation, these horizons would be almost indistinguishable from the average NT, which contains between 1,300 and 1,600 ppm Ni in olivine (Fig.3.7B). NT olivine also have an average Co/Ni ratio (0.17 ±0.05 1σ; n=289) comparable to VTT olivine, but with a higher Co variability (Fig.3.7C). The average Cr content of NT olivine is also similar to that in olivine from the VTT (~79 ppm; Fig.3.7D). Although Mn and Zn contents are relatively constant, with the bulk of the olivine containing ~2,600 ppm Mn and 280 ppm Zn (Fig.3.7E–F), sample VB544-1 (melatroctolite interval in the NT) contains unzoned olivine with exceptionally low Zn contents (up to 100 ppm) that approach the values for primitive mantle olivine but, paradoxically, have much lower forsterite values (Fo80 ±1 1σ) (Fig.3.10D). Compared to the surrounding NT, this "primitive" olivine sample lies within a greenish-gray, mostly fine-grained melatroctolite, with a sugary texture and a weakly developed magmatic layering. The olivine abundance is higher (50–60 vol.%) than in the typical NT, whereas the individual grains are rounded to equant and exhibit advanced serpentinization (Fig.3.8C). Even though the texture and mineral mode is remarkably similar to the measured melatroctolite fragment (UMF) from the BBS (Fig.3.8D), the chemical composition of the olivine is strikingly different. Olivine from the UMF is on average

much more evolved than that from this most primitive interval in the NT (Fig.3.12A–B).
Similar to the samples with extremely high Ni (VB266-3.1 and -27) and low Ni (VB544-5A) olivine (Fig.3.5B and 3.6B), this lowest Zn sample appears to represent a petrographically defined stratigraphic interval in the otherwise relatively homogeneous NT (Fig.3.6F).
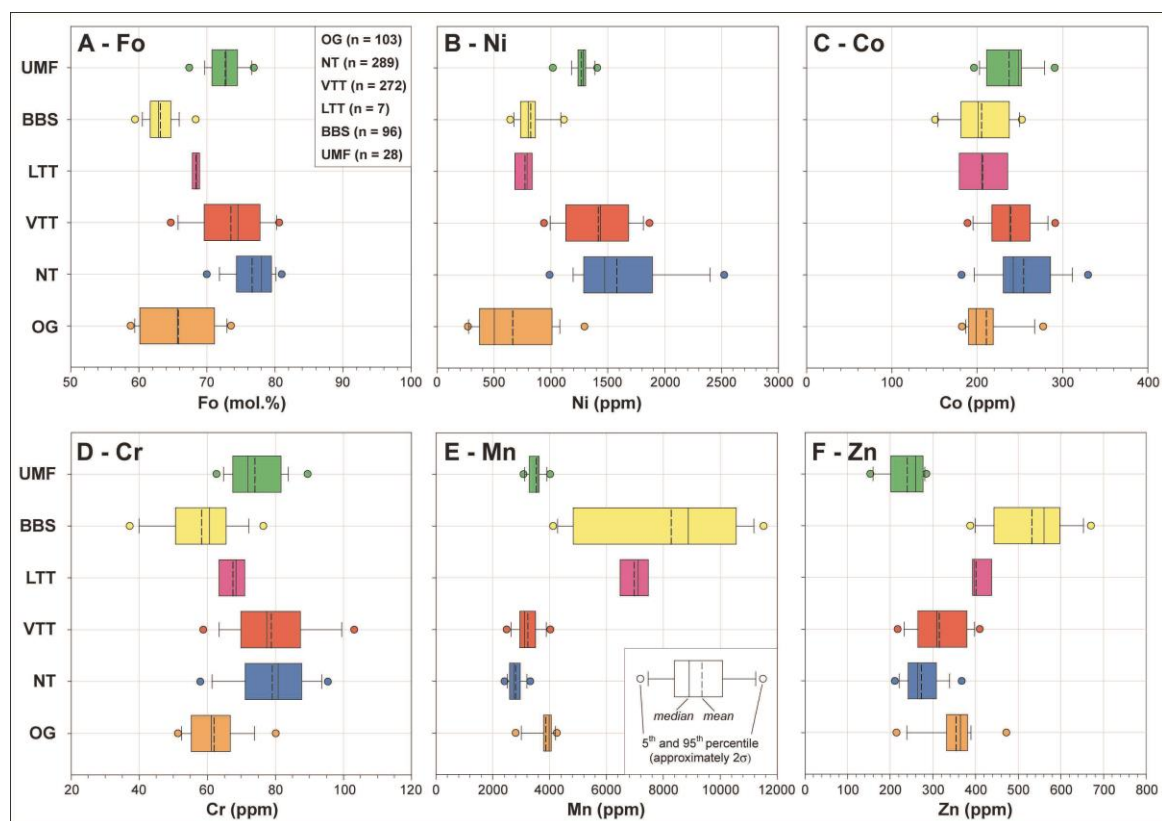

Fig. 3.7: Box plots depict the Fo contents and concentration ranges for Ni, Co, Cr, Mn, and Zn of olivine from the major lithologies (OG, NT, VTT, LTT, BBS, and UMF). Individual boxes include the median (solid line), the mean (dashed line) of the olivine populations, whereas the dots to the left and right of the box constrain the 5th and 95th percentile, respectively, which approximately represents the 2σ range (see inset). Roughly similar lithological trends for Fo, Ni, Co, and Cr are visible. Mn and Zn also display a co-variation. See text for detailed discussion.

3.3.3.4. Olivine from the OG

The OG sequence contains olivine with variable Fo contents (Fo66 ±5 1σ; n=103), but comparatively homogeneous trace element compositions (Fig.3.7B–F). On the basis of Ni contents, two distinct groups of OG olivine can be distinguished; one with lower Ni values (200–600 ppm), and one with higher Ni values (1,000–1,300 ppm) (Fig.3.7B). The forsterite compositions vary discernibly between high-Ni (average; Fo62) and low-Ni (average; Fo68) type olivine. Concomitantly, Co/Ni ratios range from 0.19 ±0.01 (1σ; n=40) for high-Ni olivine, to 0.59 ±0.18 (1σ; n=63) for low-Ni olivine, whereas the average Co concentration of OG olivine is low (~210 ppm Co; Fig.3.7C). A limited number of samples from the EDI (VB544-13.1, VB552-1 and -3), and all samples from top of the Reid Brook Zone (VB449), fall in the low Ni group. Olivine from the OG is also low in Cr (62 ±9 ppm 1σ; n=103; Fig.3.7D), with Mn (~3,900 ppm) and Zn (~350 ppm) values at the upper range of the EDI olivine spectrum (Fig.3.7E–F).

3.3.4. Compositional Variations of Olivine Distal and Proximal to Massive Sulfide Mineralization

The massive sulfide ores in the EDI are associated with the brecciated and contaminated basal sequence. The most obvious differences in olivine composition between the nominally barren NT and mineralized VTT-BBS units are the decrease in Cr-Co-Ni contents and the increase in Fe-Mn-Zn (Fig.3.7). Figure 3.9 shows the Mn-Zn variations in olivine relative to the vertical proximity to massive sulfide in the EDI. The relative

vertical proximity factor (RVP) is calculated as the depth of the sample divided by the depth of the first occurrence of mineralization in the measured DDH multiplied by the relative sulfide content (e.g., VB552-13.1 VTT, 792m, first occurrence of massive sulfide at 911m with 95% sulfide – from unpublished Vale log files; RVP=792/(911*0.95)=0.83; Table 3.1). Olivine with RVP values close to 1 are in direct proximity to massive sulfides, whereas values below 0.4 imply the absence of a detectable signal of major mineralization. This threshold at an RVP value of 0.4 corresponds to a maximum distance to massive sulfide of less than 450m. From 0.4 to 1 the increase in Mn-Zn in olivine from VTT and BBS is readily visible (Fig.3.9). From 0.4 to 0, on the other hand, some NT-VTT-BBS samples also display elevated values for Mn and Zn. These enriched samples, however, have higher (disseminated) sulfide contents (NT ~5 vol.%, VTT 5–15 vol%, BBS ~20 vol.%; Fig.3.9 – green field) than the nominally barren (~1 vol.%) NT-VTT samples that fall in this range of RVP values. Therefore, these VTT-BBS samples can be excluded as prospective olivine based on petrographic observations, the stratigraphic position in the EDI, their elevated, but still less enriched Mn-Zn contents, and their multi-trace element signature (see Discussion in section 3.6.).

3.3.5. Summary of Key Results

(1) Individual olivine grains in the OG, NT, and UMF are chemically unzoned, whereas grains in the mineralized VTT and BBS that are enclosed by sulfide mineral phases display a variably pronounced trace element zonation (Mn>Ni>Co>Zn) with homogeneous Fo contents (Fig.3.4).

(2) The Fo, Ni, Co, and Cr contents decrease with depth in the EDI, and correspond to changes in lithology (Fig.3.7) – from the highest values in the NT at the top to the lowest in the BBS at the base (Fig.3.5A–D and 3.6A–D).

(3) Mn and Zn concentrations in olivine from the EDI show a positive co-variation; they increase in unison with depth, from the lowest values in the NT (Fig.3.7E–F), to intermediate in the lower VTT towards the highest in the BBS (Fig.3.5E–F and 3.6E–F).

(4) Ni-rich and Ni-depleted olivine intervals in the barren NT sequence (Figs.3.5B and 3.6B) show a maximum variation in Ni concentration of almost 2,500 ppm, whereas the average Ni concentration in olivine bracketing these horizons is relatively uniform at ~1,500 ppm (Fig.3.7B).

(5) The composition of olivine (e.g., Fo content, V, Ni, Mn, Zn, Sr, and Y) in nominally melatroctolite samples (top of NT and UMF in BBS; Fig.3.8C–D) varies systematically with the host lithology (NT vs. BBS) and the stratigraphic position in the EDI.

(6) The gradual increase in Mn and Zn abundance in olivine is correlated with the transition from the weakly mineralized lower part of the VTT into the massive sulfide-bearing BBS from below circa 500m in VB266 (Fig.3.5E) and below 550m in VB544 (Fig.3.6E). Other DDH data (VB552; see Table 3.1) further corroborate the presence of anomalously Mn-Zn-rich olivine in proximity to the massive sulfide occurrence in the EDI (Fig.3.9).
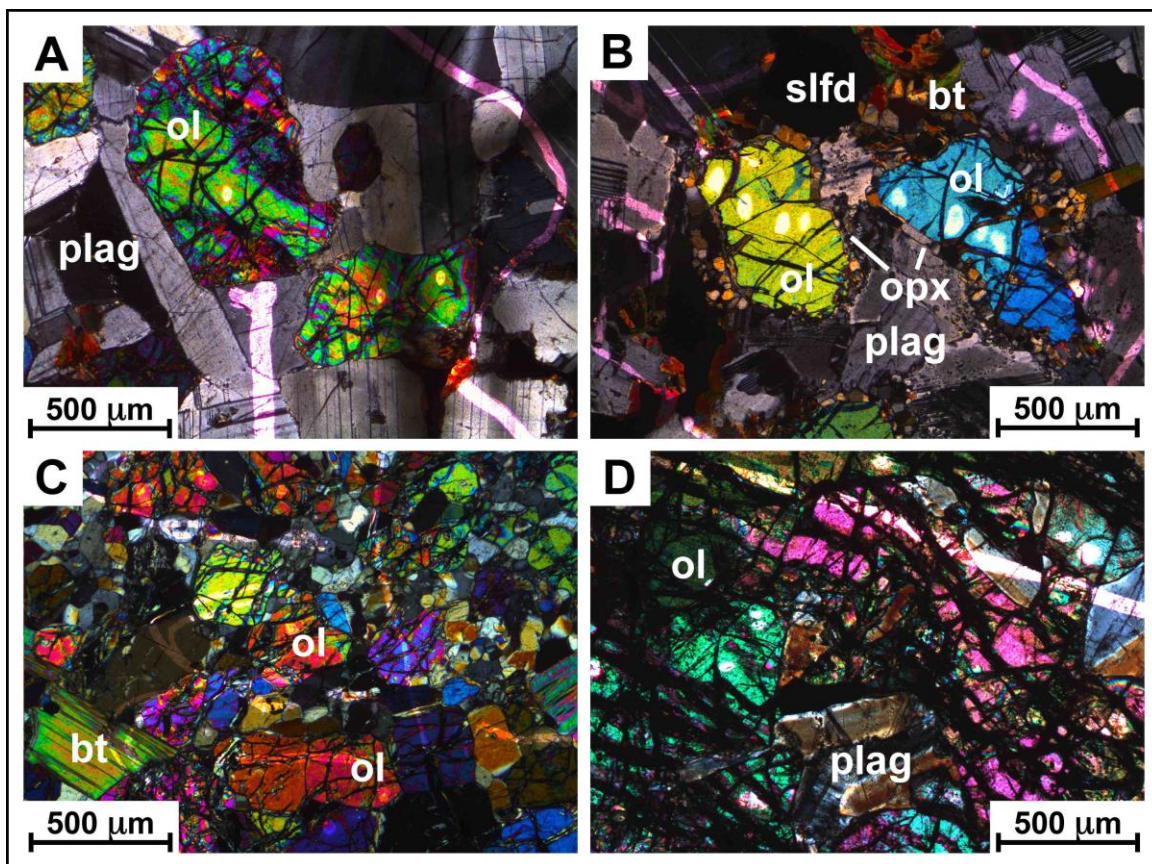
Fig. 3.8: Photomicrographs of olivine grains that are texturally characteristic for the Ni-rich, Ni-poor and primitive olivine samples in the NT unit from VB266 and VB544 and the UMF from VB552. Cross-polarized light. A) shows the Ni-rich interval, B) the Ni-poor interval, C) the primitive olivine horizon on top of the NT, and D) the UMF in the BBS. Key for minerals: ol = olivine, plag = plagioclase, bt = biotite, oxp = orthopyroxene slfd = sulfide.
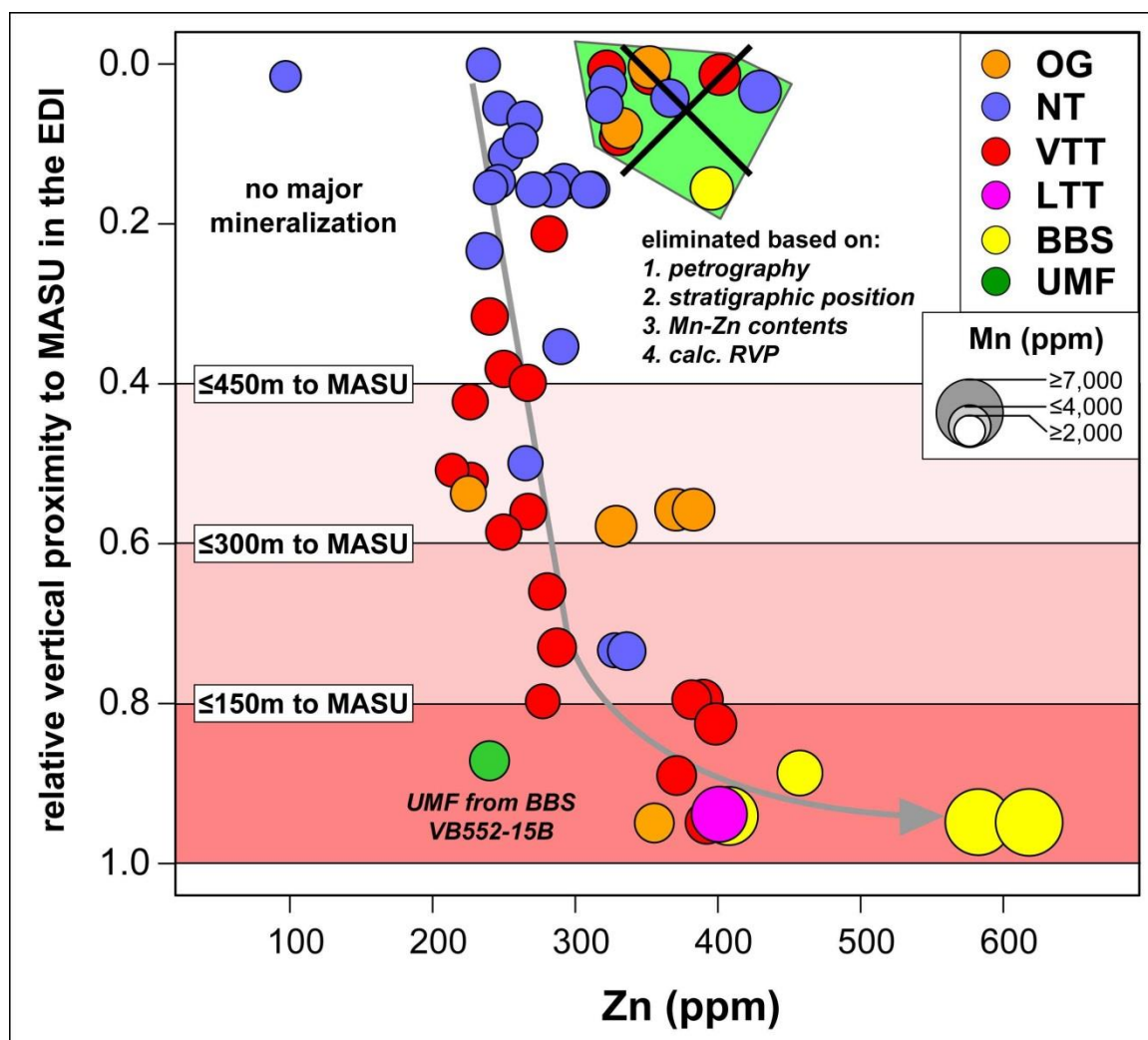
Fig. 3.9: Mn and Zn variations with relative vertical proximity to massive sulfide mineralization (RVP factor; y-axis) in the EDI. Bubble size corresponds to the Mn content (ppm), which exceeds the 2,000 ppm threshold commonly at RVP values greater than 0.6. Values of RVP close to 1 imply proximity to massive sulfide mineralization (MASU), whereas all olivine with RVP values below 0.4 is not associated with major mineralization. The VTT-BBS samples with elevated Mn-Zn contents (green field) are all from VB451, which does not intersect massive sulfide (Fig.3.2; Table 3.1). Even though the olivine have Mn-Zn contents close to values for prospective olivine from, for example VB266, their overall potential is lower, and the VTT and BBS samples can be eliminated based on several characteristics: VTT – composition of Fo, Cr, Ni, ±Mn, ±Zn and thus low *calculated* RVP, BBS – relatively *low* Mn-Zn concentrations with respect to exact stratigraphic position at base of BBS (see also Discussion 3.6.).

3.4. Discussion

3.4.1. Link between Olivine Composition and Magmatic Episodicity

3.4.1.1. Controls on the Compositional Variations of Ni-rich and Ni-poor NT Olivine

Fractional crystallization processes and subsolidus reequilibration with intercumulus silicate and sulfide liquids most likely controlled the olivine composition in the VBI (e.g., Sato, 1977; Hart and Davis, 1978; Rajamani and Naldrett, 1978; Fleet et al., 1981; Barnes, 1986; Li and Naldrett, 1999). The interaction between silicate melt, olivine and sulfide liquid with regard to the exchange of Fe and Ni has been studied extensively, particularly in sulfide-ore-bearing systems (e.g., Clark and Naldrett, 1972; Hart and Davis, 1978; Fleet et al., 1981; Fleet and MacRae, 1983; Holzheid et al., 1997; Brenan and Caciagli, 2000; Li et al., 2003b). Generally, two processes can provoke Ni depletion of olivine: (1) a silicate melt − sulfide liquid interaction, in which the silicate melt gets stripped of Ni prior to, or during, olivine crystallization (e.g., Hart and Davis, 1978; Rajamani and Naldrett, 1978; Fleet et al., 1981), or (2) olivine − sulfide liquid re-equilibration that induces a syn- or post-magmatic Fe-Ni exchange (e.g., Clark and Naldrett, 1972; Barnes and Naldrett, 1985; Li and Naldrett, 1999; Li et al., 2000).

Both the geochemical and petrographic evidence is in accord with the derivation of the Ni-rich and Ni-poor olivine through fractional crystallization (FC) of a parental magma of broadly basaltic composition, with an initial MgO content of 8 wt.% (FeO/MgO=1.25) − comparable, for example, to uncontaminated tholeiitic to picritic basalts from the Noril'sk area (Li and Naldrett, 1999; Li et al., 2000; Scoates and Mitchell, 2000; Li et al., 2003a).

Model lines for FC processes were simulated under the assumption that the (weight) ratio (FeO/MgO)$_{olivine}$/(FeO/MgO)$_{liquid}$=0.3 (±0.03; Roeder and Emslie, 1970; see also Table 3.1) was constant during fractional crystallization of olivine (ol)+plagioclase (plag)+clinopyroxene (cpx) (modal ratio of 1:3:0.2) as liquidus phases (FC A). Each model line was delineated using Fo contents calculated for increments of 5% progressive crystallization based on the (FeO/MgO)$_{liquid}$ (Li et al., 2007). Perfect FC (unlikely in natural systems), as opposed to equilibrium crystallization, will produce the maximum compositional shift in the silicate melt, and the fractionating mineral phases and is regarded as a limiting case for our models (Li et al., 2007). Petrographic observations of EDI troctolites support the ol:plag:cpx crystallization sequence. The first olivine to crystallize has a Fo content of 82, which resembles the composition of the most primitive NT olivine from this study.

The fractionation of several trace elements (Ni, Co, V, Cr, Mn, Zn) was then calculated following the approach of Li et al. (2003a, 2007) – the trace element content of the initial melt (C$_O$; inferred from average composition of Proterozoic basalts; Condie, 1993; Table 3.1), the partition coefficients (e.g., D$Ni_{ol/sil}$ = concentration in olivine / concentration in liquid) for olivine, plagioclase, clinopyroxene, sulfide liquid, and Fe-Ti oxide (Table 3.1), the degree of fractionation, and the proportion of the remaining liquid (F) (from 100% − 1 to 0% − 0 in 5% − 0.05 increments; used to compute the bulk D), were used to calculate the composition of the residual liquid (C$_L$) according to the equation:

$$C_L = C_O F^{(D-1)}$$

The model lines in Figure 3.10A (FC model lines A_1, A_2, and B) bracket the apparent Ni and Fo co-variation and can explain the formation of most EDI olivine. Under these conditions, the Ni-rich olivine would have crystallized from a silicate melt with 290 ppm Ni (FC A_1), but their Fo contents may have been subsequently reduced by interaction with a trapped silicate liquid (up to 9 mol.% maximum trapped liquid shift (TLS) in NT olivine as calculated by Li et al., 2000; Venables, 2003) (e.g., Barnes, 1986; Chalokwu and Grant, 1987) (Fig.3.10A). The composition of the Ni-poor olivine on the other hand, is explicable by precipitation from a batch of slightly more differentiated silicate melt (higher Fe-Sr-Y; Fig.3.12A–B), which in this case segregated a sulfide liquid after 10% crystallization in the modal ratio of 1 ol: 3 plag: 0.2 cpx: 0.08 sulfide (Fig.3.10A; FC B). This sulfide segregation (process 1) strongly depleted the silicate melt in Ni (~9 ppm with $DNi_{ol/sil}=9$; Li et al., 2003b) and Co (~50 ppm with $DCo_{ol/sil}=3.5$; Beattie et al., 1991) prior to olivine crystallization, whereas the slightly higher amount of trapped silicate liquid (evident by higher amount of hydrous intercumulus phases) later resulted in a greater reduction of the Fo content in the Ni-poor olivine (~Fo66). The FC model is favored over a Ni depletion of the Ni-poor NT olivine by subsolidus reequilibration with sulfides (process 2), as proposed for olivine in the BBS (Li and Naldrett, 1999), because: firstly, the overall sulfide content in this sample is too low (~3 vol.%); secondly, none of the olivine grains is enclosed by sulfides – but rather rimmed by orthopyroxene; and thirdly, these olivine grains are unzoned in Ni and Fe (Fig.3.10A). In comparison, all olivine in contact with sulfide in the VTT and BBS exhibits variable core-rim changes in Ni and Co (VTT) and Mn (±Zn) (BBS) concentration (Fig.3.4). These profiles likely

reflect subsolidus, solid-liquid diffusive exchange, because once segregated, sulfide liquid tends to be quite immobile, with only a limited tendency for migration through cumulate pore space (Barnes et al., 2008). Therefore, the complete physical separation of the Ni-poor NT olivine and interstitial sulfide liquid between the point of equilibration (lower chamber or conduit) and the site of final emplacement (upper part of NT in EDI) is doubtful (e.g., Bremond d'Ars et al., 2001) – even in a dynamic and turbulent environment like the VBI – especially since the Ni-poor interval is bracketed by olivine with uniform Ni composition. Finally, the presence of the orthopyroxene selvages around the Ni-poor olivine might have shielded them from later Ni and Fe exchange, whereas early depletion to the very low apparent Ni concentration (~18x less Ni than average BBS olivine) would have likely required a long equilibration time.

Instead, we conclude that the initial batch of melt must have lost most of its Ni in a lower staging chamber prior to olivine crystallization (FC B). Alternatively, it may have interacted with a sulfide melt during ascent through the conduit, either by undergoing intrinsic sulfide saturation, or by assimilating sulfides during an earlier saturation event. Model FC A_2 simulates this intermediate case, where ol:plag:cpx crystallized from a melt with an initial Ni content of 100 ppm (C_O=100) instead of 290 ppm, because the sulfides would have scavenged the silicate melt of chalcophile elements in an R-factor process – likely in the order Ni>Cu>Co (MacLean and Shimazaki, 1976) – leaving behind a depleted melt reservoir from which the Ni-poor olivine subsequently crystallized. Parts of this enriched sulfide fraction may now be preserved as the high tenor disseminated sulfides observed towards the base of the VTT.
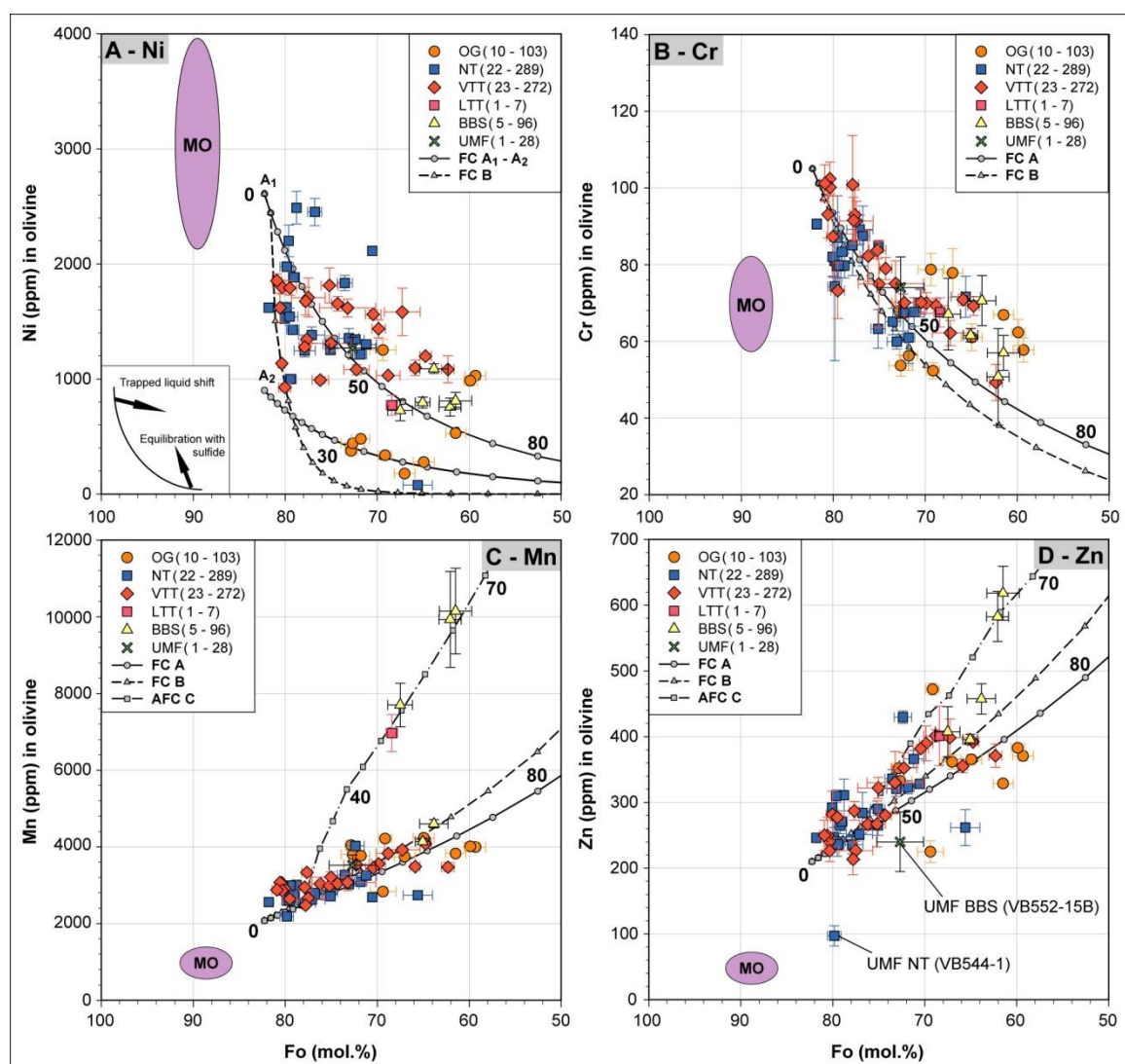
Fig. 3.10: Plots of selected trace elements versus forsterite content of VBI olivine. The sample type follows abbreviations used in the text (e.g., OG – olivine gabbro, UMF – ultramafic fragment) and in brackets is the number of samples per unit and the total number of measured data points in olivine for each specific lithology. Error bars denote 1σ sample internal error (inter-granular variability). Inset in A) shows the potential change in composition due to the trapped liquid shift and equilibration with sulfide (Li et al., 2000). MO indicates the composition of primitive mantle olivine (partly from DeHoog et al., 2010; partly unpublished data). Black lines denote calculated Rayleigh fractionation model lines (FC A, B, and D) and the Assimilation FC model (AFC C) to replicate and bracket the apparent olivine trends derived from four possible scenarios: **A** the crystallization of ol:plag:cpx, in a ratio of 1:3:0.2 (solid line); **B** the segregation of a sulfide liquid after 10% crystallization of ol:plag:cpx in a ratio of 1:3:0.2 to 0.08 sulfide (dashed line); **C** is based on model curve A with the silicate melt assimilating 10% of Mn-rich (enderbitic-Nain) orthogneiss

(dashed and dotted line) after 25% crystallization. Symbols (and numbers) on model lines indicate the degree of crystallization in 5% increments. Parameters used for calculations are listed in Table 3.1. See text for further discussion.
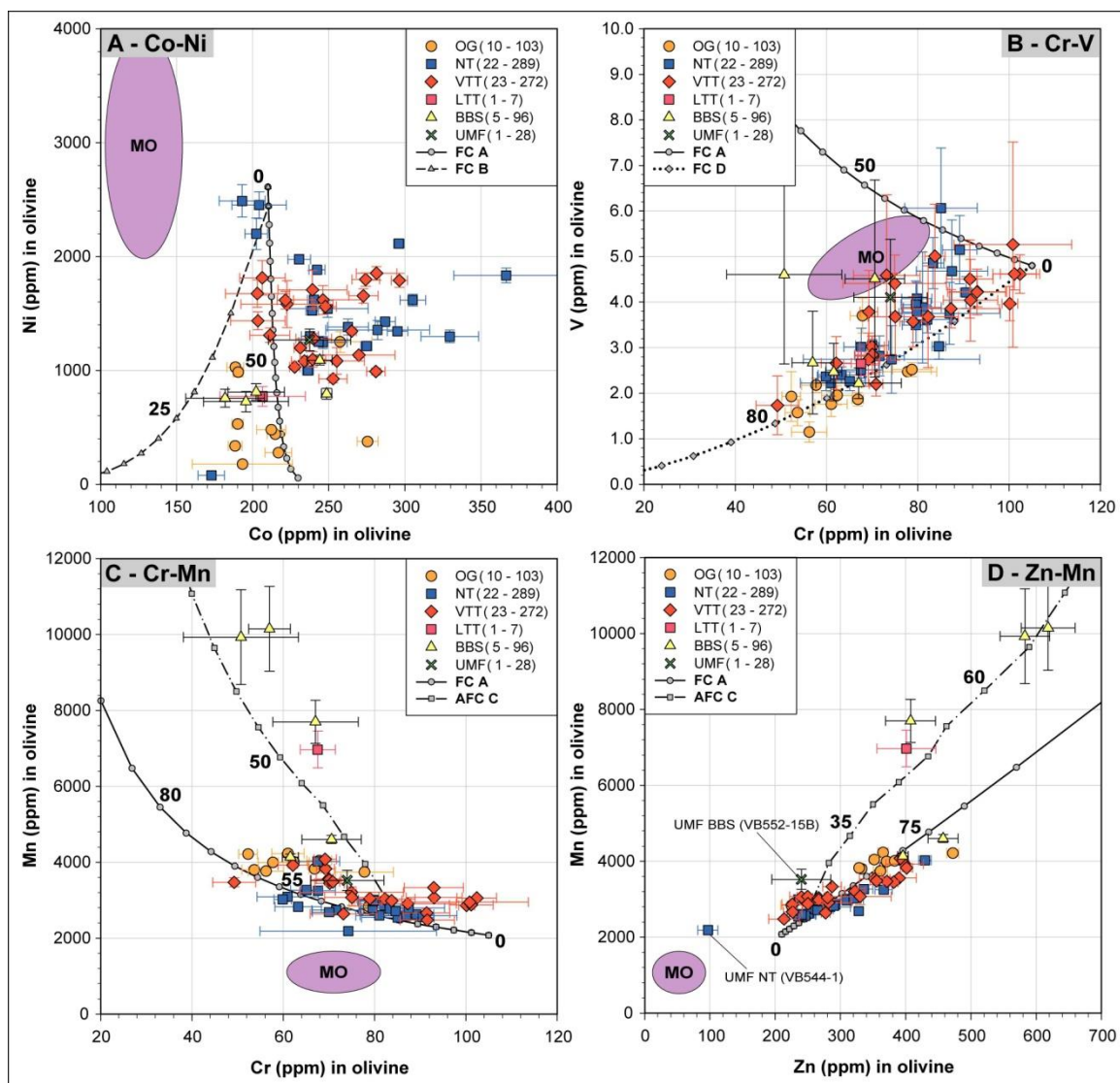
Fig. 3.11: Plots of selected trace elements from VBI olivine. B) displays Cr versus V with FC model **D**, the crystallization of ol:plag:cpx and a Fe-Ti oxide phase (ilmenite, ±titanomagnetite, ±magnetite) in a ratio of 1:3:0.45:0.3 (dotted line). See Fig.3.10 for description of legend and other FC models.

3.4.1.2. Petrogenesis of Olivine in Melatroctolite

The two melatroctolite samples analyzed were from the BBS (UMF BBS; 836m, VB552-15B) and the nominal top of the NT unit (UMF NT; 11m, VB544-1) and contain olivine that diverges from the other populations described (Fig.3.10D, 3.11D, 3.12C–D). The stratigraphic continuity of the primitive olivine horizon near the top of the NT sequence is still somewhat cryptic − especially its lateral and vertical extent. Its precise contact relationships (footwall and hanging wall) are slightly diffuse and oriented at ~80° to core axis. However, textural and geochemical evidence support a petrogenesis different from that of the surrounding NT, and it is possible that this section represents a large, partially serpentinized ultramafic fragment − a cumulate remnant of an earlier magmatic event. Alternatively, it might represent an ultramafic sill with an eroded hanging wall contact, intruded syn- or post-magmatically relative to the main EDI intrusive event. A truly intrusive relationship to the main EDI, however, seems doubtful because, even though the footwall contact is slightly diffuse, it shows no textural evidence of either metamorphism/metasomatism or a chilled margin. In addition, the primitive olivine contained in the melatroctolite is strongly serpentinized, whereas olivine from the surrounding NT is fairly fresh and unaltered, which suggests that the primitive olivine horizon was altered prior to emplacement of the NT, and is therefore older. Olivine from the UMF NT sample also has a more primitive composition than average NT olivine (lower Ca-Sc-Ti-V-Mn-Zn-Y-Zr), not dissimilar to mantle olivine (Fig.3.12C, MO; from Western Gneiss Region, Norway; F.Bulle, unpublished data). For these reasons, the primitive olivine is interpreted as a product of a compositionally different, and more

primitive, parental magma that evolved along a separate FC path in an earlier intrusive phase than the one that generated the NT and VTT units (Fig.3.12C).

In contrast, the melatroctolite fragment from the BBS (UMF BBS), even though texturally similar to the primitive olivine interval in the NT, contains more differentiated olivine (higher Sc-Mn-Fe-Y; Fig.3.12C–D). The evolved Fo and Ni compositions of the olivine in this sample are comparable to the range of published values for other UMF from the VBI (Li and Naldrett, 1999). Assuming that their similar petrography indicates that both melatroctolite fragments share the same parental magma origin, their presence in various parts of the EDI stratigraphy would imply that they were either incorporated episodically from a lower chamber, or that they were emplaced via discrete magma conduits (Lightfoot and Evans-Lamswood, 2012). The chemical composition of the olivine from the UMF in the BBS might then be a result of a post-crystallization trace element overprint. As this UMF was entrained in the sulfide- and xenolith-rich melt of the BBS, trace element diffusion between the olivine in the UMF and the contaminated melt (or a volatile-rich fluid), might have altered the olivine composition over time. The small olivine grain size and preferred fluid pathways through the UMF could have enhanced element diffusion (especially of Mn-Fe-Zn) into the olivine structure, producing enriched, yet unzoned olivine crystals (Costa and Dungan, 2005). Olivine of the UMF in the BBS is enriched by up to 1,300 ppm in Mn in comparison to those from the primitive interval of the NT (Fig.3.12C), an enrichment that is comparable to that observed in the zoned BBS olivine that are in contact with sulfides. Therefore, Mn-Zn and other trace elements were likely exchanged between olivine in the UMF and the surrounding contaminated melt.

During turbulent transit through the magma conduit, this UMF effectively interacted with trace element-rich contaminated material – and the olivine was able to reequilibrate to a secondary composition. Conversely, the primitive olivine interval in the upper part of the NT unit likely retains its primary composition.
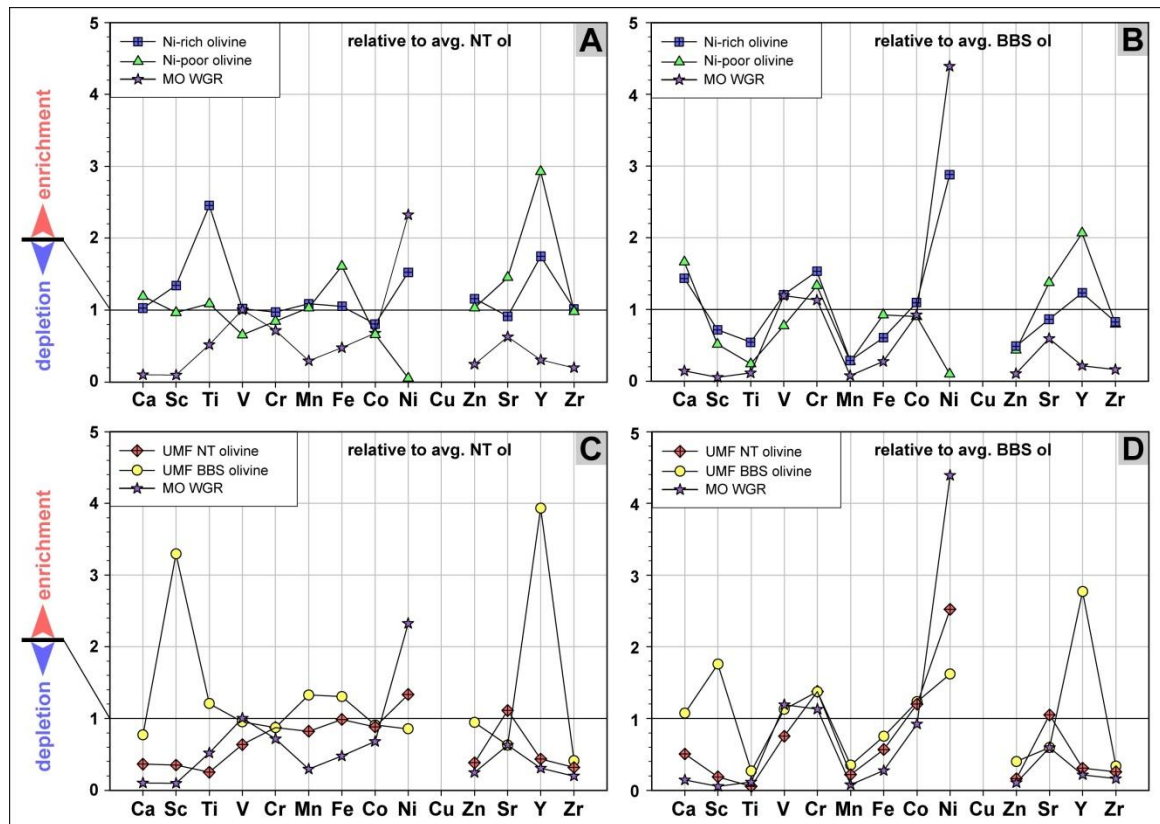

Fig. 3.12: Enrichment-depletion diagrams showing the enrichment factors for the trace element composition of the average Ni-rich and Ni-poor olivine intervals in the NT relative to A) average NT olivine and B) to average BBS olivine, and the average UMF NT olivine and UMF BBS olivine relative to C) average NT olivine and D) to average BBS olivine, both from VB266. The mantle olivine composition depicted is from a spinel-garnet peridotite from the Western Gneiss Region, Norway (MO WGR; F.Bulle, unpublished data – Chapter 2).

3.4.2. Olivine Composition as a Record of Contamination Processes

The petrogenesis of the Voisey's Bay magmatic sulfide deposit is intimately related to country rock assimilation and contamination (e.g., Naldrett, 1997; Lambert et al., 1999; Lightfoot and Naldrett, 1999; Ripley et al., 1999, 2002). In order to saturate ultramafic to mafic melts in sulfur and provoke the segregation of economic quantities of immiscible sulfide liquid, contamination through assimilation of SiO_2-rich country rock ("felsification"; Irvine, 1975, 1977) or the assimilation of external sulfur are required (e.g., Ripley, 1981; Keays, 1995; Naldrett, 1997; Keays and Lightfoot, 2010; Ripley and Li, 2013). This segregation is considered essential for the formation of most Ni-Cu-Co sulfide ore deposits (Ripley and Li, 2013).

For the VBI, the addition of crustal sulfur through desulfurization of the enclosing sulfide-bearing Tasiuyak paragneiss is likely the major factor that forced the VBI parental melt(s) to the point of sulfide saturation (Ripley, et al., 1999; 2000; 2002; Scoates and Mitchell, 2000). Although felsification through the input of bulk crustal contamination and silica enrichment has been argued to be minor on geochemical grounds (Amelin et al., 2000) and on isotopic grounds (Lambert et al., 2000), petrographic, mineralogical and stable isotopic evidence, particularly in the heavily sulfide mineralized, breccia-bearing marginal units of the EDI (e.g., BBS), indicate an assimilation and elemental exchange with the surrounding country rock (e.g., Lightfoot and Naldrett, 1999; Ripley et al., 1999; Li and Naldrett, 2000; Mariga et al., 2006a). The entrained fragments of Tasiuyak paragneiss in the BBS and lower VTT are partially digested and altered through contact metamorphism, and the primary metamorphic minerals (garnet, cordierite, K-feldspar

etc.) are progressively replaced by assemblages dominated by hercynite and magnetite (Li and Naldrett, 2000; Mariga et al., 2006a). The degree of reaction increases in conjunction with the FeO-MnO-ZnO contents of hercynite from the Reid Brook Zone towards the EDI (Li and Naldrett, 1999; Li and Naldrett, 2000).

3.4.2.1. Effect of Contamination on the Olivine Composition

The Fe-Ni-Cr-V composition of olivine in the lower VTT and BBS is consistent with derivation through fractional crystallization (Fig.3.10A–B; FC A) from the same parental melt that crystallized most NT-VTT olivine. The slightly elevated contents of Cr (+V) relative to the Fo content (BBS and some VTT fall above the model lines in Fig.3.10B and 3.11B) likely result from either a limited crystallization of olivine before Fe-Ti oxide phases entered the liquidus (Cr-V contents start following model line FC D at circa 10% FC; Fig.3.11B), or a minor subsolidus increase through the trapped liquid shift. However, FC processes alone cannot explain the Mn-Zn-rich signature of most of the BBS (and LTT) olivine. Instead, the BBS olivine data can be simulated more closely if a finite assimilation of a Mn-Zn-rich reservoir is considered (AFC Model Line C). For the AFC modeling, conservative partition coefficients were used for Mn-Zn between olivine and basaltic melt (D$Mn_{ol/sil}$=1.3–1.6; D$Zn_{ol/sil}$=1.5–2.2; e.g., Kohn and Schofield, 1994; Table 3.1). We applied relatively simple conditions, using the AFC equation from DePaolo (1981), to calculate the incremental Mn-Zn enrichment of the residual melt (C_L) adding 10% of a potential contaminant (20,000 ppm Mn and 250 ppm Zn) to a silicate melt at 25% crystallization (Fig.3.10C–D, 3.11C–D). The Mn-Zn variations with depth

(Fig.3.5E–F and 3.6E–F) indicate the limited extent of this contaminated melt and gneissic fragment mixture. With increasing depth in the BBS (e.g., 609m to 651m in VB266), Mn and Zn contents in olivine increase from 4,000 to a maximum of ~9,000 ppm (subsolidus enrichment not considered), and 420 to 680 ppm, respectively. The Fo content, on the other hand, remains stable at close to Fo62. This implies that even though the Fe content of the melt was fairly homogeneous, the Mn and Zn concentrations were able to increase strongly with depth. The implied increased availability of Mn and Zn in the BBS magma is also consistent with the observed Mn-Zn enrichment of hercynite from the Reid Brook Zone to the EDI (Li and Naldrett, 2000).

The enderbitic orthogneiss (±Nain orthogneiss at depth) and the Tasiuyak paragneiss – the host rocks of the Eastern and Western Deeps Intrusions, respectively – can be considered as potential contaminants. The enderbitic orthogneiss suite (referred to as metaplutonic rocks by Rawlings-Hinchey et al., 2003) contains average Mn and Zn concentrations of 790 ppm Mn and 40 ppm Zn, respectively (Rawlings-Hinchey et al., 2003). However, especially along their western contact with the Nain orthogneiss, intercalations of presumably Tasiuyak paragneiss occur (Rawlings-Hinchey et al., 2003). Some orthogneiss samples, particularly from the Nain orthogneiss, have very high Mn contents (up to 4.5 wt.% MnO, up to 200 ppm Zn; Vale, unpublished data). The Tasiuyak paragneiss on the other hand contains less Mn (~570 ppm Mn; Thériault and Ermanovics, 1997), but more Zn (~140 ppm Zn; Vale, unpublished data). Consequently, the enderbite and Nain orthogneisses are regarded as the most likely source of Mn. Zinc on the contrary might have been supplied primarily by the Tasiuyak paragneiss – with Zn presumably

concentrated in the most pelitic, sulfide-rich intervals. Again, only a minor increase of Zn in the silicate melt (from 140 ppm in the parental melt to 250 ppm in the contaminated melt) seems to have been sufficient to generate the elevated values observed in the BBS olivine, because partition coefficients for both Mn and Zn gradually increase with melt SiO_2 (Kohn and Schofield, 1994).

The chemical trends of olivine from the BBS may reflect crystallization from a melt that became enriched in Mn and Zn in several stages – thermal constraints favor an initial contamination by enderbite and Nain orthogneiss (~54 wt.% SiO_2; Rawlings-Hinchey et al., 2003), followed by a progressively more significant input from the entrained Tasiuyak paragneiss fragments (~66 wt.% SiO_2; Thériault and Ermanovics, 1997; Ryan, 2000), as indicated by the higher degree of xenolith reaction from the WDI towards the EDI (Li and Naldrett, 2000). This later stage may have been penecontemporaneous with the entry of fragment-laden magmas near the base of the EDI. The final enrichment of olivine in Mn (±Zn) occurred after crystallization, by solid-liquid diffusion with surrounding sulfide melt. The near symmetrical zonation patterns (Fig.3.4) for one olivine from VB266-43 demonstrates a core-rim increase of up to 3,500 ppm Mn (and a less-pronounced decrease in Ni and Co). BBS olivine grains were hence further enriched in Mn beyond their already high background concentration (~8,000 ppm), whereas Fe-Mg-Zn remained largely unaffected. Modeling of Mn diffusion profiles (vertical and horizontal; Fig.3.4) based on Fick's Second Law of diffusion (e.g. Petry et al., 2004; Costa and Dungan, 2005) predicts an equilibration time span between ~30 yrs to ~160 yrs at 1,100°C and 1,000°C, respectively (Fig.3.4; for calculation see Appendix 6.3.). Even at temperatures

below 1,000°C this number will probably remain <1,000 yrs, which is similar to the time calculated for oxygen isotope homogenization of corundum-hercynite pairs (as part of the BBS xenolith inclusion mineral assemblage; Mariga et al., 2006b).

Sulfide saturation and sulfide segregation appears to have occurred after crystallization of olivine commenced, perhaps contemporaneous with the BBS intrusion into the EDI. BBS olivine still has relatively high Ni and Co concentrations (albeit with a core-rim decrease) relative to their Fo content, implying that most of the Ni and Co was already partitioned into olivine before sulfide saturation. During subsequent immersion in sulfide, only minor amounts of Ni could diffuse out of the olivine (Fig.3.4), emphasizing that the diffusion process is rather ineffective in upgrading the metal tenor of a surrounding sulfide liquid at this stage of petrogenesis. This effect may have limited the tenor of the associated massive sulfides at the base of the EDI (3–4 wt.% Ni; Lightfoot et al., 2012).

3.4.2.2. Trapped Silicate Liquid Shift

Substantial influence of the trapped silicate liquid shift (TLS) (e.g., Barnes, 1986; Chalokwu and Grant, 1987; Li and Naldrett, 1999) on the Mn-Zn composition of BBS olivine is considered improbable based on several observed characteristics. All measured olivine gains in the BBS display a zonation in Mn (±Zn) (and to a variable degree in Co and Ni; Fig.3.4), but not in Fe (or generally the Fo content). However, bivalent trace (Mn, Zn) and major (Mg, Fe) elements diffuse at similar rates within the olivine structure (Ito et al., 1999; Costa and Chakraborty, 2004; Petry et al., 2004; Costa and Dungan, 2005) and thus chemical homogenization of BBS olivine should have been achieved quasi-

simultaneously during the cooling interval of the EDI. This chemical zonation is also most prominent in olivine that is partly or completely immersed in sulfide, or shows textural signs of resorption (Fig.3.3G–H, Fig.3.4). The morphological differences indicate that at least two generations of olivine crystals are present in the BBS (Fig.3.13); a first generation that likely crystallized early (stage 1) and was transported through the magma conduit before it was partly dissolved (embayment through corrosion) by the increasingly contaminated and differentiated silicate melt (stage 2) (Tsuchiyama, 1986; Boudier, 1991) (Fig.3.13A), and a second generation that was enclosed by sulfide liquid after crystallization from the differentiated silicate melt (stage 1) and thus preserved in euhedral form (stage 2) (Fig.3.13B). Sulfide liquids have a limited tendency to percolate through partially crystallized zones (Barnes et al., 2008) and tend to accumulate only after transport through a magma conduit (Bremond d'Ars et al., 2001). As a result, the euhedral olivine likely crystallized upon entering the EDI and was enclosed when the entrained sulfides accumulated at the base of the intrusion. The BBS is therefore not a cumulate *sensu stricto*, but rather a section of highly mixed, sulfide- and xenolith-rich magmatic breccia, containing silicates that mostly crystallized during transport through the conduit rather than *in situ* in a static chamber (Li et al., 2000). We propose that the Mn-Fe-Zn enrichment of the BBS olivine is directly associated with the increasing assimilation of gneissic country rock, and a subsequent solid-liquid diffusive trace element exchange with the enclosing sulfide liquid resulted in further enrichment in Mn ($\pm$Zn) and depletion in Co and Ni of olivine rims, evident by their incongruent zonation (Fig.3.13A–B).
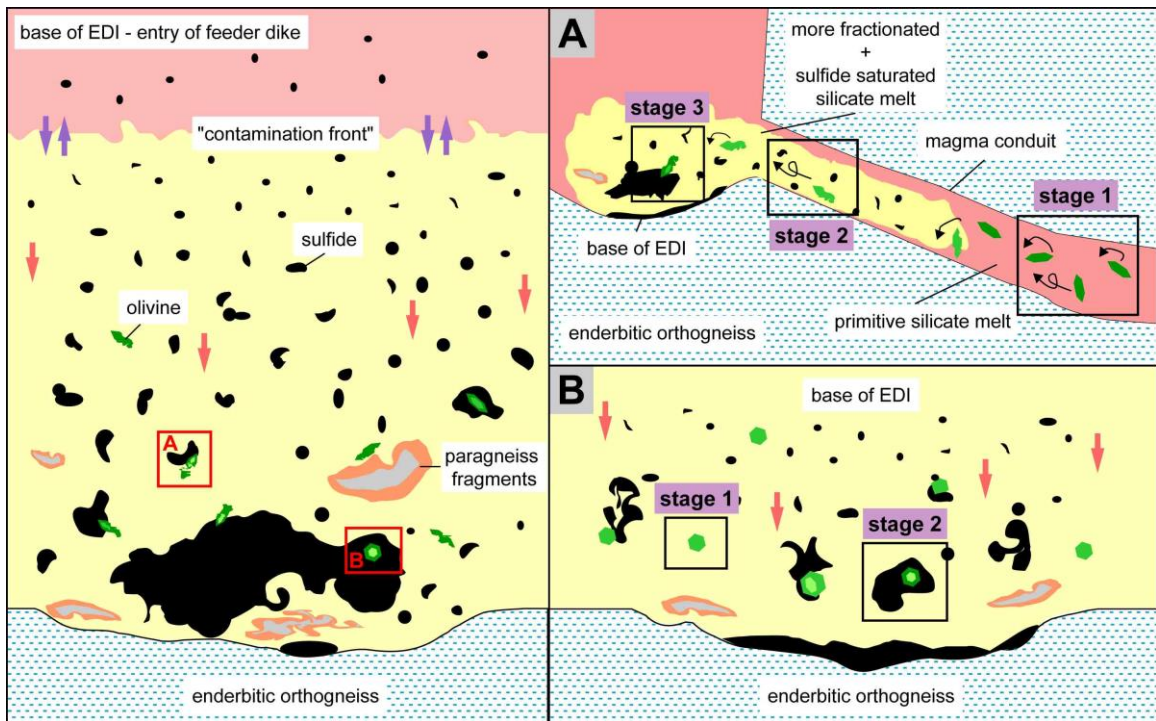
Fig. 3.13: Left Panel. Simplified schematic geological model for the basal area where the feeder dike enters the EDI. Entrained sulfide droplets (black) settle and accumulate (red arrows) at the base of the EDI. At least two generations of olivine crystals (green) interact (A) and precipitate (B) from contaminated and sulfide-rich melt. A (several?) meter-thick "contamination front" develops at the boundary between the BBS and the lower VTT with limited element exchange (purple arrows). Panels A)–B). Schematic models for the formation of the two texturally different olivine generations – Stage 1: crystallization; Stage 2: transport and interaction with more fractionated silicate melt; Stage 3: interaction and reequilibration with (partly) enclosing sulfide liquid.

3.5. Genetic Model for the Compositional Variations in EDI Olivine

Figure 3.14 is a schematic representation of a conceptual section through the VBI, summarizing our interpretation of the timing of magmatic events in parts of the upper troctolitic unit (NT) and brecciated basal margin (BBS) of the EDI (Fig.3.14A–B) based on olivine trace element data. The magmatic sequence commenced with the emplacement of parts of the olivine gabbro (OG) unit at the top of the EDI, which were likely forced upwards and disrupted by subsequent pulse(s) of primitive troctolitic melt (containing olivine of relative homogeneous composition; Fig.3.14A). Suspended in the primitive troctolite melt were also fragments of serpentinized ultramafic material (up to several m), represented by the melatroctolite sample in VB544 that contains olivine compositionally similar to primitive mantle olivine. Other ultramafic intervals in the upper troctolite unit in VB266 (130m; Li et al., 2000; Lightfoot et al., 2012) might be of similar origin, and all are certainly derived from an earlier magmatic event. The presence of geochemically distinct olivine in the melatroctolite intervals high in the EDI stratigraphy compared to the ultramafic inclusions in the BBS also supports the recent idea that multiple magma conduits (Fig.3.14) transported the troctolitic melt(s) upwards, after branching off from the WDI or another concealed lower chamber (Lightfoot and Evans-Lamswood, 2012). Subsequently, pulses of more primitive (Ni-rich olivine interval) and chalcophile-depleted (Ni-poor interval) magma intruded episodically and promoted limited trace element exchange through mixing and mingling of trapped silicate and sulfide liquids in the partially crystallized zones (Fig.3.14A). Since both intervals are bracketed by NT containing olivine of more uniform Ni composition (~1,400 ppm Ni), sulfide saturation

events must have occurred more frequently than previously thought, and in response to episodic contamination and silicate magma mixing (Scoates and Mitchell, 2000). The compositional diversity in olivine indicates that sulfides likely segregated from localized melt volumes (lower chamber – conduit(s) – upper chamber) and systematically depleted aliquots of mafic melt at varying R-factors, preceding or contemporaneous with olivine precipitation. With reference to the heterogeneity of olivine compositions, the difference in sulfide Ni (and Co) tenors between disseminated and massive sulfide mineralization (Evans-Lamswood et al., 2000; Lightfoot et al., 2012) might reflect not only variations in the R-factor, but also a contrasting point of origin of the sulfides in the VBI system (e.g., Ripley et al., 1999, 2000).

Subsequent to the emplacement of the thick sequence of NT and VTT (Fig.3.14A), a final pulse of more contaminated mafic melt, carrying sulfides, recrystallized fragments of Tasiuyak paragneiss and reequilibrated ultramafic fragments, was transported upwards and intruded along the basal contact of the EDI, forming the BBS, and inducing a several meter-thick "contamination front" (contaminated silicate melt circulating through intragranular space) at the contact with the VTT. Upon entering the chamber, most of the entrained sulfides delivered with this pulse coalesced and rapidly accumulated as massive and semi-massive sulfides in a depression close to the bottom of the EDI. The gradual transition downward from the lower, weakly mineralized part of the VTT into the heavily mineralized BBS is marked by morphologically different olivine with progressively higher concentrations of Mn-Fe-Zn, which likely reflects continued olivine crystallization from an increasingly contaminated and sulfide-rich melt (Fig.3.14B). A subsolidus,

diffusive trace element exchange between olivine and surrounding sulfide melt further enriched or depleted individual olivine grains.
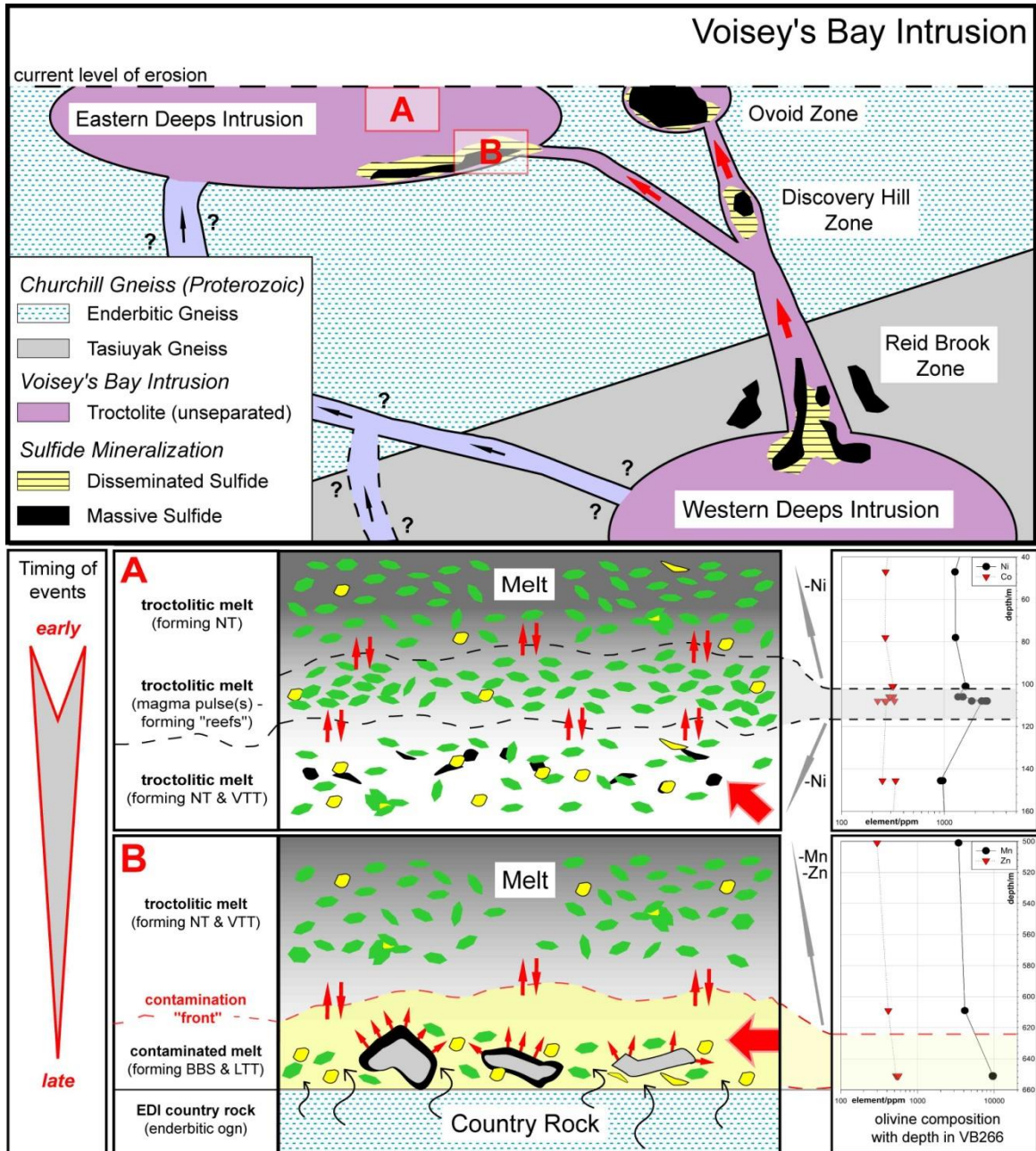
Fig. 3.14: Upper Panel. Simplified schematic conceptual model for the VBI showing the location of mineralization with respect to the chamber and conduit system (modified after Lightfoot et al., 2012). Panels A)–B). Schematic models for the formation of the intervals in the NT unit and the trace element-rich

BBS olivine at the basal margin of the EDI derived from observations of the olivine chemistry (insets on the right display the olivine composition with depth in VB266). Graphics denote olivine crystals (green), entrained sulfide liquid (yellow) and Fe-Ti oxides (black). Large red arrows indicate the inferred inflow direction of the melt/crystal mixture. Small red arrows imply a limited trace element exchange (mainly through magma mixing) between the different mafic magma pulses in the NT (through peritectic reaction – Fig.1.4), and the incorporated paragneiss fragments and the host enderbitic orthogneiss with the contaminated melt (BBS).

3.6. Application to Mineral Exploration

The trace element data indicate that the observed variations in olivine composition within the EDI are diagnostic of the stratigraphic position, the olivine host lithology, and the proximity to massive sulfide (Fig.3.5−3.7 and 3.9). The enrichment of Mn-Zn in olivine, which extends well above the basal massive sulfide layer and the BBS into the lower VTT (Fig.3.9), implies the utility of these elements, in particular, as first order indicators of proximity to economic ore mineralization (implying threshold values in Mn-Zn for prospective VTT and BBS olivine). Figure 3.9 demonstrates that the olivine Mn-Zn contents routinely increase with proximity to massive sulfide ore in the EDI. The visible increase in Mn-Zn concentrations in olivine from the studied DDH starts at less than 450m proximity (RVP of 0.4) to massive sulfide (Fig.3.9). However, this simple bi-element signature can be ambiguous; as some olivine from less mineralized OG-VTT-BBS intervals (specifically from VB451) can also contain elevated Mn-Zn contents. For this reason, the Mn-Zn data must be augmented with Cr-Co-Ni data to provide a second level of discrimination – which will objectively eliminate olivine from olivine gabbro and normal troctolite (OG-NT). In a final step, a predicted RVP factor of remaining

prospective olivine can be *calculated* based on a multiple, full-model regression analyses including V-Cr-Mn-Fe-Co-Ni-Zn (see Appendix 6.4). Only olivine from VB266-VB544-VB552 was used to calculate the coefficients of the initial regression, which yields a R^2=0.78. Olivine with a high probability of being in the vicinity to massive sulfide has a *calculated* RVP (see Table 3.1) of ≥0.5 (in VTT) and ≥0.8 (in BBS). This effectively eliminates the VTT samples (RVP <0.5; Table 3.1) that fall in the green field in Figure 3.9. However, the BBS sample VB451-7 has a calculated RVP (0.5) similar to that of BBS sample VB266-12 (0.5), even though VB266 intersects massive sulfide, and VB451 does not. In this case the stratigraphic position in the BBS interval is vital – VB266-12 samples the uppermost part of the first BBS occurrence in VB266, whereas VB451-7 is from the lowest part of the BBS interval in VB451, close to the contact with enderbitic orthogneiss. The BBS sample from VB266 thus implies a higher probability of intersecting massive sulfide mineralization further downhole than the BBS sample from VB451.

The application of the multi-trace element signature (V-Cr-Mn-Fe-Co-Ni-Zn) of olivine in the EDI, may thus be used in conjunction with petrographic observation and the exact stratigraphic position of the sample within the specific host unit (e.g., upper BBS versus lower BBS), and will be most useful for DDH that terminate blindly in the VTT or BBS, to potentially predict if massive sulfide mineralization is expected in the proximity of the DDH terminus.

3.7. Summary and Conclusions

(1) SIMS trace element measurements of olivine (V, Cr, Mn, Fe, Co, Ni, Zn, Sr, and Y) significantly expand and refine the information provided by traditional microanalysis using EPMA (Fo, Ni).

(2) Olivine in the BBS enclosed by sulfides is compositionally zoned in some elements (Mn>Ni>Co). Modeling of the Mn-Ni diffusion profiles indicates an immersion time of olivine in the sulfide melt of <<1,000 yrs, likely during cooling and accumulation of sulfides at the base of the EDI.

(3) Horizons of Ni-rich olivine in the NT likely precipitated from a primitive, sulfide undersaturated parental magma, whereas intervals of Ni-poor olivine crystallized after a batch of magma with a higher degree of differentiation experienced sulfide saturation and segregation that depleted the silicate melt in chalcophile elements (Ni>Co). Parts of this enriched sulfide fraction might now be preserved in the high Ni tenor disseminated sulfide mineralization in the lower VTT. These observations imply that discrete sulfide saturation events were more numerous than previously inferred in the VBI.

(4) Increasing Mn-Fe-Zn concentrations in olivine from the lower VTT, which continue into the ore-hosting BBS in the EDI, are gradational and likely reflect olivine

crystallization from a increasingly country rock-contaminated, sulfide-saturated silicate melt, and subsequent trace element exchange with enclosing sulfide liquid.

(5) Olivine associated with the lower tenor massive sulfides in the BBS displays the highest values of Mn and Zn, whereas olivine with elevated concentrations of these same elements is associated with the high tenor disseminated sulfide within the lower VTT.

(6) The chemical composition (V-Cr-Mn-Fe-Co-Ni-Zn) of olivine from the EDI provides a potential vector for mineral exploration in terms of establishing the relative vertical proximity (up to 150m scale) to the economic massive sulfide mineralization associated with the contaminated BBS in the EDI. This may be particularly valuable when assessing exploration DDH that terminate blindly within the VTT lithology.

(7) The olivine data support the interpretation that the EDI formed as part of an episodic, open-system magma conduit, in which successive injections of compositionally diverse mafic magma – some more differentiated and sulfide saturated and others more primitive and sulfide undersaturated – intruded into the EDI. A series of early pulses formed the upper troctolite sequence (NT and upper part of VTT). Subsequent silicate magma injections became progressively richer in sulfide and entrained gneissic fragments (lower part of VTT), before ultimately the fragment-laden and sulfide-rich BBS was injected, concluding the magmatic sequence preserved in the

EDI. Some of our observations also support the possibility of multiple magma conduits having fed the EDI during its formation.

3.8. References

Amelin, Y., Li, C., Naldrett, A.J., 1999. Geochronology of the Voisey's Bay intrusion, Labrador, Canada, by precise U-Pb dating of coexisting baddeleyite, zircon, and apatite. Lithos 47, 33–52.

Amelin, Y., Li, C., Valeyev, O., Naldrett, A.J., 2000. Nd-Pb-Sr isotope systematics of crustal assimilation in the Voisey's Bay and Mushuau intrusions, Labrador, Canada. Economic Geology 95, 815–830.

Andrews, M.S., Ripley, E.M., 1989. Mass transfer and sulfur fixation in the contact aureole of the Duluth complex, Dunka Road Cu–Ni deposit, Minnesota. Canadian Mineralogist 27, 293–310.

Arndt, N.T., Lesher, C.M., Czamanske, G.K., 2005. Mantle-derived magmas and magmatic Ni-Cu-(PGE) deposits. Economic Geology 100th Anniversary Volume, 5–23.

Barnes, S.J., 1986. The effect of trapped liquid crystallization on cumulus mineral compositions in layered intrusions. Contributions to Mineralogy and Petrology 93, 524–531.

Barnes, S.J., Fiorentini, M.L., Austin, P., Gessner, K., Hough, R.M., Squelch, A.P., 2008. Three-dimensional morphology of magmatic sulfides sheds light on ore formation and sulfide melt migration. Geology 36, 655–658.

Barnes, S.J., Naldrett, A.J., 1985. Geochemistry of the J-M (Howland) Reef of the Stillwater complex, Minneapolis Adit Area. I. Sulfide chemistry and sulfide-olivine equilibrium. Economic Geology 80, 627–645.

Beattie, P., 1994. Systematics and energetics of trace-element partitioning between olivine and silicate melts: Implications for the nature of mineral/melt partitioning. Chemical Geology 117, 57–71.

Beattie, P., Ford, C., Russel, D., 1991. Partition coefficients for olivine-melt and orthopyroxene-melt systems. Contributions to Mineralogy and Petrology 109, 212–224.

Bindeman, I.N., Davis, A.M. and Drake, M.J., 1998. Ion microprobe study of plagioclase-basalt partition experiments at natural concentration levels of trace elements. Geochimica et Cosmochimica Acta 62, 1,175–1,193.

Boudier, F., 1991. Olivine xenocrysts in picritic magmas. Contribution to Mineralogy and Petrology 109, 114–123.

Bougault, H., Hekinian, R., 1974. Rift valley in the Atlantic Ocean near 36 degrees 50'N; petrology and geochemistry of basalt rocks. Earth and Planetary Science Letters 24, 249–261.

Bremond d'Ars, J., Arndt, N.T., Hallot, E., 2001. Analog experimental insights into the formation of magmatic sulfide deposits. Earth and Planetary Science Letters 186. 371–381.

Brenan, J.M., Caciagli, N.C., 2000. Fe–Ni exchange between olivine and sulfide liquid: Implications for oxygen barometry in sulfide-saturated magmas. Geochimica et Cosmochimica Acta 64, 307–320.

Campbell, I.H., Naldrett, A.J., 1979. The influence of silicate:sulfide ratios on the geochemistry of magmatic sulfides. Economic Geology 74, 1503–1505.

Chalokwu, C.I., Grant, N.K., 1987. Reequilibration of olivine with trapped liquid in the Duluth complex, Minnesota. Geology 15, 71–74.

Clark, T., Naldrett, A.J., 1972. The distribution of Fe and Ni between synthetic olivine and sulfide at 900°C, Economic Geology 67, 939–952.

Condie, K.C., 1993. Chemical composition and evolution of the upper continental crust: contrasting results from surface samples and shales. Chemical Geology 104, 1–37.

Costa, F., Chakraborty, S., 2004. Decadal time gaps between mafic intrusion and silicic eruption obtained from chemical zoning patterns in olivine. Earth and Planetary Science Letters 227, 517–530.

Costa, F., Dungan, M., 2005. Short time scales of magmatic assimilation from diffusion modeling of multiple elements in olivine. Geology 33, 837–840.

De Hoog, J.C.M., Gall, L., Cornell, D.H., 2010. Trace-element geochemistry of mantle olivine and application to mantle petrogenesis and geothermobarometry. Chemical Geology 270, 196–215.

DePaolo, D.J., 1981. Trace element and isotopic effects of combined wallrock assimilation and fractional crystallization. Earth and Planetary Science Letters 53, 189–202.

Duke, J.M., 1976. Distribution of the period four transition elements among olivine, calcic clinopyroxene and mafic silicate liquid; experimental results. Journal of Petrology 17(4): 499–521.

Emslie, R.F., Hamilton, M.A., Thériault, R.J., 1994. Petrogenesis of a mid-Proterozoic anorthosite-mangerite-charnockite-granite (AMCG) complex: Isotopic and chemical evidence from the Nain Plutonic Suite. Journal of Geology 102, 539–558.

Evans-Lamswood, D.M., Butt, D.P., Jackson, R.S., Lee, D.V., Muggridge, M.G., Wheeler, R.I., Wilton, D.H.C., 2000. Physical controls associated with the distribution of sulfides in the Voisey's Bay Ni-Cu-Co deposit, Labrador. Economic Geology 95, 749–769.

Ewart, A. and Griffin, W.L., 1994. Application of proton-microprobe data to trace-element partitioning in volcanic rocks. Chemical Geology 117, 251–284.

Fleet, M.E., MacRae, N.D., Osborne M.D., 1981. The partition of Ni between olivine, magma and immiscible sulfide liquid. Chemical Geology 32, 119–127.

Fleet, M.E., MacRae, N.D., 1983. Partition of Ni between olivine and sulfide and its application to Ni-Cu sulfide deposits. Contribution to Mineralogy and Petrology 83, 75–83.

Gaetani, G.A. and Grove, T.L., 1997. Partitioning of moderately siderophile elements among olivine, silicate melt, and sulfide melt: Constraints on core formation in the Earth and Mars. Geochimica et Cosmochimica Acta 61, 1,829–1,846.

Grant, N.K., Chalokwu, C.I., 1992. Petrology of the Partridge River Intrusion, Duluth complex, Minnesota: II. Geochemistry and strontium isotope systematics in drill core DDH-221. Journal of Petrology 33, 1007–1038.

Hart, S.R., Davis, K.E., 1978. Nickel partitioning between olivine and silicate melt. Earth and Planetary Science Letters 40, 203–290.

Hervig, R.L., Mazdab, F.K., Williams, P., Guan, Y., Huss, G.R., Leshin, L.A., 2006. Useful ion yields for Cameca IMS 3f and 6f SIMS: Limits on quantitative analysis. Chemical Geology 227, 83–99.

Holzheid, A., Palme, H., Chakraborty, S., 1997. The activities of NiO, CoO and FeO in silicate melts. Chemical Geology 139, 21–38.

Huminicki, M.A.E., Sylvester, P.J., Shaffer, M., Wilton, D.H.C., Evans-Lamswood, D., Wheeler, R.I., 2011. Systematic and integrative ore characterization of massive sulfide deposits: An example from Voisey's Bay Ni-Cu-Co Ovoid orebody, Labrador, Canada. Exploration and Mining Geology, 20, 53–86.

Irvine, T.N., 1975. Crystallization sequences of the Muskox intrusion and other layered intrusions: II. Origin of chromitite layers and similar deposits of other magmatic ores. Geochimica et Cosmochimica Acta 39, 991–1020.

Irvine, T.N., 1977. Origin of chromitite layers in the Muskox intrusion and the other stratiform intrusions: A new interpretation. Geology 5, 273–277.

Ito, M., Yurimoto, H., Morioka, M., Nagasawa, H., 1999. Co^{2+} and Ni^{2+} diffusion in olivine determined by secondary ion mass spectrometry. Physics and Chemistry of Minerals 26, 425–431.

Jang, Y.D., Naslund, H.R., McBirney, A.R., 2001. The differentiation trend of the Skaergaard intrusion and the timing of magnetite crystallization: iron enrichment revisited. Earth and Planetary Science Letters 189, 189–196.

Jones, R.H., Layne, G.D., 1997. Minor and trace element partitioning between pyroxene and melt in rapidly cooled chondrules. American Mineralogist 82, 534–545.

Keays, R.R., 1995. The role of komatiitic and picritic magmatism and S-saturation in the formation of ore deposits. Lithos 34, 1–18.

Keays, R.R., Lightfoot, P.C., 2010. Crustal sulfur is required to form magmatic Ni–Cu sulfide deposits: evidence from chalcophile element signatures of Siberian and Deccan Trap basalts. Mineralium Deposita 45, 241–257.

Klemme, S., Gunther, D., Hametner, K., Prowatke, S. and Zack, T., 2006. The partitioning of trace elements between ilmenite, ulvospinel, armalcolite and silicate melts with implications for the early differentiation of the moon. Chemical Geology 234, 251–263.

Kloeck, W. and Palme, H., 1988. Partitioning of siderophile and chalcophile elements between sulfide, olivine, and glass in a naturally reduced basalt from Disko Island, Greenland. In: Proceedings of the Lunar and Planetary Science Conference 18, Ryder, G. (eds.), 471–483.

Kohn, S.C., Schofield, P.F., 1994. The importance of melt composition in controlling trace-element behaviour: an experimental study of Mn and Zn partitioning between forsterite and silicate melts. Chemical Geology 117, 73–87.

Lambert, D.D., Frick, L.R., Foster, J.G., Li, C., Naldrett, A.J., 2000. Re-Os isotope systematics of the Voisey's Bay Ni-Cu-Co magmatic sulfide system, Labrador, Canada: II. Implications for parental magma chemistry, ore genesis, and metal redistribution. Economic Geology 95, 867–888.

Li, C., Lightfoot, P.C., Amelin, Y., Naldrett, A.J., 2000. Contrasting petrological and geochemical relationships in the Voisey's Bay and Mushuau intrusions, Labrador, Canada: implications for ore genesis. Economic Geology 95, 771–799.

Li, C., Naldrett, A.J., 1999. Geology and petrology of the Voisey's Bay intrusion: Reaction of olivine with sulphide and silicate liquids. Lithos 47, 1–31.

Li, C., Naldrett, A.J., 2000. Melting reactions of gneissic inclusions with enclosing magma at Voisey's Bay, Labrador, Canada: Implications with respect to ore genesis. Economic Geology 95, 801–814.

Li, C., Naldrett, A.J., Ripley, E.M., 2001. Critical factors for the formation of a nickel-copper deposit in an evolved magma system: lessons from the comparison of the Pants Lake and Voisey's Bay sulfide occurrences in Labrador, Canada. Mineralium Deposita 36, 85–92.

Li, C., Naldrett, A.J., Ripley, E.M., 2007. Controls on the Fo and Ni contents of olivine in sulfide-bearing mafic/ultramafic intrusions: Principles, modeling, and examples from Voisey's Bay. Earth Science Frontiers 14, 177–185.

Li, C., Ripley, E.M., Maier, W.D., Gromwe, T.E.S., 2002. Olivine and sulfur isotope compositions of the Uitkomst Ni–Cu sulfide ore-bearing complex, South Africa:

evidence for sulfur contamination and multiple magma emplacements. Chemical Geology 188, 149–159.

Li, C., Ripley, E.M., Naldrett, A.J., 2003a. Compositional variations of olivine and sulfur isotopes in the Noril'sk and Talnakh Intrusions, Siberia: Implications for ore-forming processes in dynamic magma conduits. Economic Geology 98, 69–86.

Li, C., Ripley, E.M., Mathez, E.A., 2003b. The effect of S on the partitioning of Ni between olivine and silicate melt in MORB. Chemical Geology 201, 295–306.

Li, C., Xu, Z., de Waal, S.A., Ripley, E.M., Maier, W.D., 2004. Compositional variations of olivine from the Jinchuan Ni–Cu sulfide deposit, western China: implications for ore genesis. Mineralium Deposita 39, 159–172.

Lightfoot, P.C., Evans-Lamswood, D.M., 2012. Magma chamber geometry and the localization of Ni-Cu±(PGE) sulphide mineralization: Global examples and their relevance to Voisey's Bay. GAC Program with Abstracts 35:78.

Lightfoot, P.C., Keays, R.R., Evans-Lamswood, D.M., Wheeler, R., 2012. S saturation history of Nain Plutonic Suite mafic intrusions: origin of the Voisey's Bay Ni–Cu–Co sulfide deposit, Labrador, Canada. Mineralium Deposita 47, 23–50.

Lightfoot, P.C., Naldrett, A.J., Hawkesworth, C.J., 1984. The geology and geochemistry of the Waterfall Gorge Section of the Insizwa complex with particular reference to the origin of the Nickel sulfide deposits. Economic Geology 79, 1857–1879.

Lightfoot, P.C., Naldrett, A.J., 1999. Geological and geochemical relationships in the Voisey's Bay Intrusion, Nain Plutonic Suite, Labrador, Canada. In Dynamic processes in magmatic ore deposits and their application in mineral exploration (Keays, R.R.,

Lesher, C.M., Lightfoot, P.C., Farrow, C.E.G., eds.). Geological Association of Canada Short Course Notes 13, 1–30.

Maclean, W.H. and Shimazaki, H., 1976. The partition of Co, Ni, Cu and Zn between sulfide and silicate liquids. Economic Geology 71, 1,049–1,057.

Maier, W.D., Barnes, S.J., de Waal, S.A., 1998. Exploration for magmatic Ni-Cu-PGE sulphide deposits: a review of recent advances in the use of geochemical tools, and their application to some South African ores. South African Journal of Geology 101, 237–253.

Maier, W.D., Barnes, S.J., Sarkar, A., Ripley, E., Li, C., Livesey, T., 2010. The Kabanga Ni sulfide deposit, Tanzania: I. Geology, petrography, silicate rock geochemistry, and sulfur and oxygen isotopes. Mineralium Deposita 45, 419–441.

Mariga, J., Ripley, E.M., Li, C., 2006a. Oxygen isotopic studies of the interaction between xenoliths and mafic magma, Voisey's Bay Intrusion, Labrador, Canada. Geochimica et Cosmochimica Acta 70, 4977–4996.

Mariga, J., Ripley, E.M., Li, C., McKeegan, K.D., Schmidt, A., Groove, M., 2006b. Oxygen isotopic disequilibrium in plagioclase–corundum–hercynite xenoliths from the Voisey's Bay Intrusion, Labrador, Canada. Earth and Planetary Science Letters 248, 263–275.

Mavrogenes, J.A., O'Neill, H.S.C., 1999. The relative effects of pressure, temperature and oxygen fugacity on the solubility of sulphide in mafic magmas. Geochimica et Cosmochimica Acta 63, 1173–1180.

Naldrett, A.J., 1997. Key factors in the genesis of Noril'sk, Sudbury, Jinchuan, Voisey's Bay and other world-class Ni-Cu-PGE deposits: Implications for exploration. Australian Journal of Earth Sciences 44, 283–315.

Naldrett, A.J., 1999. World-class Ni-Cu-PGE deposits: key factors in their genesis. Mineralium Deposita 34, 227–240.

Naldrett, A.J., Singh, J., Kristic, S., Li, C., 2000. The mineralogy of the Voisey's Bay Ni-Cu-Co deposit, northern Labrador, Canada: Influence of oxidation state on textures and mineral compositions. Economic Geology 95, 889–900.

Ottolini, L., Bottazzi, P., Vannucci, R., 1993. Quantification of Lithium, Beryllium, and Boron in silicates by secondary ion mass spectrometry using conventional energy filtering. Analytical Chemistry 65, 1960–1968.

Paster, T.P., Schauwecker, D.S. and Haskin, L.A., 1974. The behavior of some trace elements during solidification of the Skaergaard layered series. Geochimica et Cosmochimica Acta 38, 1,549–1,577.

Pedersen, A.K., 1979. Basaltic glass with high-temperature equilibrated immiscible sulfide bodies with native iron from Disko, central west Greenland. Contributions to Mineralogy and Petrology 69, 397–407.

Petry, C., Chakraborty, S., Palme, H., 2004. Experimental determination of Ni diffusion coefficients in olivine and their dependence on temperature, composition, oxygen fugacity, and crystallographic orientation. Geochimica et Cosmochimica Acta 68, 4179–4188.

Rajamani, V., Naldrett, A.J., 1978. Partitioning of Fe, Co, Ni, and Cu between sulfide liquid and basaltic melts and the composition of Ni-Cu Sulfide deposit. Economic Geology 73, 82–93.

Rawlings-Hinchey, A.M., Sylvester, P.J., Myers, J.S., Dunning, G.R., Kosler, J., 2003. Paleoproterozoic crustal genesis: calc-alkaline magmatism of the Torngat orogen, Voisey's Bay area, Labrador. Precambrian Research: 125, 55–85.

Ripley, E.M., 1981. Sulfur isotopic studies of the Dunka Road Cu-Ni deposit, Duluth intrusion, Minnesota. Economic Geology 76, 610–620.

Ripley, E.M., Li, C., 2003. Sulfur isotope exchange and metal enrichment in the formation of magmatic Cu-Ni-(PGE) deposits. Economic Geology 98, 635–641.

Ripley, E.M., Li, C., 2013. Sulfide saturation in mafic magmas: Is external sulfur required for magmatic Ni-Cu-(PGE) ore genesis? Economic Geology 108, 45–58.

Ripley, E.M., Li, C., Shin, D., 2002. Paragneiss assimilation in the genesis of magmatic Ni-Cu-Co sulfide mineralization at Voisey's Bay, Labrador: δ^{34}S, δ^{13}C, and Se/S evidence. Economic Geology 97, 1307–1318.

Ripley, E.M., Park, Y.R., Li, C., Naldrett, A.J., 1999. Sulfur and oxygen isotopic evidence of country rock contamination in the Voisey's Bay Ni-Cu-Co deposit, Labrador, Canada. Lithos 47, 53–68.

Ripley, E.M., Park, Y.R., Li, C., Naldrett, A.J., 2000. Oxygen isotope studies of the Voisey's Bay Ni-Cu-Co deposit, Labrador, Canada. Economic Geology 95, 831–844.

Ripley, E.M., Taib, N.I., Li, C., Moore, C.H., 2007. Chemical and mineralogical heterogeneity in the basal zone of the Partridge River Intrusion: implications for the

origin of Cu–Ni sulfide mineralization in the Duluth complex, midcontinent rift system. Contributions to Mineralogy and Petrology 154, 35–54.

Roeder, P.L., Emslie, R.F., 1970. Olivine-liquid equilibrium. Contributions to Mineralogy and Petrology 29, 275–289.

Rollinson, H.R., 1993. Using geochemical data: evaluation, presentation, interpretation. Longman, UK. 352 pp.

Ryan, B., 2000. The Nain-Churchill boundary and the Nain Plutonic Suite: A regional perspective on the geologic setting of the Voisey's Bay Ni-Cu-Co deposit. Economic Geology 95, 703–724.

Ryan, B., Wardle, R.J., Gower, C.F., Nunn, G.A.G., 1995, Nickel-copper sulfide mineralization in Labrador: The Voisey Bay discovery and its exploration implications: Newfoundland Department of Mines and Energy, Geological Survey, Current Research Rept. 95–1, 177–204.

Sato, H., 1977. Nickel content of basaltic magmas: identification of primary magmas and a measure of the degree of olivine fractionation. Lithos 10, 113–120.

Scoates, J.S., Mitchell, J.N., 2000. The evolution of troctolitic and high-Al basaltic magmas in Proterzoic anorthosite plutonic suites and implications for the Voisey's Bay massive Ni-Cu sulfide deposit. Economic Geology 95, 677–701.

Shimizu, N., Semet, M.P., Allègre, C.J., 1978. Geochemical applications of quantitative ion-microprobe analysis. Geochimica et Cosmochimica Acta 42, 1321–1334.

Sun, S.S., 1982. Chemical composition and origin of the earth's primitive mantle. Geochimica et Cosmochimica Acta 46, 179–192.

Thériault, R.J., Ermanovics, I., 1997. Sm-Nd isotopic and geochemical characterisation of the Paleoproterozoic Torngat orogen, Labrador, Canada. Precambrian Research 81, 15–35.

Tsuchiyama, A., 1986. Experimental study of olivine-melt reaction and its petrological implications. Journal of Volcanology and Geothermal Research 29, 245–264.

Tyson, R.M., Chang, L.L.Y., 1984. The petrology and sulfide mineralization of the Partridge River troctolite, Duluth complex, Minnesota. Canadian Mineralogist 22, 23–38.

Venables, A., 2003. Magmatic processes associated with the Voisey's Bay Ni-Cu-Co sulfide deposit, Labrador, Canada. Ph.D. thesis, Open University, UK, 313 pp.

Weinbruch, S., Specht, S., Palme, H., 1993. Determination of Fe, Mn, Ni and Sc in olivine by secondary ion mass spectrometry. European Journal of Mineralogy 5, 37–41.

Yurimoto, H., Yamashita, A., Nishida, N., Sueno, S., 1989. Quantitative SIMS analysis of GSJ rock reference samples. Geochemical Journal 23, 215–236.

CHAPTER 4 - Trace Element Variations in Olivine as Geochemical Signatures of Ni-Cu Sulfide Mineralization in Mafic Magma Systems – Examples from Voisey's Bay and Pants Lake Intrusions, Labrador, Canada

Florian Bulle[1*], Graham D. Layne[1]

[1]Department of Earth Sciences, Memorial University of Newfoundland, St. John's, Canada NL A1B 3X5

*Corresponding author. Fax +1-709 737 2589; Email: fbulle@mun.ca

Abstract

Olivine from the olivine-gabbro to troctolite intrusions at Voisey's Bay (VBI) and at Pants Lake (PLI), both Labrador was analyzed for multiple elements (Ca, Sc, Mg, Si, Ti, V, Cr, Mn, Fe, Co, Ni, Cu, Zn, Sr, Y, and Zr) with Secondary Ion Mass Spectrometry (SIMS). Both intrusions have similar lithologies and petrographic characteristics and are approximately coeval (1.34 Ga and 1.32 Ga, respectively) members of the Mesoproterozoic Nain Plutonic Suite (NPS). The Voisey's Bay Intrusion hosts a producing economic Ni-Cu-Co sulfide deposit. The Pants Lake Intrusion displays evidence of Ni-Cu sulfide mineralization but, to date, a viable ore deposit has not been discovered. Olivine from both barren and mineralized lithologies were analyzed to assess the potential of olivine trace element compositions for providing a record of silicate melt evolution and sulfide saturation related to ore localization.

Two detailed transects were sampled, using 5 diamond drill holes that laterally approach the basal massive sulfide occurrence in the Voisey's Bay Intrusion from the barren central part. Olivine displays distinct trace element distributions that vary coherently with host lithology and proximity to ore mineralization. In particular, olivine shows an increase in Fe (~Fo80 to ~Fo60), Mn (~2,500 to 5,000 ppm) and Zn (~280 to 700 ppm), generally coupled with a decrease in Ni (~1,600 to ~900 ppm), Co (~270 to ~190 ppm) and Cr (~110 to 45 ppm), from barren troctolite (normal troctolite – NT) and weakly mineralized troctolite (variable-textured troctolite – VTT) towards the heavily mineralized, brecciated basal succession (basal breccia sequence – BBS). The enrichment in Fe-Mn-Zn is most pronounced in samples that laterally approach, but are not directly in contact with the

massive sulfide deposit at the base of the intrusion, particularly in samples from the lower VTT and BBS lithologies.

Olivine from gabbroic lithologies within the basal gabbro (BG) and upper gabbro (UG) of the PLI are fairly homogeneous (~Fo60, ~4,300 ppm Mn, ~460 ppm Zn, ~340 ppm Ni, ~50 ppm Cr), with a more evolved composition (~2,100 ppm Ca, ~20 ppm Sc, ~300 ppm Ti, ~4 ppm Y) than the average of the VBI (~570 ppm Ca, ~6 ppm Sc, ~65 ppm Ti, ~0.3 ppm Y). PLI olivine also commonly lack the mutually Mn-Zn-rich signature of olivine from the EDI BBS that is characteristic of contamination of the parent magma by country rock gneiss, and there reflects a close proximity to massive sulfides. In conjunction with petrographic observation and the stratigraphic context, a multiple-trace element (V-Cr-Mn-Co-Ni-Zn) statistic can be applied to determine the predicted vertical and lateral proximity of measured olivine to massive sulfide mineralization in the EDI, over a distance exceeding 150m.

The presence of strongly bimodal olivine populations (primitive and evolved; Ni-rich and Ni-depleted) in the EDI – as represented by abrupt changes in, for example, the Ni-Fo composition of olivine in several upper NT intervals – indicates that multiple, successive, sulfide saturated and unsaturated magma pulses contributed to the formation of the EDI. The homogeneous, generally Ni-depleted, and more evolved olivine grains from the PLI on the other hand, likely reflect crystallization from a single pulse of more differentiated parental melt that experienced early sulfide saturation. The silicate magma episodicity in the EDI, which has not been detected within the PLI, therefore promoted a higher R-factor (integrated silicate:sulfide ratio) and the subsequent metal tenor upgrading of the

fractionated sulfide liquids. The distinct chemical variations in olivine from the economic EDI (bimodality, primitiveness) and the sub-economic PLI (homogeneous, evolved) provide potential as a regional-scale mineralogical indicator of fertility in mafic intrusions.

Keywords: Cu-Ni sulfides, melt differentiation, mafic intrusion, Eastern Deeps Intrusion, Nain Plutonic Suite, Ni-exploration

4.1. Introduction

The Voisey's Bay Ni-Cu-Co deposit is hosted by a troctolite and olivine-gabbro intrusion in the Nain Plutonic Suite (NPS), Labrador a large Mesoproterozoic AMCG (Anorthosite-Mangerite-Charnockite-Granite) intrusive complex (e.g., Emslie et al., 1994; Ryan, 2000, and references therein). Prior to the discovery of the Voisey's Bay deposit, these highly differentiated igneous systems were not widely regarded as exploration targets for magmatic Ni-Cu-Co mineralization (e.g., Scoates and Mitchell, 2000). To date, the only other notable Ni-Cu sulfide occurrence in the NPS is found in another series of troctolitic to olivine-gabbroic intrusions in the Pants Lake area, ~80 km south of the Voisey's Bay Intrusion (VBI) (e.g., Kerr, 1999; Li et al., 2001; Kerr, 2003). In addition to comparable host rocks, the VBI and the Pants Lake Intrusion (PLI) both display the presence of a country rock-contaminated basal sequence, a broadly similar style of sulfide mineralization – and both, at least in part, intrude the same sulfide-bearing Tasiuyak paragneiss unit (e.g., Lightfoot and Naldrett, 1999; Kerr, 2003). Compared to the VBI deposit ($[Ni]_{100}$=~4%; Lightfoot et al., 2012), however, the sulfide mineralization discovered by initial exploration of the PLI has lower average Ni ($[Ni]_{100}$=~2%) and Cu ($[Cu]_{100}$=<2%) tenors, with many of the massive sulfide intersections – which are generally <1m thick (Smith, 2006) – showing Ni grades of $[Ni]_{100}$=~1% (e.g., Kerr, 1999). Thus, although both intrusions display several comparable geological features, evidence of some important ore-forming processes, for example a high silicate melt to sulfide liquid ratio (R-factor; Campbell and Naldrett, 1979) and structural traps that favor dynamic accumulation of entrained sulfides (cf. perceived topology of magma conduits at

VBI; Evans-Lamswood et al., 2000; Lightfoot et al., 2012), have not yet been observed in the explored portions of the PLI (Li et al., 2001; Smith, 2006).

Other essential factors in the global exploration for magmatic sulfide deposits are the presence of an olivine-normative and chalcophile element-rich parental melt, and an interaction of this parental melt with a sulfide-rich country rock during magma ascent, allowing either assimilation of crustal sulfur, or bulk-rock silica-enriching contamination (Naldrett, 1997, 1999; Arndt et al., 2005, and references therein). Since olivine is an early crystallizing phase, and one of the major rock-forming minerals in the gabbroic rocks throughout the VBI and PLI, its chemical composition records petrogenetic processes such as melt fractionation (e.g., Roeder and Emslie, 1970; Sato, 1977), magma mixing, country rock assimilation and contamination, as well as segregation and interaction with an immiscible sulfide fraction. As a result, the composition of olivine contains valuable information about the history, and mineralization potential, of a mafic intrusion and can provide indirect indications of the presence of magmatic sulfides (e.g., Fleet and McRae, 1983; Lightfoot et al., 1984; Tyson and Chang, 1984; Barnes and Naldrett, 1985; Chalokwu and Grant, 1987; Li and Naldrett, 1999; Li et al., 2002; Li et al., 2003a; Li et al., 2004; Maier et al., 2010). The importance of olivine in tracing ore-forming processes has been established by this previous work, and its common association with magmatic Ni-Cu-Co sulfide mineralization provides a systematic petrogenetic record. Based on the synergetic behavior of Mg and Ni with progressive differentiation of the primitive melt (e.g., Sato, 1977), and the high sensitivity of Ni to sulfide saturation and segregation, a strong Ni depletion with respect to MgO in olivine is commonly interpreted as an

indication of an earlier removal of Ni from the silicate melt by an immiscible sulfide liquid (e.g., Hart and Davis, 1978; Rajamani and Naldrett, 1978; Fleet et al., 1981). In contrast, if olivine is later immersed in a sulfide liquid, an oxygen fugacity-dependent (fO_2) reequilibration occurs, in which Ni and Fe are exchanged, resulting in a positive correlation between the Ni and Fe concentration of the olivine (e.g., Clark and Naldrett, 1972; Fleet and McRae, 1983; Brenan and Caciagli, 2000; Brenan, 2003).

The Fo and Ni composition of VBI olivine, in particular, records fractional crystallization, sulfide saturation and isolated reequilibration, and the influence of the trapped silicate liquid shift. Previous literature data for olivine indicate that multiple pulses of compositionally diverse mafic magma contributed to the VBI, and the associated magmatic sulfide deposits (Li and Naldrett, 1999; Li et al., 2000; Venables, 2003; Chapter 3).

Our initial study of multi-trace element distribution in olivine established an olivine chemostratigraphy in a series of vertical profiles directly above the major mineralized zone in the Eastern Deeps deposit of the VBI (Chapter 3). The different styles of mineralization (disseminated versus massive) were linked to specific olivine compositions, and it was demonstrated that Mn-Zn-enrichment trends in olivine from the basal brecciated sequence, which is associated with massive sulfide mineralization, recorded their precipitation from mafic melt contaminated with country rock, and variable interaction with a contamination front that extended upwards into overlying gabbroic lithologies. The anomalous geochemical signature of olivine from mineralized units in the

VBI thus appears intimately related to ore formation, and therefore represents a potential tool for mineral exploration (Chapter 3).

Existing literature data for olivine from the PLI, on the other hand, are limited to Fo and Ni compositions, and have been interpreted as indicative of a regular silicate melt differentiation trend with an early extraction of a sulfide liquid, and possible late stage reequilibration of some olivine with sulfide melt (Li et al., 2001; Smith, 2006). Multi-trace element data for PLI olivine was generated during our current study to allow an additional means of comparison between the VBI and the PLI.

The impetus of this study is the investigation of 1) *lateral* variations in olivine composition distal to the heavily mineralized base of the Eastern Deeps zone of the VBI, in order to identify geochemical vectors and anomalies in the mainly barren overlying intrusive rocks, 2) the comparison between the multi-trace element composition of olivine from the economic VBI and the barren to sub-economic PLI to determine the geochemical signature of ore-forming processes recorded by olivine from these two separate magmatic systems, and, 3) the potential of multi-trace element analyses in olivine as a geochemical tool in regional Ni-exploration.

4.2. Geological Setting

4.2.1. Regional Geology

The VBI and PLI are mafic members of the anorogenic Mesoproterozoic Nain Plutonic Suite, which covers an area of almost 20,000 km^2 in northern Labrador (Fig.4.1A)

(Emslie et al., 1994; Ryan, 2000; Kerr, 2003). The NPS mainly consists of massive anorthosite, granite, diorite and troctolite intrusions that punctured the Paleoproterozoic Torngat orogen between ~1,350 and 1,290 Ma, as a result of limited intracontinental rifting, mantle upwelling and crustal anatexis (Emslie et al., 1994; Ryan, 2000). The Archean Nain Province, which consists mainly of amphibolitic orthogneiss with retrogressed granulite- and amphibolite-facies mineral assemblages, lies east of this tectonic boundary, whereas the mostly Paleoproterozoic Churchill Province, comprising granulite-facies pelitic paragneiss, which is locally sulfide- and graphite-bearing and commonly known as "*Tasiuyak gneiss*", and minor massive to lineated enderbitic orthogneiss ("metaplutonic rocks"; Rawlings-Hinchey et al, 2003), is situated to the west (e.g., Li and Naldrett, 1999; Ryan, 2000; Li et al., 2001).

The 1,332.7 ±1.0 Ma VBI (Amelin et al., 1999) straddles this major tectonic boundary and consists of two olivine-gabbroic to troctolitic bodies; the buried Western Deeps Intrusion (or Reid Brook Zone; RBZ) intruded into Tasiuyak gneiss, and the partly exposed Eastern Deeps Intrusion (EDI) hosted mainly in Paleoproterozoic enderbitic gneiss and Archean orthogneiss, which are linked by a partially outcropping olivine gabbro dike (Fig.4.1B) (Lightfoot and Naldrett, 1999; Evans-Lamswood et al., 2000; Lightfoot et al., 2012). Major sulfide mineralization is recognized in this gabbroic feeder dike (e.g., Reid Brook Zone, Discovery Hill) and in bulges (Ovoid) and entry points of the dike into the magma chambers (EDI) (e.g., Lightfoot and Naldrett, 1999; Evans-Lamswood et al., 2000; Lightfoot et al., 2012). Metal tenors in the sulfides vary systematically, with the highest found in a halo of disseminated mineralization in the

EDI, intermediate tenors in the massive sulfides of the EDI and the Ovoid, and the lowest in the immediate dike environment (e.g., Reid Brook Zone). These variations have been ascribed to variations in the integrated silicate:sulfide melt ratio (R-factor) during the segregation and emplacement of the immiscible sulfide liquid (Lightfoot et al., 2012).

The PLI is broadly composed of two separate intrusions, the 1,337 ±2 Ma South Intrusion and the younger 1,322.2 ±2 Ma North Intrusion (Smith, 2006, and references therein; Fig.4.1C). Both intrusions are linked by a smaller (~1km long and ~150m thick) gabbroic body known as the Worm Intrusion or Central Gabbro (Smith, 2006), which is also regarded as a southern extension of the North Intrusion (Kerr, 2003). All parts of the PLI have a horizontal to sub-horizontal sheet-like geometry (Fig.4.1C inset) and mainly intrude Tasiuyak paragneiss of the Churchill Province ~15 km west of the above mentioned major terrane junction (Kerr, 2003; Smith, 2006). The recognized sulfide mineralization is largely disseminated with small lenses of massive sulfide (generally less than 1 meter wide; Smith, 2006), and is concentrated at the base of the intrusions. The basal contact of the North Intrusion has a "mineralized sequence" containing a "leopard-textured gabbro" followed upwards by a xenolith-rich "composite gabbro", whereas the South Intrusion has an up to 50m thick zone of disseminated sulfides in the basal "melagabbro" (Kerr, 1999, 2003; Smith, 2006). Absolute metal tenors observed to date are low, implying a lower overall R-factor than at the VBI (Li et al., 2001; Kerr, 2003).
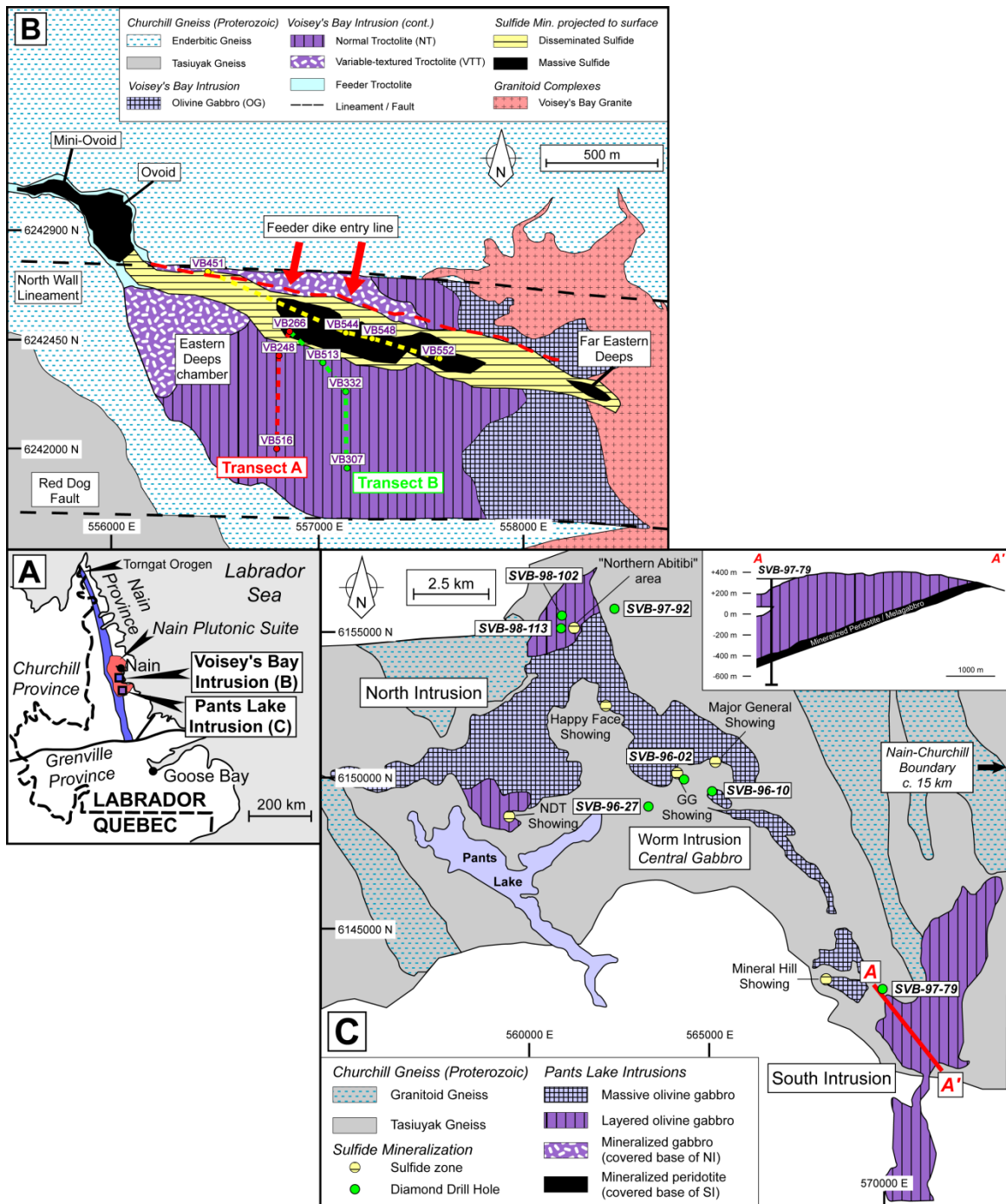
Fig. 4.1: The inset A) shows the position of the VBI and PLI in the NPS and the regional tectonic framework of coastal Labrador (after Li and Naldrett, 1999). B) Schematic geological map of the EDI in the eastern part of the VBI (modified after Lightfoot et al., 2012). The position of the sampled DDH from transects A and B is marked with red and green circles/dashes and their identification number. Yellow

circles mark sampled DDH from Chapter 3. C) Simplified geological map of the North, South and Central Intrusions of the PLI. Sampled DDH are marked with green dots and their identification number (modified after Kerr, 2003; Smith, 2006). The cross section from the South Intrusion is modified after Kerr (2003).

4.2.2. Petrology and Mineralogy

This section presents a short review of the intrusive lithologies important to this study, and highlights the key mineralogical and textural characteristics of olivine from the VBI and the PLI. Detailed petrographic descriptions of VBI and PLI lithologies are presented elsewhere (e.g., Chapter 3, Lightfoot and Naldrett, 1999; Li and Naldrett, 1999; Li et al., 2000; Lightfoot et al., 2012 for the VBI; e.g., Kerr, 1999; Kerr, 2003; Smith, 2006 for the PLI) (photomicrographs of all measured samples are also in Appendix 6.6.).

4.2.2.1. The Eastern Deeps Segment of the Voisey's Bay Intrusion

The EDI (Fig.4.1B) contains a large portion of the economically important sulfide mineralization at Voisey's Bay. Massive sulfide occurs at the base of the intrusion, where a feeder dike enters from the north, and is associated with a compacted "basal breccia sequence" (BBS), containing inclusions of ultramafic rocks (ultramafic fragments – UMF) and abundant heavily altered and reacted xenolith fragments presumed to have originated from the Tasiuyak paragneiss (Lightfoot and Naldrett, 1999; Li and Naldrett, 1999; Lightfoot et al., 2012). The BBS is overlain by a very heterogeneous (e.g., grain size, texture, inclusion content, sulfide content) "variable-textured troctolite" (VTT), which has appreciable amounts of high-Ni tenor disseminated sulfides and xenolith

inclusions close to its contact with the BBS (Lightfoot and Naldrett, 1999; Li and Naldrett, 1999; Lightfoot et al., 2012). In the upper part of the EDI, the VTT is overlain by a homogeneous, dark-grey, sulfide-poor (<2 vol.%), olivine-plagioclase cumulate of uniform texture termed "normal troctolite" (NT). The NT unit is devoid of paragneiss inclusions and is overlain by a medium- to coarse-grained olivine gabbro (OG) that contains texturally and compositionally different olivine than the underlying NT and VTT units (Li and Naldrett, 1999; Li et al., 2000; Chapter 3). Olivine from the NT and VTT is medium-grained, generally sub- to euhedral, mostly prismatic crystals (Fig.4.2A). Epitaxial overgrowths of augite (±orthopyroxene) on olivine are common, especially in the VTT, whereas green-brown hornblende and biotite mostly occur as rims on olivine in contact with sulfide and Fe-Ti oxide phases. Olivine in the BBS is fine- to medium-grained, irregular poikilitic or sub- to euhedral, and commonly embayed by alteration and resorption features where in contact with sulfide (Fig.4.2B). The UMF found in the basal part of the EDI contain olivine that range from fine- to medium-grained, pristine and euhedral cumulus crystals (Fig.4.2C) to fine-grained, strongly serpentinized, rounded grains.

4.2.2.2. The Pants Lake Intrusion(s)

The stratigraphy of the PLI is composed of several petrographically variable olivine gabbroic subunits with different texture, grain size, color etc. (Kerr, 1999; Kerr, 2003; Smith, 2006). Following the classification scheme of Smith (2006), the PLI can be subdivided into two major gabbro units, the Upper Gabbro (UG) and the mineralized

Basal Gabbro (BG), each composed of several subunits (Fig.4.1C). Despite their nominally common host and origin, the principal features of the subunits vary considerably between the North and South Intrusion, and Smith (2006) focused his detailed classification scheme solely on the North Intrusion. However, in order to keep the subdivision presented here clear and concise, it was also adopted for the South Intrusion. The UG basically comprises a coarse-grained massive olivine gabbro, found at the top of the North and Worm Intrusions, which is underlain by a finer-grained well-layered olivine gabbro. This layered olivine gabbro unit dominates the South Intrusion (Kerr, 2003; Smith, 2006). The BG occupies the basal contact of the PLI and is distinguished from the UG mainly by the presence of partially digested paragneiss inclusions (presumably of Tasiuyak origin), disseminated to semi-massive sulfide mineralization, and the appearance of olivine as a major cumulus phase in the South Intrusion. The thickness varies significantly – between 6m in parts of the North Intrusion to almost 100m in a DDH intersecting the South Intrusion (Smith, 2006).

The UG and BG have a relatively sharp contact, marked by the presence of a brecciated sequence termed "Transition Gabbro" (Smith, 2006). In contrast to the North Intrusion, the South Intrusion consists of peridotite to melagabbro cumulates in the lowermost part of the BG, which display interlayering and gradational contacts with the associated layered olivine gabbro (Kerr, 1999; Smith, 2006). Cumulus olivine is mostly sub- to euhedral (Fig.4.2F), but intercumulus olivine tends to be anhedral poikilitic or granular (Fig.4.2D). Olivine ranges from 10–15 vol.% in olivine gabbro to about 50 vol.% in melagabbro. The degree of alteration is gradational in many samples and ranges from

fresh to strongly serpentinized olivine, especially in proximity to xenolith inclusions in units from the BG (Fig.4.2E). Unlike olivine from the VBI, epitaxial overgrowth of augite (±orthopyroxene) is very rare, and the presence of green-brown hornblende and biotite as alteration products or intercumulus phases is mostly less than 2 vol.%.

4.3. Previous Studies

Previous microanalyses of olivine from the VBI indicate an extreme variability in Ni and forsterite contents (Fo). Values range from Fo42–83, with the lowest found in olivine in the feeder gabbro and the BBS, and the highest primarily in the NT. Average Ni contents range from 800–1,700 ppm, with a largely positive correlation with Fo values (Li and Naldrett, 1999; Li et al., 2000; Venables, 2003; Chapter 3). The Fo content and trace element concentration of olivine in the EDI exhibit systematic broad scale stratigraphic variations, for instance a decrease of the Fo and Ni content with depth (Li and Naldrett, 1999; Li et al., 2000; Chapter 3), whereas Mn and Zn concentrations increase downward from the NT towards the BBS (Chapter 3). The most *primitive* olivine is found in the NT (and UMF) and in an altered melatroctolite horizon encountered in the NT, whereas the most *evolved* compositions occur in the OG and the BBS (Chapter 3). Li and Naldrett (1999) suggested that the distinct composition of OG olivine (more evolved, slightly Ni depleted) indicate their derivation from an earlier magma pulse than the more primitive NT and VTT sequences, which experienced sulfide fractionation prior to final emplacement. It has also been suggested in this study that olivine with distinct trace element enrichment or depletion signatures that appear in discrete intervals within the NT

and VTT sequences of the EDI might also be related to additional discrete magma batches that experienced isolated sulfide saturation events (Chapter 3).

In summary, compositional data for olivine from the VBI have revealed important aspects of the petrogenesis and ore-forming processes, such as the differentiation and episodicity of the host gabbroic rocks, the timing and frequency of sulfide saturation events and the mineralogical signature of country rock contamination (Li and Naldrett, 1999; Li et al., 2000; Venables, 2003; Chapter 3). The relationship between olivine composition and assimilation/contamination consequently suggests a potential vector to zones of economic sulfide mineralization (Chapter 3).

Olivine from the PLI appears compositionally more homogeneous and has on average much lower Fo and Ni contents (~Fo58 with ~644 ppm Ni) (Li et al., 2001; Smith, 2006) than their VBI counterparts. In addition, systematic stratigraphic variations between olivine from different units in the intrusion (here the Upper and Basal Gabbro), as evident in NT and BBS samples from the VBI (Chapter 3), are noticeably absent in the PLI. Both UG and BG olivine display a very similar range of compositions (Fo31–48 and 63–240 ppm Ni in the UG; Fo33–58 and 76–644 ppm Ni in the BG), and these variations are generally in accord with simple fractional crystallization of olivine (Li et al., 2001; Smith, 2006). However, olivine from the sulfide-rich "leopard-textured gabbro" at the base of the North Intrusion, displays an increase in Ni with Fe content, which is attributed to a post-crystallization exchange reaction with a coexisting sulfide liquid (Li et al., 2001).
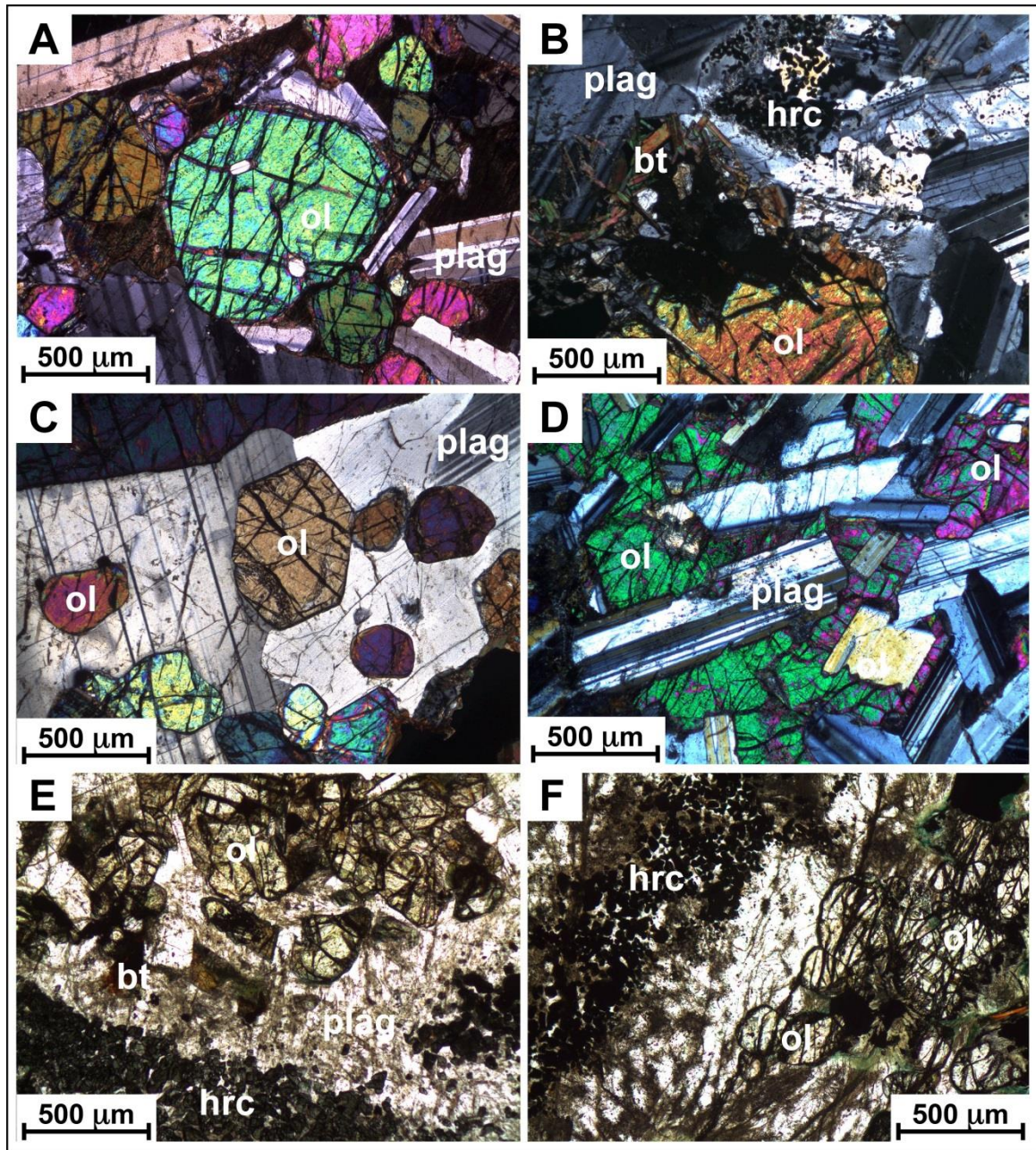
Fig. 4.2: Photomicrographs of olivine grains that are texturally characteristic of their individual lithologies. XPL (A-D) and PPL (E-F). A) to C) are from the VBI, and D) to F) are from the PLI. A) VTT from VB307-12. B) BBS with hercynite grains from VB513-24. C) Cumulus olivine in UMF from VB248-14. D) Coarse-grained gabbro with intercumulus olivine from SVB98-102-150. E) Hercynite-bearing transition gabbro from SVB96-10-91. F) Hercynite-bearing melagabbro from SVB97-79-144. See text for discussion. Key for minerals: ol=olivine, plag=plagioclase, bt=biotite, hrc=hercynite.

4.4. Scientific Approach

4.4.1. Sampling Procedure

4.4.1.1. Samples from the Eastern Deeps Intrusion

Five DDH were sampled from two roughly N-S trending transects through the EDI (Fig.4.1A). The anchor point for both transects (A and B) was DDH VB-96-266 (shortened to VB266), in the northern part of the EDI, a hole which was previously investigated in great detail for whole-rock geochemistry (Li et al., 2000; Lightfoot et al., 2012) and olivine composition (Li and Naldrett, 1999; Li et al., 2000; Chapter 3). Except for VB266, none of the DDH sampled directly intersect the massive sulfide body or the halo of disseminated sulfide at the base of the EDI – VB266 is therefore regarded as the endpoint of a potential geochemical vector towards mineralization.

Transect A trends N-S (Fig.4.1A) and comprises 18 samples from 2 DDH (VB-96-248 and VB-99-516). The geometry of the EDI (steep north wall with a more gently north-dipping southern margin) dictates that both of these DDH intersect NT at their tops, followed by a variably thick VTT interval, in which the furthest south DDH VB516 terminates, whereas VB248 also intersects the BBS close to the center of the chamber.

Transect B trends NW-SE (Fig.4.1A) comprises 37 samples from 3 DDH (VB-99-513, VB-96-332 and VB-96-307). Similar to Transect A, the DDH furthest to the south (VB307) only intersects NT and VTT, whereas VB332 also contains sporadic OG intervals, and VB513 samples an ultramafic (dunite to melatroctolite) interval and terminates in the BBS.

In all DDH, olivine-bearing lithologies were sampled from top to end of hole to provide the high sample resolution required to identify geochemical trends and to allow a potential spatial connection of intervals with anomalous olivine compositions, especially to those that were previously identified in a central vertical transect of the EDI (Chapter 3). Both transects were specifically selected to move laterally away from the major mineralized horizon in the EDI, since a primary objective was the identification of variable olivine signatures in the sulfide-poor chamber troctolites (NT and VTT), which might be used as a potential exploration vector towards substantial sulfide mineralization.

4.4.1.2. Samples from the Pants Lake Intrusions

Samples from the PLI were made with permission of Mr. Rod Smith from off-cuts from his 2006 study. The sample numbers and codes were also kept consistent with those in Smith (2006). In total 12 samples, from 7 DDH, were utilized for olivine analyses. Figure 4.1B shows the locations and identification codes of the sampled DDH. Samples were taken from throughout the PLI, with 8 from the North Intrusion, 2 from the Worm Intrusion (Central Intrusion) and 2 from the South Intrusion – representing both Upper (fine- to coarse grained olivine gabbro and transition gabbro) and Basal Gabbro subdivisions. Specific samples with textural features comparable to VBI rocks, especially from xenolith inclusion-rich mineralized sequences in the North and South Intrusion (BG and melagabbro) of the PLI, were selected. These sample selections were designed to determine how olivine trace element compositions from lithologies associated with economic mineralization at the VBI compare with those at the PLI.

4.4.2. Analytical Methods

4.4.2.1. Secondary Ion Mass Spectrometry (SIMS)

Olivine major and trace element analyses were performed with a Cameca IMS 4f SIMS instrument at the Memorial University microanalysis facility (MAF-IIC). An O^- primary beam (4.5 kV) with a beam current of ~20 nA, was focused with 40 to 50 μm spot diameters onto the gold-coated sample. For each sample, several suitable olivine grains were analyzed, with a maximum of 8–10 spots per sample. Each analysis comprised 10 cycles of peak counting on $^{40}Ca^{++}$, $^{45}Sc^{++}$, $^{25}Mg^+$, $^{30}Si^+$, $^{47}Ti^+$, $^{51}V^+$, $^{52}Cr^+$, $^{55}Mn^+$, $^{57}Fe^+$, $^{59}Co^+$, $^{60}Ni^+$, $^{63}Cu^+$, $^{66}Zn^+$, $^{88}Sr^+$, $^{89}Y^+$, $^{90}Zr^+$, plus counting on a background position to monitor detection noise. The measured count rates were normalized to the count rate of $^{30}Si^+$. Very low abundance elements were measured for 6 to 10 s per cycle, whereas major elements plus background and first order transition metals were measured for 2 to 6 s per cycle, respectively. Absolute detection limits were estimated following the procedure of Jones and Layne (1997). Typical interference-free detection limits calculated based on the accepted composition of San Carlos olivine ranged from 5 ppb for V, Cr, Mn, Cu, Sr, Y, Zr; to 10–40 ppb for Ca, Ti, Co, and Ni; to ~90 ppb for Sc and Zn. Measured secondary ion intensities were quantified using a calibration curve method (e.g., Shimizu et al., 1978; Yurimoto et al., 1989; Jones and Layne, 1997), with adjustments as described in detail in Chapter 2. The relative analytical error (internal precision), which is described as the standard deviation (2σ) of a single spot analysis (comprising a maximum of 10 cycles), is on average 1.5% for Mg, Mn and Fe, 4.0% for Cr, Co, Ni, and Zn, 15% for Ca, Ti and V, and ~20% for Cu, Sr, Y and Zr.

4.4.2.2. Scanning Electron Microscopy

For further post-SIMS characterization of selected high-Ti olivine samples, the Quanta FEI 650 FEG ESEM at Memorial University's MAF-IIC microanalysis facility was used to image micro-inclusions in olivine in secondary electron (SE) and backscattered electron (BSE) mode. Additionally, energy-dispersive X-ray spectroscopy (EDS) was used to qualitatively determine the mineralogy of the inclusions.

4.5. Results

The concentration of several trace elements and the forsterite content of olivine from the VBI and PLI are shown in Figures 4.4 to 4.13 (and summarized in Table 4.1). In these Figures, individual plotted data points represent the mean of 8–10 spots, on several olivine grains per sample (e.g., VB516-4, n=10), with the plotted 1 sigma uncertainty (1σ; standard deviation based on n analyses) reflecting the magnitude of the intra-sample chemical variability. In general, olivine from VBI and PLI are unzoned in major elements, whereas minor variations in trace element composition in some grains (mainly in VTT and BBS olivine from EDI) likely reflect a weak chemical zonation. However, relative individual concentration gradients are less than ±10% (total element concentration), which is much less than previously reported values for olivine from the mineralized BBS in the EDI (e.g., up to ±40% in VB266; Chapter 3). The intra-sample variability is in general very similar to the average SIMS analytical uncertainty (e.g., sample VB332-15, n=9, 1,365 ±37 ppm 1σ Ni with an average analytical spot precision

of ±24 ppm 1σ). Notable exceptions are the elevated Ti concentrations of some EDI olivine, in particular in samples from VB248 and VB513 (Fig.4.3A–B; Table 4.1). The high Ti values are coupled with a very high intra-sample variability (e.g., VB248-1, n=10, 280 ±180 ppm 1σ Ti).
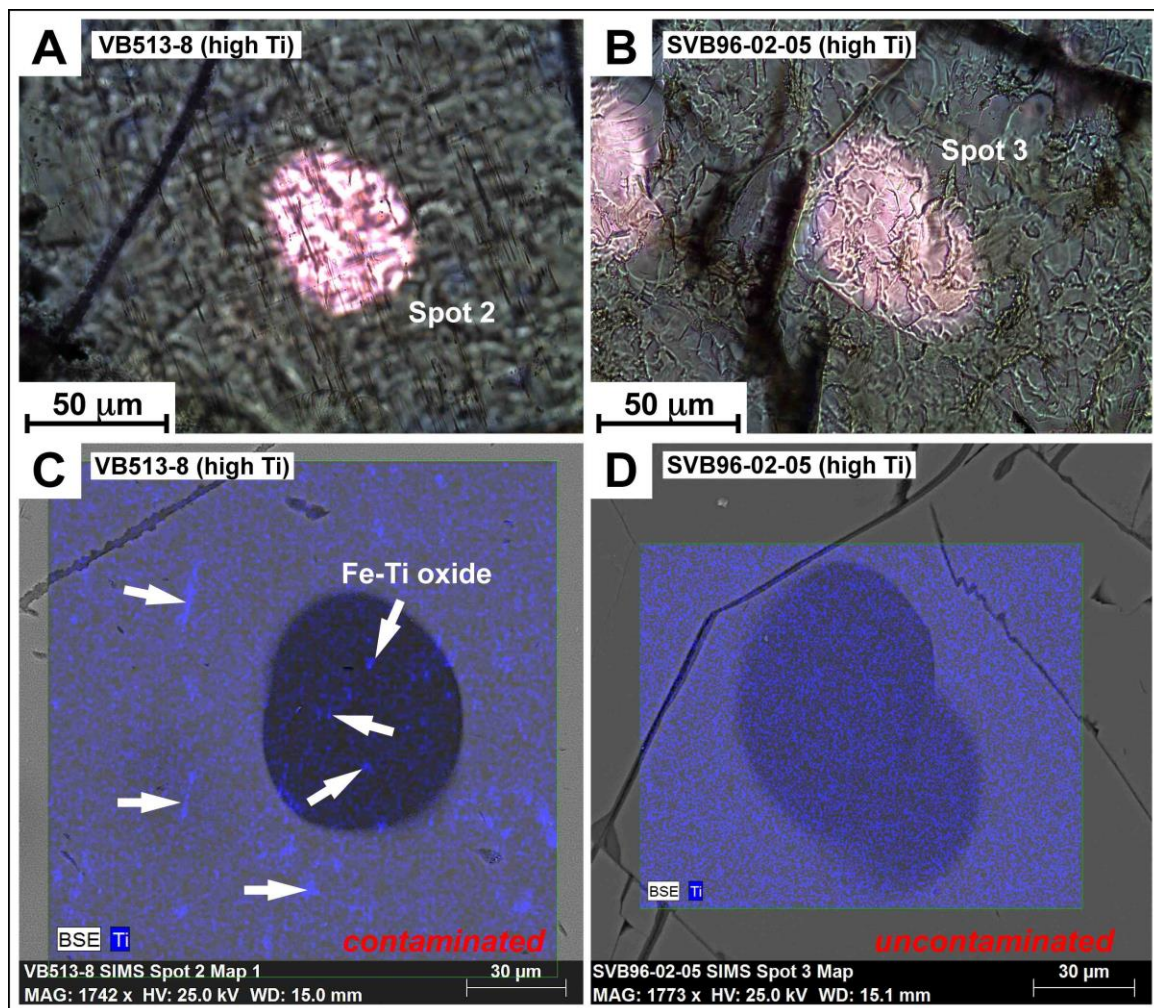
Fig. 4.3: Photomicrographs of SIMS spots on high-Ti olivine grains with A) and without B) exsolution of Fe-Ti oxides. Plane-polarized light (PPL). C) and D) show BSE images of the same locations and immediate surrounding area, overlain by a qualitative EDX map detecting the higher Ti concentrations (blue) in the exsolved oxides (shown with arrows).

Post-SIMS SEM analyses (BSE and EDX) revealed the presence of abundant smaller than 2 μm round to lath-shaped micro-inclusions of Fe-Ti oxides (likely ilmenite ±titanomagnetite) within SIMS spot sputter craters in the high-Ti olivine (Fig.4.3A and 4.3C). The distribution and abundance of these is uniformly high in EDI olivine of more primitive composition (VB248 and VB513), resulting in "positively biased" Ti concentrations. More evolved olivine from other samples in the EDI generally lack micro-inclusions of Fe-Ti oxides and the resulting uncontaminated ("true") Ti concentrations are low with a lower intra-sample variability (e.g., VB332-9, n=9, 51 ±8 ppm 1σ Ti). Micro-inclusions are also very rare in olivine from the PLI (Fig.4.3B and 4.3D), and thus the high Ti contents represent "true" values (e.g., SVB97-79-144, n=7, 423 ±20 ppm 1σ Ti).

4.5.1. Chemostratigraphy of the Olivine Composition in the EDI

4.5.1.1. Transect A – VB516 and VB248

This transect comprises 2 DDH (VB516 and VB248) analyzed in this study, as well as data for VB266 from Chapter 3. Results are presented in Figure 4.4 and Table 4.1. The transect stretches from the shallow DDH VB516 (~300m to end of hole) drilled near the southwest terminus of the EDI, through the almost 600m VB248 (~531m north of VB516), towards the ~700m VB266 (~140m northeast of VB248) in the north of the EDI that represents the deepest part of the magma chamber. At various stratigraphic intervals, the younger Voisey's Bay granite is intercalated with the mafic lithologies of the EDI,

intruding the chamber primarily from the east to southeast (e.g., Lightfoot and Naldrett, 1999; Lightfoot et al., 2012).

Olivine compositions in the NT of VB516 deviate significantly from data trends previously reported for olivine in the EDI (Li and Naldrett, 1999; Venables, 2003; Chapter 3). Specifically, olivine samples from NT in VB516 contain, on average, less Cr (58 ppm ±4.8 1σ) than olivine from the underlying VTT (Cr 75ppm ±10 1σ) (Fig.4.4A) and other NT intervals. In contrast to the high Ni and Co concentrations of average NT olivine (~1,500 ppm Ni and 255 ppm Co; Fo76 ±4 1σ; Chapter 3), the NT interval in VB516 contains olivine with anomalously low average Ni (106 ppm ±22 1σ) and Co (203 ppm ±11 1σ) contents, that are coupled with low average Fo compositions (61 mol.% ±3 1σ) and relatively high Mn concentrations (3,240 ppm ±230 1σ) (Fig.4.4D). The entire NT succession in VB516 is petrographically characterized by the presence of up to 35 vol.% of (cumulus) Fe-Ti oxide(s) (probably ilmenite ±titanomagnetite), and a higher modal abundance of (clino)pyroxene at the expense of primarily plagioclase.

In samples from the underlying VTT, however, olivine has an average Fo content of Fo72 (±4 1σ), whereas Ni and Co concentrations also return to the EDI average range, with 1,480 ppm (±83 1σ) Ni and 233 ppm (±11 1σ) Co, respectively (Fig.4.4B and 4.4E). The Mn content mimics the above-mentioned trends in Ni and Co, with an overall decrease in Mn from ~3,240 ppm in NT olivine to 2,770 ppm in VTT olivine. Previous work demonstrated that Mn and Zn concentrations are predominantly positively correlated (VB266; Chapter 3), however, in olivine from VB516 these two elements are largely decoupled, even though Zn concentrations are slightly higher in the basal, xenolith-

bearing part of the VTT (~303 ppm Zn) than in the uncontaminated upper NT (~286 ppm Zn). The positive correlation of Mn and Zn on the other hand is again typical for olivine from the contaminated BBS and lower VTT, and becomes increasingly pronounced towards the center of the EDI (VB248 to VB266; Fig.4.4A–F).

Olivine from VB248 exhibits a combined increase in Mn and Zn with depth; from 2,037 ppm (±29 1σ; VB248-9) to 2,509 ppm (±48 1σ; VB248-14) Mn and 214 ppm (±9 1σ; VB249-9) to 313 ppm (±6 1σ; VB248-12) Zn in the overlying NT and VTT, increasing to 4,375 ppm (±118 1σ; VB248-15) Mn and 724 ppm (±21 1σ; VB248-15) Zn in olivine from the BBS (Fig.4.4E). This trend partly resembles the Mn and Zn enrichment of BBS olivine from VB266 (Fig.4.4F; Chapter 3), although the absolute increase in Mn is less dramatic in VB248 (~4,400 ppm) than in VB266 (~10,000 ppm), which intersects a greater thickness of the BBS associated with massive sulfide. Also in accordance with the general depth progression originally observed in VB266, Ni, Co and Fo contents display a variably pronounced decrease in the BBS, from a maximum of Fo82 (±0.4 1σ) with ~1,466 ppm Ni and 255 ppm Co in the upper VTT, to Fo62 (±0.7 1σ) with around 935 ppm Ni and 196 ppm Co in the BBS (Fig.4.4B and 4.4E). Sample VB248-14 is a melatroctolite (UMF; Fig.4.2C) that contains recrystallized paragneiss inclusions (now mainly hercynite) and has a sulfide content of ~10 vol.% – as such, this olivine displays a more primitive composition for Fo and most trace elements (~Fo80; 1,877 ppm Ni; 220 ppm Co; 135 ppm Cr; 2,591 ppm Mn), whereas the Zn content (237 ppm) is elevated with respect to the apparent Fo composition. The Cr content in the olivine also decreases

towards the base of VB248 (from ~93 ppm in the VTT to less than 65 ppm in the BBS) with the exception of the melatroctolite sample at 442m (Fig.4.4).

The downhole olivine data for VB266 are taken from Chapter 3. Besides the presence of several distinct Ni, Co and Cr excursions in the NT and VTT sequences, with the highest Ni values (~2,450 ppm) encountered in olivine at 108m (Fig.4.4C and 4.4F), a key observation is the presence of a distinct gradual Mn and Zn enrichment in olivine from the lower part of the VTT that continues into the BBS. This signature is associated with a systematic downward decrease in Ni, Co, Cr, and the Fo content (Chapter 3; Fig.4.4C and 4.4F).

In summary, the key aspects of the olivine chemostratigraphy in Transect A are:

1. The presence of strongly Ni-Co-Cr-depleted, Mn-Fe-enriched olivine throughout the ~140m thick, Fe-Ti oxide-rich NT succession at the top of VB516.

2. The pronounced decrease in Ni-Co-Cr-Fo concentrations in olivine from the BBS of VB248 (530m north of VB516).

3. The Zn enrichment relative to the Fo content of olivine in the UMF sample from the contaminated, lower VTT in VB248.

4. The Mn-Zn enrichment in lower VTT and BBS olivine from VB248, which closely resembles the Mn-Zn contamination signature of the VTT and BBS olivine from DDH VB266, where it intersects the massive sulfide deposit at the base of the EDI, approximately 140m to the northeast.
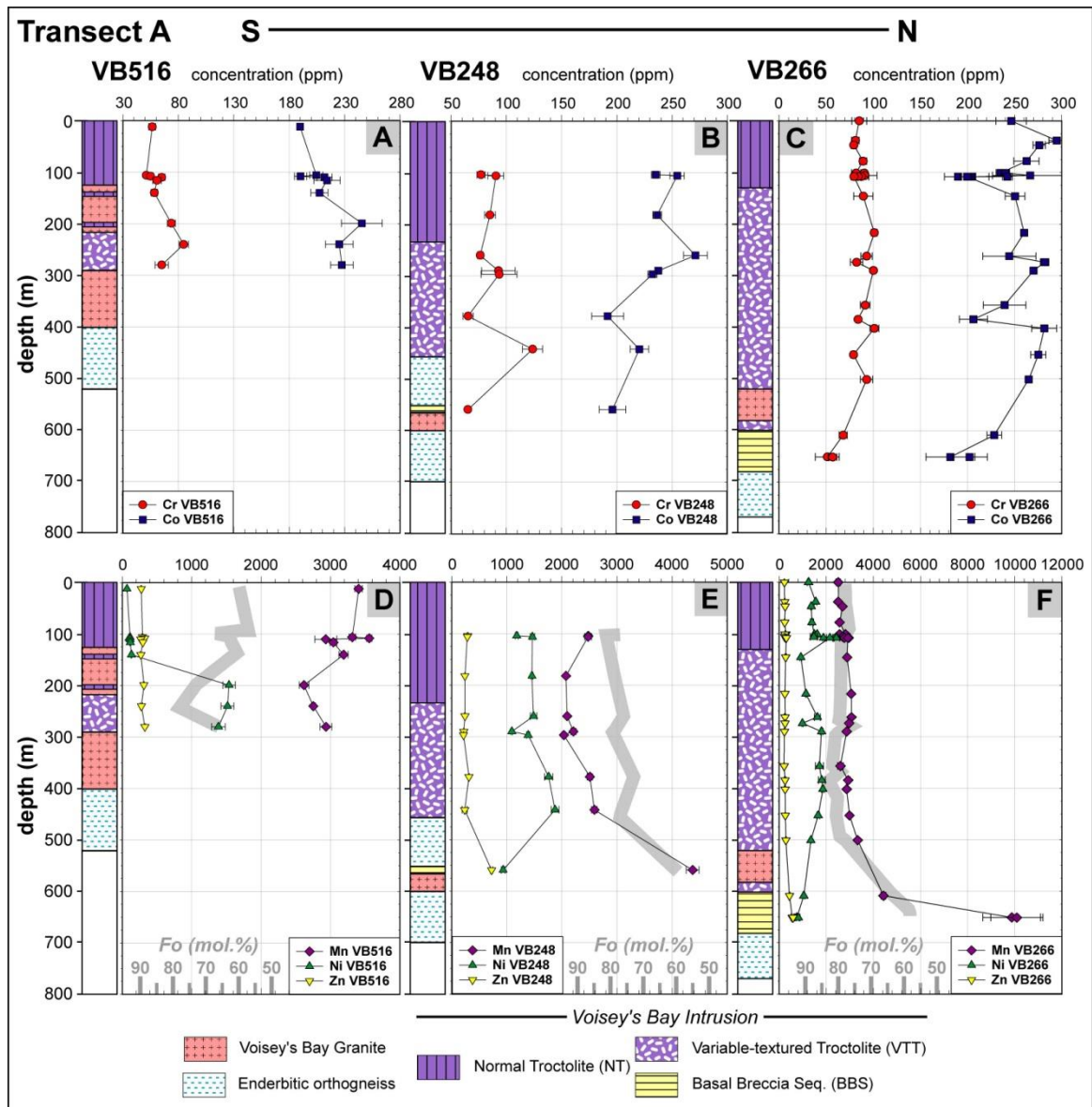
Fig. 4.4: Chemostratigraphic profiles of sampled olivine from transect A (VB516–VB248–VB266) in the EDI. Data for VB266 are from Chapter 3. The transect is depicted from S to N with the concentrations of Cr and Co in olivine in the upper row, and Mn, Ni, and Zn in the lower row. Error bars show standard deviations of averages (1σ). The forsterite content is displayed in the lower row as light grey bar with the corresponding scale.
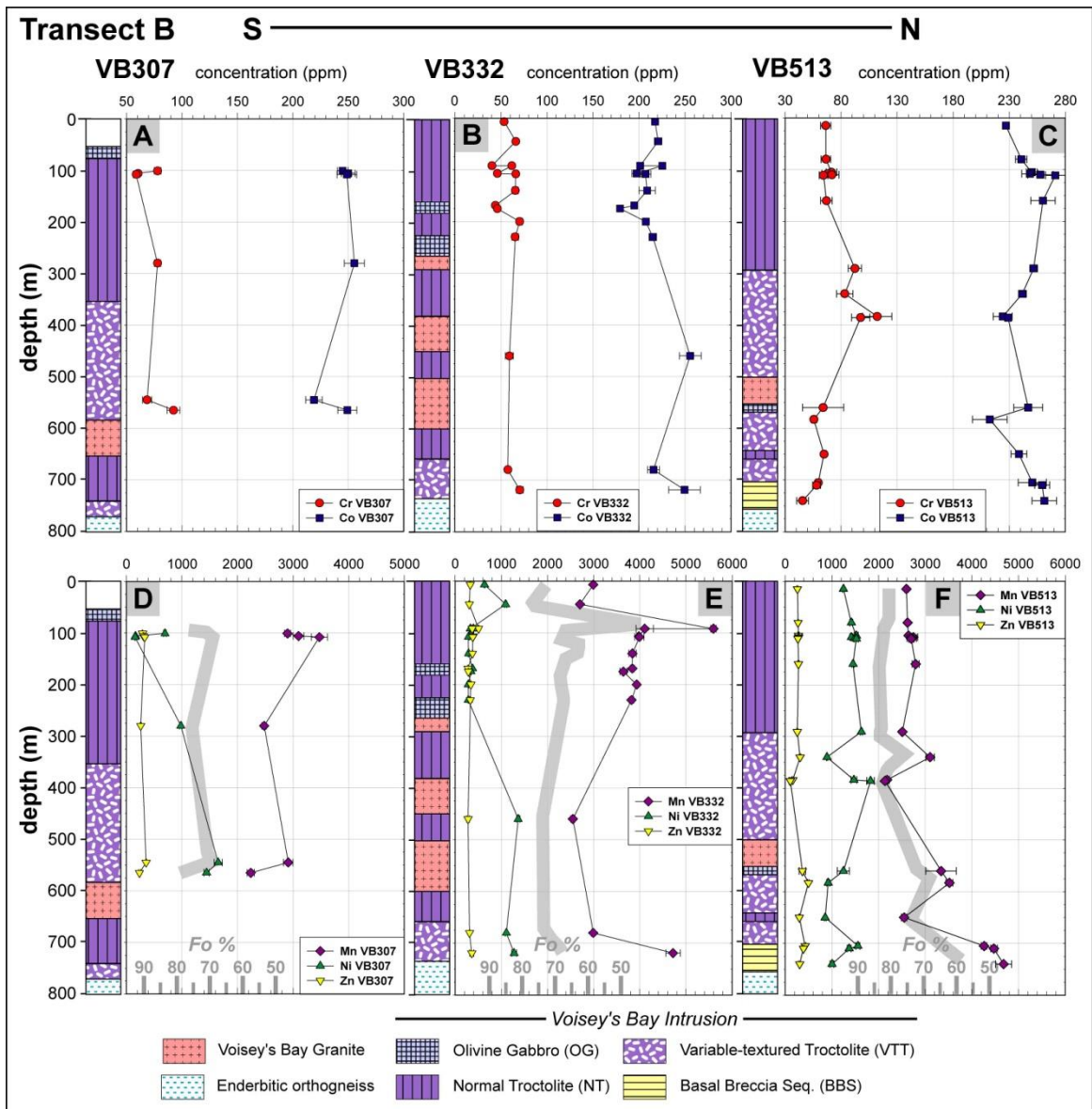
Fig. 4.5: Chemostratigraphic profiles of sampled olivine from transect B (VB307–VB332–VB513) in the EDI. The transect is depicted from S to N with the concentrations of Cr and Co in olivine in the upper row, and Mn, Ni, and Zn in the lower row. Error bars show standard deviations of averages (1σ). The forsterite content is displayed in the lower row as light grey bar with the corresponding scale.

4.5.1.2. Transect B – VB307, VB332, and VB513

This transect is 250 – 400m further east in the EDI than Transect A, and comprises 3 DDH (Fig.4.1 and 4.5). VB307, which is ~780m southeast of VB266, intersects a thin cap of OG, followed by 775m of troctolitic rocks (NT, VTT) containing several variably thick, intruding granitic dikes. VB332 is ~400m north of VB307 and contains a 676m sequence of NT, erratically crosscut by granitic dikes, followed by a ~65m interval of VTT with locally developed BBS and thin veins of massive sulfide. VB513, which is another 210m northwest of VB332 and ~180m southeast of VB266, is closest to the known massive sulfide deposit at the base EDI. This drill hole contains ~300m of NT, followed by ~410m of VTT with meter-thick intercalations of OG, NT and granite. The base of the hole comprises a 60m succession of BBS, containing disseminated and blotchy sulfides, as well as recrystallized and sheared paragneiss fragments.

Olivine from VB307 exhibit, independent of their specific host rocks (NT and VTT), a fairly homogeneous Cr and Zn distribution, with 73 ppm (±13 1σ) Cr and 296 ppm (±44 1σ) Zn, and forsterite contents ranging from Fo67 (±2 1σ) in NT olivine (VB307-7; Table 4.1) to Fo80 (±1 1σ) in VTT (VB307-12) olivine (Fig.4.5A and 4.5D). In contrast, the Ni, Co and Mn compositions vary considerably in VB307. The lowest Ni and Co values occur in olivine from a NT interval (VB307-6 and -7 at 106 to 108m), and those contain ~161 ppm Ni and 249 ppm Co, whereas Mn concentrations are high with up to 3,285 ppm (Fig.4.5A and 4.5D). The olivine with this anomalous trace element distribution has a mean Fo of 69 mol.% (±3 1σ) and is associated with a very high Fe-Ti oxide (cumulus) content (up to 45–50 vol.% in VB307-6), and is petrographically similar to the low-Ni

olivine samples (NT) in VB516. However, the NT samples above and below this interval (VB307-4 at 10m; VB307-9 at 280m) have no cumulus Fe-Ti oxides, an olivine composition of Fo75 (±0.2 1σ), and average 696 ppm (±25 1σ) Ni and 980 ppm (±23 1σ) Ni, respectively, ~250 ppm (± 8 1σ) Co, 2,689 ppm (± 298 1σ) Mn, and 76 ppm (±0.1 1σ) Cr (Fig.4.5A and 4.5D). The VTT samples at the base of VB307 indicate an increase in Fo and trace element content (Fig.4.5D) rather than the usual decrease with proximity to BBS (VB248, VB266), but a detectable depletion is not expected because of distance from the mineralized VTT and BBS horizons. The increase occurs mainly because the terminal sample VB307-12 (565m) is a fairly primitive troctolite with almost 30 vol.% olivine and only small amounts of interstitial sulfide (~2 vol.%).

VB332 (Fig.4.5B and 4.5E) contains compositionally heterogeneous olivine, and has been subdivided into three general subsections. The first section includes the upper part of the NT (7–45m; VB332-1 and -2), which comprises olivine of "typical" NT composition; Fo73–78, 635–1,093 ppm Ni, ~218 ppm Co, ~2,850 ppm Mn and ~57 ppm Cr. Deeper samples from NT and interbedded OG intervals are distinctly different. In particular, olivine from the second section at VB332 (92 to 230m) have much more fractionated compositions, with Fo62–68, less than 398 ppm Ni and 225 ppm Co. On the other hand, Mn and Zn are consistently high, with up to 4,105 ppm Mn and 393 ppm Zn. In contrast to the low-Ni olivine samples from VB516 and VB307, those in this section are devoid of (cumulus) Fe-Ti oxides. Sample VB332-4 (92m), which exhibits a prominent compositional excursion, especially in Mn and Fo content (Fig.4.5E), occurs at a sharp contact between the NT and an intruding granitic dike (see photomicrograph in Appendix

6.6.). This sample contains two distinct populations of olivine (Ol1 and Ol2), mainly characterized by their degree of (metasomatic) alteration. Contact metamorphism during the intrusion of the dike pervasively metasomatized the NT mineralogy in the contact area (modal metasomatism), and as a result, the overprinted olivine has preserved cores, which display strong serpentinization and are enclosed by a complex polymineralic alteration corona of primarily (clino)pyroxene, green hornblende and green biotite overgrowths (see Appendix 6.6.). This low-grade metamorphic overprint caused a major and trace element migration (cryptic metasomatism), resulting in a compositionally distinct olivine (Ol1) with low Mg, Cr, Co, and Ni contents (Fo47 ($\pm$0.3 1σ); 40 ppm ($\pm$1 1σ) Cr; 201 ppm ($\pm$2 1σ) Co and 329 ppm ($\pm$8 1σ) Ni; Table 4.1) and high Fe, Mn and Zn contents (5,595 ppm $\pm$58 1σ Mn; 506 ppm $\pm$6 1σ Zn). Conversely, the less altered olivine (Ol2) has a composition similar to those primary olivine described above for this specific section in VB332 (Fig.4.5; Table 4.1). The last three samples define the final section in core VB332 (460 to 719m) and illustrate the expected enrichment in Mn and Zn of olivine towards the mineralized and contaminated units at the base of the EDI, with an increase to 4,718 ppm ($\pm$158 1σ) Mn and to 360 ppm ($\pm$47 1σ) Zn. The concentrations of Cr, Co, and Ni also increase, whereas the Fo content displays a minor decrease towards the base of the hole (Fo71 $\pm$1 1σ) (Fig.4.5B and 4.5E).

Even though olivine from VB513 has diverse trace element compositions, the general downhole trend resembles that of VB266, which lies 180m further to the north (Fig.4.4 and 4.5). A prominent basal decrease in Cr, Ni, and Fo content is visible, and local excursions of those elements and Co and Mn occur in the VTT sequence (Fig.4.5C and

4.5F). Samples at 384m and 386m in particular, taken from an ultramafic interval (UMF) of melatroctolitic to dunitic composition, contain olivine of primitive composition, with ~Fo82, ~1,650 ppm Ni, ~105 ppm Cr, ~2,160 ppm Mn and ~136 ppm Zn (Table 4.1). Another sample with more primitive olivine is encountered in a thin NT interval at 650m (Fig.4.5F). The upper part of VB513 is composed of regular and homogeneous NT. However, olivine shows a steady downward increase in Fo (~Fo79–82), Co (~227–271 ppm) and Ni (~1,247–1,524 ppm) content, with the peak values at around 111m (Fig.4.5C and 4.5F). The spatial position of this interval coincides with the high-Ni olivine excursion at ~108m in VB266, which contains olivine with the highest average Ni concentration in the EDI (~2,450 ppm; Chapter 3). Close to the end of the hole, VB513 intersects the BBS (710–740m) at the base of the EDI, and the olivine here are variably enriched in Mn (~4,576 ppm) and Zn (~352 ppm). However, the highest Zn content (~498 ppm) is actually found in olivine from a VTT sample – VB513-19 at 583m (Fig.4.5F). The Mn content in olivine in VB513-19 is lower than in BBS olivine (~3,500 ppm), which indicates that Mn and Zn concentrations are likely decoupled in this interval.

In summary, the key observations from Transect B are:

1. The reappearance of Fe-Ti oxide-rich, low-Ni olivine-bearing intervals at the top of the NT sequence in VB307 in a similar stratigraphic horizon as in VB516 (Transect A).

2. The presence of a ~140m thick interval of "regular" NT (with intercalated OG) in the upper part of VB332 ("second section"; 92m to 230m) that also contains olivine with low Ni concentration.

3. That contact metamorphically altered olivine in VB332 is compositionally distinct from the most differentiated and trace element-rich olivine found in the BBS (e.g., VB266).

4. That two UMF samples from the upper, less contaminated VTT in VB513 contain primitive olivine with low Zn concentrations.

5. The basal enrichment in Mn-Zn-Fe increases from VB332 towards VB513, which intersects the EDI in close proximity to the known occurrence of massive and disseminated sulfide in VB266 a further 180m to the north.

4.5.2. Trace Element Relationships in Olivine

Olivine data are presented in Figures 4.6–4.8 to show trace element variations with Fo content (mol.%; Fig.4.6), incompatible versus compatible trace element variations (Fig.4.7), and modified multi-trace element "spidergram" plots comparing petrologically important lithologies of the VBI and PLI (Fig.4.8). The trace element selection in Figures 4.6 to 4.7 is based primarily on geochemical affinities, in order to best visualize the three primary petrological processes active in mafic magmatic and ore-forming environments – differentiation and fractional crystallization (FC model lines – see discussion), sulfide saturation and interaction with segregated sulfide, and assimilation and contamination by country rock (AFC model line – see discussion). Four possible FC-AFC scenarios were modeled (see caption Fig.4.6) – for each step (5% increments) in the FC-AFC models the Fo content of crystallizing olivine was calculated based on the $(FeO/MgO)_{liquid}$ (Li et al.,

2007), and the concentration of specific trace elements was computed according to the equation:

$$C_L = C_O F^{(D-1)}$$

Here the trace element content of the initial melt (C_O; inferred from average composition of Proterozoic basalts; Condie, 1993; Table 4.1), the partition coefficients (e.g., $DNi_{ol/sil}$ = concentration in olivine / concentration in liquid) for olivine, plagioclase, clinopyroxene, sulfide liquid, and Fe-Ti oxide (Table 4.1), the degree of fractionation, and the proportion of the remaining liquid (F) (used to compute the bulk D), were used to calculate the composition of the fractionating residual liquid (C_L).

Melt differentiation and FC of olivine is primarily characterized by a decrease in compatible elements like Mg, Ni, and to a lesser degree Co and Cr, reflecting their depletion in the melt during this process. On the other hand, the concentration of highly incompatible trace elements such as Ca, Sc, V, Ti, Cu and (variably) Sr and Y increases. Due to their high oxidation states, systematic variations in V (mainly 3^+ or 4^+) and Ti (4^+) contents in the melt/olivine system are also a function of the prevalent oxygen fugacity (fO_2) (e.g., Gaetani and Grove, 1997; Canil and Fedortchouk, 2001; Zanetti et al., 2004; Papike et al., 2005; Shearer et al., 2006, and references therein). In addition, V, Ti, and Cr concentrations in olivine likely reflect the onset of Fe-Ti oxide(s) crystallization and therefore further constrain the melt evolution of magma systems like the VBI and the PLI (e.g., Snyder et al., 1993; Jang et al., 2001, and references therein).

Since Ni, Cu and to a lesser extend Co, are very sensitive to sulfide saturation (e.g., Hart and Davis, 1978; Rajamani and Naldrett, 1978; Fleet et al., 1981; Gaetani and Grove,

1997; Li et al., 2003b), very low Ni values in olivine indicate an earlier removal of Ni (±Co) by sulfide melt, whereas more erratic distributions are interpreted to result from reequilibration with a sulfide liquid (e.g., Clark and Naldrett, 1972; Li and Naldrett, 1999).

Other trace elements (e.g., Ca, Sc, Mn, Zn, Sr, and Y), however, are relatively unaffected by the fractionation of a sulfide melt, but may instead record the assimilation of country rocks such as the Tasiuyak and Nain gneisses. For example, contamination of the primary mafic melt by externally derived Mn and Zn is the most likely explanation for their dramatic increase in BBS olivine of VB266, which is several magnitudes higher than their expected enrichment due to fractional crystallization (Chapter 3).

The multi-trace element plots presented in Figure 4.8 depict all measured elements from left to right in a sequence of increasing compatibility in olivine ($D^{element}_{ol/sil}$) – and thus form sub-groups with certain geochemical affinities. The concentration of the lithophile elements from Zr through Cr is primarily controlled by melt differentiation and fractional crystallization, whereas Mn and Zn are also introduced by the assimilation of upper crustal rocks. The siderophile and chalcophile elements from Fe through Cu are, in ascending order, progressively more sensitive to sulfide saturation and thus partition strongly into a fractionating sulfide liquid ($D^{element}_{ol/sul}$) (MacLean and Shimazaki, 1976; Hart and Davis, 1978; Rajamani and Naldrett, 1978; Fleet et al., 1981; Gaetani and Grove, 1997; Li et al., 2003b).

Table 4.1: SIMS analytical data for olivine (averages) from the EDI and PLI

Sample	Rock type	depth	RVP calc[a]	n	forsterite	1σ[3]	MgO	FeO	Ca	1σ	Sc	1σ	Ti	1σ	V	1σ	Cr	1σ
VB307-4	NT	101	0.26	11	74.9	1.4	39.08	21.80	671	159	5.56	1.47	89.1	67.6	3.35	0.59	78.0	3.2
VB307-6	NT	106	0.24	10	70.9	1.7	36.59	24.85	748	144	9.53	1.83	90.2	45.0	4.08	0.55	60.4	1.9
VB307-7	NT	108	0.33	9	67.4	2.1	34.35	27.60	1031	193	13.0	1.58	68.6	19.1	3.57	1.44	58.7	2.7
VB307-9	NT	280	0.28	10	75.1	1.6	39.22	21.62	778	198	3.42	0.61	88.5	57.2	3.08	0.32	77.9	2.8
VB307-11	VTT	545	0.44	7	70.7	2.3	36.43	25.05	1385	216	3.27	0.60	82.8	42.6	3.44	0.29	68.5	4.2
VB307-12	VTT	565	0.18	11	79.5	1.0	42.11	18.09	393	163	5.19	0.74	126	94.9	5.14	0.93	92.4	5.7
VB332-1	NT	7	0.33	7	72.9	0.8	37.15	24.15	647	95	9.14	1.50	57.2	23.8	3.21	0.27	53.4	1.2
VB332-2	NT	45	0.28	10	77.7	0.6	40.34	20.22	433	70	6.50	0.99	166	100	3.64	1.14	66.1	2.6
VB332-4 Ol1	NT	92	0.88	4	47.0	0.3	21.51	43.48	674	161	1.62	0.48	9.6	1.7	0.72	0.05	40.1	0.9
VB332-4 Ol2	NT	92	0.52	4	65.2	1.0	32.30	30.18	544	94	4.12	0.67	44.0	13.5	1.66	0.10	61.7	1.1
VB332-6	NT	107	0.50	9	65.2	0.6	32.24	30.20	658	147	7.20	1.57	67.1	48.7	2.18	1.19	46.0	2.1
VB332-7	NT	108	0.45	9	65.5	0.7	32.43	29.96	576	164	10.0	1.24	74.8	26.1	2.91	0.56	66.1	2.7
VB332-9	NT	140	0.41	9	67.6	0.7	33.74	28.35	614	190	6.28	1.85	51.1	8.3	3.05	1.00	65.6	3.1
VB332-10	OG	169	0.62	9	62.3	0.7	30.45	32.41	683	144	5.36	2.21	38.4	21.5	1.26	0.21	43.9	1.5
VB332-11	OG	175	0.54	6	62.1	0.3	30.33	32.55	738	268	10.4	1.10	120	128	3.11	1.35	46.1	2.0
VB332-12	NT	200	0.47	6	66.0	0.4	32.72	29.60	637	148	6.56	1.05	40.9	6.5	2.25	0.29	70.3	2.9
VB332-13	OG	230	0.47	6	66.2	0.4	32.85	29.44	750	395	5.13	1.28	41.2	11.4	1.97	0.20	65.4	3.6
VB332-15	NT	460	0.41	9	74.9	1.4	38.47	22.51	290	52	1.57	0.62	31.1	29.7	1.77	0.19	59.1	4.3
VB332-16	VTT	680	0.43	9	73.2	0.5	37.32	23.93	319	59	4.00	1.53	35.9	7.9	2.17	0.20	57.5	2.5
VB332-17	VTT	719	0.58	11	71.2	1.1	36.03	25.52	499	144	7.49	2.66	40.7	7.4	2.10	0.26	70.5	3.7
VB513-1	NT	15	0.29	7	78.7	0.4	41.01	19.39	416	43	4.17	1.43	271	200	3.77	1.46	66.3	4.6
VB513-2	NT	80	0.30	6	79.9	0.3	41.82	18.39	289	50	4.40	1.21	270	163	3.23	0.86	66.4	4.1
VB513-4	NT	105	0.30	9	81.2	0.3	42.69	17.32	294	61	3.69	1.10	183	98.3	2.87	0.65	71.3	4.8
VB513-5	NT	108	0.31	7	80.4	0.5	42.13	18.02	299	46	4.12	2.07	91.1	80.7	2.63	0.32	68.0	5.1
VB513-6	NT	110	0.30	8	80.9	0.4	42.48	17.59	292	73	3.68	1.40	117	119	2.79	0.42	71.8	6.3
VB513-7	NT	111	0.32	8	82.0	0.3	43.26	16.63	218	63	2.74	1.38	143	134	2.16	0.18	64.2	3.8
VB513-8	NT	160	0.29	8	82.2	0.5	43.36	16.50	372	50	3.68	1.19	268	126	2.82	0.46	66.8	5.2
VB513-10	NT	291	0.25	8	81.6	0.1	43.01	16.94	311	39	4.14	1.01	239	135	3.79	0.42	92.3	5.9
VB513-12	VTT	340	0.27	9	77.3	0.2	40.06	20.56	375	57	6.65	1.31	70.1	48.1	3.23	0.25	83.2	7.4
VB513-13	UMF	384	0.19	12	80.7	0.6	42.33	17.77	293	135	4.90	1.61	185	130	5.27	1.14	112	13.0
VB513-14	UMF	386	0.29	9	81.8	0.2	43.14	16.77	143	16	5.19	0.77	113	72.5	4.34	0.65	97.4	8.2
VB513-16	OG	560	0.39	8	72.6	3.5	36.95	24.39	684	144	5.76	1.71	187	127	3.57	2.12	64.0	18.3
VB513-19	VTT	583	0.44	7	68.5	0.7	34.30	27.66	540	92	6.48	2.37	54.8	19.9	2.35	0.29	55.7	2.4
VB513-21	NT	650	0.35	9	73.2	1.0	37.31	23.94	357	52	1.93	0.79	238	190	1.89	0.27	64.7	1.9
VB513-23	VTT	705	0.66	10	64.8	1.7	31.97	30.53	463	86	7.05	1.19	37.7	7.9	1.60	0.16	59.6	2.2
VB513-24	BBS	710	0.67	9	64.1	0.8	31.54	31.05	366	63	10.2	2.00	35.8	9.0	1.69	0.26	58.1	3.6
VB513-25	BBS	740	0.75	7	59.9	1.7	29.00	34.20	416	169	10.4	1.20	52.2	8.0	1.31	0.15	45.6	5.1
VB516-1	NT	12	0.45	9	61.2	1.5	30.60	32.22	787	146	14.8	1.78	66.8	16.6	3.43	0.43	56.4	3.1
VB516-4	NT	106	0.51	10	57.2	1.8	28.17	35.22	1685	284	6.80	1.98	76.5	12.5	2.79	0.51	51.0	1.4
VB516-6	NT	108	0.49	7	58.3	2.6	28.88	34.34	1102	219	13.5	1.17	69.6	12.3	3.25	1.17	54.9	2.6
VB516-7	NT	110	0.30	7	66.7	2.8	33.96	28.09	597	115	11.2	1.06	67.5	12.2	4.15	0.72	65.0	3.1
VB516-9	NT	116	0.35	8	63.2	2.8	31.81	30.73	1198	316	8.50	0.85	90.4	40.6	4.14	1.40	60.7	3.8
VB516-10	NT	140	0.41	10	61.5	2.0	30.75	32.04	1395	165	6.34	0.99	81.4	26.8	3.80	1.49	58.3	3.0
VB516-11	VTT	199	0.42	7	71.5	1.2	36.97	24.39	252	42	1.65	0.49	34.8	12.5	2.49	0.22	73.6	3.6
VB516-13	VTT	240	0.33	11	76.2	0.6	39.92	20.76	394	106	3.89	0.44	49.1	8.4	4.02	0.36	84.8	4.2
VB516-16	VTT	280	0.46	10	67.3	1.5	34.32	27.64	1044	473	9.46	3.51	59.1	18.9	3.35	0.77	65.0	6.0
VB248-1	NT	104	0.17	10	78.4	0.6	41.37	18.99	687	193	5.71	1.37	289	180	5.46	1.39	76.9	3.6
VB248-2	NT	106	0.22	8	81.7	0.4	42.96	16.88	361	52	2.75	0.70	220	157	3.54	0.42	90.4	7.1
VB248-5	NT	182	0.26	11	79.0	0.6	41.10	19.18	302	60	3.86	1.26	206	129	3.37	0.56	85.1	4.8
VB248-7	VTT	260	0.27	8	78.1	0.3	40.54	19.87	228	50	4.08	0.58	189	125	3.41	0.67	76.3	2.6
VB248-8	VTT	290	0.18	9	80.6	0.4	42.19	17.83	298	54	5.72	1.54	209	115	4.00	0.88	92.8	15.3
VB248-9	VTT	297	0.17	12	79.8	0.8	41.66	18.49	465	112	4.43	1.24	324	124	5.34	1.20	93.4	16.3
VB248-12	VTT	378	0.39	9	74.7	0.6	38.28	22.66	550	64	4.14	0.95	418	80.9	4.17	1.27	65.2	4.6
VB248-14	UMF	442	0.18	8	79.6	0.6	41.60	18.66	470	112	7.66	1.45	223	161	7.41	1.40	124	9.1
VB248-15	BBS	559	0.54	6	67.7	0.7	30.06	32.89	501	116	6.11	1.54	54.1	30.4	1.67	0.32	65.1	1.7
SVB96-02-02	OG	8		10	60.3	0.8	29.19	33.96	1890	383	18.0	2.49	272	10.4	7.61	1.35	46.9	1.9
SVB96-02-03	OG	22		8	57.0	0.9	27.25	36.36	2093	478	22.8	5.49	297	25.4	9.93	3.03	44.6	2.3
SVB96-02-05	OG	69		9	52.6	1.5	24.69	39.53	2409	502	21.0	3.99	324	87.1	5.57	1.71	47.9	3.5
SVB96-10-90	TG	21		8	55.2	1.8	26.17	37.69	3299	702	25.0	3.08	307	52.6	11.93	2.44	47.1	5.0
SVB96-10-91	TG	30		8	58.1	1.3	27.88	35.58	1828	504	24.4	4.41	294	29.2	8.12	2.08	45.4	2.9
SVB96-27-08	Cg G	1.2		6	58.2	2.0	27.95	35.49	3089	889	18.1	3.99	318	55.9	9.93	1.19	40.6	3.7
SVB98-113-168	Fg G	98.9		10	57.7	3.5	27.66	35.85	821	222	13.3	2.96	263	61.6	4.78	1.84	60.2	9.2
SVB97-92-161	Fg G	246.6		9	61.1	1.4	29.71	33.32	843	183	18.8	5.22	192	57.4	6.14	1.52	58.7	4.3
SVB97-79-144	Mg G	632.6		7	79.6	0.3	41.60	18.67	1057	166	11.2	1.94	423	20.7	9.52	1.03	81.5	5.7
SVB97-79-147	Mg G	729.3		9	62.1	0.7	30.28	32.41	5785	356	10.7	1.98	473	33.2	2.72	0.43	54.2	4.4
SVB97-92-03-Ol1	Cg BG	186.8		4	43.0	1.4	19.34	46.18	1384	107	22.1	3.09	266	169	4.86	2.87	36.3	1.0
SVB97-92-03-Ol2	Cg BG	186.8		4	64.4	3.4	31.76	30.78	993	398	15.2	3.21	244	52.9	7.62	3.33	71.6	14.4
SVB98-102-150	Cg BG	75.8		9	49.4	3.1	22.90	41.75	905	238	21.6	3.61	259	92.2	2.37	0.67	37.9	4.7

Parameters for AFC modeling (compositions of model liquids)[1]

							MgO	FeO							V	1σ	Cr	1σ
basaltic liquid[X]							8.0	10							160		140	
model gneiss[Y]							4.3	10.8							108		80	

Partition coefficients (D[min/melt]) for basaltic melt[2]

							MgO	FeO							V		Cr	
olivine							5.2	1.6							0.03		0.80	
plagioclase							0.04	0.10							0.20		0.02	
clinopyroxene							2.5	0.65							6		34	
sulfide								9							0.60		0.90	
Fe-Ti oxide[Z]								1.3							60		15	

[a]: relative proximity factor calculated based on results from multiple regression of V-Cr-Mn-Fe-Co-Ni-Zn and RVP with data from Chapter 3 (see Appendix 6.4.)

[1]: FC calculation: $C_L / C_O = F^{(D-1)}$ (Rollinson, 1993; Li et al., 2007); AFC modeling was performed using the equation $C_L/C_O=f'+r / (r-1+D) * C_A / C_O(1-f')$ from DePaolo (1981)

[X]: basaltic liquid composition inferred after Condie (1993) Proterozoic basalts

[Y]: model gneiss composition - Mn based on Mn-rich enderbitic/Nain orthogneiss (Vale, unpublished data); Zn based on Tasiuyak paragneiss (Vale, unpublished data)

[2]: sources for mineral D values are given in Chapter 3

[3]: 1σ error is standard deviation of n analyses on individual sample ("inter-sample variability") - average analytical error in Analytical Method section; (N.M.) - not measured

light grey: BG from North Intrusion; OG-olivine gabbro; TG-transition gabbro; Cg-fg G-coarse- to fine-grained gabbro

Table 4.1 (cont): SIMS analytical data for olivine (averages) from the EDI and PLI

Sample	Rock type	depth	Mn	1σ	Co	1σ	Ni	1σ	Cu	1σ	Zn	1σ	Sr	1σ	Y	1σ	Zr	1σ
VB307-4	NT	101	2899	55	245	4.8	696	25.2	2.22	0.64	291	6	0.824	0.483	0.545	0.201	0.359	0.170
VB307-6	NT	106	3097	95	250	6.1	165	4.6	3.94	1.03	306	6	0.547	0.145	0.135	0.023	0.225	0.045
VB307-7	NT	108	3472	145	249	9.0	158	4.5	3.14	0.83	330	7	0.694	0.170	0.267	0.057	0.261	0.056
VB307-9	NT	280	2478	39	256	9.1	979	22.8	3.54	0.64	260	11	1.644	0.921	0.246	0.057	0.422	0.131
VB307-11	VTT	545	2912	83	219	7.5	1652	75.0	7.21	1.62	355	8	3.573	1.269	1.496	0.659	1.407	0.928
VB307-12	VTT	565	2237	67	249	8.7	1443	48.4	3.85	0.91	236	16	0.578	0.293	0.335	0.218	0.813	0.604
VB332-1	NT	7	2990	35	218	3.3	634	9.4	3.44	0.58	327	9	0.657	0.285	0.704	0.112	0.296	0.051
VB332-2	NT	45	2705	30	221	4.0	1093	22.6	5.03	1.48	306	10	0.378	0.059	0.361	0.095	0.779	0.570
VB332-4 Ol1	NT	92	5595	58	201	2.0	329	7.7	3.68	0.37	506	6	0.269	0.068	0.143	0.078	0.154	0.016
VB332-4 Ol2	NT	92	4105	188	225	1.4	398	7.7	4.06	0.65	368	7	0.255	0.048	0.147	0.059	0.256	0.053
VB332-6	NT	107	3978	48	197	5.0	306	6.7	3.49	0.68	393	10	0.345	0.089	0.910	0.336	0.205	0.057
VB332-7	NT	108	3991	99	207	5.9	286	3.0	3.42	0.74	381	11	0.339	0.125	0.255	0.087	0.298	0.058
VB332-9	NT	140	3839	80	209	8.9	290	8.4	4.34	0.56	374	7	0.460	0.121	0.218	0.045	0.357	0.070
VB332-10	OG	169	3836	42	195	3.8	377	9.0	3.16	1.10	278	8	0.508	0.176	0.098	0.042	0.267	0.089
VB332-11	OG	175	3643	76	179	2.0	344	4.3	3.33	0.69	286	14	0.506	0.087	0.497	0.166	0.289	0.135
VB332-12	NT	200	3931	36	207	1.7	284	7.4	2.97	0.56	340	10	0.500	0.221	0.332	0.107	0.220	0.047
VB332-13	OG	230	3819	46	215	4.1	285	9.5	3.89	0.82	328	9	0.763	0.761	0.291	0.252	0.210	0.044
VB332-15	NT	460	2547	45	256	11.7	1365	36.6	3.14	0.73	278	31	0.600	0.216	0.069	0.020	0.382	0.427
VB332-16	VTT	680	2989	36	216	6.5	1109	23.8	2.42	0.41	312	5	0.626	0.679	0.124	0.065	0.289	0.259
VB332-17	VTT	719	4718	157	249	17.1	1277	51.9	3.35	0.46	360	47	0.715	0.283	0.508	0.377	0.259	0.034
VB513-1	NT	15	2598	37	227	2.6	1247	17.6	3.50	1.49	262	11	0.368	0.038	0.205	0.046	0.942	0.803
VB513-2	NT	80	2621	27	241	5.2	1417	30.4	3.50	1.21	276	7	0.365	0.049	0.134	0.036	1.380	0.820
VB513-4	NT	105	2642	28	250	4.8	1524	39.7	2.99	0.86	284	14	0.381	0.051	0.114	0.032	0.790	0.445
VB513-5	NT	108	2748	92	248	7.2	1418	33.5	2.72	1.11	292	12	0.334	0.032	0.123	0.030	0.489	0.279
VB513-6	NT	110	2713	103	258	11.4	1491	31.7	2.01	0.73	281	15	0.402	0.150	0.074	0.011	0.558	0.492
VB513-7	NT	111	2701	56	271	8.8	1524	38.9	3.23	0.97	272	18	0.442	0.075	0.060	0.011	0.650	0.568
VB513-8	NT	160	2795	74	260	10.9	1455	23.9	4.99	1.78	284	16	0.502	0.019	0.145	0.045	1.237	0.734
VB513-10	NT	291	2511	28	252	3.4	1633	23.6	3.60	0.98	259	12	0.401	0.025	0.082	0.022	1.180	0.834
VB513-12	VTT	340	3106	89	242	3.5	895	12.8	2.28	0.50	319	15	0.385	0.157	0.412	0.149	0.374	0.236
VB513-13	UMF	384	2183	46	224	8.3	1472	62.4	2.93	1.03	163	16	0.361	0.054	0.061	0.021	0.528	0.303
VB513-14	UMF	386	2136	16	229	2.4	1830	82.3	3.28	1.12	108	24	0.471	0.106	0.061	0.018	0.501	0.278
VB513-16	OG	560	3341	327	247	12.9	1248	128.9	3.44	0.64	369	69	0.547	0.094	0.111	0.035	0.347	0.265
VB513-19	VTT	583	3518	74	213	15.5	921	33.8	2.27	0.29	498	16	0.474	0.067	0.310	0.175	0.261	0.040
VB513-21	NT	650	2548	57	239	7.0	855	17.2	4.09	1.71	302	9	0.624	0.208	0.070	0.015	0.831	0.628
VB513-23	VTT	705	4261	58	251	12.4	1556	43.2	2.80	0.52	428	11	0.644	0.182	0.365	0.177	0.263	0.017
VB513-24	BBS	710	4473	71	259	6.6	1371	42.6	3.58	0.55	392	15	0.619	0.140	0.877	0.138	0.297	0.034
VB513-25	BBS	740	4680	170	261	11.0	1004	42.6	4.89	1.39	311	16	0.990	0.852	0.521	0.159	0.307	0.038
VB516-1	NT	12	3406	54	190	2.7	66	2.2	2.20	0.31	272	5	0.296	0.052	0.366	0.115	0.228	0.029
VB516-4	NT	106	3314	48	204	6.0	111	6.9	5.29	0.83	290	8	1.475	0.587	0.247	0.164	0.442	0.140
VB516-6	NT	108	3558	37	190	5.6	98	3.0	4.21	1.07	321	7	0.852	0.309	0.639	0.134	0.447	0.122
VB516-7	NT	110	2931	159	212	6.8	112	3.0	2.28	0.44	267	9	0.360	0.188	0.134	0.050	0.159	0.034
VB516-9	NT	116	3042	48	214	11.9	115	6.4	4.58	1.19	295	11	0.928	0.303	0.186	0.040	0.639	0.329
VB516-10	NT	140	3189	66	207	7.8	131	5.8	5.28	1.16	267	10	0.914	0.222	0.236	0.035	0.811	0.427
VB516-11	VTT	199	2619	69	245	18.4	1539	89.4	3.16	0.66	310	6	0.740	0.174	0.069	0.017	0.234	0.023
VB516-13	VTT	240	2753	29	225	12.5	1516	92.4	2.21	0.63	275	18	0.498	0.057	0.143	0.034	0.320	0.058
VB516-16	VTT	280	2936	86	227	10.2	1385	96.8	4.01	1.12	324	9	1.404	0.758	0.615	0.116	0.630	0.224
VB248-1	NT	104	2480	22	235	4.0	1180	25.0	6.22	1.80	291	11	0.977	0.410	0.428	0.131	2.023	1.336
VB248-2	NT	106	2476	64	255	6.5	1466	40.7	4.50	0.95	285	15	0.448	0.077	0.100	0.041	1.171	1.112
VB248-5	NT	182	2075	15	236	4.0	1457	19.7	5.13	1.01	240	4	0.522	0.116	0.115	0.022	1.001	0.632
VB248-7	VTT	260	2096	17	271	10.8	1486	60.1	4.58	0.81	241	6	0.414	0.045	0.106	0.031	0.911	0.664
VB248-8	VTT	290	2209	48	238	2.7	1091	14.8	3.56	0.71	219	5	0.316	0.032	0.139	0.028	1.030	0.773
VB248-9	VTT	297	2036	29	232	4.2	1389	28.2	4.23	0.96	214	9	0.495	0.215	0.416	0.432	2.527	1.161
VB248-12	VTT	378	2509	48	192	14.5	1760	74.0	4.82	1.41	313	6	0.810	0.187	0.211	0.070	1.267	0.304
VB248-14	UMF	442	2591	51	220	8.4	1877	70.2	4.49	1.44	237	47	0.559	0.125	0.402	0.205	1.285	0.694
VB248-15	BBS	559	4375	118	196	12.0	935	34.6	3.77	1.16	724	21	0.546	0.108	0.251	0.130	0.533	0.446
SVB96-02-02	OG	8	3846	59	224	8.6	512	32.5	3.39	0.31	443	8	0.372	0.088	5.215	2.021	1.894	0.408
SVB96-02-03	OG	22	3919	32	262	6.1	581	48.9	4.09	0.65	463	12	0.508	0.204	5.721	1.080	2.204	0.412
SVB96-02-05	OG	69	4746	208	233	7.9	186	15.9	4.56	1.15	541	16	0.532	0.194	8.008	1.173	2.223	0.471
SVB96-10-90	TG	21	4496	237	241	14.9	635	20.5	4.53	0.62	539	23	0.621	0.376	8.319	2.072	1.896	0.505
SVB96-10-91	TG	30	4042	320	238	8.8	281	93.2	3.80	0.76	437	36	0.508	0.132	6.126	2.414	2.941	0.823
SVB96-27-01	Cg G	1.2	4237	125	184	6.0	178	9.1	5.23	1.73	410	7	0.407	0.289	5.770	2.463	1.926	0.929
SVB98-113-168	Fg G	98.9	3723	109	284	12.1	498	37.6	6.28	1.16	525	40	0.468	0.123	0.983	0.520	0.989	0.416
SVB97-92-161	Fg G	246.6	4332	97	235	33.1	360	43.3	6.80	0.65	524	22	0.534	0.269	1.683	0.889	0.406	0.066
SVB97-79-144	Mg G	632.6	2598	38	209	11.7	1437	66.2	4.55	1.82	280	11	0.679	0.262	1.705	0.185	2.258	0.294
SVB97-79-147	Mg G	729.3	4290	82	219	9.2	440	28.9	6.76	1.43	484	21	0.731	0.125	3.558	0.902	1.702	0.699
SVB97-92-03-Ol1	Cg BG	186.8	5378	145	178	2.1	117	2.4	6.61	0.99	455	29	0.540	0.262	2.316	0.924	0.897	0.632
SVB97-92-03-Ol2	Cg BG	186.8	3948	358	220	3.9	192	28.6	6.74	1.24	321	30	0.377	0.039	0.820	0.398	0.578	0.162
SVB98-102-150	Cg BG	75.8	4635	336	186	13.0	137	5.2	5.04	1.05	396	23	0.294	0.127	2.389	1.756	1.617	0.888

Parameters for AFC modeling (compositions of model liquids)[1]

basaltic liquid[X]			1600		75		290				140							
model gneiss[Y]			20000		30		50				250							

Partition coefficients ($D_{min/melt}$) for basaltic melt[2]

olivine			1.3-1.6		3.5		9.0				1.5-2.2							
plagioclase			0.04		0.10		0.06				0							
clinopyroxene			1.2		1.3		2.1				0							
sulfide			0.30		61		200				1							
Fe-Ti oxide[Z]			1.9		2.2		3.8				0							

Fig. 4.6 (previous page): Plots of selected trace elements versus forsterite content of VBI and PLI (abbreviated as SVB for South Voisey's Bay) olivine. The samples are plotted as averages from individual lithologies. In brackets is the number of samples per lithology and the total number of measured olivine data points. Error bars denote 1σ sample internal error (variability). Colored fields enclose olivine from similar host rocks. Inlet in A) implies the potential change in composition due to the trapped liquid shift and reequilibration with sulfides (after Li et al., 2000). Ellipses with MO indicate the composition of primitive mantle olivine (partly from DeHoog et al., 2010; partly unpublished data from WGR olivine – Chapter 2). Fields of VB266 in E) and F) are BBS samples from Chapter 3. Black lines denote calculated Rayleigh fractionation model lines (FC and AFC ML) to replicate the apparent olivine trends derived from four possible scenarios (see Chapter 3 for details): **1** – the crystallization of ol:plag:cpx, in a ratio of 1:3:0.2 (solid lines with circles; 1_{290} and 1_{60} have an initial melt Ni content of 290 and 60 ppm, respectively); **2** – the segregation of a sulfide liquid after 10% crystallization of ol:plag:cpx in a ratio of 1:3:0.2 to 0.08 sulfide (solid line with triangles); **3** – the crystallization of ol:plag:cpx and a Fe-Ti oxide phase (ilmenite $\pm$titanomagnetite $\pm$magnetite) in a ratio of 1:3:0.45:0.3 (solid line with squares); **4** – is based on model curve FC-1 with the fractionated melt assimilating 10% of Mn-Zn-rich upper crustal rock (solid line with diamonds) after 45% crystallization. Symbols (and numbers) on model lines indicate the degree of crystallization in 5% increments. Parameters used for calculations are listed in Table 4.1 and described in detail in Chapter 3.
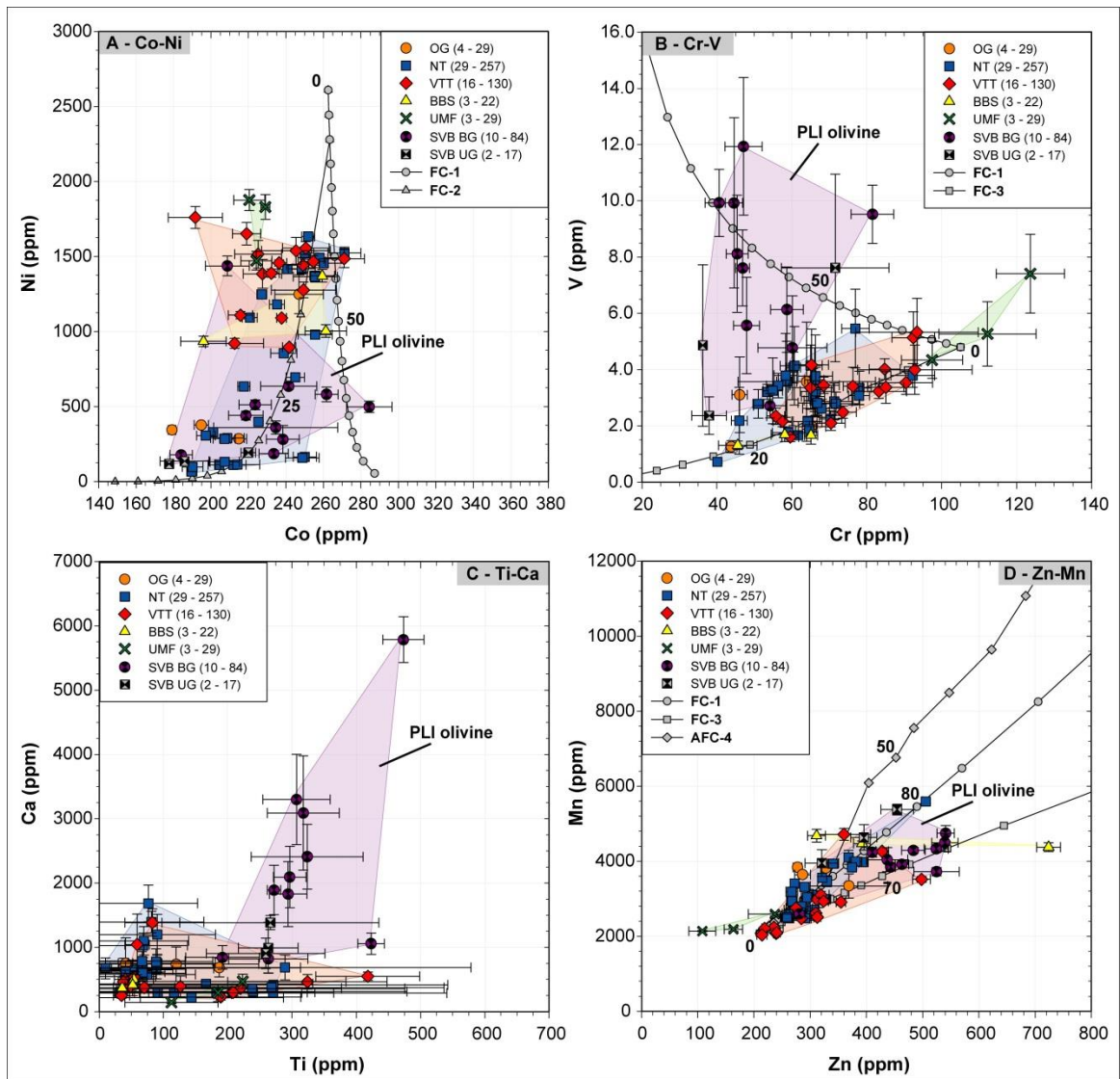
Fig. 4.7: Plots of selected trace elements from EDI and PLI olivine. See Fig.4.6 for description of model lines.

4.5.2.1. Olivine from the Voisey's Bay and Pants Lake Intrusions

(1) Nickel. Ni concentrations in the VBI vary considerably in accord with the Fo content, from 66 ppm (Fo61; VB516-1-NT) to 1,877 ppm (Fo80; VB248-14-UMF) (Fig.4.6A). UMF samples contain the most primitive olivine (high Ni-Fo; Fig.4.6A – green field), and BBS, the lower part of the VTT, and the OG the most evolved (low Ni-Fo; Fig.4.6A). There are also some exceptional excursions – the low-Ni olivine from the Fe-Ti oxide-rich succession in the NT (VB516 and VB307) and the Ni-depleted interval in VB332 (92–230m). Two general groups can be subdivided; group one contains olivine with more than 500 ppm Ni and group two comprises olivine with less than 500 ppm Ni (Fig.4.6A). Olivine from the PLI has on average low Ni concentrations, coupled with higher Fo contents (117 ppm to 635 ppm Ni; Fo43 to Fo64) and falls in group two (Fig.4.6A – purple field). However, a single melagabbro sample from the SI (SVB97-79-144) has a more primitive composition (1,437 ppm Ni and Fo80) and lies in the group one field for EDI olivine (Fig.4.6A). Nickel is negatively correlated with the Fo content, and decreases with proceeding differentiation of the melt, whereas the Fo-Ni heterogeneity in most NT-VTT olivine from the EDI is most likely a result of the trapped liquid shift, where interaction with an intercumulus silicate liquid caused a (disequilibrium) increase in Fe relative to Ni (Barnes, 1986; Chalokwu and Grant, 1987; Fig.4.6A inset). The positive correlation of Fo-Ni in some BG olivine from the PLI implies a reequilibration with a sulfide-liquid (Li et al., 2001).

(2) Cobalt. Co varies from 179 ppm (VB332-11-OG) to 271 ppm (VB248-7) in VBI olivine and from 178 ppm (SVB97-92-03) to 284 ppm (SVB98-113-168) in PLI olivine

(Fig.4.6B). The Co concentration in olivine is, in both intrusions, positively correlated with the sulfide content of the sample. For example, the highest Co sample from the PLI contains ~20 vol.% sulfide, whereas the lowest Co samples have less than 1.5 vol.% (Fig.4.6B – purple field). Only in samples from the EDI does Co show a weak negative correlation with Fo (Fig.4.6B – blue-red fields). The lack of a systematic relationship between Ni and Co (Fig.4.7A) in EDI olivine indicates that the Co composition was also influenced by sulfide saturation and reequilibration processes in an open magma system, although to a lesser extend than Ni. The Co content in olivine from the PLI displays a weak positive correlation with Ni (Fig.4.7A – purple field) that might indicate a systematic decrease through FC or an increase through subsolidus reequilibration with sulfides.

(3) Chromium. Cr is a refractory element, even though slightly incompatible in olivine ($D^{Cr}_{ol/sil}$~0.8; Beattie, 1994; Gaetani and Grove, 1997), and displays an overall gradual and continuous decline with increasing Fo content in EDI olivine (from primitive Mg-rich to more evolved Fe-rich); from 124 ppm (VB248-14-UMF) to 44 ppm (VB332-10-OG), (Fig.4.6C). In the PLI, olivine has an average Cr content of ~50 ppm and falls on the lower end of the Cr-Fo trend (Fig.4.6C – purple field). The Cr content of most VBI olivine also decreases in tandem with the V concentration (Fig.4.7B), which is attributable to the preferred partition of both elements by co-crystallizing Fe-Ti oxides – as evident by the low Cr contents of NT olivine associated with cumulus Fe-Ti oxides (e.g., VB513).

(4) Titanium. Ti ranges from 32 ppm (VB332-15-NT) to 418 ppm (VB248-12-VTT) in EDI olivine, and from 192 ppm (SVB97-92-161) to 473 ppm (SVB97-79-147) in PLI olivine (Fig.4.6D). The uncontaminated Ti values in the PLI are consistently high and have no systematic correlation with the Fo content (Fig.4.6D – purple field). In the EDI, only the "contaminated" olivine from DDH VB248 and VB513 contain anomalously high Ti contents (circa >120 ppm Ti), whereas all other samples exhibit a narrow compositional range (30–80 ppm) and a weak positive correlation with Fo (Fig.4.6D). These low values are common for mantle olivine (e.g., O'Reilly et al., 1997; DeHoog et al., 2010) and reflect the very low partition coefficient of Ti between olivine and silicate melt ($D^{Ti}_{ol/sil}$ ~0.052; Zanetti et al., 2004 and references therein).

(5) Manganese. Mn varies from 2,037 ppm (VB248-9-VTT) to 4,718 ppm (VB332-17-VTT) in EDI olivine and generally increases from the upper NT to the lower part of the VTT and BBS (Fig.4.6E – blue and red fields). Concentrations in olivine from the PLI are higher, with an average of ~4,299 ppm Mn (Fig.4.6E – purple field). The melagabbro sample SVB97-79-144 has the lowest Mn content (2,598 ppm ±39 1σ) (Fig.4.6E). All samples show a positive correlation of Mn with the Fe content, and the average Fe/Mn ratio of VBI olivine is ~62 and of PLI olivine ~64. This is much higher than the average Fe/Mn ratio of ~25 for BBS olivine from VB266 (Chapter 3; shown as a separate field outline in Fig.4.6E) and of ~7 for average mantle olivine (e.g., O'Reilly et al., 1997). Manganese is also positively correlated with Zn, reflecting their mutual correlation with Fe (Fig.4.7D), with a progressive increase in both elements from the most primitive olivine (UMF interval of VB513) towards the most evolved olivine (lower VTT and BBS

samples). Olivine from the PLI is generally even more differentiated than those from the VBI, and most plot in the highest Mn-Zn segment (Fig.4.7D – purple field).

(6) Zinc. Zn ranges from 108 ppm (VB513-14-UMF) to 724 ppm (VB248-15-BBS) in EDI olivine, and from 281 ppm (SVB97-79-144) to 541 ppm (SVB96-02-05) in PLI olivine (Fig.4.6F). The low Zn values from UMF sample VB513-14 fall in the field for presumably uncontaminated ultramafic samples (VB544-1; Chapter 3) and thus represent the most primitive olivine found in this study. In general, Zn exhibits a negative correlation with the Fo content and describes a FC trend whereby the PLI olivine are the most evolved, occupying the high-Zn, low-Fo area (Fig.4.6F – purple field). In addition, PLI samples form two sub-groups with different Zn-Fo(-Mn) slopes (Fig.4.6F and 4.7D). Olivine from the UG has less Zn with decreasing Fo than olivine from the BG (Fig.4.6F – grey and purple symbols, respectively). The barren troctolitic lithologies in the EDI (NT and upper VTT) contain olivine with lower Zn concentrations than the mineralized lower VTT and the BBS, and the highest Zn sample (VB248-15-BBS) also lies in the field for BBS olivine from VB266. However, in contrast to the high Zn and high Mn samples from VB266 (Fig.4.7D), EDI samples from this study have much less Mn.

(7) Vanadium. V ranges from 1.3 ppm (VB332-10-OG) to 7.4 ppm (VB248-14-UMF) in VBI olivine, and from 2.4 ppm (SVB98-102-150) to 12 ppm (SVB96-10-90) in PLI olivine (Fig.4.7B). The average value of ~6.8 ppm V for PLI olivine is higher than values of typical mantle olivine (~4.3 ppm V; DeHoog et al., 2010) and is twice as high as for the EDI (~3.2 ppm V). However, olivine from the EDI trend from a higher to lower V-Cr composition with increasing grade of differentiation (UMF-NT-VTT-OG-BBS),

reflecting a decrease in V-Cr concentration from UMF and NT olivine to OG and BBS olivine (Fig.4.7B). Samples from the PLI have very diverse V compositions but lack the systematic relationship with Cr content (Fig.4.7B – purple field).

(8) Calcium. The large divalent Ca cation is highly incompatible in olivine ($D^{Ca}_{ol/sil}=$ ~0.052; Zanetti et al., 2004 and references therein), but readily fractionates into anorthite-rich plagioclase, which co-precipitated with olivine in the EDI and PLI. Concentrations in EDI olivine vary from 143 ppm Ca (VB513-14-UMF) to 1,685 ppm Ca (VB516-4-NT). PLI olivine has much higher Ca contents (821 ppm to 5,785 ppm). Variable pronounced positive correlations exist between Ca and Fo in EDI olivine, and Ca and Ti in olivine from the PLI (Fig.4.7C). However, the Ca and "true" Ti values of NT-VTT olivine from VB516 (Fig.4.7C) exhibit an almost identical slope to those from the PLI, except the lower total element concentration, whereas the biased Ti-rich olivine from the VBI has lower Ca concentrations.

4.5.2.2. Trace Element Abundance Distribution in EDI and PLI Olivine

In Figure 4.8A olivine from all sampled UMF from the EDI (from VB513 and VB248), the melagabbro sample from the South Intrusion at Pants Lake (SVB97-79-144), and two UMF samples previously presented in Chapter 3 (VB552-15B and VB544-1) are normalized to the composition of primitive mantle olivine (MO, Western Gneiss Region, Norway; unpublished data – Chapter 2). The olivine compositions are more variable from Zr to Cr, although with very uniform values for Sr and Cr, than from Mn to Cu. The PLI melagabbro contains the most evolved olivine, whereas olivine from the melatroctolite

VB544-1 is the least evolved. Figure 4.8A also demonstrates that UMF olivine is fairly heterogeneous in composition, based on the overall distribution of incompatible elements.
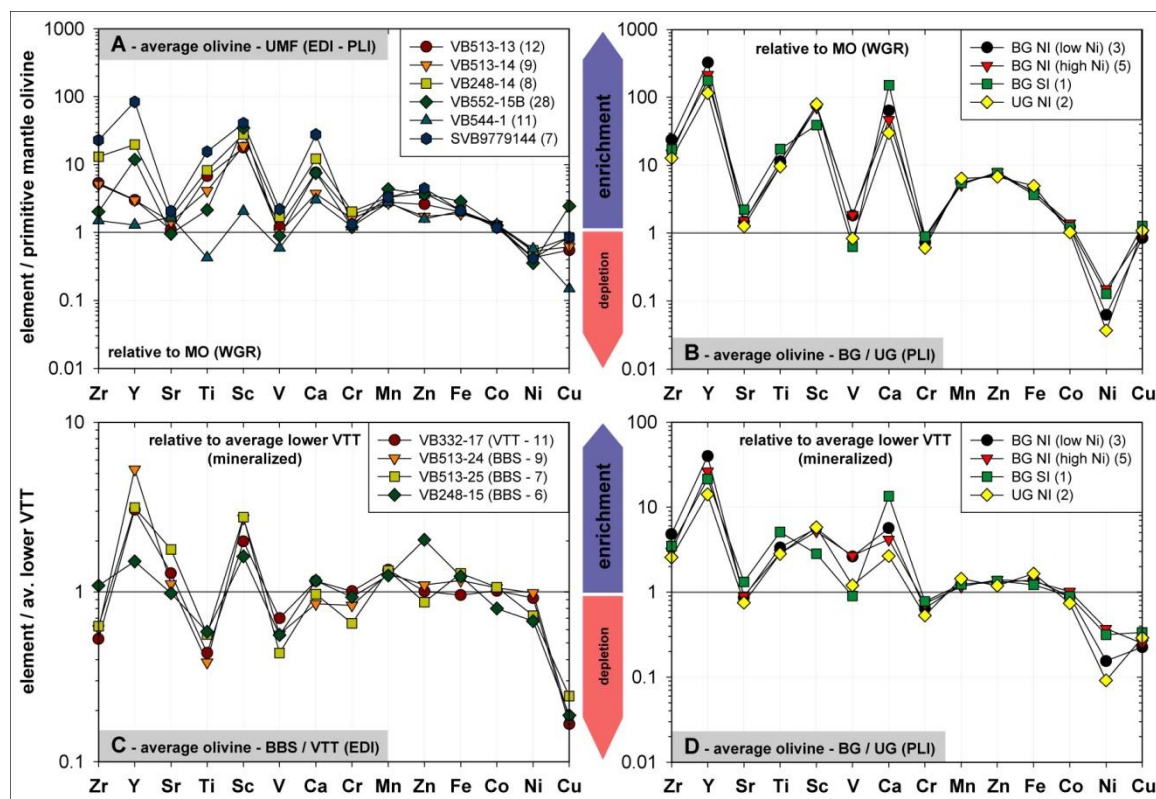
Fig. 4.8: Multi-trace element diagrams showing the average olivine composition of selected lithologies from the EDI and PLI. Primitive mantle olivine normalized (MO WGR, unpublished data – Chapter 2) multi-trace element diagrams displaying the average olivine composition from A) UMF olivine from this study and samples VB552-15B and VB544-1 (presented in Chapter 3) and B) Olivine from the UG and BG sequence of the PLI. C) and D) depict enrichment-depletion diagrams relative to average lower VTT olivine from VB266 and VB552 (Chapter 3) for the trace element composition of EDI olivine from the BBS and lower VTT intervals, and the UG and BG sequence from the PLI, respectively.

In Figure 4.8B, samples from the PLI are subdivided into Upper and Basal Gabbro (UG and BG) successions from the NI and the SI respectively. The olivine compositions are relatively homogeneous, and all PLI gabbro samples illustrate pronounced enrichments in Zr, Y, Ti, Sc, and Ca content (up to 200x MO). The transition metal concentrations (plus Mn and Zn), especially, are nearly constant in all samples (Fig.4.8B), with the highest enrichment values in Mn and Zn (~6x MO). The one exception is the Ni distribution, which is distinctly lower in olivine from the PLI, with the lowest concentrations in UG olivine (0.04x MO).

In Figures 4.8C and 4.8D, respectively, EDI samples from the BBS and lower part of the VTT that contain potentially prospective olivine compositions for Ni-exploration, and the grouped gabbro samples from the PLI (from Fig.4.8B), were plotted relative to the average composition of olivine from the mineralized, lower VTT that is intersected in VB266-VB552 (Chapter 3). The mineralized, lower VTT contains olivine with elevated Mn and Zn contents, which reflect a transition from the nominally barren upper VTT towards the BBS sequence, which is associated with massive sulfide mineralization in VB266-VB552. The progressively Mn-Zn-rich composition most likely represents crystallization (±olivine-sulfide liquid interaction) in a very favorable sulfide ore-forming environment and proximity to massive sulfide mineralization, and as such is of great interest as a geochemical indicator of proximal ore mineralization (Chapter 3). Unlike VB266 (or VB552), the additional BBS (VB513 and VB248) and VTT (VB332) samples from this study do not explicitly transect the massive sulfide mineralization at the base of the EDI and the immediately proximal BBS. In that specific case, olivine from the

troctolitic chamber horizons is expected to be less enriched in Mn and Zn than olivine from the heavily contaminated and sulfide-rich VB266 (and other DDH) (Fig.4.8C). The distribution of most other trace elements in olivine from BBS and VTT, however, is quite similar to lower VTT olivine, with the notable exception of Y and Sc, which are 2 to 5 times more enriched (Fig.4.8C), and Ti and V, which are slightly depleted (0.4 to 0.6x).

The gabbroic rocks from the PLI on the other hand, contain olivine of very different composition (Fig.4.8D). All measured olivine grains from UG and BG lithologies are strongly enriched in the incompatible elements Zr, Y, Ti, Sc, and Ca, with enrichment factors of 2 (for V) to almost 40 (for Y). The mafic melt reservoir crystallizing the PLI olivine must have been much richer in lithophile incompatible elements (more differentiated) than the contaminated (BBS and VTT) melt(s) at the EDI. The Cr and Ni contents of PLI olivine are uniformly depleted with respect to lower VTT olivine from the EDI. This observation is in accord with the derivation of PLI olivine by FC from a melt with a higher degree of differentiation that experienced late sulfide segregation and concomitant Ni depletion.

In summary, the key trace element variations in olivine from the EDI and PLI are:

1. The olivine chemistry in the EDI is characteristic of their specific host lithologies – UMF and the NT contain the most primitive olivine (Fo-Ni-Cr-rich), the VTT contains olivine of intermediate composition, and the lower VTT, BBS and OG have the most evolved olivine (Fe-Mn-Zn-rich).

2. EDI olivine is on average more primitive than PLI olivine, with higher Fo-Cr-Co-Ni contents – exceptions are the Ni-poor NT intervals in the EDI.

3. PLI olivine has much higher contents of incompatible, lithophile elements such as Y, Ti, Sc, and Ca than EDI olivine, and is generally Ni poor (<500 ppm).

4. UMF olivine shows a range in chemistry (e.g., low to high Zn) with respect to its stratigraphic position in the EDI (upper VTT or contaminated, lower VTT).

5. Olivine from DDH that intersect the VTT and BBS distal to the massive sulfide mineralization in the EDI shows an increase in Mn-Zn, but are not as enriched in these elements as olivine in direct proximity to massive sulfides (e.g., VB266 and VB552 – Chapter 3).

4.6. Discussion

4.6.1. The Petrogenetic Importance of Ultramafic Rocks in the Formation of the EDI

Ultramafic inclusions in the EDI (UMF) primarily comprise fragments of dunite to melatroctolite, and are most commonly associated with the BBS and the lower part of the VTT (e.g., Lightfoot and Naldrett, 1999; Li and Naldrett, 1999; Li et al., 2000). They are centimeter-sized, irregularly-shaped and commonly highly serpentinized. The most primitive olivine composition observed within the UMF (Fo81 and 2,619 ppm Ni; Li and Naldrett, 1999) is commonly used as a starting point for VBI fractional crystallization models, since the UMF are interpreted as disrupted remnants of early (primary) magmatic cumulates (Lightfoot and Naldrett, 1999; Li and Naldrett, 1999; Li et al., 2000). However, olivine from UMF, overall, displays considerable variations in Fo and Ni

contents (Fo71 and 1,283 ppm Ni to Fo81 and 2,619 ppm Ni; Li and Naldrett 1999), which may reflect more their spatial position in the VBI magmatic system (conduit-mineralized *versus* chamber-sulfide-bearing to sulfide-free environment; RBZ *versus* EDI etc.) than their magmatic origin. It is therefore essential to first link UMF olivine compositions to a specific magmatic environment before using them as a compositional anchor in petrogenetic studies.

This consideration is especially important because UMF are also reported from the NT at the top of the EDI stratigraphy (e.g., VB266 – Lightfoot et al., 2012; VB544 – Chapter 3), and a continuous melatroctolite horizon is partly exposed on surface for several hundred meters (P. Lightfoot pers. comm.). This same outcropping sequence of sugary-textured and weakly layered melatroctolite appears intersected by VB544 (VB544-1; Chapter 3) where it contains strongly serpentinized olivine of very primitive composition, distinctly different to that found in the partially mineralized UMF from the BBS (Fig.4.8A; Chapter 3). Consequently, it was concluded in Chapter 3 that at least two compositionally different UMF generations (UMF in NT *versus* UMF in the BBS) occur in the VBI, which may record, 1) multiple generations of variably primitive early-magmatic cumulate(s) transported upwards episodically (with NT, VTT and finally BBS) from a lower (staging) chamber at various times during the petrogenesis of the VBI, or 2) a diffusive reequilibration of UMF olivine entrained and turbulently transported in a contaminated and sulfide-rich carrier melt that eventually produced the BBS in the EDI (Chapter 3), or 3) several alternative (early-genetic, in the case of the UMF in the NT)

emplacement routes (feeder conduits) into the EDI (see Lightfoot and Evans-Lamswood, 2012; Lightfoot et al., 2012).

We examined these hypotheses with specific reference to UMF samples from two intervals in the VTT (VB248-14; VB513-13 and-14) and a comparative ultramafic sample from the PLI (SVB97-79-144). Samples from VB513 are dunitic in composition and occur in a VTT succession about 400m above the BBS, whereas the UMF from VB248 is a melatroctolite from a variably contaminated VTT sequence ~110m above the BBS (Vale, unpublished DDH logs). In accord with hypothesis 2), the two VBI intervals contain compositionally different olivine (Fig.4.8A), VB248-14, from the more contaminated VTT, has a higher concentration of incompatible trace elements (Zr, Y, Ti, Sc, V, Ca) for its nominal Fo content than the UMF from VB513, and also Mn and Zn contents closer to UMF from the BBS (VB552-15B; Chapter 3). Conversely, the two dunitic samples from VB513 have compositions similar to the more primitive UMF from the NT (VB544-1; Chapter 3), including equally low Mn and Zn (see also Fig.4.7D) – the element concentrations that are most obviously increased by assimilation of country rock.

In addition to UMF from VBI, the cumulate melagabbro sample (SVB97-79-144) from the BG in the South Intrusion of the PLI was plotted on Figure 4.8A. This altered, serpentinized melagabbro contains reacted (Tasiuyak) paragneiss inclusions (hercynite ±albite-rich plagioclase assemblage; Fig.4.2F). The olivine analyzed in the direct vicinity of these inclusions is found to be as trace element enriched and reequilibrated as the UMF from the BBS at VBI (VB552-15B; Fig.4.8A). Except for the Fe and Mn contents, which are more primitive in the PLI, their composition is in fact quite similar, and thus, on a

geochemical basis, two endmember compositions for olivine from UMF can be established; 1) an enriched composition (VBI BBS and to a lesser extent the PLI melagabbro), and 2) a primitive composition (NT UMF – VB544-1). All other measured UMF samples fall approximately in a compositional array between those two endmembers (Fig.4.8A). This implies that the presence of, and the proximity to, partially reacted (paragneissic) xenolith inclusions induces an olivine trace element enrichment, whereas UMF further removed from contaminated sequence(s) retain their more primitive olivine composition.

As a potential explanation, diffusive reequilibration (solid-liquid) of especially Mn, Zn and Fe into the olivine, and Ni and Mg out of the olivine into the surrounding melt has likely caused the selected element enrichment in UMF olivine entrained in the BBS (Chapter 3). In fact, the partial assimilation of ultramafic cumulates by ascending basaltic melts and the simultaneous diffusive reequilibration of remnant olivine xenocrysts has been demonstrated for very short timescales in volcanic environments (Costa and Dungan, 2005) and also for BBS olivine enclosed by sulfide (Chapter 3). Divalent cations such as Fe-Mg, or Co, Ni, Mn and Zn have the highest diffusivity in olivine, depending on temperature, pressure, oxygen fugacity and composition (e.g., Ito et al., 1999; Petry et al., 2004; Costa and Dungan, 2005; Chakraborty, 2008; Spandler and O'Neill, 2010; Quian et al., 2010). In UMF olivine, these particular elements are preferably enriched (Fe, Mn, Zn) or depleted (Mg, Ni) relative to the most primitive olivine composition. It was shown in Chapter 3 that ~3,000 ppm Mn can diffuse a distance of 0.7mm in the olivine structure in less than 160 yrs at 1,000ºC. In a scenario where centimeter-sized xenoliths of

UMF containing olivine in the size range smaller than 0.5mm are entrained and transported in a contaminated basaltic melt, solid-liquid diffusive reequilibration between olivine and surrounding melt can thus rapidly modify and homogenize the olivine composition depending on the temperature and immediate melt environment (strong chemical gradient) (e.g., Costa and Dungan, 2005).

In conclusion, the observed trace element enrichment and chemical homogeneity at crystal-scale and at xenolith-scale in UMF olivine incorporated in the contaminated BBS and lower VTT is likely obtained through diffusion during transport in a contaminated and sulfide-rich basaltic carrier liquid, after disaggregation of initial cumulate layers in a lower staging chamber, and thus does not necessarily reflect a primary magmatic feature. The UMF (melatroctolite horizon) in the NT (VB544-1), on the other hand, did not experience this reequilibration process, since the lack of a chemical gradient between the incorporated UMF and the primitive and uncontaminated primary melt of the NT probably retarded any subsequent trace element diffusion and thus compositional modifications of the olivine. In addition, an alternative emplacement route into the EDI may have aided in the preservation of their original composition.

4.6.2. Compositional Variability of Olivine as a Response to Open-System Processes

4.6.2.1. Link between Ti and V in Olivine, Precipitation of Fe-Ti oxides, and fO₂

Ti and V are similarly incompatible in olivine (e.g., Colson et al., 1988; Beattie, 1994; Zanetti et al., 2004), but the partitioning behavior of V between olivine and basaltic melt is strongly governed by the valence of V (which is either V^{3+} and V^{4+} in most terrestrial magmas), and thus depends strongly on the prevalent fO_2 (Canil, 1997; Canil and Fedortchouk, 2001; Papike et al., 2005). Olivine prefers to incorporate V^{3+} – and since the V^{3+}/V^{4+} ratio of a mafic melt decreases substantially with increasing fO_2, the bulk partition coefficient $D^V_{ol/sil}$ decreases as well. Therefore, V partitioning into olivine has been used as an alternative oxygen barometer in various studies of terrestrial and extraterrestrial basalts (Canil, 1997; Canil and Fedortchouk, 2001; Papike et al., 2005; Shearer et al., 2006).

Titanium, in contrast, is only present as Ti^{4+} under terrestrial fO_2 conditions and the substitution into olivine is, paradoxically, unaffected by small changes in the oxygen fugacity of a mafic melt (Papike et al., 2005 and references therein). This behaviour is similar to Cr ($D^{Cr3+}_{ol/si}$ and $D^{Cr2+}_{ol/si}$), which is also consistent over a range of fO_2 conditions. As a result, the co-variation of V with Ti and Cr (and other trace elements) during crystallization is affected by the fO_2 via changes in V partitioning. However, the co-precipitation of Fe-Ti oxides such as ilmenite and titanomagnetite, which have variable, but strong, preferences for V, Ti and Cr (e.g., Klemme et al., 2006) will deplete the melt in all three (as reflected by model line FC-3 in Fig.4.6C–D and 4.7B). This latter

process is recorded by the positive correlation of V-Cr (Fig.4.7A – FC-3) in EDI olivine. Olivine from the PLI on the other hand, has erratic V-Cr (Fig.4.7A – purple field) distributions, and this decoupling (and the generally elevated V and Ti concentrations) could be a reflection of the observed absence of Fe-Ti oxides co-crystallizing with olivine on the liquid line of descent (e.g., Smith, 2006). Most of the high Ti (more than 200 ppm) values in VBI olivine reflects the incorporation of μm-sized lamellae of Fe-Ti oxide(s) (Fig.4.3) into the analyses, and these likely exsolved from the host olivine during cooling of the intrusion. Similar occurrences have been identified in olivine from layered intrusions, such as the Upper Zone in the Skaergaard Intrusion, or the Eucrite Series in the Cullin Complex, Isle of Skye, and may in fact be common in slowly cooled mafic intrusions (Moseley, 1981). During the crystallization of olivine, Ti^{4+} likely substituted for tetrahedral-coordinated Si^{4+} and subsequently exsolved during subsolidus cooling, forming a stable separate phase (ilmenite ±titanomagnetite) (Moseley, 1981). Intercumulus Fe-Ti oxides in these exsolution-bearing olivine samples indicate the availability of Ti^{4+} in the primary melt. In contrast, several samples from VB516 and VB307 that contain early-crystallizing liquidus Fe-Ti oxides have olivine with low, "uncontaminated" Ti and V concentrations, and which are largely devoid of any exsolution lamellae. This correlation indicates that Fe-Ti oxides are equilibrium, liquidus minerals in this sequence of the NT. The associated olivine, however, are also highly Ni-depleted (Fig.4.6A). This Ni (±Co) depletion can result from sulfide segregation after 10% FC (Fig.4.6A–B – FC-2) or an interaction with a Ni-poor sulfide fraction that initially scavenged the primitive melt (FC-1$_{290}$) of chalcophile elements (primarily Ni and

Co) before olivine crystallization commenced (FC-1$_{60}$), leaving behind a depleted silicate melt reservoir (~12 ppm Ni at 45% crystallization – Fig.4.6A; with D$^{Ni}_{ol/sil}$ = 9, Li et al., 2003b). This reequilibration may also have caused a concomitant increase in fO$_2$ due to an increase in melt Fe^{3+} (e.g., Baker and Moretti, 2011 and references therein), which in turn may have provoked the crystallization of ilmenite ±titanomagnetite (e.g., Snyder et al., 1993). The petrogenesis of this Fe-Ti oxide-rich, and Ni-depleted, interval in the NT may thus be intimately related to the observed process of metal tenor upgrading in the VBI – with the high tenor disseminated sulfides in the "chamber" of the EDI (e.g., [Ni]$_{100}$ = 4–8%; Lightfoot et al., 2012) derived from the same process that produced primary titanomagnetite and induced the Ni depletion in olivine.

In contrast, the gabbroic rocks of the PLI have no Fe-Ti oxides (ilmenite or titanomagnetite) and only minor occurrences of magnetite (as a late-crystallizing or alteration phase), with the exception of some rare "early" magnetite in the sulfide-rich fractions of the PLI (e.g., in disseminated sulfides of the "leopard-texture gabbro"; e.g., Kerr, 1999). Consequently, V-Cr (Fig.4.7A) values of olivine display no correlation, and absolute V and Ti concentrations are generally higher than at the VBI. Further, the elevated Ti contents are much more homogeneous (lower intra-sample variation; Table 4.1) than for the lamellae-bearing "biased" EDI olivine. Post-SIMS characterization of two PLI samples by SEM revealed that exsolution lamellae of Fe-Ti oxides are generally absent (Fig.4.3B and 4.3D). This implies that the PLI olivine precipitated from an Fe-Ti oxide undersaturated magma, very likely at lower prevalent fO$_2$ than the EDI. In addition,

conditions in the PLI favored a higher V^{3+}/V^{4+} ratio and thus a preferred partitioning of V into olivine (e.g., Canil and Fedortchouk, 2001).

As is the case for the VBI, the assimilation of Tasiuyak paragneiss, which is both sulfide- and graphite-bearing, by PLI magma(s), might have acted as a significant reducing agent (Brenan and Li, 2000; Brenan and Caciagli, 2000). In comparison to the EDI, however, the PLI was deprived of subsequent fresh surges of primitive, more oxidized (and potentially sulfur saturated) mafic melts, and hence the oxygen fugacity probably remained too low for the precipitation of primary Fe-Ti oxides – instead producing only minor late-stage magnetite. The lower average Cr contents of PLI olivine also support this hypothesis. Partitioning of Cr into olivine is relatively unaffected by fO$_2$ variations (Papike et al., 2005 and references therein), and the Cr distribution shows no correlation with V and is hence also unaffected by oxide fractionation. The uniformly low Cr concentration must therefore either reflect an earlier Cr depletion of the primary magma of the PLI (e.g., higher differentiation state) or retention of Cr in the mantle source, as opposed to the more primitive Cr-rich composition of the VBI magma(s).

In summary, the presence of abundant liquidus Fe-Ti oxides associated with Ni-depleted olivine in a laterally correlatable NT succession in the EDI may be a petrological record of an early silicate:sulfide melt interaction in this batch of mafic magma, which was conducive to high R-factor metal tenor upgrading of an existing sulfide fraction – a process considered extremely beneficial to the formation of an economic Ni-Cu sulfide deposit (e.g., Naldrett, 1997, 1999; Maier et al., 2001). Thus far, a similar record has not been detected within the PLI (Li et al., 2001).

4.6.2.2. Link between Contamination and Economic Sulfide Ore Formation

The requirement for a primitive basaltic melt to incorporate external sulfide or silica-rich crustal material in order to achieve timely sulfide saturation is commonly regarded as a necessity in the formation of economic Ni-Cu sulfide deposits (e.g., Naldrett, 1997, 1999; Arndt et al., 2005; Keays and Lightfoot, 2010; Ripley and Li, 2013). The VBI is no exception, and several studies have proposed that the Tasiuyak paragneiss is the likely source of external sulfur that promoted sulfide saturation in VBI magmas (e.g., Lightfoot and Naldrett, 1999; Ripley et al., 2002). However, contributions from the surrounding orthogneiss lithologies (Nain and Enderbitic Gneisses) are also evident (e.g., Lightfoot and Naldrett, 1999; Lambert et al., 2000; Amelin et al., 2000) and display an apparently increasing role from the western part (RBZ) towards the EDI (Ripley et al., 2002 and references therein), which is mainly emplaced in enderbitic orthogneiss. A clear discrimination between the multitude of potential contaminants based solely on bulk rock chemistry (isotope and elemental) is still highly ambiguous, and very likely impossible due to the inherent mixing and mechanical mingling of all components in the VBI. Although a deconvolution of the major contaminants at the VBI is hence problematic (Lambert et al., 2000; Ripley et al., 2002; Chapter 3), the contaminated basal sequence (BG) in the PLI is probably unbiased by these multiple mixing signatures, and should reflect exclusively the input of its Tasiuyak paragneiss host (e.g., Kerr, 1999; 2003). The fact that economically significant sulfide mineralization is currently only recognized in the VBI may be used as starting point to examine the link between contamination, sulfide mineralization and olivine composition.

Stable isotope (δ^{34}S, δ^{18}O; Ripley et al., 2002 and references therein) and radiogenic

isotope (Re-Os, Rb-Sr, Sm-Nd, U-Th-Pb; Amelin et al., 1999, 2000; Lambert et al., 2000;

Li et al., 2000) analyses (of both sulfide minerals and whole-rock) have previously been

used to characterize the degree of crustal contamination in the VBI. Quantifications for

the VBI range from 5 to 30% assimilation of Tasiuyak paragneiss (Ripley et al., 1999;

Amelin et al., 2000) to ~16% of Nain orthogneiss (Lambert et al., 2000). Petrographic

evidence at VBI and PLI – such as the presence of the highly reacted paragneissic

inclusions in the BBS, VTT, and BG respectively – also indicates the significant

contribution of crustal material and the accompanying modifications to the bulk

chemistry of the melt (e.g., Li and Naldrett, 2000; Li et al., 2001). Based on olivine

analyses from the EDI of the VBI, it was demonstrated in Chapter 3 that the Mn and Zn

concentrations of olivine records assimilation-induced changes in the bulk composition of

the melt. Olivine from several BBS and LTT samples related to the major massive sulfide

mineralized zone at the base of the EDI contains very high concentrations of Mn and Zn

(VB266 in Fig.4.6E–F), which are decoupled from their Fo contents and can therefore not

result solely from fractional crystallization (Chapter 3). Instead, the progressive reaction

of entrained paragneissic inclusions from the RBZ during transit through the magma

conduit(s) into the EDI has locally enriched the melt in incompatible elements, especially

Mn and Zn (Fig.4.6E–F – model line AFC-4; Chapter 3). Most of the enriched olivine is

also chemically zoned with regard to Mn, Ni, Co when in direct contact with, or enclosed

by, sulfides (Chapter 3). This disequilibrium zoning indicates a solid-liquid diffusive

element exchange between olivine and surrounding sulfide melt, and diffusion profiles

show similar trends to those reported from volcanic xenocrysts (Costa and Dungan, 2005), with a slight center to rim decrease in Ni-Co and an increase in Mn (~2,700 ppm) and partially Zn (~60 ppm) (Chapter 3). In addition, the composition of the recrystallizing hercynite, a component of the xenolith-replacement mineralogy of the original paragneissic mineral assemblage, also changes from the RBZ towards the EDI, presumably as response to an advancing degree of xenolith-melt reaction (Li and Naldrett, 1999; Li and Naldrett, 2000). The hercynite composition displays an increase in FeO at the expense of MgO (transition from spinel-dominated to hercynite-dominated composition), and simultaneous increases in Mn (from ~1,000 to ~1,800 ppm) and Zn (from ~2,000 to ~9,000 ppm) (Li and Naldrett, 2000). This observation supports the hypothesis of an incremental addition of Mn and Zn to the contaminated melt environment, whereas the contrasting element enrichment vectors in hercynite (high Zn) and olivine (high Mn) result from their specific mineral/melt partition coefficients.

It was demonstrated earlier (Section 4.5.2.) that even though a general increase in Fo, Mn and Zn exists in olivine from the southern and central part of the EDI, it is far less pronounced than in olivine from the heavily mineralized BBS (e.g., VB266, VB552; Chapter 3). Olivine from this study displays the highest Mn and Zn contents in the DDH that are closest to the massive sulfide mineralized horizon in the EDI (VB248 and VB513; Fig.4.1A, Fig.4.4B–D and 4.5C–F). Although the Zn contents of two samples (VB513-19 and VB248-15) are in the range of potentially contaminated olivine (Fig.4.6F), they are decoupled from the corresponding Mn concentrations (Fig.4.6E and 4.7D). In the VB266 olivine, the mutually high Mn and Zn contents are the prime

diagnostic signature for contamination and it was speculated in Chapter 3 that this reflects the joint incorporation of Tasiuyak paragneiss (primarily Zn) and enderbitic orthogneiss (primarily Mn) (AFC-4 in Fig.4.6E–F and Fig.4.7D). The apparent lack of correlation displayed in the more distal (from the mineralized sequence in the EDI) samples from this study supports this speculation, since the chemical interaction with the Enderbite Gneiss is probably limited to the immediate footwall contact area in the EDI and is generally less extensive due to thermal constraints, whereas Tasiuyak paragneiss fragments are entrained and dynamically mixed with higher relative volumes of mafic melt during transport. Even this signature, however, is restricted to a halo directly above (~150m; Chapter 3) and further south (~180m; Fig.4.5F) of the massive and disseminated mineralization in the EDI suggesting that contamination is localized at this 100m scale.

Although the Mn content in most non-BBS olivine from this study is primarily explained by regular FC (Fig.4.6E – model line FC-1), some very high Zn values still require an external input (Fig.4.6F – model line AFC-4). In this regard, olivine compositions from the PLI are very informative; the Zn concentrations in olivine from BG samples (one criteria for the original subdivision between UG and BG was the presence of Tasiuyak paragneiss xenoliths in the BG) are on average higher than those from the UG at similar or even lower Fo contents (Fig.4.6F – purple circles). These elevated Zn concentrations in BG olivine might then be derived from the exclusive assimilation of Tasiuyak paragneiss, as the single major contaminant in the PLI, whereas the Mn contents simply reflect regular FC (Fig.4.6E – model line FC-1). The lower overall Zn content compared to VB266 olivine on the other hand is likely caused by the lower degree of integrated

reaction between xenoliths and mafic melt at the PLI (as also evidenced by MgO-rich hercynite composition, presence of corundum in residual assemblage etc.; Li et al., 2001). The assimilation of Tasiuyak paragneiss likely resulted in sulfide saturation event(s), which triggered the fractionation of sulfide liquid(s), while promoting contemporaneous trace element transfer into the mafic melt at both the VBI and PLI. These processes are recorded in associated olivine by their overall lower Ni contents, uncharacteristically high Mn and Zn concentrations, and the apparent chemical zonation of BBS olivine in contact with sulfides (Chapter 3). In the EDI, this geochemical signature is detectable *vertically* and *laterally* in olivine from BBS associated with massive sulfide mineralization, the lower disseminated sulfide-bearing VTT, and for some distance beyond these zones. Approaching this major sulfide zone in the EDI from the unmineralized troctolitic parts of the magma chamber yields an olivine geochemical vector of increasingly pronounced Mn and Zn enrichment (Fig.4.4 and 4.5) that culminates in the presumably maximum values in the BBS of VB266 and other DDH that transect the basal massive sulfide body (Chapter 3). Even though the BG of the PLI is also characterized by reacted Tasiuyak paragneiss inclusions, significant massive sulfide occurrences remain to be discovered. Amongst other factors (e.g., low R-factor; Li et al., 2001; higher differentiation grade of the mafic melt; Fig.4.8B), the lower degree of integrated xenolith-melt interaction has likely not permitted the adequate incorporation of crustal sulfides, and has concomitantly retarded the enrichment of Mn (absence of a second contaminant), and Zn, in olivine. Based on our data, the observed olivine chemistry at PLI therefore documents a less

favorable environment for economic sulfide mineralization, at least in the portions of the intrusive complex explored to date.

In summary, the assimilation of the sulfide-rich Tasiuyak paragneiss recorded in BBS, VTT and BG alone is not diagnostic for the presence of massive sulfide mineralization. However, if a favorable degree of interaction between paragneiss and mafic melt has occurred, the probability of significant ore mineralization increases dramatically as evident at the EDI. The trace element composition of olivine records this process in both the EDI and PLI. However, only the chemical signature recognized in BBS and other ore-proximal olivine at VBI may exactly reflect the most favorable ore-forming conditions in evolved mafic magmatic systems.

4.6.3. Trace Element Distribution in Olivine as a Ni-Exploration Tool

4.6.3.1. Lateral Variations in Olivine Chemistry in the EDI

The economic massive sulfide mineralization within the EDI is intimately associated with the BBS, whereas the lower VTT contains mainly disseminated sulfides (e.g., Lightfoot and Naldrett, 1999; Li and Naldrett, 1999). Vectoring laterally towards the massive sulfide mineralization based on the olivine chemistry from DDH that terminate in the barren to weakly mineralized VTT in the EDI would thus be a major asset. The Ni and Fo composition of EDI olivine is geochemically oblivious to the relationship between host rock and sulfide mineralization, unless augmented with values for multiple elements (V, Cr, Mn, Co, Fe, Ni, and Zn). It was demonstrated in Chapter 3 that a characteristic olivine

composition records the genetic link between crystallization of olivine, sulfide fractionation caused by contamination, and the possible subsolidus equilibration of olivine with sulfide liquid of economically favorable composition. This specific composition was then linked to the relative vertical proximity to massive sulfide (RVP factor − 1.0 directly associated with massive sulfide, 0.0 completely remote from major sulfide mineralization, Chapter 3, Fig.3.9). For DDH that intersected massive sulfide mineralization, the relative vertical proximity factor (RVP) was calculated as the depth of the sample divided by the depth of the first occurrence of mineralization in the measured DDH multiplied by the relative sulfide content (e.g., VB552-13.1 VTT, 792m, first occurrence of massive sulfide at 911m with 95% sulfide − from unpublished Vale log files; RVP=792/(911*0.95)=0.83; Chapter 3, Table 3.1). A multiple regression based on these data was then used here to calculate a *predicted* relative proximity for the samples from this study (Fig.4.9 and 4.10). The multiple regression has a R^2 of 0.78 plus individual uncertainties related to the regression coefficients (Appendix 6.4.) and should thus be only applied in conjunction with petrographic and stratigraphic observations − to exclude obviously non-prospective olivine that yield apparently high relative proximity factors (e.g., metasomatized olivine, non-prospective VTT olivine; Fig.4.9). In general, the compositional variations in olivine are stratigraphically sensitive and detectable in DDH that terminate in VTT (VB332; Fig.4.10E), and in BBS intervals not associated with massive sulfides (VB248 and VB513; Fig.4.9, Fig.4.10B and 4.10F). The lateral proximity to massive sulfide mineralization relative to the occurrence in VB266 is predicted with high probability at up to 180m (Fig. 4.10). As shown in Figures 4.9 and

4.10, results from the multiple regression analysis provide a readily calculable, potential olivine geochemical vector towards mineralized parts in the EDI based on host rock (Fig.4.9) and stratigraphic depth (Fig.4.10). This analytical and geochemical approach could thus prove valuable in further exploration activities at the VBI, especially in prospective areas in the EDI and comparable zones elsewhere in the magma conduit system (e.g., RBZ).
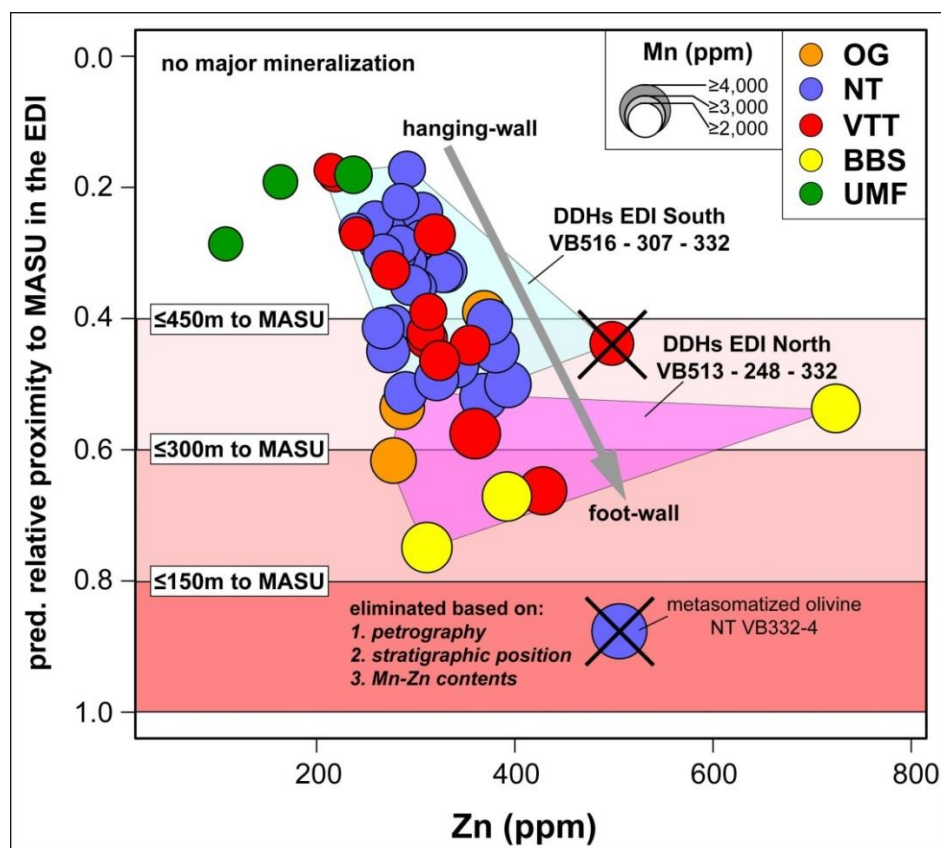
Fig. 4.9: Mn and Zn variations in olivine with the *predicted* relative proximity (RVP) to massive sulfide mineralization ordered in the EDI. Bubble sizes correspond to the Mn content (ppm), which exceeds the 2,000 ppm threshold commonly at *predicted* RVP values greater than 0.5. Values for the *predicted* RVP close to 1 imply an immediate proximity to massive sulfide mineralization, whereas olivine with values below 0.4 is not associated with major mineralization. The *predicted* RVP was calculated based on the results from the multiple regression statistics with data from Chapter 3 (Appendix 6.4.). Data are given in Table 4.1. See text for discussion.

Fig. 4.10: Lateral variations of the *predicted* relative proximity to massive sulfide with depth. With few exceptions, the lateral proximity to the massive sulfides at the base of the EDI (VB266 as reference) is reflected in the *predicted* relative proximity values (potential) of VTT and BBS lithologies not directly associated with massive sulfides (*predicted* RVP calculated based on regression equation in Appendix 6.4.).

4.6.3.2. Olivine as a Fertility Indicator for Mafic Intrusions on a Regional Scale

Utilizing the olivine data from Chapter 3, and from this study, enables a comprehensive compositional comparison of olivine populations from the major lithologies at the VBI

with those from the PLI (Fig.4.11 to 4.13). The kernel density estimates (KDE; see Appendix 6.5.) in Figure 4.11 and 4.12 display the distribution of Ni, Co, Mn and Zn in olivine from major lithologies in the VBI and the PLI on the basis of frequency (as reflected by the density function) of spot analyses versus elemental composition. The data in these Figures show the progression from homogeneous olivine in the NT (single pronounced peak – except for the bimodality in Ni contents when Fe-Ti oxide-rich and Ni-rich (108m, VB266, Chapter 3) horizons are considered) to the increasingly more compositionally heterogeneous olivine in VTT and BBS (multiple peaks). This progression reflects their common co-genesis and petrological correlation through differentiation, contamination and sulfide saturation (Fig.4.6 and 4.7; FC–AFC model lines). The UMF and OG on the other hand, contain chemically distinct, yet bimodal, olivine populations, indicative of a discrete (earlier) petrogenesis, mostly unrelated to the (later) troctolitic lithologies of the VBI – as was proposed by Li and Naldrett (1999) and others (Fig.4.12).

Olivine from the PLI is compositionally very similar to OG olivine (Fig.4.12), except that the Zn concentration is higher which, as is discussed above, likely relates to dominantly Tasiuyak paragneiss contamination, an input that appears absent in the measured OG olivine from VBI. This apparent chemical resemblance is informative from an exploration standpoint and supports the observation of Li et al. (2001), that the sampled portion of the PLI may be deficient in economic sulfide concentrations since the host rocks essentially fractionated from a single pulse of more evolved mafic magma that experienced low R-factor sulfide saturation – as opposed to the multiple (chalcophile-undepleted) magma

surges (high R-factor) that generated the EDI and other ore zones in the VBI and, most importantly, upgraded the metal-tenor of the already existing sulfides (e.g., Lightfoot and Naldrett, 1999; Lightfoot et al., 2012).

In order to better visualize the primary compositional dependences of the diverse olivine populations from the economic VBI and the sub-economic PLI, and to further distinguish them on a regional scale, a principal component analysis (PCA) was performed using the PAST software (Hammer et al., 2001). The results of the data reduction are depicted in the biplot in Figure 4.13 and demonstrate that ~60% of the variation in our multivariate dataset can be explained by the first two principal components, or axes of maximal variance, (PC 1 and PC 2) (Fig.4.13 inset). As expected, the olivine from the VBI and PLI occupy distinct areas in the biplot, whereas the discrete vectors for individual elements further characterize specific olivine populations (Fig.4.13). Olivine from the VBI is characterized by a pronounced bimodality of primitive and evolved compositions. The more primitive troctolitic olivine are best described by the distribution of MgO, Ni, Cr and Co, whereas the more evolved olivine from the VTT, the OG, and especially the BBS, can be described largely by the distribution of FeO, Zn and Mn. The PLI olivine is described mainly by Y, Sc and Ca, without the obvious signs of bimodality (except for olivine in the melagabbro from the PLI, Fig.4.12I–L). Even though the PCA itself has no definitive significance, with the principal components representing *only* hypothetical variables, the results clearly discriminate the prospective olivine populations in the VBI from the non-prospective olivine in the PLI.
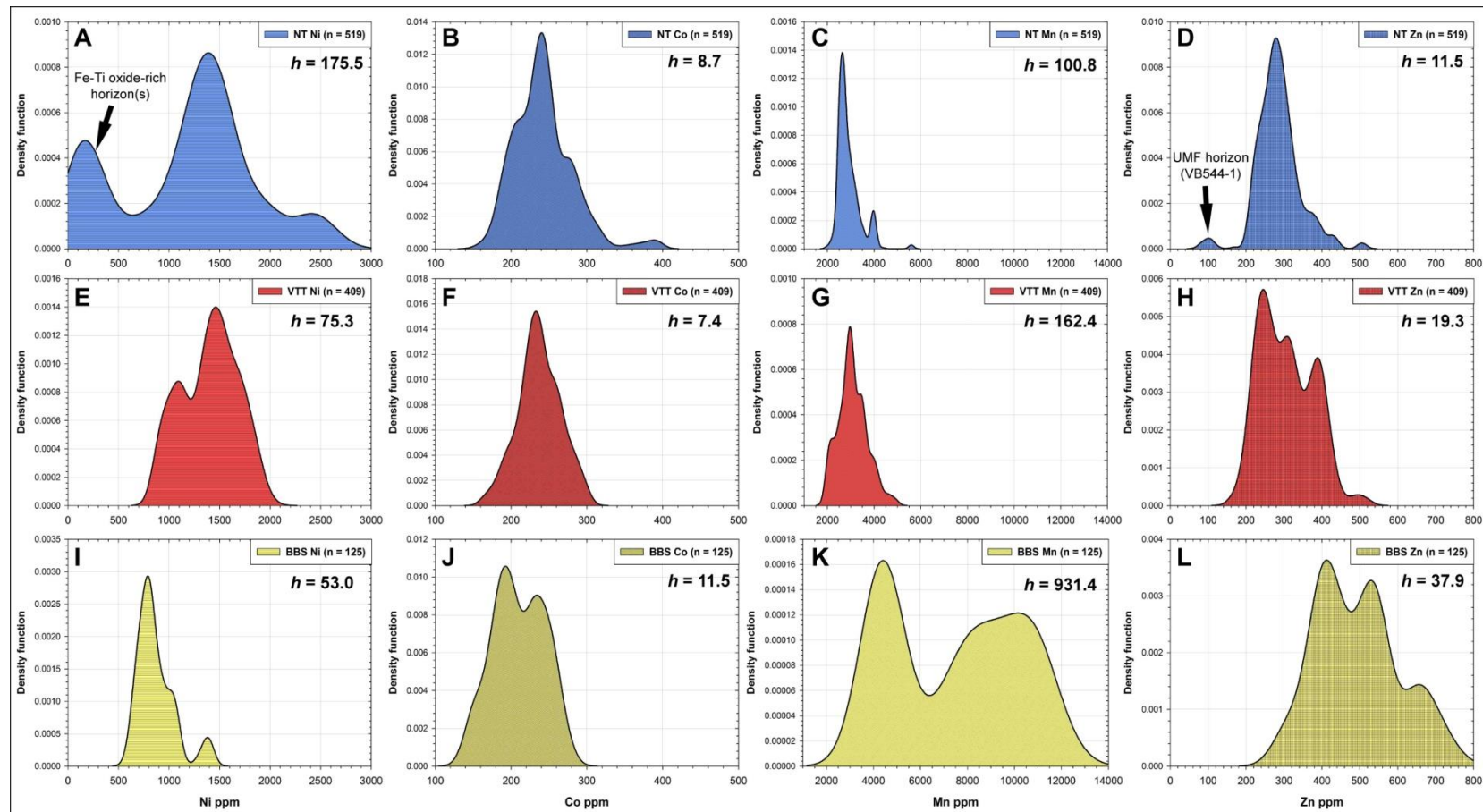
Fig. 4.11: Kernel Density Estimates of lithology-specific olivine populations from the VBI (NT, VTT, and BBS). The optimal bandwith (h) was automatically calculated with the AMC KDE MS-Excel® Add-in (see Appendix 6.5.). A), E), I) show the Ni distribution, B), F), J) the Co concentrations, C), G), K) the Mn contents, and D), H), L) the Zn concentrations. Data are combined from this study and Chapter 3. See text for further discussion.
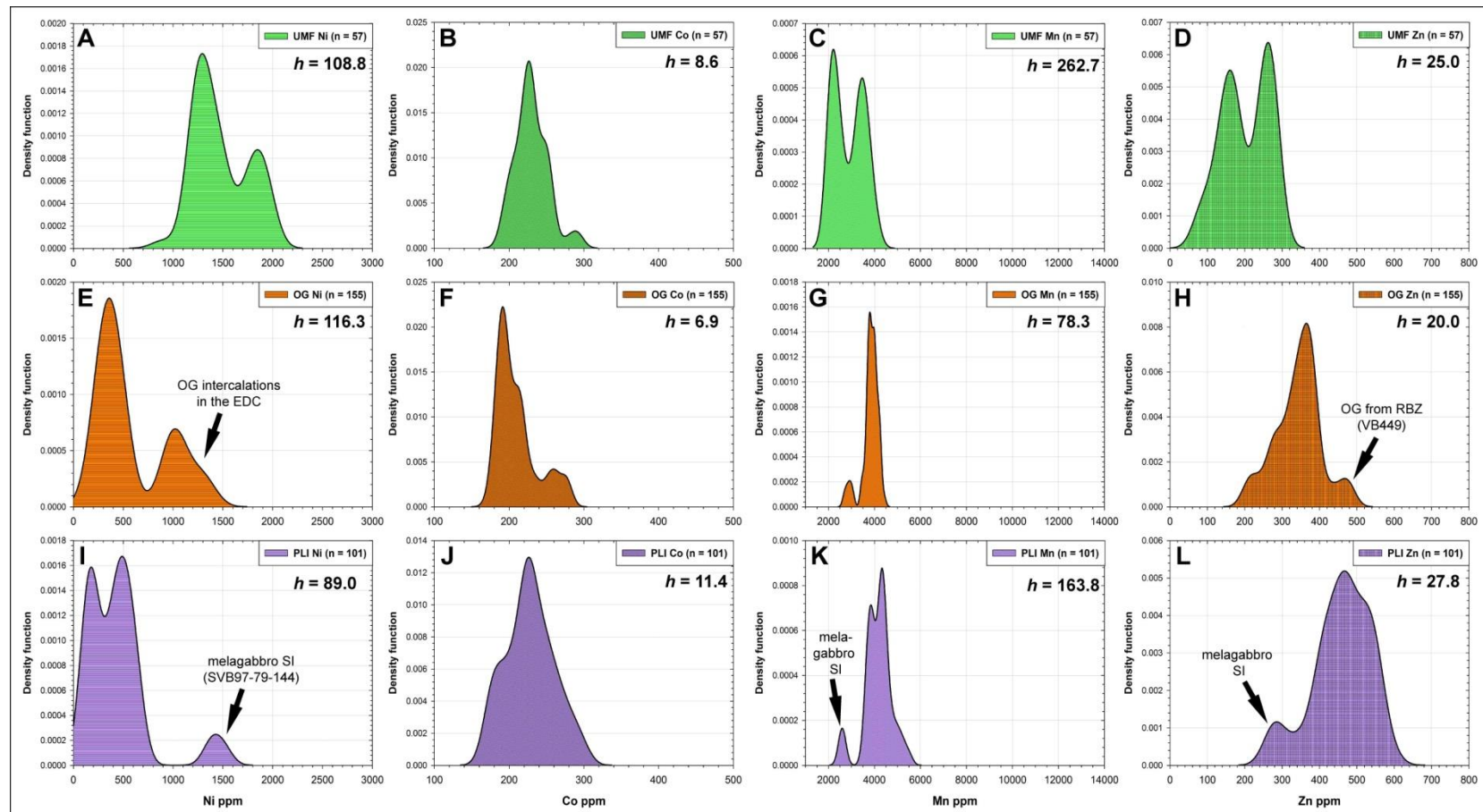
Fig. 4.12: Kernel Density Estimates (see Appendix 6.5.) of lithology-specific olivine populations from the VBI (UMF, OG) and the unseparated data from the PLI. A), E), I) show the Ni distribution, B), F), J) the Co concentrations, C), G), K) the Mn contents, and D), H), L) the Zn concentrations. Data are combined from this study and Chapter 3. See text for further discussion.
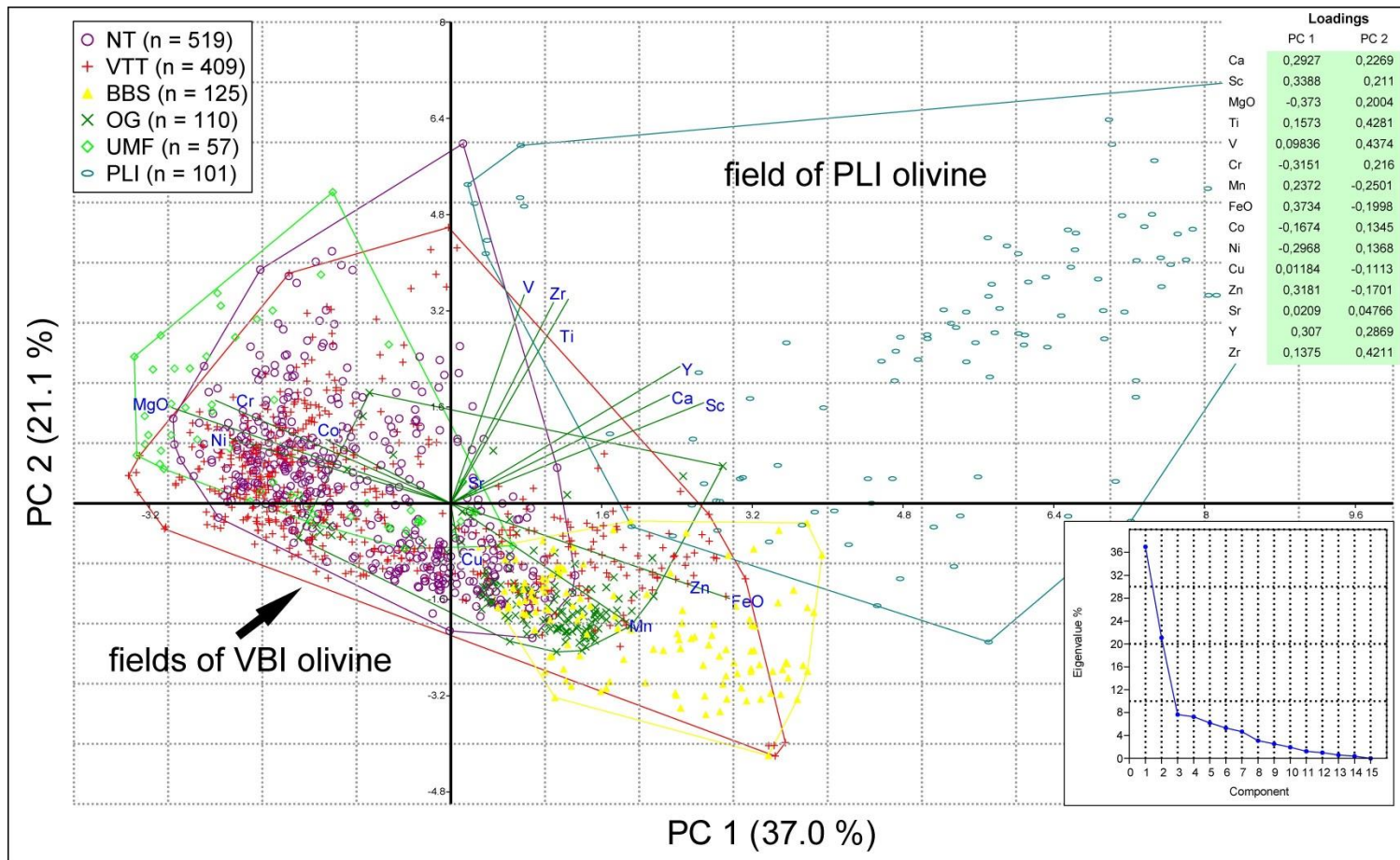
Fig. 4.13: Depicted are the results from the principal components analysis (PCA). The PAST software from Hammer et al. (2001) was used for the data reduction. The biplot of scores and loadings on PC 1 and PC 2 contains all olivine data (this study and Chapter 3). Insets show the scree plot with the relative importance of the individual principal components, and the loadings for PC 1 and PC 2. See text for further discussion.

Further expanding the olivine dataset to other developed Ni-Cu sulfide deposits and prospects of similar genesis, the compositional information can be precisely adjusted for specific ore-forming environments (chamber *versus* conduit; dynamic accumulation *versus* gravitational settling etc.), and thus elevate the multi-trace element distribution in olivine to a more universally applicable mineral exploration tool (Fig.4.14). In conjunction with other commonly applied geochemical exploration methods, for example in-situ stable/radiogenic isotope analyses and whole-rock geochemistry, the multi-trace element method could then be deployed as a valuable fertility indicator and vectoring tool in greenfield Ni-exploration on a regional scale (Fig.4.14).

Fig. 4.14: Generalized geochemical identification criteria for sulfide mineralization based on the multi-trace element distribution in olivine from the VBI and PLI. Check marks and cross marks indicate that criteria are either satisfied or not satisfied.

4.7. Summary and Conclusions

1. Correlatable stratigraphic horizons containing olivine populations of discrete composition are found in the NT (Ni-rich and Ni-depleted), VTT (higher Mn and Zn), OG (high Fe and low Ni), and BBS (high Fe, very high Mn and Zn) lithologies of the EDI. The chemistry of these olivine grains varies closely with the specific host lithology, and clearly reflects FC (NT, VTT, OG), AFC (BBS) processes and interaction with a sulfide fraction (Ni-depleted in NT).

2. Strongly Ni-depleted olivine occurs exclusively in the NT, in a laterally correlatable horizon found so far in 3 DDH. This olivine is mostly associated with Fe-Ti oxide-rich intervals, where ilmenite (±titanomagnetite) is an early crystallizing liquidus phase. The Ni depletion of the primary silicate melt (and hence the potential upgrading of a sulfide melt), and the precipitation of Fe-Ti oxides may be intimately related to interaction with a sulfide fraction, and the accompanying increase in melt fO_2.

3. There are at least two distinct populations of UMF present in the EDI, which contain compositionally distinct, bimodal olivine populations (primitive *versus* evolved). The chemistry of the more evolved olivine found in UMF entrained in BBS may be the result of a solid-liquid diffusive reequilibration during transit in the contaminated melt that eventually crystallized to form the BBS. The UMF in the NT on the other

hand, comprise very primitive olivine that likely represent disrupted, primitive, early magmatic cumulates.

4. BBS olivine (and olivine from the overlying VTT) with mutually high Mn-Zn contents probably precipitated from an Mn-Zn-enriched melt, contaminated by enderbitic orthogneiss and Tasiuyak paragneiss (FC-AFC modeling). In contrast, olivine from the PLI has high Zn concentrations only, which may be a result of the largely exclusive assimilation of Tasiuyak paragneiss as the primary contaminant in the region.

5. PLI olivine is compositionally similar to OG olivine from the EDI and very likely share a similar petrogenesis. The absence of economic sulfide mineralization in the portions of the PLI explored to date is best explained by fractionation from a single magma pulse (closed system) – rather than from the multiple pulses apparent in the EDI (open system) – which experienced a sulfide saturation event, likely through the addition of limited Tasiuyak paragneiss material (as recorded by the elevated Zn in PLI olivine). However, due to a low degree of xenolith-melt reaction and the paucity of further episodic intrusions of undepleted mafic magma, the fractionated sulfides were not upgraded in metal tenor (low R-factor) and remained sub-economic.

6. The apparent Fe-Mn-Zn enrichment of olivine from the lower VTT and the BBS increases from the barren parts in the south of the EDI towards the mineralized basal

succession in the northern part, and hence constitutes a potential first-order geochemical vector towards massive sulfide mineralization. In conjunction with petrographic and stratigraphic observation, a multiple regression based on the distribution of V-Cr-Mn-Fe-Co-Ni-Zn in EDI olivine can effectively predict the lateral proximity of lower VTT and BBS olivine (VB513, VB248 and VB332) to massive sulfides in the EDI.

7. Olivine from the VBI and the PLI is compositionally distinct. Based on the multivariate olivine data (PCA loadings) presented here and in Chapter 3, the bimodal and mutually Mn-Zn-rich composition of VBI olivine records a petrogenetic link to massive sulfide mineralization in an evolved mafic magma system. In the PLI, olivine of that prospective composition has not yet been observed, even though the lithology, texture and petrographic characteristics of the intrusive rocks are generally similar to those of the VBI. Therefore, trace element distribution in olivine can be a fertility indicator for ore mineralization in evolved mafic intrusions on a regional scale and after defining PCA vectors for other mafic intrusions, may provide a valuable tool for Ni-exploration.

8. The olivine data demonstrate that the element distribution of Cr, Mn, Fe, Co, Ni, and Zn is highly sensitive to a) assimilation and contamination through country rock and b) sulfide segregation and equilibration. Therefore, this selection comprises the key elements for the exploration-relevant trace elements-in-olivine routine.

4.8. References

Amelin, Y., Li, C., Naldrett, A.J., 1999. Geochronology of the Voisey's Bay intrusion, Labrador, Canada, by precise U-Pb dating of coexisting baddeleyite, zircon, and apatite. Lithos 47, 33–52.

Amelin, Y., Li, C., Valeyev, O., Naldrett, A.J., 2000. Nd-Pb-Sr isotope systematics of crustal assimilation in the Voisey's Bay and Mushuau intrusions, Labrador, Canada. Economic Geology 95, 815–830.

Arndt, N.T., Lesher, C.M., Czamanske, G.K., 2005. Mantle-derived magmas and magmatic Ni-Cu-(PGE) deposits. Economic Geology 100th Anniversary Volume, 5–23.

Baker, D.R., Moretti, R., 2011. Modeling the solubility of sulfur in magmas: A 50-year old geochemical challenge. Reviews in Mineralogy and Geochemistry 73, 167–213.

Barnes, S.J., 1986. The effect of trapped liquid crystallization on cumulus mineral compositions in layered intrusions. Contributions to Mineralogy and Petrology 93, 524–531.

Barnes, S.J., Naldrett, A.J., 1985. Geochemistry of the J-M (Howland) Reef of the Stillwater complex, Minneapolis Adit Area. I. Sulfide chemistry and sulfide-olivine equilibrium. Economic Geology 80, 627–645.

Beattie, P., 1994. Systematics and energetics of trace-element partitioning between olivine and silicate melts: Implications for the nature of mineral/melt partitioning. Chemical Geology 117, 57–71.

Brenan, J.M., 2003. Effects of fO$_2$, fS$_2$, temperature, and melt composition on Fe-Ni exchange between olivine and sulfide liquid: Implications for natural olivine-sulfide assemblages. Geochimica et Cosmochimica Acta 67, 2663–2681.

Brenan, J.M., Caciagli, N.C., 2000. Fe-Ni exchange between olivine and sulfide liquid: Implications for oxygen barometry in sulfide-saturated magmas. Geochimica et Cosmochimica Acta 64, 307–320.

Brenan, J.M., Li, C., 2000. Constraints on oxygen fugacity during sulfide segregation in the Voisey's Bay intrusion, Labrador, Canada. Economic Geology 95, 901–915.

Campbell, I.H., Naldrett, A.J., 1979. The influence of silicate:sulfide ratios on the geochemistry of magmatic sulfides. Economic Geology 74, 1503–1505.

Canil, D., 1997. Vanadium partitioning and the oxidation state of Archaean komatiite magmas. Nature 389, 842–845.

Canil, D., Fedortchouk, Y., 2001. Olivine-liquid partitioning of vanadium and other trace elements, with application to modern and ancient picrites. The Canadian Mineralogist 39, 319–330.

Chakraborty, S., 2008. Diffusion in solid silicates: A tool to track timescales of processes comes of age. Annual Review of Earth and Planetary Sciences 36, 153–190.

Chalokwu, C.I., Grant, N.K., 1987. Reequilibration of olivine with trapped liquid in the Duluth complex, Minnesota. Geology 15, 71–74.

Clark, T., Naldrett, A.J., 1972. The distribution of Fe and Ni between synthetic olivine and sulfide at 900°C, Economic Geology 67, 939–952.

Colson, R.O., McKay, G.A., Taylor, L.A., 1988. Temperature and composition dependencies of trace element partitioning: Olivine/melt and low-Ca pyroxene/melt. Geochimica et Cosmochimica Acta 52, 539–553.

Costa, F., Dungan, M., 2005. Short time scales of magmatic assimilation from diffusion modeling of multiple elements in olivine. Geology 33, 837–840.

De Hoog, J.C.M., Gall, L., Cornell, D.H., 2010. Trace-element geochemistry of mantle olivine and application to mantle petrogenesis and geothermobarometry. Chemical Geology 270, 196–215.

Emslie, R.F., Hamilton, M.A., Thériault, R.J., 1994. Petrogenesis of a mid-Proterozoic anorthosite-mangerite-charnockite-granite (AMCG) complex: Isotopic and chemical evidence from the Nain Plutonic Suite. Journal of Geology 102, 539–558.

Evans-Lamswood, D.M., Butt, D.P., Jackson, R.S., Lee, D.V., Muggridge, M.G., Wheeler, R.I., Wilton, D.H.C., 2000. Physical controls associated with the distribution of sulfides in the Voisey's Bay Ni-Cu-Co deposit, Labrador. Economic Geology 95, 749–769.

Fleet, M.E., MacRae, N.D., Osborne M.D., 1981. The partition of Ni between olivine, magma and immiscible sulfide liquid. Chemical Geology 32, 119–127.

Fleet, M.E., MacRae, N.D., 1983. Partition of Ni between olivine and sulfide and its application to Ni-Cu sulfide deposits. Contribution to Mineralogy and Petrology 83, 75–83.

Gaetani, G.A., Grove, T.L., 1997. Partitioning of moderately siderophile elements among olivine, silicate melt, and sulfide melt: Constraints on core formation in the Earth and Mars. Geochimica et Cosmochimica Acta 61, 1829–1846.

Hammer, Ø., Harper, D.A.T., Ryan, P.D., 2001. PAST: Paleontological statistics software package for education and data analysis. Palaeontologia Electronica 4(1): 9pp.

Hart, S.R., Davis, K.E., 1978. Nickel partitioning between olivine and silicate melt. Earth and Planetary Science Letters 40, 203–290.

Hervig, R.L., Mazdab, F.K., Williams, P., Guan, Y., Huss, G.R., Leshin, L.A., 2006. Useful ion yields for Cameca IMS 3f and 6f SIMS: Limits on quantitative analysis. Chemical Geology 227, 83–99.

Ito, M., Yurimoto, H., Morioka, M., Nagasawa, H., 1999. Co^{2+} and Ni^{2+} diffusion in olivine determined by secondary ion mass spectrometry. Physics and Chemistry of Minerals 26, 425–431.

Jang, Y.D., Naslund, H.R., McBirney, A.R., 2001. The differentiation trend of the Skaergaard intrusion and the timing of magnetite crystallization: iron enrichment revisited. Earth and Planetary Science Letters 189, 189–196.

Jones, R.H., Layne, G.D., 1997. Minor and trace element partitioning between pyroxene and melt in rapidly cooled chondrules. American Mineralogist 82, 534–545.

Keays, R.R., Lightfoot, P.C., 2010. Crustal sulfur is required to form magmatic Ni-Cu sulfide deposits: evidence from chalcophile element signatures of Siberian and Deccan Trap basalts. Mineralium Deposita 45, 241–257.

Kerr, A., 1999. Mafic rocks of the Pants Lake intrusion and related Ni-Cu-Co mineralization in north–central Labrador. Newfoundland Department of Mines and Energy, Geological Survey Branch, Report 99-1, pp 215–253.

Kerr, A., 2003. Nickeliferous gabbroic intrusions of the Pants Lake area, Labrador, Canada: Implications for the development of magmatic sulfides in mafic systems. American Journal of Science 303, 221–258.

Klemme, S., Gunther, D., Hametner, K., Prowatke, S. and Zack, T., 2006. The partitioning of trace elements between ilmenite, ulvospinel, armalcolite and silicate melts with implications for the early differentiation of the moon. Chemical Geology 234, 251–263.

Lambert, D.D., Frick, L.R., Foster, J.G., Li, C., Naldrett, A.J., 2000. Re-Os isotope systematics of the Voisey's Bay Ni-Cu-Co magmatic sulfide system, Labrador, Canada: II. Implications for parental magma chemistry, ore genesis, and metal redistribution. Economic Geology 95, 867–888.

Li, C., Lightfoot, P.C., Amelin, Y., Naldrett, A.J., 2000. Contrasting petrological and geochemical relationships in the Voisey's Bay and Mushuau intrusions, Labrador, Canada: implications for ore genesis. Economic Geology 95, 771–799.

Li, C., Naldrett, A.J., 1999. Geology and petrology of the Voisey's Bay intrusion: Reaction of olivine with sulphide and silicate liquids. Lithos 47, 1–31.

Li, C., Naldrett, A.J., 2000. Melting reactions of gneissic inclusions with enclosing magma at Voisey's Bay, Labrador, Canada: Implications with respect to ore genesis. Economic Geology 95, 801–814.

Li, C., Naldrett, A.J., Ripley, E.M., 2001. Critical factors for the formation of a nickel-copper deposit in an evolved magma system: lessons from a comparison of the Pants Lake and Voisey's Bay sulfide occurrences in Labrador, Canada. Mineralium Deposita 36, 85–92.

Li, C., Naldrett, A.J., Ripley, E.M., 2007. Controls on the Fo and Ni contents of olivine in sulfide-bearing mafic/ultramafic intrusions: Principles, modeling, and examples from Voisey's Bay. Earth Science Frontiers 14, 177–185.

Li, C., Ripley, E.M., Maier, W.D., Gromwe, T.E.S., 2002. Olivine and sulfur isotope compositions of the Uitkomst Ni-Cu sulfide ore-bearing complex, South Africa: evidence for sulfur contamination and multiple magma emplacements. Chemical Geology 188, 149–159.

Li, C., Ripley, E.M., Mathez, E.A., 2003b. The effect of S on the partitioning of Ni between olivine and silicate melt in MORB. Chemical Geology 201, 295–306.

Li, C., Ripley, E.M., Naldrett, A.J., 2003a. Compositional variations of olivine and sulfur isotopes in the Noril'sk and Talnakh intrusions, Siberia: Implications for ore-forming processes in dynamic magma conduits. Economic Geology 98, 69–86.

Li, C., Xu, Z., de Waal, S.A., Ripley, E.M., Maier, W.D., 2004. Compositional variations of olivine from the Jinchuan Ni–Cu sulfide deposit, western China: implications for ore genesis. Mineralium Deposita 39, 159–172.

Lightfoot, P.C., Evans-Lamswood, D.M., 2012. Magma chamber geometry and the localization of Ni-Cu±(PGE) sulphide mineralization: Global examples and their relevance to Voisey's Bay. GAC Program with Abstracts 35:78.

Lightfoot, P.C., Keays, R.R., Evans-Lamswood, D.M., Wheeler, R., 2012. S saturation history of Nain Plutonic Suite mafic intrusions: origin of the Voisey's Bay Ni–Cu–Co sulfide deposit, Labrador, Canada. Mineralium Deposita 47, 23–50.

Lightfoot, P.C., Naldrett, A.J., Hawkesworth, C.J., 1984. The geology and geochemistry of the Waterfall Gorge section of the Insizwa complex with particular reference to the origin of the nickel sulfide deposits. Economic Geology 79, 1857–1879.

Lightfoot, P.C., Naldrett, A.J., 1999. Geological and geochemical relationships in the Voisey's Bay intrusion, Nain Plutonic Suite, Labrador, Canada. In Dynamic processes in magmatic ore deposits and their application in mineral exploration (Keays, R.R., Lesher, C.M., Lightfoot, P.C., Farrow, C.E.G., eds.). Geological Association of Canada Short Course Notes 13, 1–30.

MacLean, W.H., Shimazaki, T., 1976. The partition of Co, Ni, Cu, and Zn between sulfide and silicate liquids. Economic Geology 71, 1049–1057.

Maier, W.D., Barnes, S.J., Sarkar, A., Ripley, E., Li, C., Livesey, T., 2010. The Kabanga Ni sulfide deposit, Tanzania: I. Geology, petrography, silicate rock geochemistry, and sulfur and oxygen isotopes. Mineralium Deposita 45, 419–441.

Maier, D.M., Li, C., de Waal, S.A., 2001. Why are there no major Ni-Cu sulphide deposits in large layered mafic-ultramafic intrusions? The Canadian Mineralogist 39, 547–556.

Moseley, D., 1981. Ilmenite exsolution in olivine. American Mineralogist 66, 976–979.

Naldrett, A.J., 1997. Key factors in the genesis of Noril'sk, Sudbury, Jinchuan, Voisey's Bay and other world-class Ni-Cu-PGE deposits: Implications for exploration. Australian Journal of Earth Sciences 44, 283–315.

Naldrett, A.J., 1999. World-class Ni-Cu-PGE deposits: key factors in their genesis. Mineralium Deposita 34, 227–240.

O'Reilly, S., Chen, D., Griffin, W.L., Ryan, C.G., 1997. Minor elements in olivine from spinel lherzolite xenoliths: implications for thermobarometry. Mineralogical Magazine 61, 257–269.

Ottolini, L., Bottazzi, P., Vannucci, R., 1993. Quantification of lithium, beryllium, and boron in silicates by secondary ion mass spectrometry using conventional energy filtering. Analytical Chemistry 65, 1960–1968.

Papike, J.J., Karner, J.M., Shearer, C.K., 2005. Comparative planetary mineralogy: Valence state partitioning of Cr, Fe, Ti, and V among crystallographic sites in olivine, pyroxene, and spinel from planetary basalts. American Mineralogist 90, 277–290.

Petry, C., Chakraborty, S., Palme, H., 2004. Experimental determination of Ni diffusion coefficients in olivine and their dependence on temperature, composition, oxygen fugacity, and crystallographic orientation. Geochimica et Cosmochimica Acta 68, 4179–4188.

Qiuan, Q., O'Neill, H.S.C., Hermann, J., 2010. Comparative diffusion coefficients of major and trace elements in olivine at ~950 °C from a xenocryst included in dioritic magma. Geology 38, 331–334.

Rajamani, V., Naldrett, A.J., 1978. Partitioning of Fe, Co, Ni, and Cu between sulfide liquid and basaltic melts and the composition of Ni-Cu sulfide deposits. Economic Geology 73, 82–93.

Ripley, E.M., Park, Y.R., Li, C., Naldrett, A.J., 1999. Sulfur and oxygen isotopic evidence of country rock contamination in the Voisey's Bay Ni–Cu–Co deposit, Labrador, Canada. Lithos 47, 53–68.

Ripley, E.M., Li, C., 2013. Sulfide saturation in mafic magmas: Is external sulfur required for magmatic Ni-Cu-(PGE) ore genesis? Economic Geology 108, 45–58.

Ripley, E.M., Li, C., Shin, D., 2002. Paragneiss assimilation in the genesis of magmatic Ni-Cu-Co sulfide mineralization at Voisey's Bay, Labrador: δ^{34}S, δ^{13}C, and Se/S evidence. Economic Geology 97, 1307–1318.

Roeder, P.L., Emslie, R.F., 1970. Olivine-liquid equilibrium. Contributions to Mineralogy and Petrology 29, 275–289.

Ryan, B., 2000. The Nain-Churchill boundary and the Nain Plutonic Suite: A regional perspective on the geologic setting of the Voisey's Bay Ni-Cu-Co deposit. Economic Geology 95, 703–724.

Sato, H., 1977. Nickel content of basaltic magmas: identification of primary magmas and a measure of the degree of olivine fractionation. Lithos 10, 113–120.

Scoates, J.S., Mitchell, J.N., 2000. The evolution of troctolitic and high Al basaltic magmas in Proterzoic anorthosite plutonic suites and implications for the Voisey's Bay massive Ni-Cu sulfide deposit. Economic Geology 95, 677–701.

Shearer, C.K., McKay, G., Papike, J.J., Karner, J.M., 2006. Valence state partitioning of vanadium between olivine-liquid: Estimates of the oxygen fugacity of Y980459 and application to other olivine-phyric martian basalts. American Mineralogist 91, 1657–1663.

Shimizu, N., Semet, M.P., Allègre, C.J., 1978. Geochemical applications of quantitative ion-microprobe analysis. Geochimica et Cosmochimica Acta 42, 1321–1334.

Smith, R.L., 2006. The basal gabbro subdivision and associated magmatic nickel-copper sulphide mineralization of the Pants Lake intrusion, Labrador, Canada: A combined geological, petrological, geochemical, and metallogenic study. M.Sc. thesis, Memorial University, CA, 363 pp.

Snyder, D., Carmichael, I.S.E., Wiebe, R.A., 1993. Experimental study of liquid evolution in an Fe-rich, layered mafic intrusion: constraints of Fe-Ti oxide precipitation on the T-f$_{O2}$ and T-p paths of tholeiitic magmas. Contributions to Mineralogy and Petrology 113, 73–86.

Spandler, C., O'Neill, H.S.C., 2010. Diffusion and partition coefficients of minor and trace elements in San Carlos olivine at 1,300°C with some geochemical implications. Contributions to Mineralogy and Petrology 159, 791–818.

Sun, S.S., 1982. Chemical composition and origin of the earth's primitive mantle. Geochimica et Cosmochimica Acta 46, 179–192.

Turner, S., Costa, F., 2007. Measuring timescales of magmatic evolution. Elements 3, 267–272.

Tyson, R.M., Chang, L.L.Y., 1984. The petrology and sulfide mineralization of the Partridge River troctolite, Duluth complex, Minnesota. Canadian Mineralogist 22, 23–38.

Venables, A., 2003. Magmatic processes associated with the Voisey's Bay No-Cu-Co sulfide deposit, Labrador, Canada. Ph.D. thesis, Open University, UK, 313 pp.

Yurimoto, H., Yamashita, A., Nishida, N., Sueno, S., 1989. Quantitative SIMS analysis of GSJ rock reference samples. Geochemical Journal 23, 215–236.

Zanetti, A., Tiepolo, M., Oberti, R., Vannucci, R., 2004. Trace-element partitioning in olivine: Modeling of a complete data set from a synthetic hydrous basanite melt. Lithos 75, 39–54.

CHAPTER 5 - Summary and Conclusions

5.1. Scientific Objectives

The major aims were to:

1) *Develop a SIMS analytical routine that allows the accurate determination of several major and trace elements in the forsterite-fayalite solid solution.*

2) *Identify systematic olivine trace element variations in the Voisey's Bay Intrusion (VBI) that can be related to key ore-forming processes and thus enable a more precise geochemical characterization of the VBI and the existing geological model.*

3) *Determine whether trace element-in-olivine analyses can be used to discriminate between barren and mineralized environments and provide a potential geochemical vector towards massive sulfide concentrations in the VBI and other evolved mafic intrusions.*

5.2. Key Results

5.2.1. Analytical Set-up

In the course of this study, a *SIMS analytical approach* for the determination of multiple trace elements and the forsterite content of compositionally variable olivine was developed:

1) A set of forsterite-fayalite (Fo_{100} to Fo_6) reference materials was geochemically characterized and used for SIMS analyses to quantify major (MgO, SiO, FeO) and trace elements (Ca, Sc, Ti, V, Cr, Mn, Co, Ni, Cu, Zn, Sr, Y, Zr).

2) Key isobaric interferences (mostly Mg-, Si-, Fe-species on the transition elements Cr, Mn, Co, Ni, Cu, and Zn) were suppressed by applying energy filtering, and SIMS matrix effects (most vigorous for transition elements with geochemical similarity to Mg and Fe, such as Mn, Co, Ni, Cu, and Zn) were overcome by standardization with a set of 5 olivine reference materials.

3) In the sequential empirical approach utilized in this study, the Fo content, the major element concentrations (wt.%) and the concentrations (ppm) of Ca, Cr, Mn, Co, Ni, and Zn were calculated based on the analyses of olivine reference materials. Low abundance elements (Sc, Ti, V, Cu, Sr, Y, Zr) were quantified conventionally using NIST (610 and 612) silicate glasses and San Carlos mantle olivine.

4) The applicability and accuracy of the SIMS analytical and empirical approach for olivine analysis (primarily the major and minor element content) was further investigated with an inter-technique (SIMS and EPMA) comparison using highly homogeneous mantle olivine (Fo_{90}) and more compositionally variable volcanic olivine (Fo_{74-89}). The SIMS results were comparable (empirically and statistically) with those determined by EPMA.

5.2.2. Olivine Major and Trace Element Composition

Compositional characteristics of olivine from a series of DDH intersecting the olivine-gabbroic to troctolitic lithologies and the major mineralization at the base of the EDI were analyzed with SIMS:

5) Although petrographically similar, olivine from the five major lithologies in the EDI (OG, NT, VTT, BBS, UMF) is compositionally variable on a vertical scale. Especially the Fo content (most primitive in NT olivine; ~Fo82 – most evolved in BBS olivine; ~Fo62), as well as the Mn, Co, Ni, and Zn concentrations vary systematically with depth (with some exceptions) from the most primitive composition in the NT (~2,500 ppm Mn, ~250 ppm Co, ~2,500 ppm Ni, ~100 ppm Zn) to the most evolved composition in the BBS (~12,155 ppm Mn, ~200 ppm Co, ~850 ppm Ni, ~680 ppm Zn).

6) Olivine from the OG differs compositionally from NT, VTT, and BBS olivine, and is generally rich in Mn and Zn, variably depleted in Ni (Ni-poor group with less than 550 ppm and Ni-rich group with more than 900 ppm) and has a lower Fo content (~Fo66).

7) Exceptionally Ni-rich (up to 2,600 ppm) and Ni-poor (~80 ppm) olivine intervals occur in the upper NT at around 108m and 67m, respectively.

8) Primitive olivine, with Zn contents ~100 ppm, ~2,000 ppm Ni, and ~Fo80, is found in an ultramafic interval in the NT at the top of the EDI (VB544).

9) The Fo content of EDI olivine correlates with the sulfide content and the amount of incorporated Tasiuyak paragneiss material in the various lithologies (NT>VTT>OG>BBS).

10) Olivine in the BBS associated with massive sulfide has a unique geochemical signature and is strongly enriched in Mn (~12,000 ppm vs. 2,500 ppm in NT) and Zn (~650 ppm vs. 250 ppm in NT) compared to NT and upper VTT olivine.

11) BBS olivine (VB266-43) enclosed by sulfides displays a variable trace element zonation (Mn>Ni>Co). Mn (±Zn) shows a coupled increase, whereas Co and Ni decrease towards the olivine-sulfide contact, and vice versa towards the interior of the grain.

12) At least two different (~Fo80 vs. ~Fo60) UMF olivine populations (UMF interval in NT *and* UMF in BBS) are present in the EDI.

In addition, olivine from several DDH spanning two approximately N-S trending transects through the EDI was analyzed to further detect compositional variations on a lateral scale. The EDI olivine data were also compared to olivine data from the barren to sub-economic PLI:

13) The observed *vertical* variations (increase in Fe, Mn, Zn) in olivine composition with proximity to the BBS (and associated massive sulfide accumulation) at the base of the EDI are also detectable on a *lateral* scale when approaching the BBS (with the basal ore-zone) from the south.

14) Both lateral transects include, stratigraphically correlative intervals of variable thickness of NT with Ni-(Co)-poor (less than 110 ppm Ni; less than 200 ppm Co) olivine that coincides with higher amounts of Fe-Ti oxides (up to 45 vol.%).

15) The additional UMF samples from the EDI and a melagabbro sample from the PLI contain olivine that spans a bimodal compositional array from enriched compositions (UMF, BBS and to a lesser extend the PLI melagabbro) to more primitive compositions (NT, UMF – VB544-1).

16) Enrichments in Mn-Zn are apparent in olivine from the lower part of the VTT and the BBS, and are most pronounced in vicinity to major sulfide mineralization (e.g., base of VB513).

17) Kernel density estimates (KDE) of the VBI olivine populations demonstrate a systematic differentiation trend (enrichment – depletion) for several elements (e.g., Mn, Co, Ni, Zn) in olivine from the most primitive NT, over the VTT, to the most evolved BBS compositions.

18) PLI olivine are in general texturally and compositionally similar to OG olivine populations from the VBI, featuring the same average evolved geochemical signature (low Fo content, low Ni, high Mn and Zn), and also the same compositional disparity between evolved and reasonably primitive olivine (Ni variability ~100 to ~1,500 ppm).

19) The observed pronounced bimodality of the VBI olivine population (NT, VTT, BBS) is absent at the PLI, where the most primitive olivine (melagabbro from South Intrusion) has a composition similar to the most primitive OG olivine from the EDI.

20) A Principal Components Analysis (PCA) revealed that the variation in PLI olivine is best described by the distribution of the incompatible elements Y, Sc, and Ca, as opposed to the bimodal (primitive and evolved) olivine population from the VBI, which is either controlled by the distribution of MgO, Ni, Cr, and Co (primitive – UMF, NT, and upper VTT), or by the concentrations of FeO, Zn and Mn (evolved – lower VTT, BBS).

5.3. Major Conclusions

In concurrence with the tripartite research objective of this thesis, the individual conclusions from Chapters 2 to 4 are condensed at this point and only the key conclusions are reiterated as follows:

1) Major and trace elements in olivine can be routinely and accurately measured with SIMS, if energy filtering and a set of compositionally versatile, well-characterized olivine reference materials is utilized to correct isobaric interferences and the occasionally strong matrix effects on some transition metals.

2) In this analytical and empirical approach, the high spatial resolution (~40 μm) and high sensitivity (ppb-level detection limit) of the SIMS technique can be fully utilized with an accuracy of ~9% and precision of ~8% for Mg, Fe, Si, Mn, and Ni concentrations, comparable to or better than EPMA for the same elements measured at wt.% levels.

3) An analytical protocol ("geochemical exploration package") could be specifically designed to allow the routine determination of the major elements (primarily Fo

content) and the petrology- and exploration-relevant trace elements (±Ca, ±Ti, ±Sc, ±V, Cr, Mn, Co, Ni, Cu, Zn, and ±Y; ± optional) in olivine in one analytical step in less than 10 to 12 min.

4) Olivine from the EDI in the VBI crystallized either from sulfide saturated (Ni-depleted) mafic magma batches (e.g., Ni-poor olivine interval in NT), Ni-undepleted primitive mafic melts (Ni-rich olivine interval in NT), variable Ni-depleted and differentiated mafic melts (VTT) and variable sulfide saturated and country rock contaminated mafic melts (BBS) in open-system processes.

5) The apparent Ni-(Co)-depletion of olivine and the presence of cumulus Fe-Ti oxides in specific NT intervals possibly both result from either a pre-crystallization sulfide saturation event or from the interaction of the mafic melt with an existing sulfide fraction, which depleted the melt in Ni and Co and increased the melt fO_2.

6) The "exceptional" composition of (most) OG olivine indicates precipitation from an earlier episode of mafic magmatism, pre-dating the later troctolitic pulses. The OG attained sulfide saturation through a combination of country rock contamination and fractional crystallization (lower Fo content, elevated Mn and Zn concentrations) before or during olivine crystallization (variable Ni depletion).

7) UMF containing primitive olivine compositions likely represent disrupted, early magmatic cumulates, whereas the more evolved olivine found in UMF entrained in BBS may have been subjected to a solid-liquid diffusive reequilibration during (dynamic) transit in the contaminated melt that eventually crystallized to form the BBS.

8) The EDI olivine data demonstrate that the trace element distribution of Cr, Mn, Co, Ni, and Zn is highly sensitive to a) assimilation and contamination through country rock and b) sulfide segregation and equilibration. Therefore, this selection comprises the key elements for the exploration-relevant trace elements-in-olivine routine.

9) BBS olivine from the EDI likely gained the Mn-Zn-rich signature through assimilation of both Tasiuyak paragneiss and enderbitic orthogneiss, whereas the only-Zn-rich olivine from the PLI might be the result of an exclusive assimilation of Tasiuyak paragneiss as the main Zn reservoir.

10) In the petrogenetic model for the EDI, a tentative order of crystallization is established on the basis of the olivine data, from early to late; UMF>OG>NT-VTT>BBS, with the key ore-forming events likely being co-eval with the NT-VTT>BBS interval.

11) The EDI olivine trace element data display clear geochemical trends and relate to some of the key ore-forming processes in a magmatic Ni-Cu-Co sulfide system (Fig.5.1), namely – **A**) primitiveness of mafic melt, **B**) country rock contamination, **C**) sulfide saturation and segregation (multiple events – open-system), **D**) mafic magmatic episodicity (*high* R-factor), **E**) dynamic transport through magma conduit(s), and **F**) the accumulation and concentration in a contaminated environment.
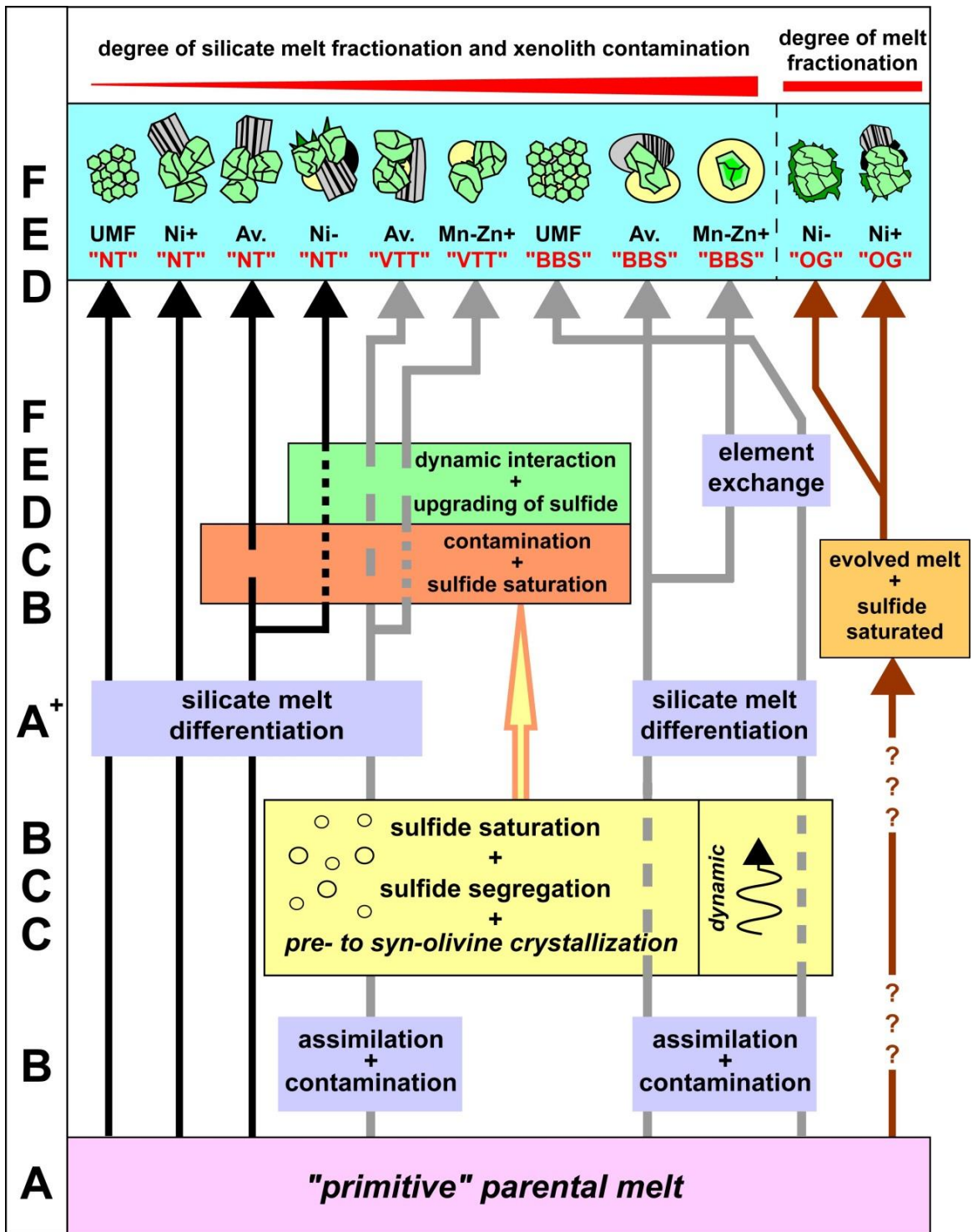
Fig. 5.1: Schematic illustration of how the key olivine compositions from the major lithologies (from UMF to OG) at the VBI reflect key ore-forming processes in the magmatic system. This conceptual figure

integrates the conclusions from the VBI olivine data. For example, following the Mn-Zn-rich (+) olivine from the VTT, their composition likely reflects crystallization from a silicate melt that experienced assimilation and contamination early in the differentiation history, which led to sulfide saturation and segregation and the syn-precipitation of olivine with lower Ni and higher Mn and Zn contents than those from average VTT, which likely crystallized earlier from a less Mn-Zn enriched and Ni depleted melt. From left to right (UMF in NT to Mn-Zn-rich BBS), the degree of silicate melt differentiation and country rock contamination increases. Capital letters (A to F) indicate stages in the igneous system where key ore-forming events occurred: **A**) "primitive" parental melt (**A+** represents more fractionated parental melt), **B**) "sulfidic" country rock contamination, **C**) sulfide saturation and segregation (multiple events at various stages), **D**) mafic magmatic episodicity (fresh pulses of mafic magma), **E**) dynamic transport through magma conduit(s), and **F**) the accumulation and concentration in a contaminated environment (partly resulting in trace element zonation of BBS olivine).

12) Olivine from the VBI (primarily EDI) is compositionally distinct and the multivariate dataset (PCA vectoring) allows the geochemical separation of prospective olivine in proximity to massive sulfides at the base of the EDI from non-prospective olivine in the barren parts of the EDI.

13) The composition of the more evolved PLI olivine is in accord with their derivation through fractional crystallization from a single pulse of silicate melt with a higher degree of differentiation (closed-system) that experienced late sulfide segregation.

14) The distinct compositional diversity of VBI and PLI olivine can be used to discriminate the prospective olivine in the VBI from the non-prospective olivine in the PLI and thus potentially identify fertile mafic intrusions on a regional scale.

15) For application in other mafic intrusion it might be necessary to adjust the multi-trace element selection to the intrusion-specific relative proximity values and to establish an intrusion-specific multivariate (PCA vector) baseline.

5.4. Advantages and Broader Impact

As opposed to the traditional Fo- and Ni-in-olivine analyses, which are only useful for the detection of chalcophile element depletion resulting from sulfide saturation (just one of various key ore-forming processes), the trace element-in-olivine approach on the other hand, adds several important petrological dimensions. The distribution of numerous trace elements that are sensitive to melt differentiation through fractional crystallization of other phases (plagioclase, pyroxenes, oxides etc.), sulfide saturation event(s), melt contamination (through assimilation of crustal rock), and a dynamic interaction with sulfide/silicate melt (e.g., in conduit environment), promotes the identification of these processes and thus advances the geological and petrogenetic model of the VBI and PLI.

This approach utilizes the analytical advantages of the SIMS (with respect to EPMA), while it also drastically increases the geochemical resolution. Processes identified in-situ on the micro-scale, for instance, trace element zonation of olivine, are translated and interpreted on macro-scale (e.g., zonation results from variable enrichment and reequilibration in contaminated and sulfide saturated environment) and thus yield important information about the magma dynamics. Finally, olivine from various Ni-Cu-Co-(PGE) sulfide deposit-types can be analyzed without difficulty and the existing Ni-in-olivine database can consequently be supplemented in order to improve the discrimination of an economically mineralized mafic intrusion from a barren, uneconomic mafic intrusion. In addition, the trace element data (especially Mn-Zn) can potentially provide a geochemical vector towards zones of sulfide mineralization in the VBI, which in turn further calibrates an existing geological model.

5.5. Open Questions and Recommendations for Future Research

This study has significantly advanced understanding of analytical and petrogenetic aspects of olivine trace element chemistry for two specific ore deposits in Labrador. However, implementation of the trace element-in-olivine approach for mineral exploration, even as a routine application at the VBI, requires a more holistic database including critical samples from other major parts of the deposit (Reid Brook Zone, base of the Ovoid, conduit at Discovery Hill etc.). This is essential in order to assure that the prospective olivine compositions, such as the Mn-Zn-rich varieties in the BBS, are indeed exclusively indicative for higher Ni tenor mineralized environment(s) in the EDI and similar magmatic environments, and that the lower Ni tenor conduit mineralization, for instance, is associated with different olivine characteristics. The demonstrated systematic olivine characteristics are thus only legitimately applicable to the EDI and extrapolation to other parts of the VBI, or even other potential target intrusions in the NPS or elsewhere, should strictly occur based on geological and petrological similarities, and must be carefully evaluated on the individual basis. In this regard, the SIMS analyses and comparison with olivine from the PLI assisted greatly in isolating important olivine trace element signatures and emphasizing the petrological importance of various trace element distributions (especially Cr, Mn, Co, Ni, Zn). In conjunction with a suitable geological model, the olivine data are a valuable fertility indicator and thus exploration- and target generation-relevant information can be extracted for the VBI (EDI) and (with restrictions) for the PLI, but must be approached cautiously and with an adjusted multi-trace element vector ("baseline") for other mafic intrusions on a regional scale.

Future research should focus on the expansion and refinement of the olivine trace element database to improve existing geological/petrogenetic models (VBI, PLI other applicable NPS intrusions) and in turn allow a more confident and statistically more robust prediction of the Ni-Cu-Co sulfide mineralization potential of mafic intrusions. The geochemical and partitioning behavior of promising elements, such as Cr, Mn, Co, and Zn in sulfide saturated and contaminated mafic melts ("open-system" conditions) must be further examined and thoroughly explored. The dynamic interaction and the resulting solid-liquid diffusion processes of entrained olivine and surrounding (cooling and crystallizing) sulfide liquid needs to be evaluated on the trace element scale (element transfer vectors). A proper quantification of diffusion rates is necessary in order to predict time scales for melt contamination, onset of sulfide saturation and chemical homogenization of olivine enclosed or surrounded by sulfide liquid or contaminated mafic melt. Recent olivine diffusion studies have demonstrated the potential of olivine in constraining the timing and duration of magma migration, interaction, and transport in volcanic systems (e.g., Costa and Dungan 2005; Turner and Costa 2007). An extension of this approach to dynamic mafic intrusive systems like the VBI would yield valuable quantitative information about crystallization, equilibration and reequilibration processes of olivine in ore-forming environments. This understanding could then be applied to enhance olivine trace element studies of mineralized mafic intrusions to a uniformly applicable exploration tool ("fertility indicator") even for other classes of mineralized mafic magmatic systems (e.g., Naldrett, 2010a-b), and then ultimately permit a more confident prediction of the mineralization potential of mafic intrusions.

CHAPTER 6 - Appendix

6.1. Detailed Calibration of SIMS Determinations

Based on the calibration analyses of the olivine reference materials (RM), quantification of major and trace elements in olivine measured by SIMS must be performed following a stepwise empirical approach, which fully accommodates the influence of significant matrix effects and isobaric interferences. In the initial step, the forsterite content is calculated. This is subsequently used in quantifying trace elements (Mn, Co, Ni, and Zn) that are significantly affected by major element matrix effects. Unaffected elements (Ca, Sc, Ti, V, Cr, Cu, Sr, Y, and Zr) are quantified using conventional working lines with one olivine RM and NIST glasses (610/612), as discussed in Section 6.1.3. A complete sequential empirical approach is presented below.

6.1.1. Determination of Forsterite and Major Element Content by SIMS

Step 1

Initially, SI intensities measured with SIMS are used to calculate the ratio $R_{Fo} = (I^{25}Mg^+/I^{30}Si^+)/(I^{25}Mg^+/I^{30}Si^+ + I^{57}Fe^+/I^{30}Si^+)$, which is then plotted against the EPMA-derived accepted Fo values (Fo $(EPMA)_{ACCPT}$) to produce a calibration curve (Chapter 2 – Fig.2.3A). Axis intercepts are fixed at (0,0) and (1,1) and this curve is fitted using a non-linear, rational equation regression. The resulting expression, of the form (*Eq.1*):

$$R_{Fo} = \frac{\left(a + Fo(EPMA)_{ACCPT}\right)}{\left(b + c \times Fo(EPMA)_{ACCPT}\right)}$$

is then used to compute the Fo values of unknown samples measured by SIMS (Chapter 2 – Fig.2.3A). The MgO, FeO and SiO_2 contents are then easily calculable from the Fo content following Step 2 based on the known stoichiometry of the ideal forsterite-fayalite series.

Step 2

By utilizing olivine crystals with a wide range of compositions as potential RM, our empirical approach accounts for the major element variations within the olivine solid solution. The major element concentrations (MgO-FeO-SiO) vary almost linearly between Fo_{100} and Fo_0 (Chapter 2 – Fig.2.3B). Our most forsteritic olivine (Ol-4, Chapter 2 – Table 2.1) has 56.66 wt.% MgO and 42.44 wt.% SiO_2 with no detectable FeO, whereas a theoretical pure fayalite (calculated value, Table 2.1) would have 70.51 wt.% FeO and 29.49 wt.% SiO_2. Therefore, common natural olivine, in the range of Fo_{85} to Fo_{40} (Deer et al., 1997), will fall on stoichiometrically determined curves between these endmembers since minor and trace element concentrations are generally less than 1 wt.%. This is portrayed graphically by plotting the wt.% of the major elements (MgO-FeO-SiO) versus the Fo contents (accepted values as determined by EPMA) of the reference olivine grains selected for this study (Chapter 2 – Fig.2.3B). The Fo value of an unknown olivine

computed through Step 1 can now be inserted to solve the individual equations for the major element concentrations in stoichiometric olivine. For example, MgO (*Eq.2*):

$$MgO\ (wt.\%) = \frac{\left(X_{MgO} \times m_{MgO}\right)}{\left(X_{MgO} \times m_{MgO} + X_{FeO} \times m_{FeO} + X_{SiO2} \times m_{SiO2}\right)}$$

where, in this case, X_{MgO} is the relative cation fraction of MgO to FeO and SiO_2 in stoichiometric olivine (e.g., Fo90 has 1.8 wt.% MgO, 0.2 wt.% FeO and 1.0 wt.% SiO_2) and m_{MgO} is the molecular weight of MgO (40.30 Da). This procedure is repeated to calculate the FeO and SiO_2 concentrations.

6.1.2. Quantification of Elements with Conventional Working Lines

Step 3

The trace elements Ca, Sc, Ti, V, Cr, Cu, Sr, Y, and Zr may be adequately quantified with a conventional working line approach (e.g., Shimizu et al., 1978; Yurimoto et al., 1989; Ottolini et al., 1993; Weinbruch et al., 1993; Jones and Layne, 1997). For each element M, the measured $^{N}M^{+}/^{30}Si^{+}$ ratios are fitted against the atomic ratios M/Si, for example, for Cr (*Eq.3*):

$$At.Ratio\ \frac{Cr}{Si_{ACCPT}} = \frac{\left(Cr_{ACCPT}/m_{Cr}\right)}{\left(Si_{ACCPT}/m_{Si}\right)}$$

where Cr (ppm)$_{ACCPT}$ is the accepted concentration of Cr in the RM (olivine or NIST glass) determined by an independent analytical technique (EPMA *or* ICP-MS) and m$_{Cr}$ is the atomic weight of Cr (51.9961 Da). This empirical relationship yields linear regressions that can then be used to easily quantify the selected element, and is quantitatively adequate for many of the trace elements assessed in this study.

6.1.3. Quantification of Elements with RSF-based Working Lines

Step 4A

The trace elements Mn, Co, Ni, and Zn are prone to significant matrix effects, and for quantification, an alternative to Step 3 has to be applied, where element-specific Relative Sensitivity Factors (RSF) are fitted against the Fo (EPMA)$_{ACCPT}$ of the measured RM. Element-specific RSF are calculated as follows (*Eq.4*) (e.g., for ^{60}Ni$^+$):

$$\mathrm{RSF}_{Ni\ \mathrm{SIMS\ -\ RM}} = \left(I^{60}Ni^+ \big/ I^{30}Si^+\right)_{\mathrm{SIMS\ -\ RM}} \times \left(\frac{SiO_2\ (\mathrm{wt.\%})}{Ni\ (\mathrm{ppm})}\right)_{ACCPT\ -\ RM}$$

where the *SIMS-RM* term incorporates measured SI intensities of the individual olivine RM and the *ACCPT-RM* term incorporates the accepted concentration of SiO_2 (wt.%) divided by the accepted concentration of the element of interest in the RM. Polynomial regressions of Equation 4 (Chapter 2 – Fig.2.4 and 2.5) are subsequently used for quantification of elemental concentrations in unknown samples.

Step 4B

For elements with non-linear variations in RSF with Fo composition, we also applied a statistical analysis (full-model multiple regression) to determine the dependency of RSF on the three major components of olivine (MgO, FeO and SiO_2). Element-specific RSF are calculated following Eq. 4, but then fitted as a function of these three components in the form ($aSiO_2$ + bMgO + cFeO). This approach has previously proven highly informative in SIMS chlorine stable isotope ($\delta^{37}Cl$) analysis for calibration of the instrumental mass fractionation (IMF) (Godon et al., 2004). Here, strong correlations (R^2 ≥0.983) are achieved for some elements, notably Cr, Mn, Co, Ni, Cu and Zn (Chapter 2 – Fig.2.6), when the RSF is expressed as a function of the three components. This routine therefore offers a potentially superior option to Step 4A for a matrix effect-corrected quantification of some trace elements in olivine.

Step 5

Once an individual working curve (i.e., polynomial regression (Step 4A) *or* linear regression (Step 4B)) is calculated for each trace element, it is most convenient to simply solve the associated regression equation to obtain the element-specific RSF based on the Fo value or the major components (MgO-FeO-SiO_2) of the olivine as determined in Steps 1 or 2. The elemental RSF can then be inserted in the following equation (*Eq. 5*) to determine the "matrix effect"-corrected trace element concentrations of an unknown sample (e.g., for $^{60}Ni^+$):

$$[\text{Ni}]\text{ppm}_{Calculated} = \left(I^{60}Ni^{+}/I^{30}Si^{+} \right)_{\text{SIMS - Sample}} \times \left(\frac{SiO_2 \; (\text{wt.\%})_{Sample}}{\text{RSF}_{Ni}} \right)$$

where RSF_{Ni} stands for the element-specific RSF obtained through Steps 4A *or* 4B, the *SIMS-Sample* term incorporates measured SI ratios of an unknown sample and SiO_2 (wt.%)$_{Sample}$ is the SiO_2 concentration of the sample calculated in Step 1.

In summary, all elements that display straight linear regressions of SI intensity ratios versus atomic weight ratios (or $^{N}M^{+}/^{30}Si^{+}$ x SiO_2 wt.% versus concentration in ppm) can be adequately quantified via the conventional working line method (Step 3), whereas elements that yield non-linear regressions need to be quantified through RSF-based working lines generated by fitting them versus the Fo content, or versus all three major components in olivine (Steps 4A/4B and 5).

6.2. Analytical Uncertainty and Error Propagation

The analytical uncertainty is calculated based on 10 cycles of peak counting on an individual spot and is reported for each element as 2σ. It strongly depends on counting statistics and the counts per second (c/s) of a specific element in the matrix. Generally, a low element abundance also translates into low c/s and conversely into a higher 2σ error. For example, $^{25}Mg^{+}/^{30}Si^{+}$ has a relative 2σ error of 0.9% in Ol-1, whereas Ol-5 has 2.4%. On the other hand, $^{40}Ca^{++}/^{30}Si^{+}$ has a relative uncertainty (2σ) of 4% in Ol-5 and circa

13% in Ol-1. To quantify (ppm) this error, the 2σ values are processed in a similar manner to isotope ratios (see Appendix 6.1.).

Error propagation was used for the calculation of the R_{Fo} analytical uncertainty (see also Chapter 2.4.3.). However, since the individual errors on $^{25}Mg^+/^{30}Si^+$ and $^{57}Fe^+/^{30}Si^+$ are extremely small, the resulting SIMS error on R_{Fo} is negligible with a range of, for instance, 0.02% for WGR and 0.11% for ICE olivine populations. A noticeable error, on the other hand, is inserted during the determination of the Fo content (see Appendix 6.1.). This 2σ empirical error is reflected by the uncertainty of the non-linear regression model used in the calculation and the associated 95% confidence interval and has a mean of 1.4%, which is based on 341 spots on seven RM from 2009-2011 (Chapter 2 – Fig.2.3A). This is circa 3x higher than the mean Fo error from EPMA measurements (circa 0.5% 2σ).

6.3. Modeling of Olivine Diffusion Profiles

To calculate the diffusion time from the trace element profiles in olivine from VB266-43 (Chapter 3 – Fig.3.9), Fick's Second Law for one-dimensional diffusion into a semi-infinite medium with a constant concentration at a fixed crystal-sulfide melt boundary and a constant diffusion coefficient (D) was applied in the form (*Eq.6*):

$$C(x,t) = C_1 + (C_0 - C_1) \times erf\left(\frac{x}{2 \times \sqrt{(D \times t)}}\right)$$

where C is the concentration (ppm), t is the time (y), D is the diffusion coefficient (mm^2/y), and x is the distance (mm) (e.g., Costa and Chakraborty, 2004; Petry et al., 2004; Costa and Dungan, 2005; Quian et al., 2010). The following initial (t=0) and boundary (t>0) conditions were used:

$$C = C_0, \qquad t = 0$$
$$C(r) = C_1, \quad t \neq 0$$

where r reflects the coordinate at the rim of the crystal with a time invariant constant composition ($C(r)$). For the diffusion calculation, the composition of the homogeneous core plateau represents the initial condition (C_0=uniform olivine composition), whereas the composition at the edge of the crystal (C_1) is taken as the boundary condition (e.g., Costa and Dungan, 2005).

All variables except the diffusion coefficients (D) for Ni and Mn were measured. To calculate the immersion time of olivine in the sulfide melt (before diffusion effectively subsided), literature values for D were utilized. In the absence of (experimental) diffusion data for olivine-sulfide melt pairs, existing values for diffusion coefficients between olivine-silicate melt were used (Petry et al., 2004). Experimental determinations of cation diffusivities in olivine demonstrate the strong dependence of D on temperature (T), oxygen fugacity (fO_2), crystallographic direction and chemical composition (Costa and Chakraborty, 2004; Petry et al., 2004, and references therein). Diffusion rates in olivine are also strongly anisotropic, and for Fe-Mg, Ni and Mn at least 6x faster parallel to the

(crystallographic) c-axis than to a or b (Costa and Chakraborty, 2004; Petry et al., 2004, and references therein).

The olivine grain in VB266-43 is probably oriented approximately parallel to the c-axis, which means that the measured transects would be parallel to a and b and thus ≤90° or ≥90° to the c-axis. However, because of the strong anisotropy and the uncertain crystallographic orientation of the sample olivine, D values parallel to the c-axis, in other words maximum D values, were used for the calculation. The Ni and Mn diffusion coefficients were taken from Petry et al. (2004), for ~1100°C and ~1000°C, respectively, for an approximate fO_2 of 10^{-11} (bar), which is close the published value of $10^{-11.1}$ for the BBS in the EDI (Brenan and Li, 2000). Furthermore, the experiments from Petry et al. (2004) were performed on olivine with Fo90 as compared to the VB266-43 sample olivine with Fo62. Since D_{Ni} varies with the Fe content of the olivine (Petry et al., 2004), our calculation of t with D_{Ni} is likely an underestimation, and is probably closer to the minimum value(s) calculated with D_{Mn} for 1100°C (Chapter 3 – Fig.3.9). D values for Mn are unaffected by the apparent Fo content of olivine (Petry et al., 2004).

In contrast, the intensive parameters (e.g., T and fO_2) and the D values for the olivine-sulfide melt pair are not well constrained for environments similar to the BBS, and the equilibration temperature might well be below a 1000°C. Since diffusion rates decrease rapidly with decreasing temperature (Ito et al., 1999; Petry et al., 2004), the maximum time span might be closer to 1,000 yrs than the calculated ~160 yrs, which, however, is still considered "rapid" in a plutonic magmatic system. The results imply that segregating sulfide melt enclosed the olivine shortly after crystallization (silicate melt was not yet Ni

depleted), probably already in the EDI or somewhere close to the final emplacement. Thus, in less than 1,000 yrs olivine and sulfide melt equilibrated in the dike, close to or at the base of the EDI (Fig.3.13). This sulfide-upgrading process was likely more static, with a lower R-factor, and thus less effective than the more dynamic upgrading of the high-tenor net-textured sulfides in the immediate dike environment. This prevented the massive sulfides in the BBS from achieving similar tenors to the net-textured sulfides in the VTT.

In summary, the presented time span is only a first-order approximation and needs to be confirmed by additional samples from the BBS and the LTT to make a reasonable assumption about the equilibration time of the olivine-sulfide melt pair, and to further yield the exact timing of initial immersion and thus the likely onset of sulfide saturation and segregation. However, initial modeling of these diffusion profiles in olivine from the BBS provides an opportunity to quantify the documented trace element exchange process and subsequently extract a time span for the onset of sulfide saturation (residence time of immersed olivine) and late-stage sulfide melt upgrading.

6.4. Relative Vertical Proximity Factor and Multiple Regression Analysis

As described in Chapter 3, the relative vertical proximity factor (RVP) is calculated as the depth of the sample divided by the depth of the first occurrence of mineralization in the DDH intersecting massive sulfide (VB266-VB544-VB552) multiplied by the relative

sulfide content (see Chapter 3 and 4). The RVP data and the composition of olivine from VB266-VB544-VB552 where then used in a full-model multiple regression (also performed in Chapter 2; see Appendix 6.1.) based on the distribution of Fe-V-Cr-Mn-Co-Ni-Zn. The resulting regression has a R^2=0.78, and was further used to calculate the *predicted* relative proximity to massive sulfide of EDI olivine from the lateral transects presented in Chapter 4 (Fig.4.9 and 4.10). Although the predicted proximity has a relatively high uncertainty (see R^2), the predicted values are, as expected, lithology-dependent and increase towards the base of DDH from the barren south to the mineralized north of the EDI. In conjunction with petrographic observations (degree of alteration, enclosure by sulfides, modal abundance of olivine etc.) and stratigraphic information (exact depth of sample in the context of the EDI), prospective olivine grains can be pre-selected for this regression analysis, to exclude non-prospective "impostor" olivine, such as the metasomatized olivine in NT sample VB332-4 (Fig.4.9). The multiple regression analysis was performed with CoStat Version 6.4 from CoHort Software.

The regression equation for the *predicted* RVP is:

$2.293e^{-6}$(**Fe**)-0.038(**V**)-0.001(**Cr**)+$8.724e^{-5}$(**Mn**)-$5.763e^{-4}$(**Co**)+$1.418e^{-4}$(**Ni**)-$4.008e^{-4}$(**Zn**)

6.5. Kernel Density Estimation (KDE)

Histograms as a means to graphically display large datasets were recently replaced by Kernel Density Estimation (KDE), a non-parametric method for the estimation of a probability density function (e.g., Thomson and Maclennan, 2013 and references therein). This method provides more statistical and physical meaning than normal histograms, for

which the plotted form of the density distribution of the data depends strongly on the selected class intervals, or the physically meaningless bin-size parameter (e.g., Thomson and Maclennan, 2013 and references therein). To avoid this, each data point in a KDE is replaced by a Gaussian (normal) function that is defined by a standard deviation (1σ), known as the bandwidth (or smoothing) parameter (h). The normal distributions are then summed and result in a smooth curve, the kernel density estimate, which offers a good estimate of the probability density function without assuming, for instance, that the data are normally distributed (e.g., Thomson and Maclennan, 2013 and references therein). The optimal bandwidth is automatically calculated to prevent over- or under-sampling of the data and in this context reflects the compositional uncertainty of the dataset (see Chapter 4, Fig.4.11 and 4.12). The calculations were performed with 512 steps in the AMC Kernel density MS-Excel® Add-in.

6.6. Sample Petrography

6.6.1. Thin-Sections of Samples Used for SIMS Analyses

In the following all samples utilized for olivine analyses in Chapter 3 and Chapter 4 are displayed with their individual DDH identification number, their specific sample code (as used in Chapter 3 and Chapter 4), the sample depth and sample lithology. The first six plates represent samples used in Chapter 3, and the last six plates samples from Chapter 4. The shown thin-sections have approximately a 1 inch (~2.5 cm) diameter.

VB96266

ED-NT-1

NT - 0 m

VB96266-1

NT - 38 m

VB96266-21

NT - 47 m

VB96266-23

NT - 78 m

VB96266-24.1

NT - 101 m

VB96266-24.2

NT - 101 m

VB96266-26A

NT - 106 m

VB96266-26B

NT - 106 m

VB96266-27A

NT - 108 m

VB96266-27B

NT - 108 m

VB96266-3.1

NT - 108 m

VB96266-3.2

NT - 108 m

VB96266

VB96266-29

VTT - 146 m

VB96266-31.1

VTT - 217 m

VB96266-33

VTT - 262 m

VB96266-34A

VTT - 274 m

VB96266-6.2

VTT - 290 m

VB96266-7

VTT - 357 m

VB96266-8

VTT - 385 m

VB96266-37

VTT - 402 m

VB96266-39

VTT - 453 m

VB96266-10.3

VTT - 501 m

VB96266-12

BBS - 609 m

VB96266-43

BBS - 651 m

VB96266

VB96266-44

BBS - 651 m

VB01552

VB01552-1

OG - 4 m

VB01552-3

OG - 77 m

VB01552-5

NT - 225 m

VB01552-6.2

VTT - 587 m

VB01552-11.1

VTT - 763 m

VB01552-11.2

VTT - 763 m

VB01552-13.1

VTT - 792 m

VB01552-20

LTT/BBS - 900 m

VB01552-15B

BBS/UMF - 836 m

VB01552-17.1

BBS - 850 m

VB01552-21.1

BBS - 902 m

VB00544

VB00544-1

NT - 11 m

VB00544-2

NT - 18 m

VB00544-4.2

NT - 36 m

VB00544-5A

NT - 67 m

VB00544-8.2
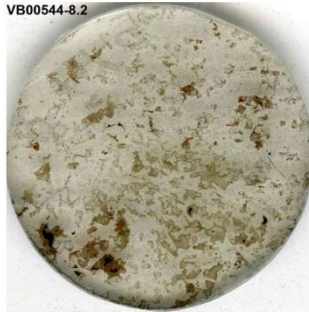
NT - 247 m

VB00544-9

NT - 349 m

VB00544-10

VTT - 355 m

VB00544-11.2

OG - 375 m

VB00544-12.1

OG - 389 m

VB00544-12.2

OG - 390 m

VB00544-13

OG - 404 m

VB00544-15

VTT - 557 m

VB00544

VB00544-17

VTT - 622 m

VB96266-18.1

VTT - 663 m

VB00544-18.2

VTT - 663 m

VB98449

VB98449-3

OG - 474 m

VB98449-4.1

OG - 513 m

VB98449-4.2

OG - 513 m

VB98451

VB98449-5

OG - 611 m

VB98451-1

VTT - 12 m

VB98451-3.1

VTT - 25 m

VB98451-3.2

VTT - 25 m

VB98451-4

VTT - 171 m

VB98451-7

BBS - 292 m

VB00548

VB00548-1

NT - 26 m

VB00548-2

NT - 33 m

VB00548-9.1

NT/VTT - 567 m

S99012

VB00544-10

NT/VTT - 569 m

S99012-1

Dunite - 8 m

VB96307

VB96307-4

NT - 101 m

VB96307-6

NT - 106 m

VB96307-7

NT - 108 m

VB96307-9

NT - 280 m

VB96307-11

VTT - 545 m

VB96307-12

VTT - 565 m

VB96332

VB96332-1

NT - 7 m

VB96332-2

NT - 45 m

VB96332-4

NT / RPGR contact - 92 m

VB96332-6

NT - 107 m

VB96332-7

NT - 108 m

VB96332-9

NT - 140 m

VB96332 (cont.)

VB96332-10

OG - 169 m

VB96332-11

OG - 175 m

VB96332-12

NT - 200 m

VB96332-13

OG - 230 m

VB96332-15

NT - 460 m

VB96332-16

VTT - 680 m

VB99513

VB96332-17

VTT - 719 m

VB99513-1

NT - 15 m

VB99513-2

NT - 80 m

VB99513-4

NT - 105 m

VB99513-5

NT - 108 m

VB99513-6

NT - 110 m

VB99513 (cont.)

VB99513-7

NT - 111 m

VB99513-8

NT - 160 m

VB99513-10

NT - 291 m

VB99513-12

VTT - 340 m

VB99513-13

UMF - 384 m

VB99513-14

UMF - 386 m

VB99513-16

OG - 560 m

VB99513-19

VTT - 583 m

VB99513-21

NT - 650 m

VB99513-23

VTT - 705 m

VB99513-24

BBS - 710 m

VB99513-25
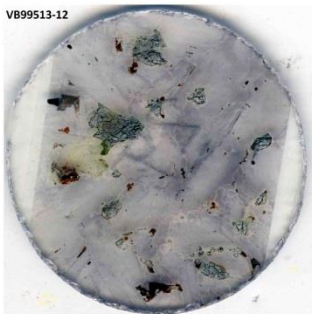
BBS - 740 m

VB99516

NT - 12 m
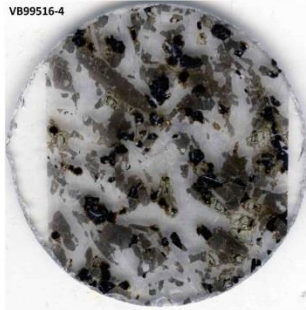
NT - 106 m

NT - 108 m

NT - 110 m

NT - 116 m

NT - 140 m

VTT - 199 m
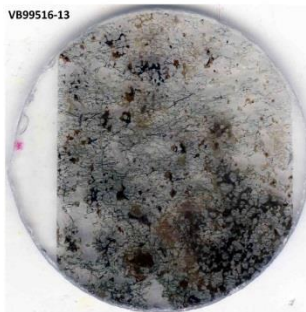
VTT - 240 m

VTT - 260 m

VB96248

VTT - 280 m

NT - 104m

NT - 106 m

VB96248 (cont.)

VB96248-5

VTT - 182 m

VB96248-7

VTT - 260 m

VB96248-8

VTT - 290 m

VB96248-9

VTT - 297 m

VB96248-12

VTT - 378 m

VB96248-14

UMF - 442 m

SVB96-02

VB96248-15

BBS - 559 m

96-02-02

OG - 8 m

96-02-03

OG/LTT - 22 m

SVB96-10

96-02-05

OG - 69 m

96-10-90

Trans. G - 21 m

96-10-91

Trans. G - 30 m
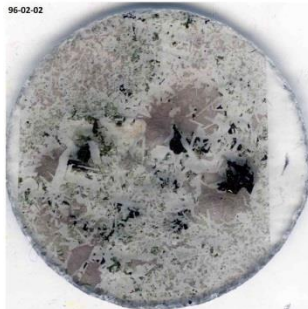
SVB96-27 G - 1 m
SVB97-79 G - 632 m G - 729 m
SVB97-92 BG - 187 m G - 247 m
SVB98-102 BG - 150 m
SVB98-113 G - 99 m
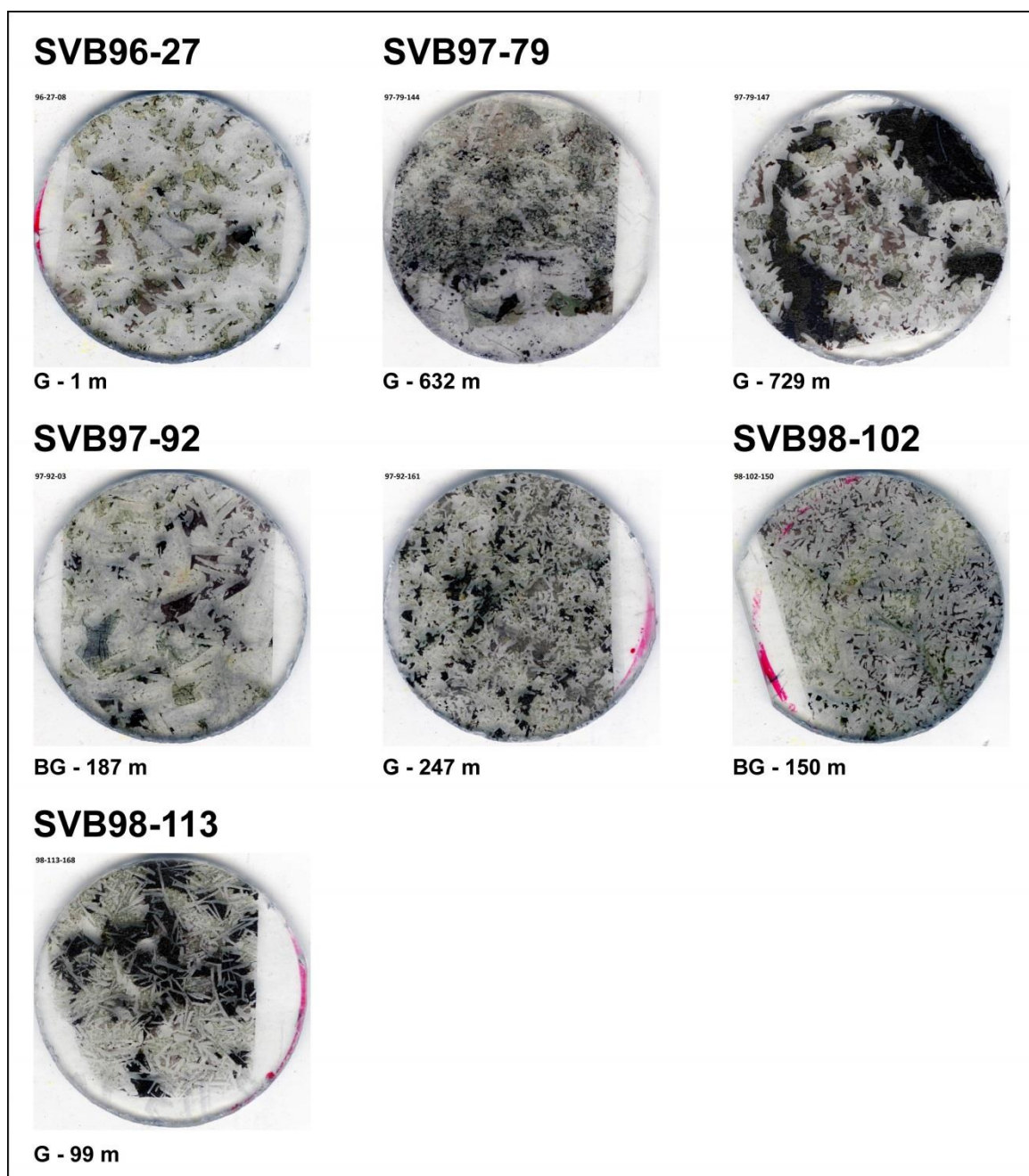
6.6.2. Photomicrographs of Samples Used for SIMS Analyses

Photomicrographs of representative olivine grains from the measured samples are presented. The scale is 5x (field of view – 4.4mm), 10x (field of view – 2.2mm), etc.

VB96266

ED-NT; 5x, XN
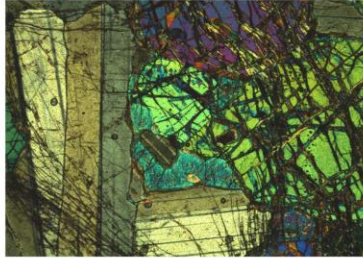
NT - 0 m

VB96266-1; 5x, XN
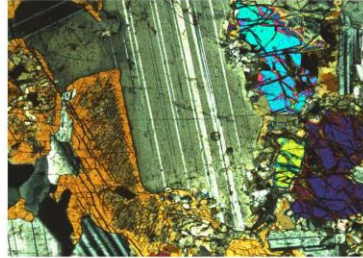
NT - 38 m

VB96266-21; 1.6x, XN
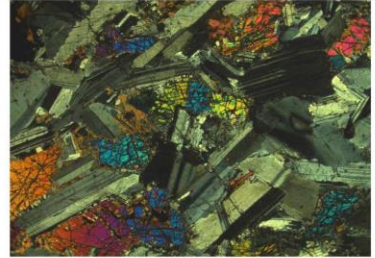
NT - 47 m

VB96266-23; 5x, XN
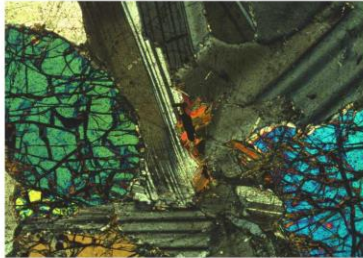
NT - 78 m

VB96266-24.1; 5x, XN
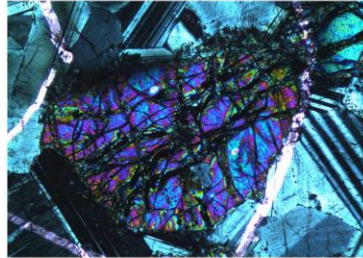
NT - 101 m

VB96266-24.2; 5x, XN
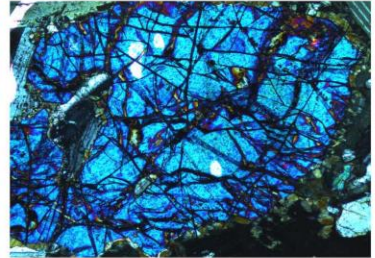
NT - 101 m

VB96266-26A; 5x, XN
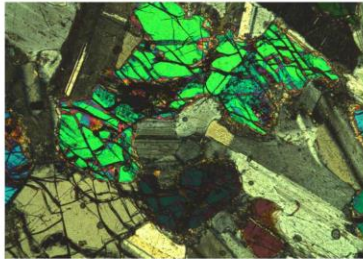
NT - 106 m

VB96266-26B; 5x, XN
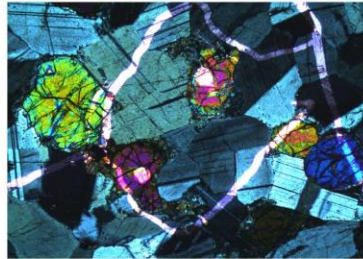
NT - 106 m

VB96266-27A; 5x, XN
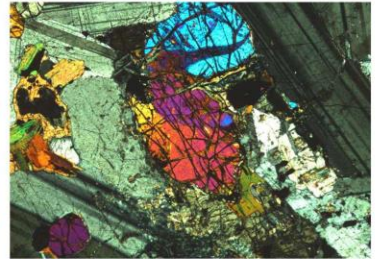
NT - 108 m

VB96266-27B; 5x, XN
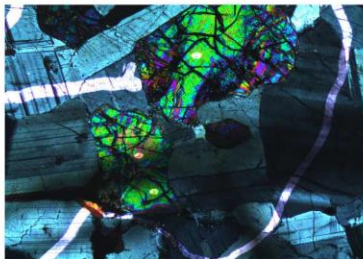
NT - 108 m

VB96266-3.1; 5x, XN
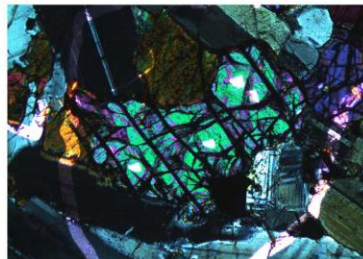
NT - 108 m

VB96266-3.2; 5x, XN
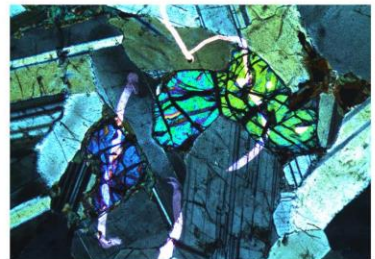
NT - 108 m

VB96266

VB96266-29; 1.6x; XN
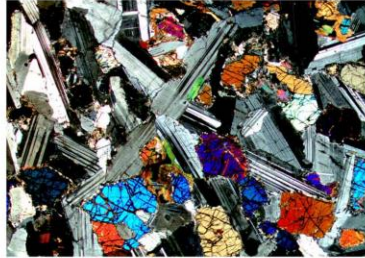
VTT - 146 m

VB96266-31.1; 5x; XN
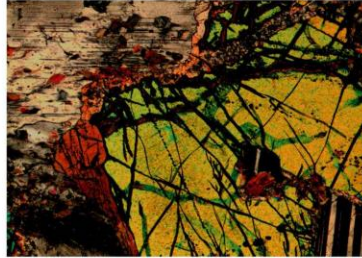
VTT - 217 m

VB96266-33; 5x; XN
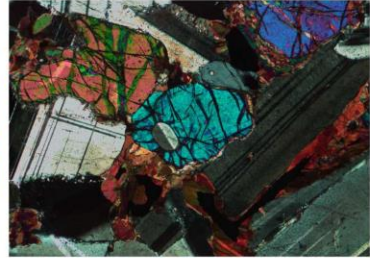
VTT - 262 m

VB96266-34A; 5x; XN
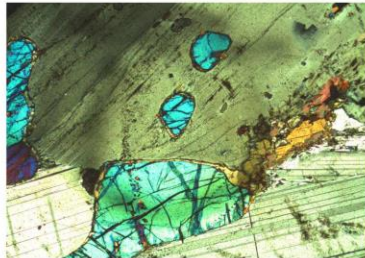
VTT - 274 m

VB96266-6.2; 5x; XN
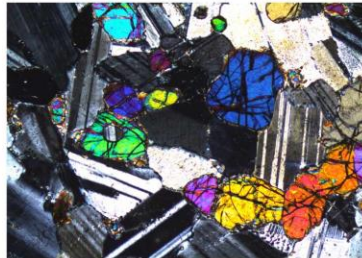
VTT - 290 m

VB96266-7; 5x; XN

VTT - 357 m

VB96266-8; 1.6x; XN
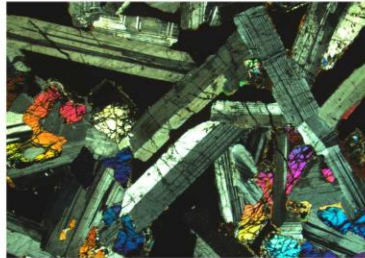
VTT - 385 m

VB96266-37; 5x; XN
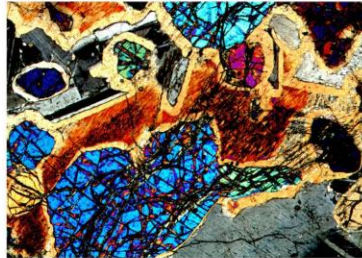
VTT - 402 m

VB96266-39; 5x; XN
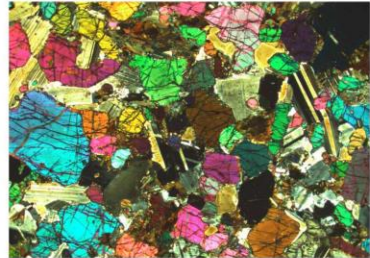
VTT - 453 m

VB96266-10.3; 5x; XN
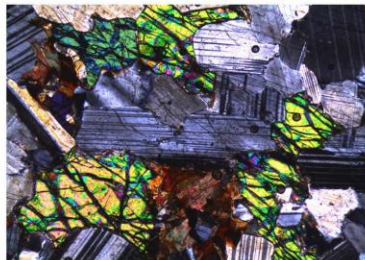
VTT - 501 m

VB96266-12; 5x; XN
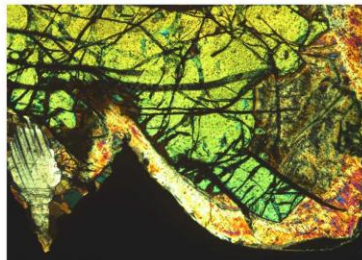
BBS - 609 m

VB96266-43; 5x; PP
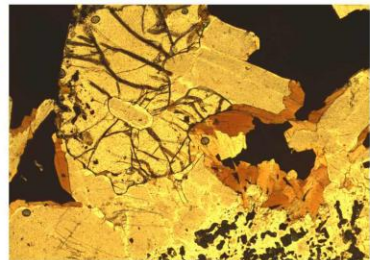
BBS - 651 m

VB96266

VB96266-44; 5x; XN
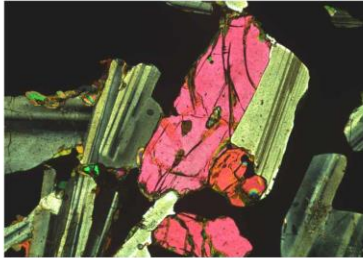
BBS - 651 m

VB01552

VB01552-1; 5x; XN
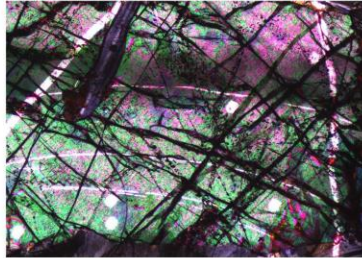
OG - 4 m

VB01552-3; 5x; XN
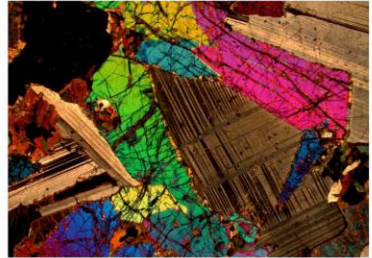
OG - 77 m

VB01552-5; 5x; XN
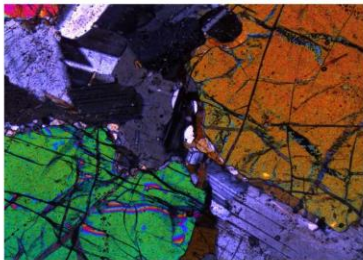
NT - 225 m

VB01552-6.2; 5x; XN
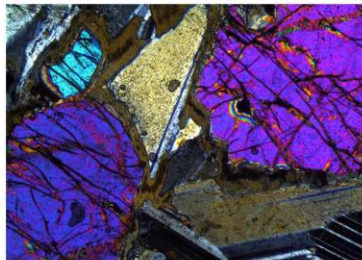
VTT - 587 m

VB01552-11.1; 5x; XN
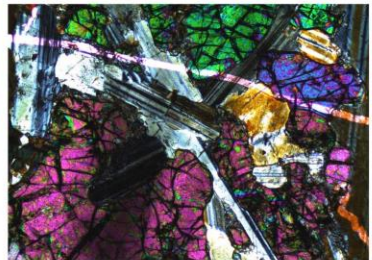
VTT - 763 m

VB01552-11.2; 5x; XN
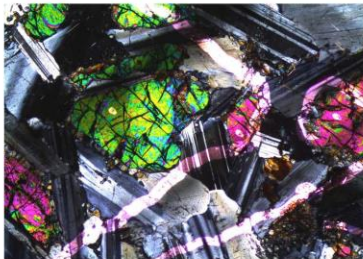
VTT - 763 m

VB01552-13.1; 5x; XN
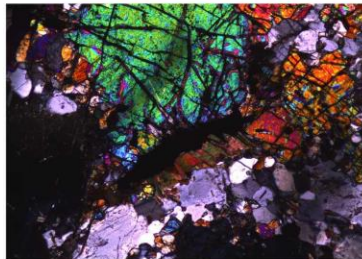
VTT - 792 m

VB01552-20; 5x; XN
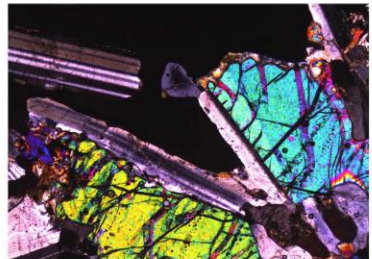
LTT/BBS - 900 m

VB01552-15B; 5x; XN
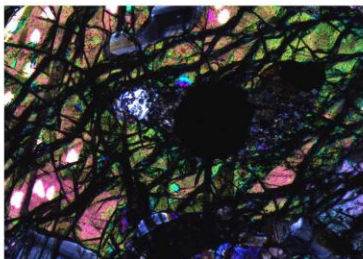
BBS/UMF - 836 m

VB01552-17.1; 1.6x; XN

BBS - 850 m

VB01552-21.1; 5x; XN
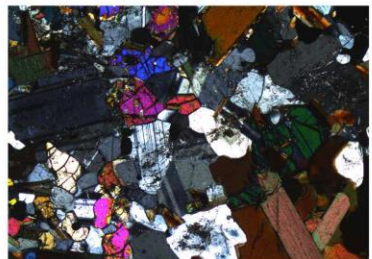
BBS - 902 m

VB00544

VB00544-1; 5x; XN
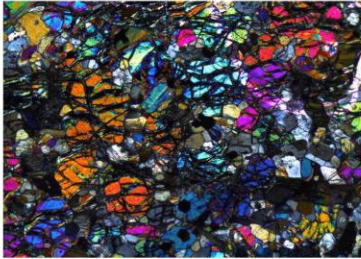
NT - 11 m

VB00544-2; 5x; XN
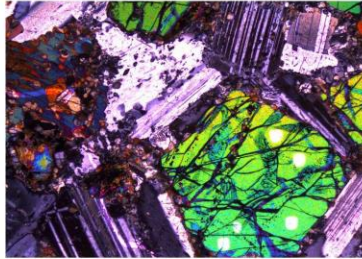
NT - 18 m

VB00544-4.2; 5x; XN

NT - 36 m

VB00544-5A; 5x; XN
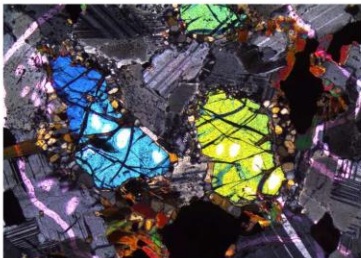
NT - 67 m

VB00544-8.2; 5x; XN
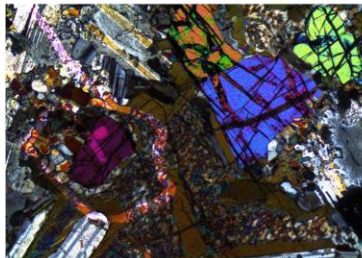
NT - 247 m

VB00544-9; 5x; XN
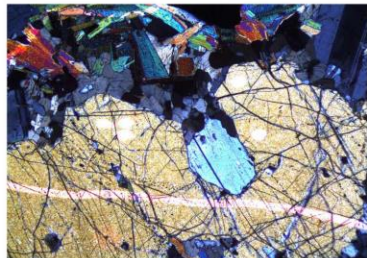
NT - 349 m

VB00544-10; 5x; XN
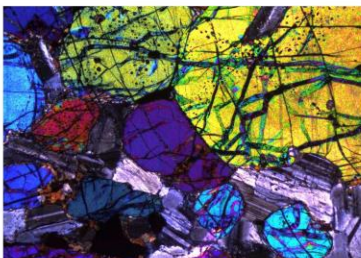
VTT - 355 m

VB00544-11.2; 5x; XN
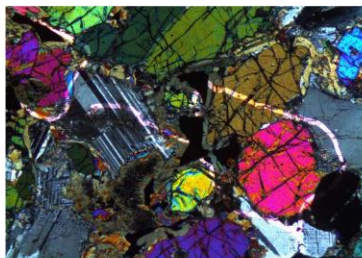
OG - 375 m

VB00544-12.1; 5x; XN
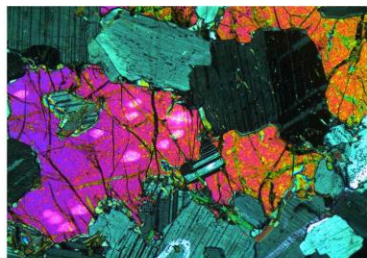
OG - 389 m

VB00544-12.2; 5x; XN
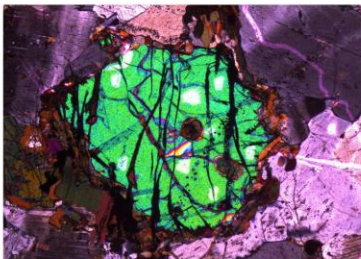
OG - 390 m

VB00544-13; 5x; XN
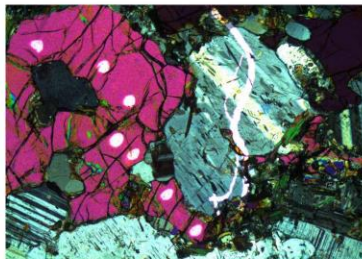
OG - 404 m

VB00544-15; 5x; XN
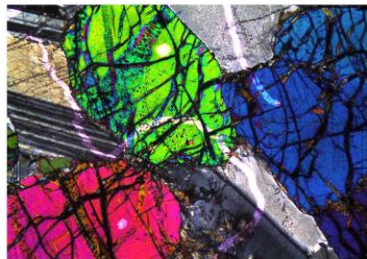
VTT - 557 m

VB00544

VB00544-17; 5x; XN
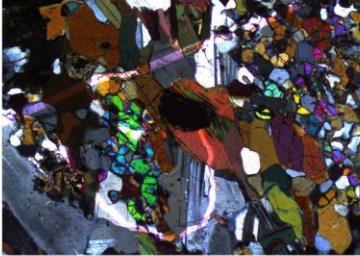
VTT - 622 m

VB00544-18.1; 5x; XN
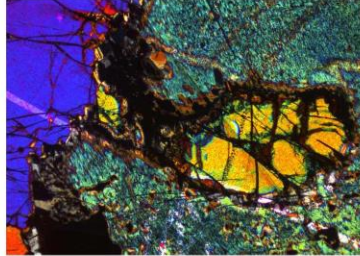
VTT - 663 m

VB00544-18.2; 5x; XN
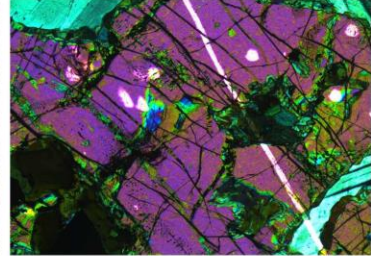
VTT - 663 m

VB98449

VB98449-3; 5x; XN
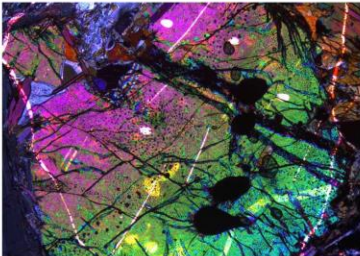
OG - 474 m

VB98449-4.1; 1.6x; XN
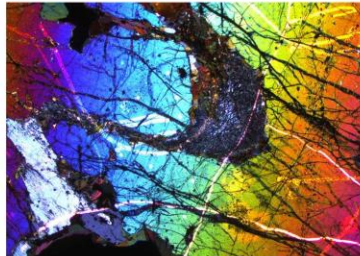
OG - 513 m

VB98449-4.2; 5x; XN
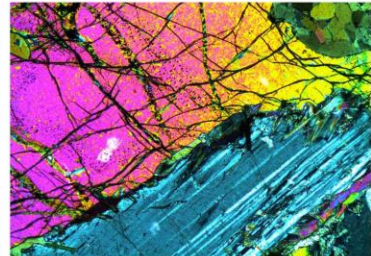
OG - 513 m

VB98451

VB98449-5; 5x; XN
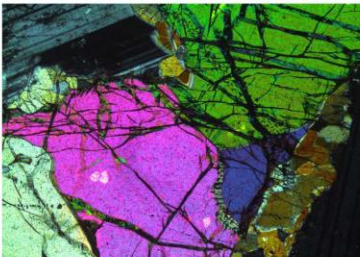
OG - 611 m

VB98451-1; 5x; XN
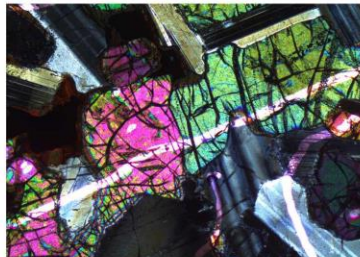
VTT - 12 m

VB98451-3.1; 5x; XN
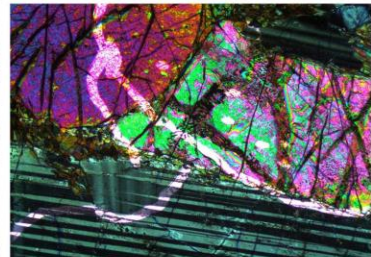
VTT - 25 m

VB98451-3.2; 5x; XN
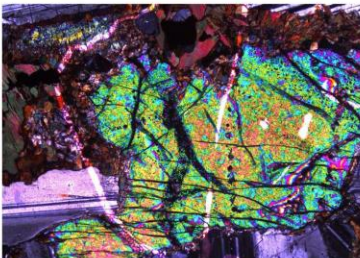
VTT - 25 m

VB98451-4; 5x; XN
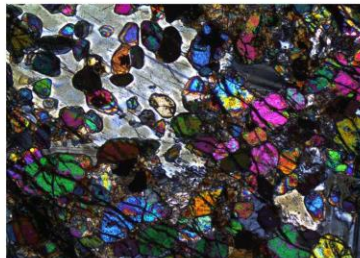
VTT - 171 m

VB98451-7; 5x; XN
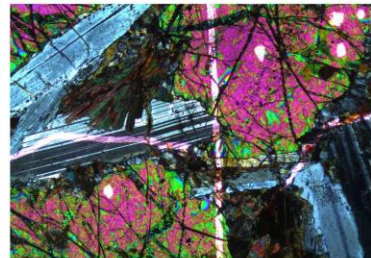
BBS - 292 m

VB00548

VB00548-1; 5x; XN
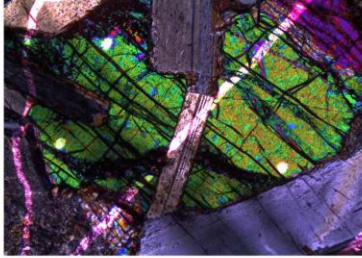
NT - 26 m

VB00548-2; 5x; XN
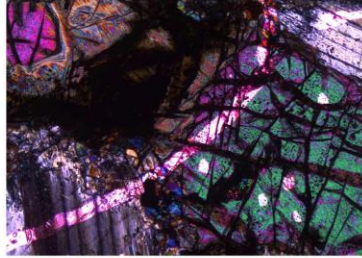
NT - 33 m

VB00548-9.1; 5x; XN
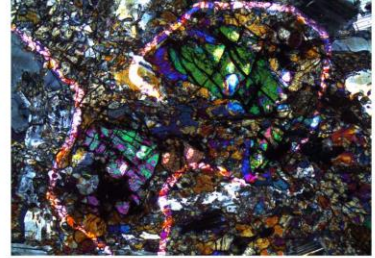
NT/VTT - 567 m

S99012

VB00548-10; 5x; XN
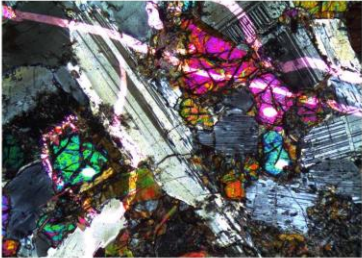
NT/VTT - 569 m

S99012-1; 5x; XN
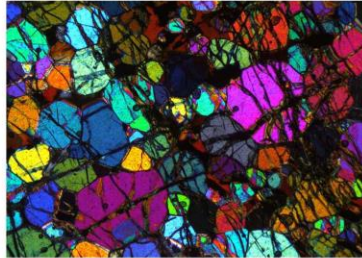
Dunite - 8 m

VB96307

VB96307-4; 5x; XN
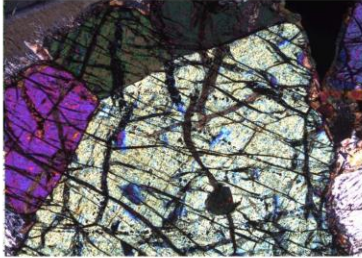
NT - 101 m

VB96307-6; 5x; XN
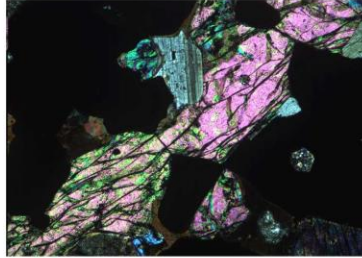
NT - 106 m

VB96307-7; 5x; XN
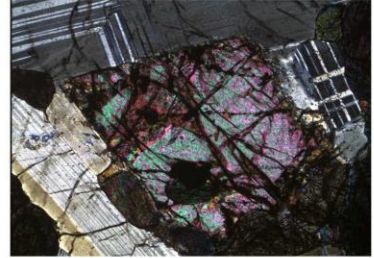
NT - 108 m

VB96307-9; 5x; XN
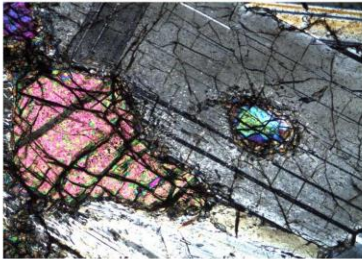
NT - 280 m

VB96307-11; 5x; XN
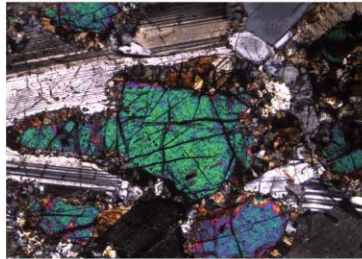
VTT - 545 m

VB96307-12; 5x; XN
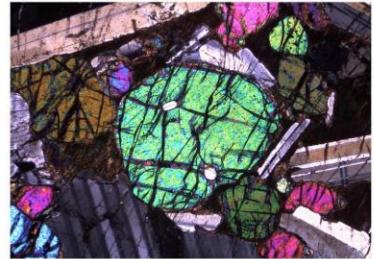
VTT - 565 m

VB96332

VB96332-1; 5x; XN
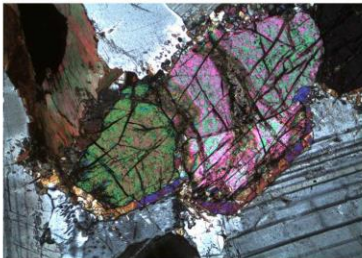
NT - 7 m

VB96332-2; 5x; XN
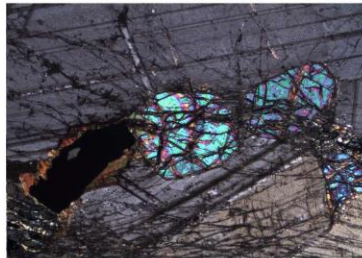
NT - 45 m

VB96332-4; 5x; PP
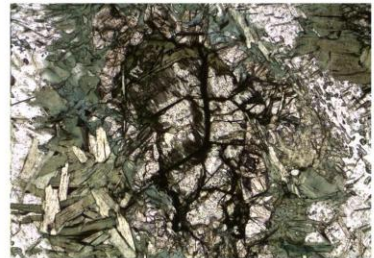
NT / RPGR contact - 92 m

VB96332-6; 5x; XN
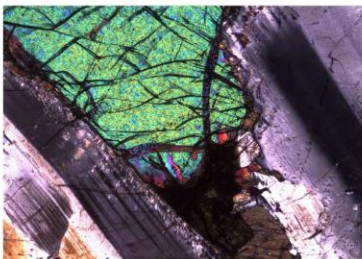
NT - 107 m

VB96332-7; 5x; XN
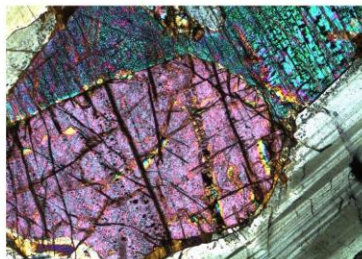
NT - 108 m

VB96332-9; 1.6x; XN
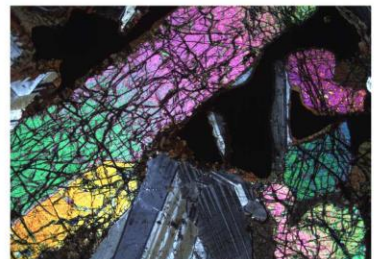
NT - 140 m

VB96332 (cont.)

VB96332-10; 5x; XN
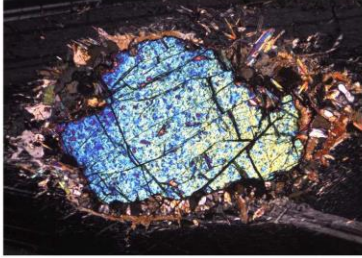
OG - 169 m

VB96332-11; 5x; XN
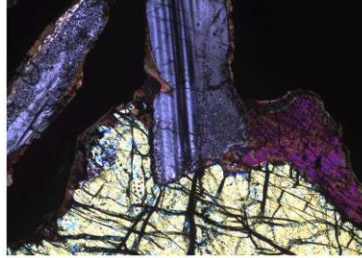
OG - 175 m

VB96332-12; 5x; XN
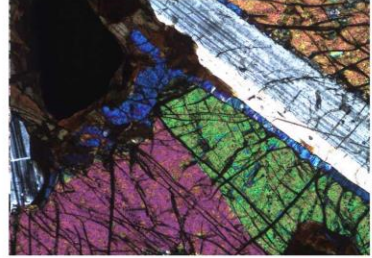
NT - 200 m

VB96332-13; 5x; XN
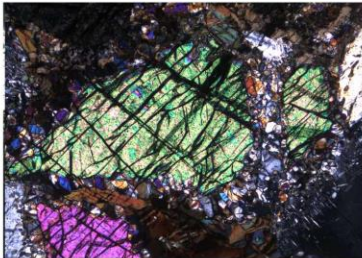
OG - 230 m

VB96332-15; 5x; XN
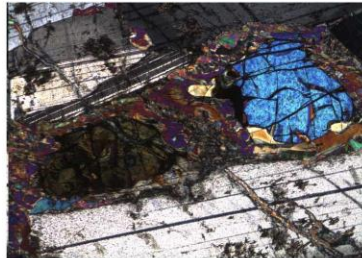
NT - 460 m

VB96332-16; 5x; XN
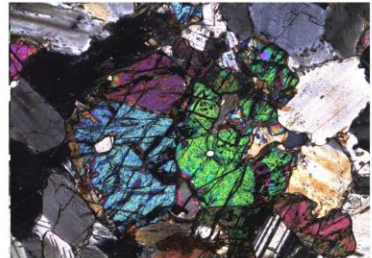
VTT - 680 m

VB99513

VB96332-17; 5x; XN
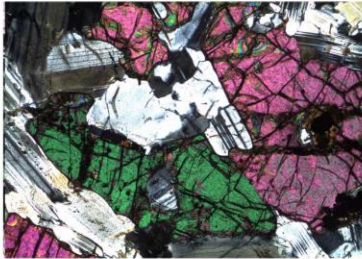
VTT - 719 m

VB99513-1; 5x; XN
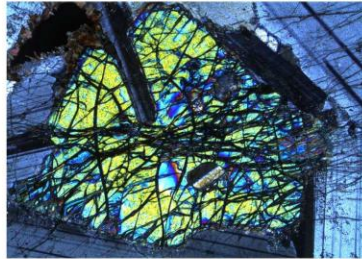
NT - 15 m

VB99513-2; 5x; XN
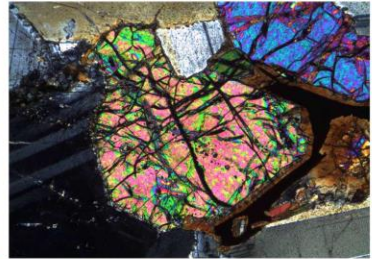
NT - 80 m

VB99513-4; 5x; XN
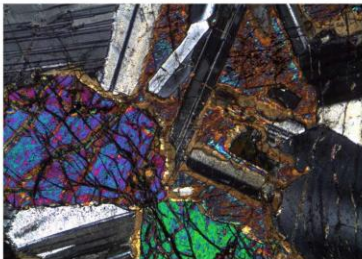
NT - 105 m

VB99513-5; 10x; XN
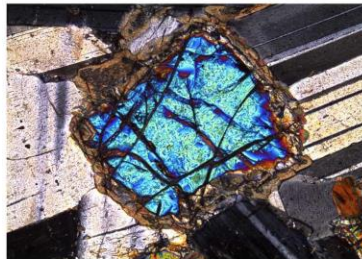
NT - 108 m

VB99513-6; 5x; XN
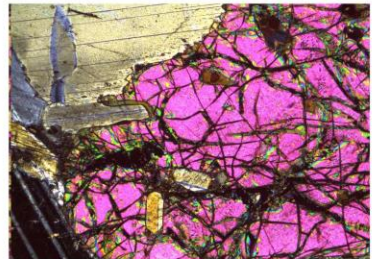
NT - 110 m

VB99513 (cont.)

VB99513-7; 5x; XN
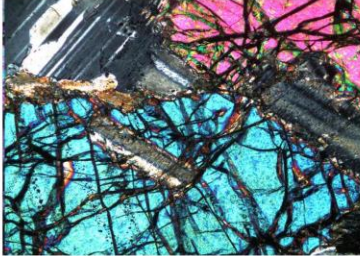
NT - 111 m

VB99513-8; 5x; XN
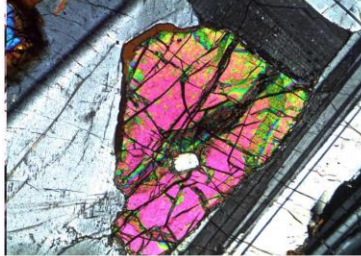
NT - 160 m

VB99513-10; 5x; XN
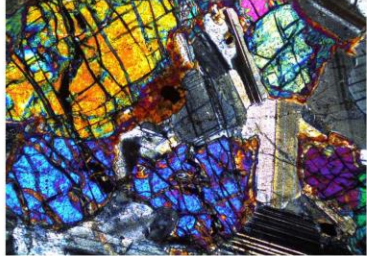
NT - 291 m

VB99513-12; 5x; XN
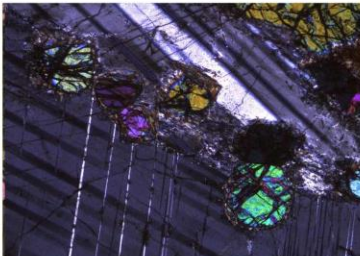
VTT - 340 m

VB99513-13; 5x; XN
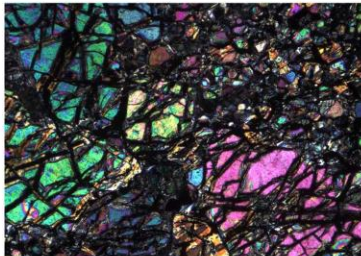
UMF - 384 m

VB99513-14; 5x; XN

UMF - 386 m

VB99513-16; 5x; XN
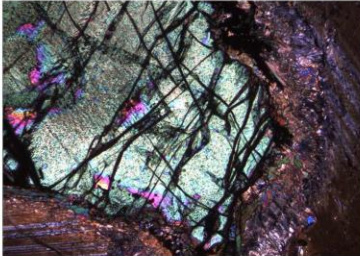
OG - 560 m

VB99513-19; 5x; XN
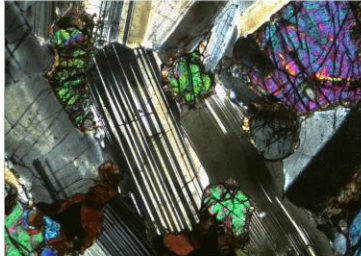
VTT - 583 m

VB99513-21; 10x; XN

NT - 650 m

VB99513-23; 5x; XN
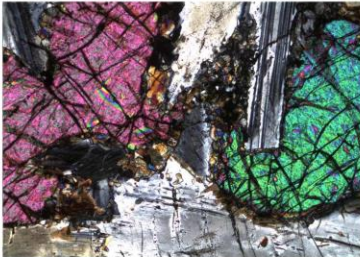
VTT - 705 m

VB99513-24; 5x; XN
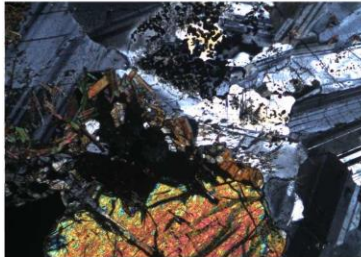
BBS - 710 m

VB99513-25; 5x; XN
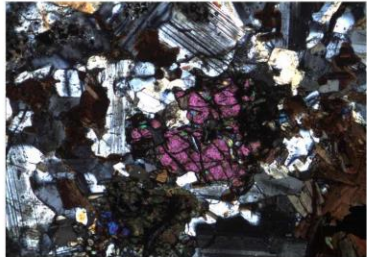
BBS - 740 m

VB99516

VB99516-1; 5x; XN
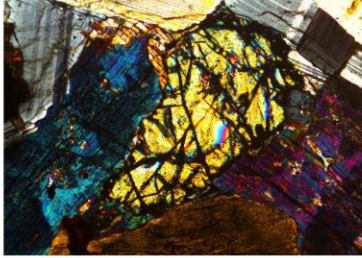
NT - 12 m

VB99516-4; 5x; XN
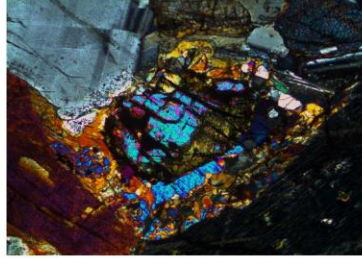
NT - 106 m

VB99516-6; 5x; XN
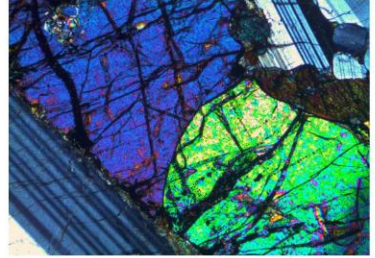
NT - 108 m

VB99516-7; 5x; PP
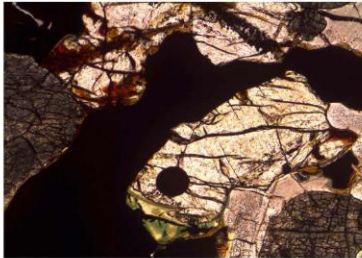
NT - 110 m

VB99516-9; 5x; XN
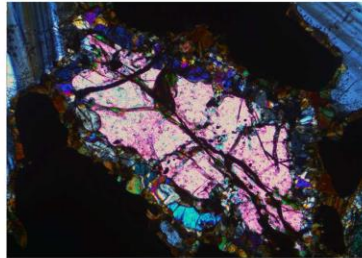
NT - 116 m

VB99516-10; 5x; XN
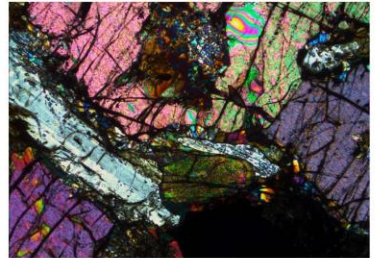
NT - 140 m

VB99516-11; 5x; XN
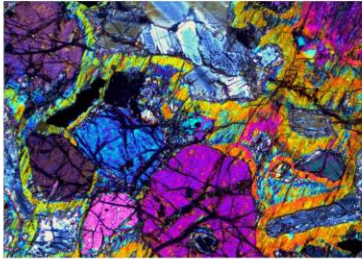
VTT - 199 m

VB99516-13; 5x; XN
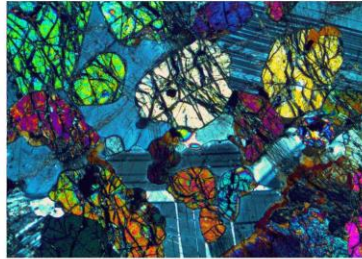
VTT - 240 m

VB99516-14; 5x; XN
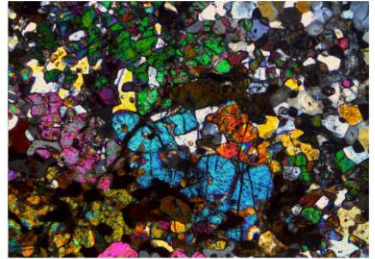
VTT - 260 m

VB96248

VB99516-16; 5x; XN
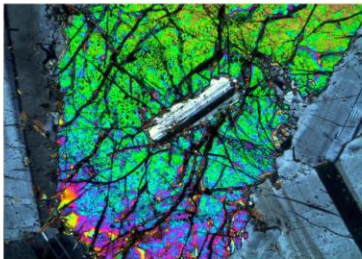
VTT - 280 m

VB96248-1; 5x; XN
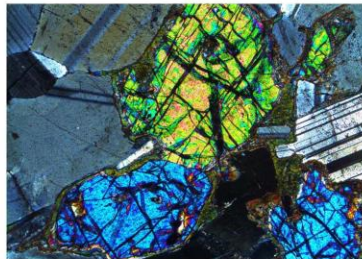
NT - 104m

VB96248-2; 5x; XN
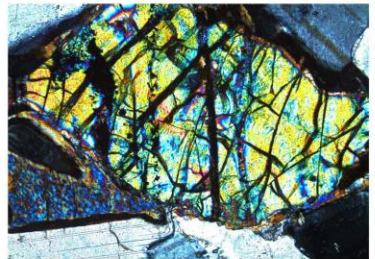
NT - 106 m

VB96248 (cont.)

VB96248-5; 5x; XN
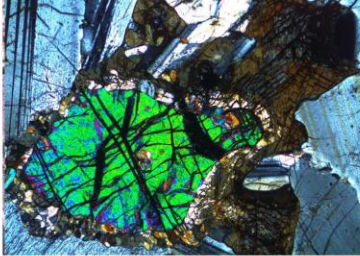
VTT - 182 m

VB96248-7; 5x; XN
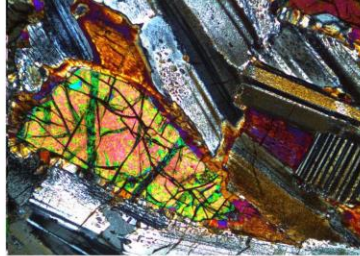
VTT - 260 m

VB96248-8; 5x; XN
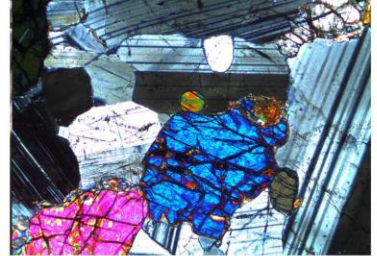
VTT - 290 m

VB96248-9; 5x; XN
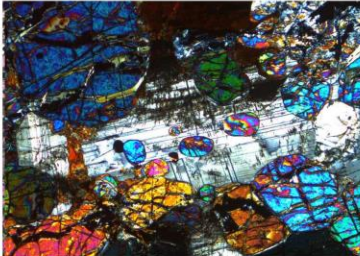
VTT - 297 m

VB96248-12; 5x; XN
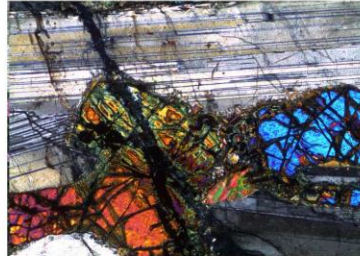
VTT - 378 m

VB96248-14; 5x; XN
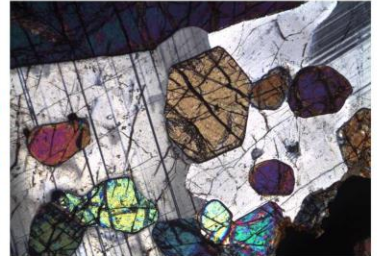
UMF - 442 m

SVB96-02

VB96248-15; 5x; XN
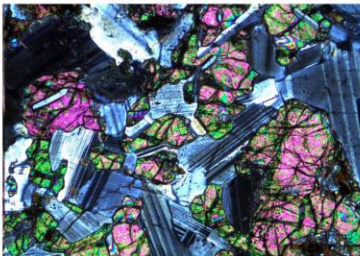
BBS - 559 m

SVB96-02-02; 5x; XN
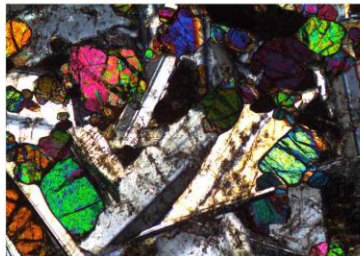
OG - 8 m

SVB96-02-03; 5x; XN
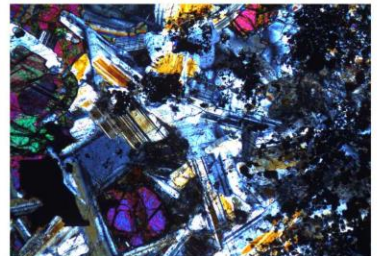
OG/LTT - 22 m

SVB96-10

SVB96-02-05; 5x; XN
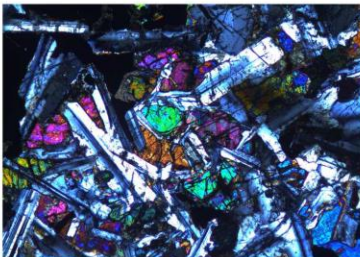
OG - 69 m

SVB96-10-90; 5x; XN
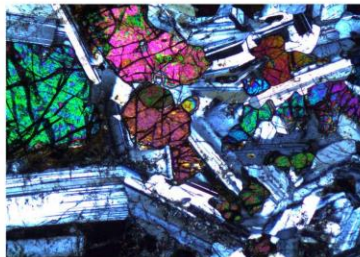
Trans. G - 21 m

SVB96-10-91; 5x; PP
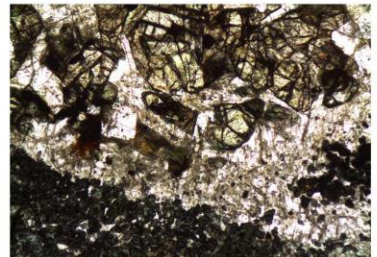
Trans. G - 30 m

SVB96-27

SVB96-27-08; 5x; XN
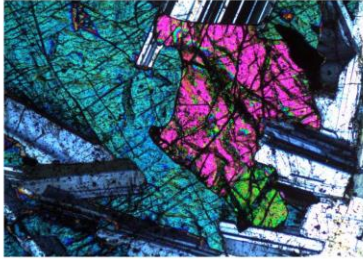
G - 1 m

SVB97-79

SVB97-79-144; 5x; XN
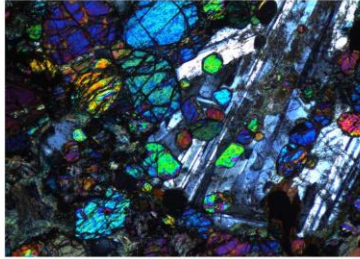
G - 632 m

SVB97-79-147; 5x; XN
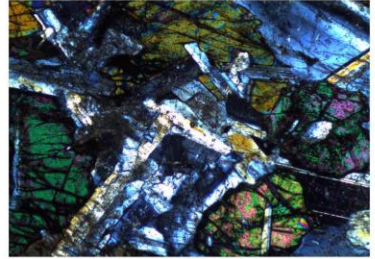
G - 729 m

SVB97-92

SVB97-92-03; 5x; XN
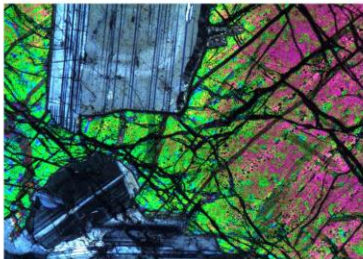
BG - 187 m

SVB97-92-161; 5x; XN
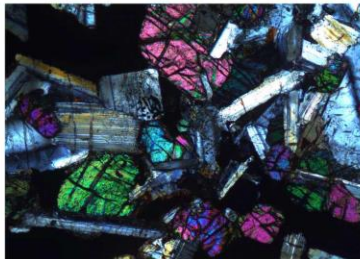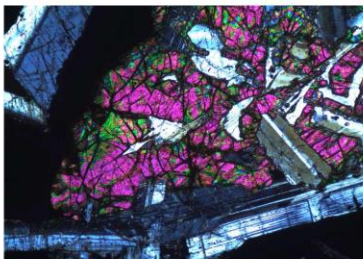

G - 247 m

SVB98-102

SVB98-102-150; 5x; XN
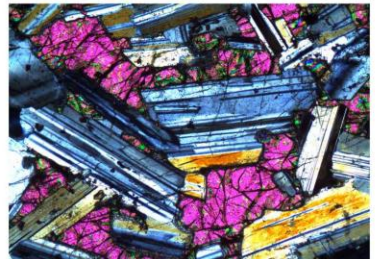
BG - 150 m

SVB98-113

SVB98-113-167; 5x; XN

G - 99 m

6.7. SIMS Raw Data

The SIMS raw data are available on request.

6.8. References

Brenan, J.M., Li, C., 2000. Constraints on oxygen fugacity during sulfide segregation in the Voisey's Bay intrusion, Labrador, Canada. Economic Geology 95, 901–915.

Costa, F., Chakraborty, S., 2004. Decadal time gaps between mafic intrusion and silicic eruption obtained from chemical zoning patterns in olivine. Earth and Planetary Science Letters 227, 517–530.

Costa, F., Dungan, M., 2005. Short time scales of magmatic assimilation from diffusion modeling of multiple elements in olivine. Geology 33, 837–840.

Deer, W.A., Howie, R.A., Zussman, J., 1997. Rock forming minerals: Orthosilicates, 2ed. Geological Society of London. 932 pp.

Godon, A., Webster, J.D., Layne, G.D., Pineau, F., 2004. Secondary ion mass spectrometry for the determination of $\delta^{37}Cl$ Part II. Intercalibration of SIMS and IRMS for aluminosilicate glasses. Chemical Geology 207, 291–303.

Ito, M., Yurimoto, H., Morioka, M., Nagasawa, H., 1999. Co^{2+} and Ni^{2+} diffusion in olivine determined by secondary ion mass spectrometry. Physics and Chemistry of Minerals 26, 425–431.

Jones, R.H., Layne, G.D., 1997. Minor and trace element partitioning between pyroxene and melt in rapidly cooled chondrules. American Mineralogist 82, 534–545.

Ottolini, L., Bottazzi, P., Vannucci, R., 1993. Quantification of lithium, beryllium, and boron in silicates by secondary ion mass spectrometry using conventional energy filtering. Analytical Chemistry 65, 1960–1968.

Petry, C., Chakraborty, S., Palme, H., 2004. Experimental determination of Ni diffusion coefficients in olivine and their dependence on temperature, composition, oxygen fugacity, and crystallographic orientation. Geochimica et Cosmochimica Acta 68, 4179–4188.

Qiuan, Q., O'Neill, H.S.C., Hermann, J., 2010. Comparative diffusion coefficients of major and trace elements in olivine at ~950 °C from a xenocryst included in dioritic magma. Geology 38, 331–334.

Shimizu, N., Semet, M.P., Allègre, C.J., 1978. Geochemical applications of quantitative ion-microprobe analysis. Geochimica et Cosmochimica Acta 42, 1321–1334.

Thomson, A., Maclennan, J., 2013. The distribution of olivine compositions in Icelandic basalts and picrites. Journal of Petrology 54, 745–768.

Weinbruch, S., Specht, S., Palme, H., 1993. Determination of Fe, Mn, Ni and Sc in olivine by secondary ion mass spectrometry. European Journal of Mineralogy 5, 37–41.

Yurimoto, H., Yamashita, A., Nishida, N., Sueno, S., 1989. Quantitative SIMS analysis of GSJ rock reference samples. Geochemical Journal 23, 215–236.